AD-A133 734 RF SYSTEMS IN SPACE VOLUME I SPACE ANTENNAS FREQUENCY 1/3
(SARF) SIMULATION(U) GENERAL RESEARCH CORP SANTA
BARBARA CA A C LUDWIG ET AL. APR 83
UNCLASSIFIED RADC-TR-83-91-VOL-1 F30602-81-C-0119 F/G 17/9 NL

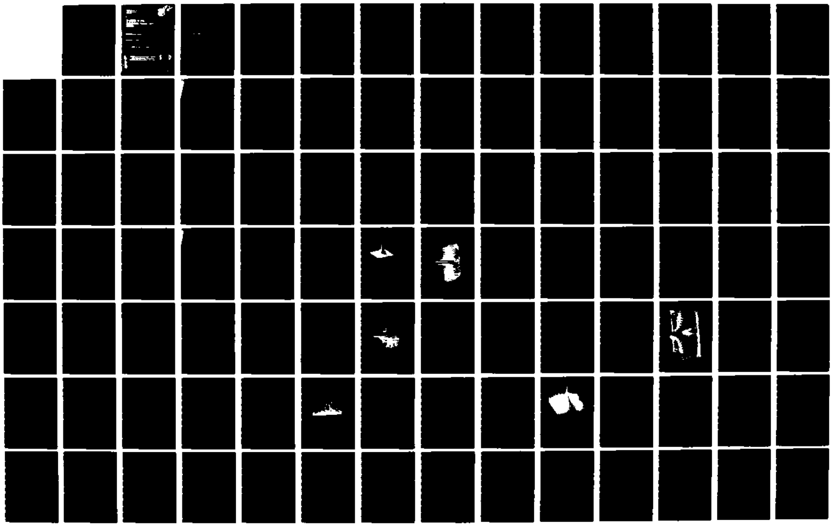

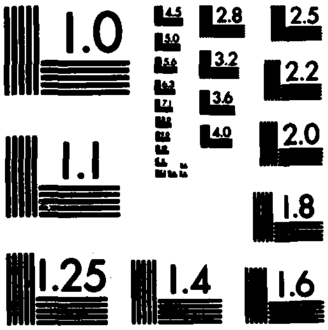

MICROCOPY RESOLUTION TEST CHART
NATIONAL BUREAU OF STANDARDS-1963-A

②

AD-A133 734

[illegible]

[illegible] report has been reviewed by the RADC Public Affairs Office (PA) and [illegible] to the National Technical Information Service (NTIS). At NTIS [illegible] releasable to the general public, including foreign nations.

[illegible]-83-91, Volume I (of two) has been reviewed and is approved for [illegible]

John C. Cleary

[illegible] C. CLEARY
Project Engineer

[illegible]

[illegible]

FOR THE COMMANDER: John P. Huss

JOHN P. HUSS
Acting Chief, Plans Office

[illegible] changed or if you wish to be removed from the RADC [illegible] or if the addressee is no longer employed by your organization, [illegible] RADC (OCSA) Griffiss AFB NY 13441. This will assist us in [illegible] current mailing list.

[illegible] copies of this report unless contractual obligations or notices [illegible] document requires that it be returned.

REPORT DOCUMENTATION PAGE		READ INSTRUCTIONS BEFORE COMPLETING FORM
1. REPORT NUMBER RADC-TR-83-91, Volume I (of two)	2. GOVT ACCESSION NO. AD-A133 734	3. RECIPIENT'S CATALOG NUMBER
4. TITLE *(and Subtitle)* RF SYSTEMS IN SPACE Space Antenna Frequency (SARF) Simulation		5. TYPE OF REPORT & PERIOD COVERED Final Technical Report
		6. PERFORMING ORG. REPORT NUMBER N/A
7. AUTHOR(s) A. C. Ludwig J. R. Freeman J. D. Capp		8. CONTRACT OR GRANT NUMBER(s) F30602-81-C-0119
9. PERFORMING ORGANIZATION NAME AND ADDRESS General Research Corporation P. O. Box 6770 Santa Barbara CA 93111		10. PROGRAM ELEMENT, PROJECT, TASK AREA & WORK UNIT NUMBERS 62702F 45061450
11. CONTROLLING OFFICE NAME AND ADDRESS Rome Air Development Center (OCSA) Griffiss AFB NY 13441		12. REPORT DATE April 1983
		13. NUMBER OF PAGES 258
14. MONITORING AGENCY NAME & ADDRESS*(if different from Controlling Office)* Same		15. SECURITY CLASS. *(of this report)* UNCLASSIFIED
		15a. DECLASSIFICATION/DOWNGRADING SCHEDULE N/A

16. DISTRIBUTION STATEMENT *(of this Report)*

Approved for public release; distribution unlimited.

17. DISTRIBUTION STATEMENT *(of the abstract entered in Block 20, if different from Report)*

Same

18. SUPPLEMENTARY NOTES

RADC Project Engineer: John C. Cleary (OCSA)

19. KEY WORDS *(Continue on reverse side if necessary and identify by block number)*

Simulation
Space-Based Radar
Space Fed Phased Array

20. ABSTRACT *(Continue on reverse side if necessary and identify by block number)*

The main objective of this effort was to develop a computer based analytical capability for simulating the RF performance of large space-based radar (SBR) systems. The model is capable of simulating corporate and space fed aperture. The model also can simulate multibeam feeds, cluster/point feeds, corporate feed and various aperture distributions. The simulation is capable of accepting Draper Labs structural data and antenna current data from Atlantic Research Corporation's (ARC) First Approximation Methods (FAM) and Higher Approximation Methods (HAM) models. In addition there is a routine to input various aper-

tures surface distortions which causes the elements in the array to be displaced from the ideal location on a planar lattice.

There were analyses looking at calibration/compensation techniques for large aperture space radars. Passive, space fed lens SBR designs were investigated. The survivability of an SBR system was analyzed. The design of ground based SBR validation experiments for large aperture SBR concepts were investigated. SBR designs were investigated for ground target detection.

Accession For	
NTIS GRA&I	☒
DTIC TAB	☐
Unannounced	☐
Justification	
By	
Distribution/	
Availability Codes	
Dist	Avail and/or Special
A	

PREFACE

This final report presents results of an 18-month study on Radio Frequency (RF) Systems in Space. The study was performed for the Rome Air Development Center (RADC) by General Research Corporation (GRC). The work performed under this contract is presented in the following five reports:

1. A.C. Ludwig, J. Feeman, A.V. Mrstik, and J. Gardner, RF Systems in Space--Interim Report, General Research Corporation CR-1-1048, September 1982.

2. A.C. Ludwig, J. Feeman, and J. Capps, RF Systems in Space--Final Report, Vol. I, Space Antenna Radio Frequency (SARF) Simulation, General Research Corporation CR-2-1048, December 1982.

3. A.V. Mrstik, D. Beste, R. Bartek, and P. Pazich, RF Systems in Space--Final Report, Vol. II, Space-Based Radar Analyses, General Research Corporation CR-2-1048, December 1982.

4. J.R. Feeman and J.D. Capps, SARF User's Manual, General Research Corporation CR-3-1048, December 1982.

5. J.R. Feeman and J.D. Capps, SARF Sample Computer Simulation Runs, General Research Corporation CR-4-1048, December 1982.

The objectives of the study are:

1. To develop and validate a space-antenna RF (SARF) simulation for modeling the RF performance of large, space-based radar systems

2. To develop calibration/compensation techniques for large-aperture space radars

3. To investigate passive, space-fed lens, space-based radar designs

4. To analyze the survivability of space radar
5. To design ground-based validation experiments for large-aperture space radar concepts
6. To investigate space radar designs for ground target detection

The first objective represents 2/3 of the total effort, and is covered by reports 1, 2, 4, and 5. The remaining objectives, 2 through 5, are covered by report 3. The technical sections of the Interim Report are reproduced as Appendix A of Vol. I.

CONTENTS

VOLUME I

VOLUME II

CONTENTS (Cont.)

ILLUSTRATIONS

ILLUSTRATIONS (Cont.)

ILLUSTRATIONS (Cont.)

ILLUSTRATIONS (Cont.)

ILLUSTRATIONS (Concl.)

ILLUSTRATIONS (Cont.)

TABLES

1 INTRODUCTION

General Research Corporation (GRC) has performed the Radio Frequency (RF) Systems in Space Study in support of the overall Rome Air Development Center (RADC) Space-Based Radar (SBR) program. The background for this program will be briefly reviewed to put the present work in context, and then a summary of results will be given, followed by an outline of the report organization.

1.1 BACKGROUND

The advanced development SBR technology program jointly sponsored by the Air Force and the Defense Advanced Research Projects Agency (DARPA) has provided a foundation in both technology and analysis to support the development of operational SBR systems. These systems are to be capable of detecting Soviet bombers, and perhaps cruise missiles, in clutter. Six or seven satellites at a 5,600 n mi altitude could put a fence around the northern United States for CONUS defense. At a 1,000 n mi altitude, 14-16 satellites would be required. In addition to CONUS defense, SBRs are applicable to

- Space object surveillance
- Missile surveillance
- Ocean surveillance

Table 1.1 lists the characteristics of a representative large-aperture space-based radar. It is a space-fed array using low-power, solid-state transmit/receive modules embedded in a light-weight membrane lens, electronically scannable over a large solid angle. Recent projections based on the technology development programs suggest that such a radar may be achievable in the mid- to late-1980s. These projections have resulted from a number of significant advances in key technology efforts, including:

- Lightweight transmit/receive modules
- Lightweight space-fed lens membranes
- Power distribution analysis

TABLE 1.1

REPRESENTATIVE SBR CHARACTERISTICS

Aperture	200λ
Number of Elements	10^5
Gain	56 dBI
Power Radiated (Average)	5 kW
Bandwidth	2 MHz
Beamforming	1 beam
Scan Angle	±25 deg
Transmit Sidelobes	Uniform aperture illumination
Receive Sidelobes	-70 dB (far out) -40 dB (near in)
Nulls	-110 dB
Temporal Sidelobes	-80 dB
Life	5 years

- Structural analysis and simulation
- Feed analysis and design
- RF analysis and simulation of space-fed lenses
- Analysis and simulation of adaptive nulling
- Design of ground-based RF system tests

As the prospects of orbiting a large-aperture radar grow nearer, it becomes increasingly important to tie together these technology programs carefully to insure that the various subsystem designs are compatible, that no gaps are overlooked, and that the total design satisfies the overall requirements for the system. The present study contributes to the RADC program for fulfilling these needs.

1.2 SUMMARY OF RESULTS: SARF SIMULATION

The SARF simulation has been developed per the statement of work, validated, and applied to selected radar concepts. The software is modular, and has a file structure that greatly facilitates any desired future modifications to the model. This file structure is based on three data sets which in principle totally define an antenna. Any antenna can be considered as an array of radiating sources, and these sources are totally defined by:

1. The complex-valued current excitation of each source
2. The x,y,z coordinates of each source
3. The radiation pattern of each source

For an array antenna, each array element may be modeled as a single source, elements may be subdivided into several sources, or several elements may be combined into a subarray source, depending on the problem at hand (see Sec. 2.1.1.2.3). For a reflector antenna, the reflector surface may be divided into sections and each section modeled as a source.[1]

Simple array models typically assume a real, scalar, isotropic, element pattern—i.e., each array element is assumed to radiate equally in all directions, and the phase and polarization characteristics of elements are ignored. The current source model in the SARF simulation includes complete phase and polarization characteristics, and allows modeling of very complex sources, including subarrays, element failures, and mutual coupling effects.

Another possible simplification is to assume a planar, periodic, array lattice. In contrast, the SARF simulation will handle rectangular or triangular lattices deformed in three dimensions, and also gore designs. An example of a circular aperture with 32 pie-slice shaped gores, where the lattice is rotated 11.25° from one gore to the next, and where the gore edges introduce gaps between the elements, is given in Sec. 2.1.3.3.

---

[1] This is not necessarily the ideal method of modeling a reflector, but it does allow use of the same software for modeling both reflectors and arrays.

The first level of modeling the aperture illumination is to assume an ideal set of current excitations—e.g., samples of a Taylor distribution--perhaps with additive Gaussian errors and/or random total failures. The SARF simulation adds the capabilities of a large menu of ideal distributions (see Sec. 2.1.1.2.1)—including monopulse difference pattern distributions—and then models distortions introduced by the feed, and by the lens. The lens effects include phase shifter quantization, non-linear behavior, and random gain (or loss) variations as well as additive Gaussian errors. In addition to total failures, the simulation can model partial power loss and/or phase bit errors, and major changes in element patterns--e.g., due to deployment failures.

The modular file structure allows a serial processing of the source excitation and location files. For example, the first stage of the excitation file is derived by sampling an ideal aperture illumination at the element locations; this file is then read and processed by a multibeam feed model to introduce feed distortions; at the next step, lens effects are introduced. Therefore, any new source excitation effects can be modeled in the future by inserting a new program module at the appropriate point in this processing chain.

An important feature of the SARF simulation is its capability for incorporating measured data. The source element patterns may be adjusted to model measured element pattern data as shown in Sec. 2.1.1.2.3; the source locations can be distorted to model measured surface data written on magnetic tape, similar to the method for incorporating computed thermal distortions as discussed in Sec. 2.3.4.2. Measured module data is well represented by the non-linear model as shown in Sec. 2.3.2.7.

The SARF simulation has been validated by comparing computed results with analytical, numerical, and experimental data. In addition to the typical analytical cases (uniform illumination, Taylor distributions, etc.), checks have been made against a binomial distribution, which provides an exact analytical standard at levels of -120 dB and lower. Recently, data has been obtained from Grumman on patterns measured using their test article 2 (TA-2) array,[1] and excellent agreement has been demonstrated between the simulated and measured patterns as shown in Sec. 2.1.2.6.

Applications of the SARF simulation have of course just begun, since the main thrust of the present effort was the development and validation of the model. Nevertheless, interesting results have already been obtained. The 32 section gore design mentioned above is shown to still produce unacceptably high sidelobes, and design and evaluation of improved gore designs is clearly one fruitful area for future work. The effect of displacing a feed for a 23 × 60 m elliptical aperture space-fed array has been briefly studied, showing that feed tilts of 1 degree and displacements of 0.05 m are acceptable even for low sidelobe illuminations. The SARF simulation has also been applied to another contract to evaluate the effect of shrapnel on a large phased array.[2] The ability of the SARF simulation to model complex element failure modes was critical to this study, since phase-bit errors were one of the primary failure modes to be studied.

The results obtained to date give some indication of the broad applicability of the SARF simulation. Some interesting future applications include:

- Design optimization (such as the gore design problem mentioned above)
- Evaluation of alternative SBR concepts
- Modeling experiments and incorporating experimental data into the model

---

[1] John R. Diglio, private communication, August 1982.

[2] Mainbeam Precursor Jammer Study, Ballistic Missile Office (BMO), Norton AFB Contract F04704-82-C-0011.

- Identification of technology gaps and potential performance payoffs if improvements can be achieved
- Parametric studies of effects such as feed displacements and module non-linearity
- Nulling studies
- Evaluation of calibration and compensation techniques

The SARF simulation was written in CIFTRAN, a GRC structured language processor for Fortran programs, and developed on the Digital Equipment Corporation VAX-11 computer at GRC; it has also been installed on the RADC VAX. Wide utilization of the model is anticipated for the above applications and for new uses that cannot be currently foreseen.

1.3 REPORT ORGANIZATION

The results of the first six months of this study have been presented in an interim report, which includes much of the analytical foundation of the SARF model, and portions of the validation data. These results are not duplicated in the main body of the report, but are summarized or referenced when appropriate; the technical sections of the Interim Report are attached as Appendix A.

Section 2, of Vol. I, of this final report, describes the development of the SARF simulation. (Volume II contains Secs. 3 through 7, which describe the results of the remaining RF Systems in Space tasks.)

Section 2.1 provides a summary of the SARF simulation accomplishments. First the simulation design and development is described in Sec. 2.1.1. We review the specifications originally given in the statement of work, and show how the simulation was developed to meet these requirements. The validation of the model is then covered in Sec. 2.1.2, including comparisons of simulated array performance and experimentally measured array patterns. Applications of the simulation to specific SBR antenna concepts are then presented in Sec. 2.1.3, including antenna pattern calculations representative of full-scale SBR designs.

As noted above, most of the supporting analysis for the simulation is given in the interim report. One particularly difficult area concerns the accuracy of the simulation for antennas with distorted surfaces. Section 2.2 presents analysis of this issue, and provides a methodology to insure accurate results for these cases.

The simulation software is described in Sec. 2.3, providing sufficient detail to understand the functions of the model. Further detail on the software is provided in the User's Manual.[1]

---

[1] J.R. Feeman and J.D. Capps, SARF User's Manual, General Research Corporation CR-4-1048, December 1982.

2 SPACE ANTENNA RF (SARF) SIMULATION

2.1 SUMMARY OF SIMULATION SPECIFICATIONS AND ACCOMPLISHMENTS

The RADC statement of work for the SARF simulation can be divided into three categories:

1. Development of a comprehensive RF computer model for space-based radar antennas
2. Validation of the model using theoretical and experimental data
3. Application of the model to selected concepts

In order to accurately evaluate performance differences between alternate SBR concepts, the model must include all significant structural and electrical effects, and be applicable to a wide scope of designs. The model development to meet these requirements is described in Sec. 2.1.1.

Since the utility of the model is completely dependent on the credibility of the results, model validation is at least as important as model design, and Sec. 2.1.2 discusses several of the procedures used to test the model, including its internal validation capability using a brute-force evaluation of the exact array equation.

The ultimate purpose of the model is, of course, to evaluate the performance of specific concepts and parametrically evaluate the effect of component and subsystem performance levels. Some initial applications of the SARF simulation are given in Sec. 2.1.3, which indicate the broad range of potential uses of the model, as well as providing some significant initial results.

2.1.1 SARF Simulation Design and Development

The SARF simulation has been designed and developed to meet the following requirements:

- Use modular software design and structured code to facilitate any desired future modifications
- Model all structural and electrical effects which significantly impact antenna performance
- Model all potentially useful antenna designs
- Output all pertinent performance parameters
- Incorporate prior technology program results to the greatest possible extent

The following sections will discuss each of these requirements in turn, describing how the simulation was structured to satisfy the specified need.

2.1.1.1 Modular Structure of the Simulation

The overall structure of the simulation is shown in Fig. 2.1. As mentioned previously, this structure is based on three sets of data which totally define the *antenna:*

- The source current excitations I_n
- The source location vector $\bar{\rho}_n$
- The source element pattern $\bar{F}_n$

The current excitations and source locations are represented by similar data files, with one entry for each array element (or other source of radiation). For the current excitation, the entry consists of a complex number representing the real and imaginary parts of I_n. For the locations, the entry consists of three numbers representing the Cartesian coordinates of the element location vector $\bar{\rho}_n$. These data files are processed in a serial manner to model various structural and electrical effects, as shown in the flow chart, Fig. 2.2. For example, as previously described, the nominal (ideal) excitation file is input to the feed/lens programs, which perturb the excitations, and write a new data file representing the true excitations.

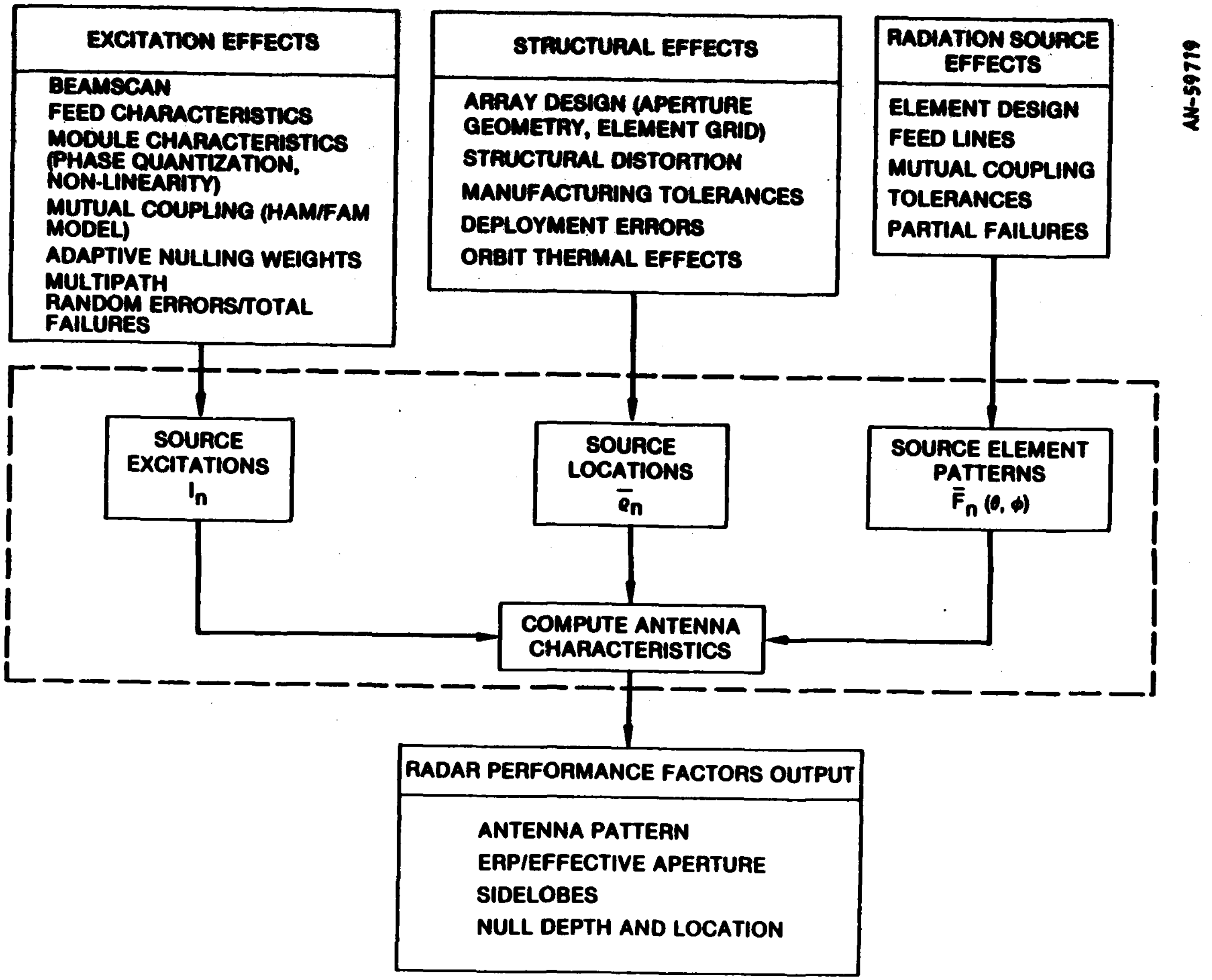

Figure 2.1. SARF Simulation Structure

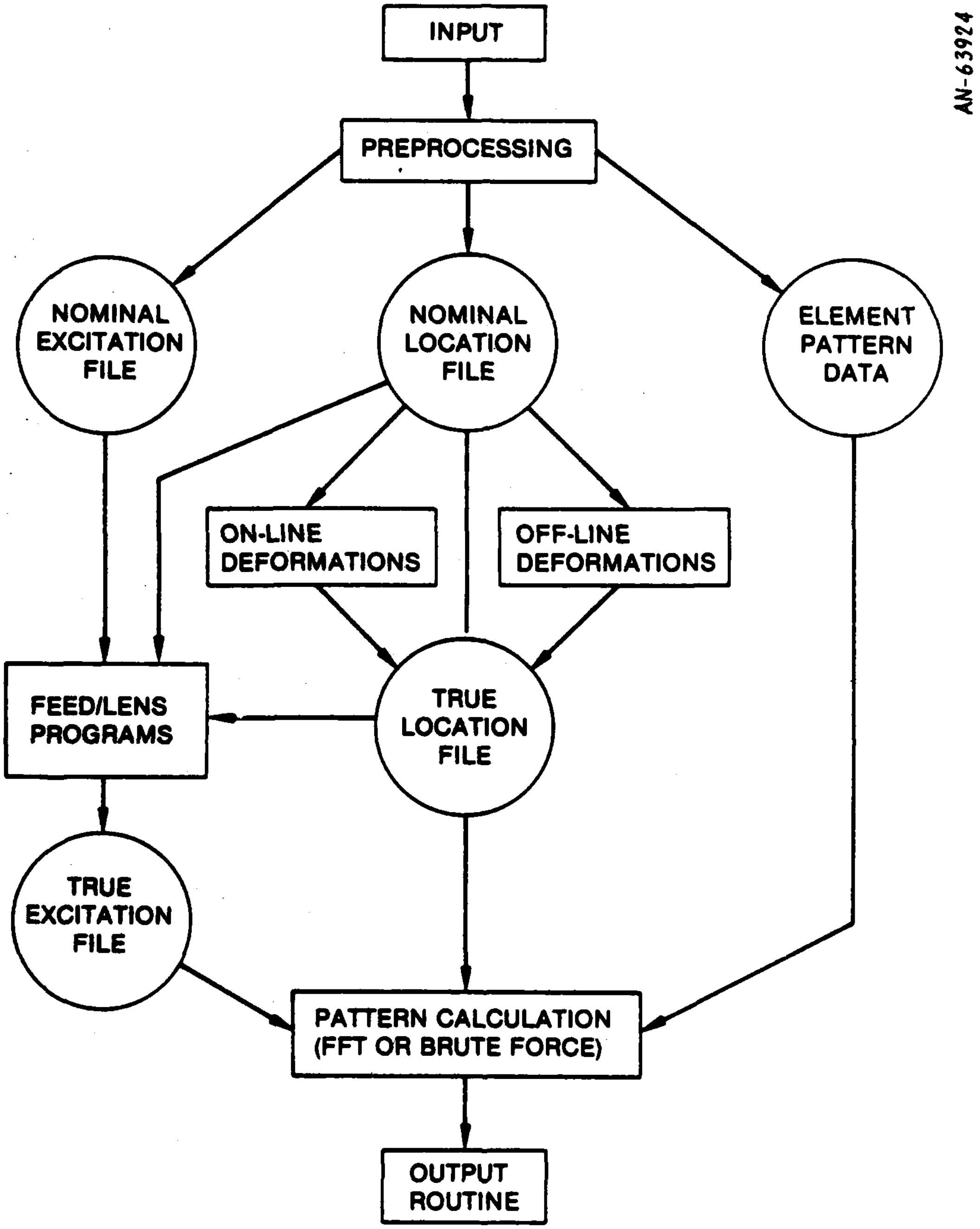

Figure 2.2. SARF Simulation Flow Chart

The source element patterns are represented by a data set for one or more distinct types of element patterns, as discussed below, and are specified in their true and final form by the input data.

Once the three basic data sets are established, they are processed by the pattern calculation software modules to compute the antenna characteristics. Finally, a set of output routines provides one or more of the user selected output options described below.

The computer code implementing this modular simulation structure is written in CIFTRAN, a GRC developed structured language preprocessor for FORTRAN programs. Detailed information on the code is contained in the User's Manual.

2.1.1.2 Structural and Electrical Effects Modeled

The primary structural and electrical effects modeled are shown in Fig. 2.1. All effects must be manifested in the three basic data sets, and the models for each set are discussed below individually.

2.1.1.2.1 Source Excitation Model

The bottom line output of the source excitation model is the data file of true source excitations I_n at the target side of the lens, as shown in Fig. 2.3. There are two stages in the model: (1) the feed, and (2) the lens. The feed portion of the model provides the excitation at the feed side of the lens, and the lens portion models the effects of the feed side elements and lens modules to transform the feed side excitation to target side excitations.

As shown in Fig. 2.3, the SARF simulation provides an option of three types of feeds, including a multibeam space feed and a corporate feed, and two lens model options. The lens can be active or passive. These models are described in detail in Sec. 2.3.2.

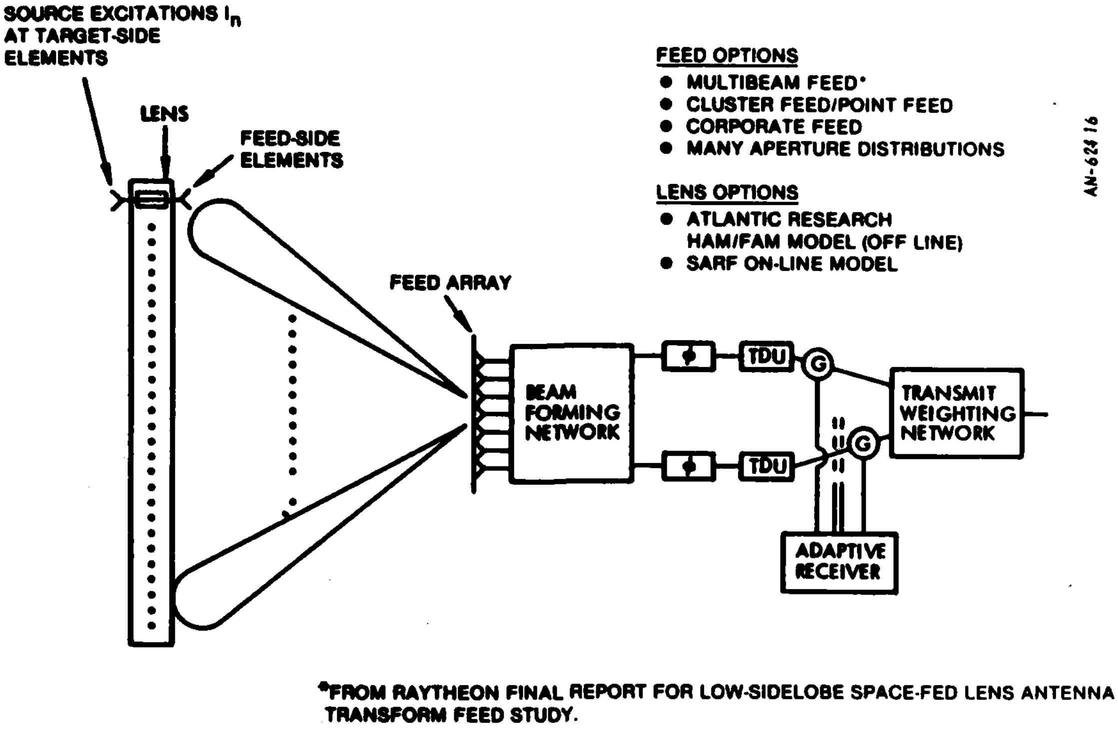

*FROM RAYTHEON FINAL REPORT FOR LOW-SIDELOBE SPACE-FED LENS ANTENNA TRANSFORM FEED STUDY.

Figure 2.3. Source Excitation Model

For corporate fed or multibeam space fed designs, the source excitation model begins with a file derived by sampling an ideal aperture illumination, which may be selected from the comprehensive menu given in Table 2.1. For the cluster feed/point feed options, the user must directly input the feed excitations.

Element failures in the feed array and/or the lens are also modeled in this section of the code, but only total failures, where the excitation current is zeroed out. More complicated failures such as a partial loss of power, dropped phase shift bits, etc., are modeled using the element patterns as discussed below.

TABLE 2.1

SARF SIMULATION NOMINAL APERTURE DISTRIBUTIONS

- Apply to Corporate-Fed or Space-Fed Designs With Array Feeds
- Sum Patterns
    - Uniform, Cosine on a Pedestal, Gaussian
    - Generalized Taylor, Bickmore-Spellmire
    - Blackman, Kaiser, Hamming
    - Triangular, Bessel, Cubic
    - Binomial, Impulse
- Difference Patterns
    - Any Sum Pattern Distribution But With Difference Phasing
    - Bayliss

2.1.1.2.2 Source Location Model

The *bottom line output of* the source location model is the data file of true source locations $\bar{\rho}_n$ at the target side of the lens. The source location model begins with a file of nominal source locations on a planar periodic grid. The options for the nominal array design include:

- Rectangular, circular, or elliptical aperture
- Rectangular or triangular element lattice
- Uniform lattice, or circular gore designs 1, 2, or 3

Examples of gore designs are given in Sec. 2.1.3.3. These nominal locations may then be perturbed systematically and/or randomly. Systematic deviations may be specified by a polynomial displacement in the x, y, and z coordinates, respectively, representing membrane in-plane perturbations (i.e., stretching), and out-of-plane perturbations, as illustrated in Fig. 2.4. Alternatively, point-by-point structural deformations obtained experimentally or by off-line analysis may be input on

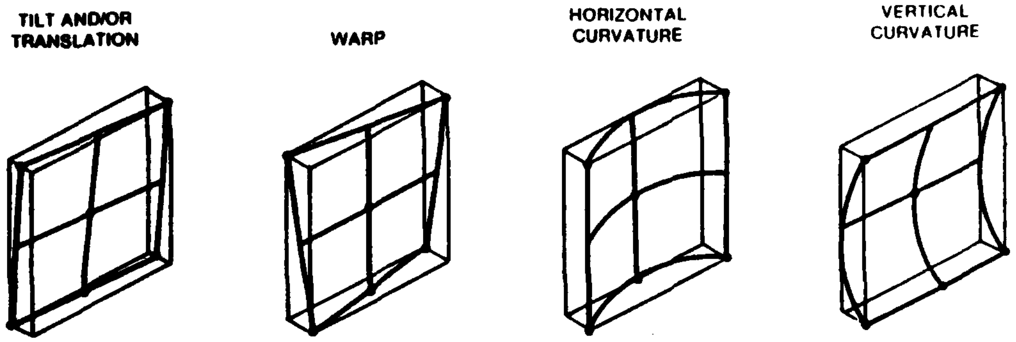

- SYSTEMATIC POLYNOMIAL DISPLACEMENT IN X, Y, AND Z COORDINATES
- POINT-BY-POINT DATA INPUT BY TAPE (E.G. DRAPER DATA)
- RANDOM DISPLACEMENTS IN 3 DIMENSIONS

Figure 2.4. Source Location Model

---

tape. An example using deformations calculated by Draper Labs for orbital thermal effects is given in Sec. 2.1.3.2. Finally, random deformations in any or all three coordinates may be specified, by inputting standard deviations σ_x, σ_y , and σ_z , one for each coordinate.

2.1.1.2.3 Source Element Patterns

The bottom line output of the source element pattern model is a complex vector valued radiation pattern $\overline{F}(\theta,\psi)$, where θ and ψ are the spherical angular coordinates of the output antenna pattern. This pattern is in general derived from a source model consisting of one or more current segments. The SARF simulation provides options for

1. A simple isotropic source pattern
2. One or more types of sources (up to 10 types)
3. One or more current segments per source (up to 50)

Simple Sources. For an isotropic source pattern, no further input is required, and a uniform amplitude, phase, and polarization pattern is used for all array elements. The next level of sophistication is to still assume all array sources are identical, so only one source type is specified, but model the source by a single current segment. This provides the amplitude (phase is uniform), and polarization characteristics of an infinitesimal dipole.

Complex Current Sources. By increasing the number of current segments, increasingly complex elements can be modeled. For example, Fig. 2.5 shows an example of a dipole over a ground plane. The dipole is represented by three segments, and the feedline by one segment, illustrated by the short arrows. The ground plane image is then represented by four additional segments for a total of eight segments. The data set for the current segments consists of

- Three numbers defining the x, y, and z coordinates of each current segment (with respect to the dipole phase center)
- Six numbers defining the real and imaginary parts of the x, y, and z components of each current segment

Therefore, each current segment is defined by nine numbers, so for the eight current segments in the example of Fig. 2.5, 72 numbers are required; typically only a few of these numbers are non-zero. For example, in many problems the feedline radiation is negligible, eliminating two segments; the dipole has only real currents in the y direction, eliminating the x and z current components, and the imaginary parts of the currents. This leaves the real part of the y current and the location of six segments to be specified, or 24 numbers.

Examples of current segment models are given in Fig. 2.6. With increasing levels of complexity we show an isotropic source, an infinitesimal dipole--which is a good representation of most short radiators,

- **COMPLETE POLARIZATION AND PHASE CHARACTERISTICS**
- **UP TO 50 SEGMENTS PER ELEMENT**
- **SUBARRAY MODELING**
- **UP TO 10 TYPES OF DEVIATIONS**
- **RANDOM PATTERN DEVIATIONS**
- **MODELING OF MUTUAL COUPLING INDUCED CURRENTS**

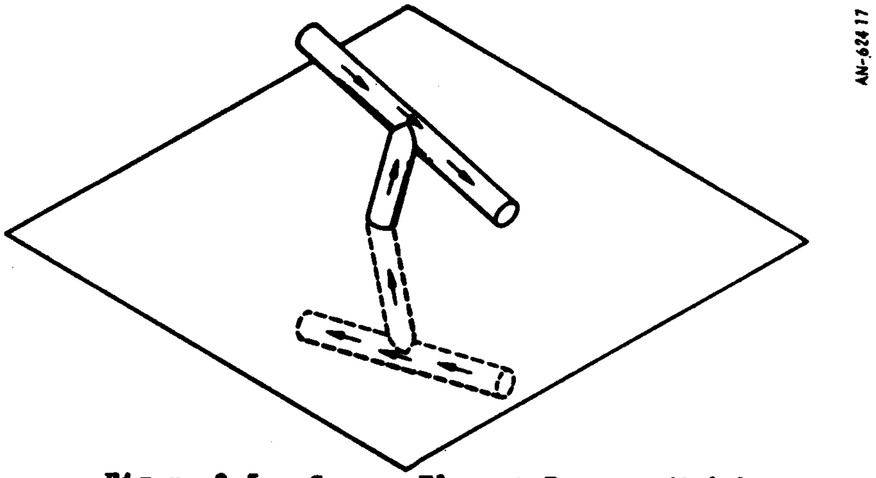

Figure 2.5. Source Element Pattern Model

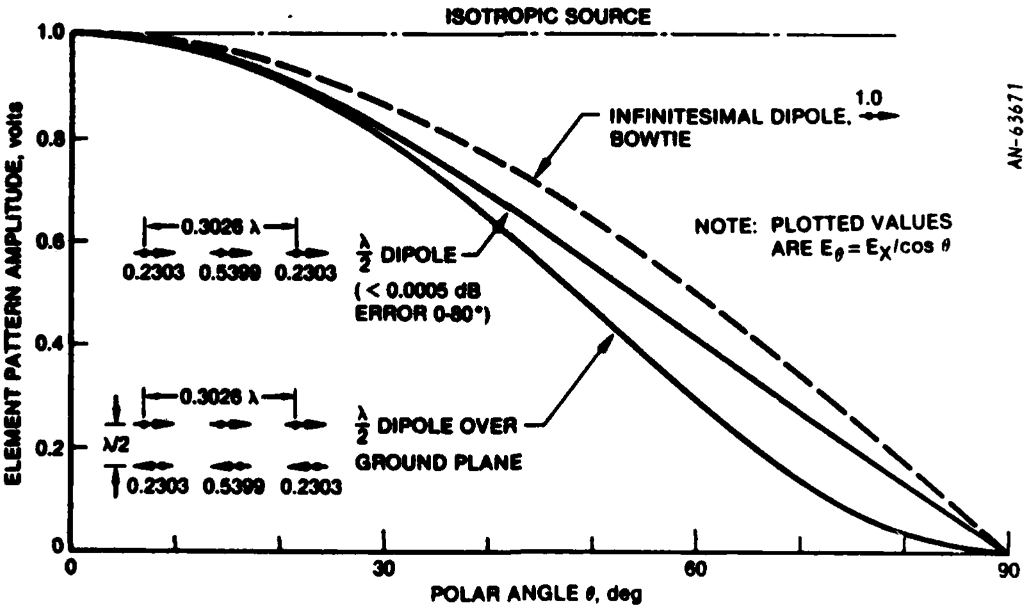

Figure 2.6. Current Segment Model Examples; E-Plane Element Patterns

such as a short bowtie—a half-wave dipole, and a half-wave dipole over a ground plane. A half-wave dipole can be modeled very accurately with three current segments with the amplitudes and spacing shown in Fig. 2.6. The discrepancy between the continuous half-wave source and the three discrete sources is less than 0.0005 dB over the 0-80° range in θ. Over a typical mid-altitude SBR coverage range of 22 degrees, there is not a great difference between the amplitude patterns shown in Fig. 2.6; however, there are cases where differences can be important:

- Differences in phase and/or polarization can have a profound effect on nulling
- Differences at wide angles are important for ECCM against satellite jammers for mid-altitude SBRs, and against earth-based jammers outside the coverage region for low altitude SBRs

Another common element type is a dipole turnstile, which provides circular polarization. A turnstile is modeled by modeling two dipoles, one polarized in the x-direction, and the other in the y-direction, with the currents of one set equal to the complex conjugate of the currents of the other.

Microstrip Radiators. A microstrip radiator may be approximated closely by the current segment model using the duality principle illustrated in Fig. 2.7. The first illustration represents the real physical problem of a conducting disk a distance h over a ground plane (the dielectric substrate and other details could be included but will be omitted for simplicity). Using image theory, this problem is equivalent to the second problem of two facing conducting disks separated by $2h$. Then the next step is to construct the "dual" of the second problem, a thin conducting ring of width $2h$, shown as problem #3. Problem #2 is in principle an exact equivalent of problem #1. However, problem #3 is not an exact equivalent of problems #1 and #2, although it may be sufficiently close. Duality is exact for some problems; the classic

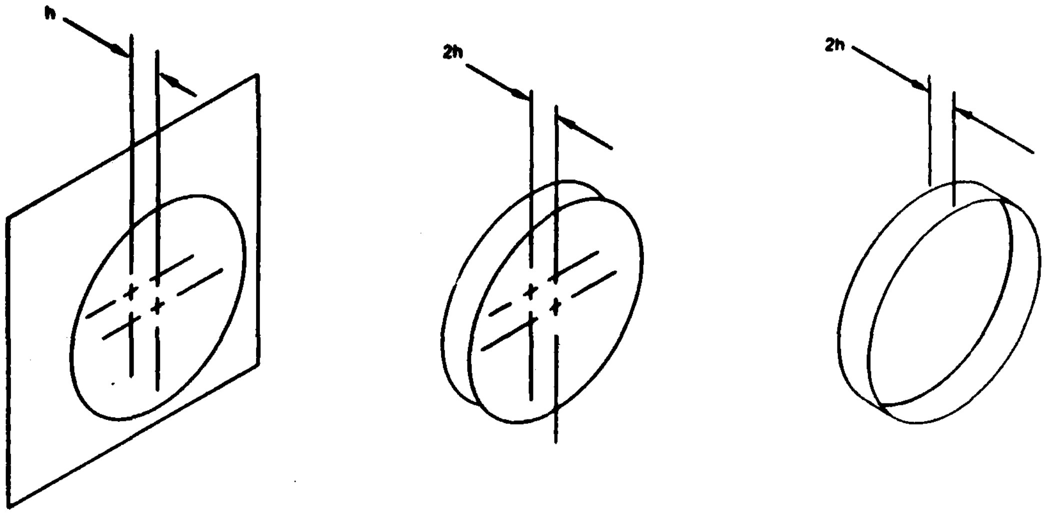

PROBLEM #1
CONDUCTING DISK OVER A
GROUND PLANE

PROBLEM #2
CONDUCTING DISK AND ITS
MIRROR IMAGE

PROBLEM #3
CONDUCTING RING
(DUAL PROBLEM)

Figure 2.7. Duality Solution for Microstrip Radiator

example is the duality between a slot in a conducting ground plane and its dual of a thin flat dipole.[1] The trouble with the particular problem we are dealing with here is illustrated in Fig. 2.8. For problem #2, the E-field lines are always exactly perpendicular to a perfectly conducting disk; for problem #3, the magnetic field lines are slightly off-perpendicular at the corresponding point on the ring plane. For small widths h the solution will certainly be very close, but if the ground spacing becomes large, a significant error may be introduced. Assuming that the duality approach is adequate, the ring may be modeled in a manner similar to a dipole, with current segments representing the ring. The electric and magnetic fields are reversed in going from problem #2 to the dual problem #3, so the resulting antenna pattern is a

---

[1] R.J. Compton and R.E. Collin, "Slot Antennas," Chapter 14 in Antenna Theory Part 1, R. Collin and F. Zucker, eds., McGraw-Hill, 1969.

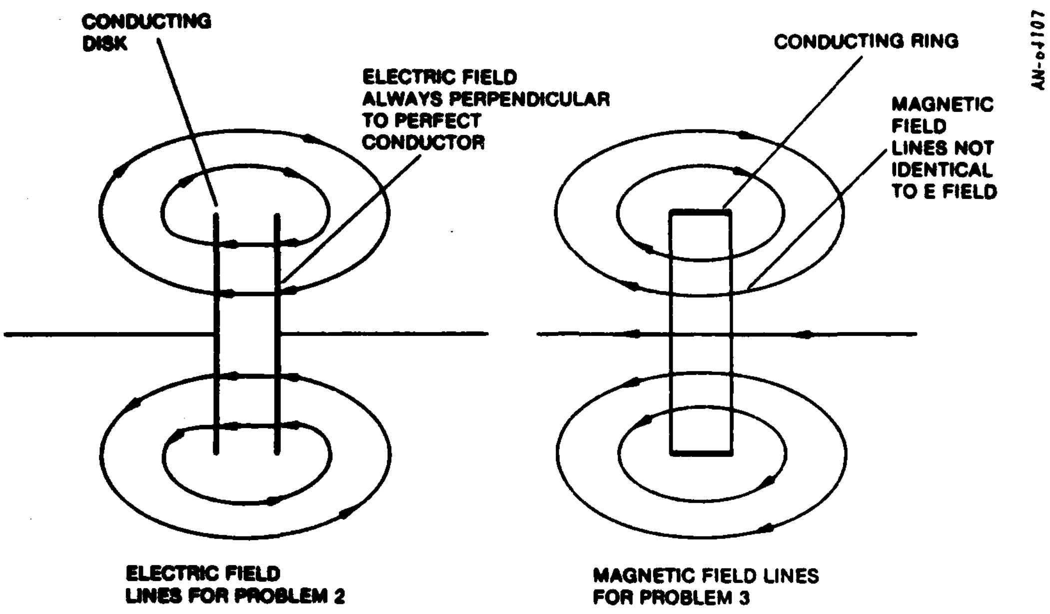

Figure 2.8. Error in Duality Solution

magnetic field pattern, which has the same amplitude and phase, but orthogonal polarization to the electric field pattern.

Reflectors. As stated previously, a reflector can be modeled by dividing the reflector surface into patches and modeling each patch as a source. In principle this procedure is quite accurate, and it has been shown that with patches 2/3 of a square wavelength in size, deriving the current segments from the physical optics approximation, very accurate results can be obtained.[1] In practice this can be very cumbersome, and since the reflector deviates substantially from a plane, the issues discussed in Sec. 2.2 can be a problem. A better alternative, based on aperture theory, is to divide the reflector aperture into equally-sized

---

[1] A.C. Ludwig, Calculation of Scattered Patterns From Asymmetrical Reflectors, Jet Propulsion Laboratory Technical Report 32-1430, February 1970.

square patches, and then model the square aperture patch by a set of current segments roughly a quarter-wavelength apart. This technique is easy to implement and will provide accuracy equivalent to aperture integration, which is quite good except at very wide angles.[1] Surface distortions can be approximately modeled by selecting the corporate feed option, and by inputting twice the axial distortion that is physically present in the reflector, to account for the two-way path length error present in the reflector. This approximation is less accurate for deep dishes (low focal length to diameter ratios), and program modifications should be made if accurate results are desired for such cases.

Subarrays. To reduce the number of phase shifters, phased array antennas frequently employ subarrays, in which several array elements are driven by a single phase shifter. Such subarrays are easily modeled using the SARF simulation source element pattern model, by defining the source to be the subarray, and inputting one (or more) current segments for each element in the subarray. The phase center of the subarray is the reference point for the current segment coordinates, and one subarray is placed at each source location point $\bar{\rho}_n$. This not only provides a faithful representation of the antenna, but reduces the computer time by a factor roughly equal to the number of elements in the subarray, and can be used for this purpose too. All of the other features discussed in this section may be applied to such subarrays, providing tremendous flexibility. The application of the SARF simulation to the defense suppression weapon concept discussed in Sec. 2.1.3.6 involves 2 × 2 subarrays with various failure modes, as an example of this capability.

Mutual Coupling. There are basically two alternative concepts for handling mutual coupling effects:

---

[1] S. Silver, Microwave Antenna Theory and Design, McGraw-Hill, 1949.

1. Neighboring elements induce currents in the element under consideration (say element n), and all of these currents are superimposed to obtain a new current excitation I_n.
2. The element under consideration induces currents in neighboring elements, and all of these induced currents are considered to be additional source currents associated with the nth element, producing a new element pattern $\overline{F}_n(\theta,\phi)$.

Both of these approaches are in principle exact, if all details are properly handled. The first approach is the one adopted by Atlantic Research Corporation in their HAM/FAM model,[1] and is manifested primarily by perturbing the element excitation file. A different set of excitations is obtained for each beam scan angle. Although the current shape also changes on each element, to the first order the element pattern $\overline{F}_n(\theta,\phi)$ is unchanged. The current segment model used by the SARF simulation is adopted from the HAM/FAM model so the currents can be read in from a tape generated by this model to include these effects as well.

The second approach can be directly implemented on-line using the SARF element model. In this case, the excitation file is unchanged by mutual coupling, and the model is valid for all scan angles.

An example of this approach is provided by the modeling of the Grumman TA-2 array data. Figure 2.9 shows the 19-element test array used to measure the embedded element patterns. The center element was driven, and the remaining 18 elements were terminated in a matched load. The numerical values shown by each element were determined empirically by GRC to match the measured element patterns. These values represent the currents induced by mutual coupling in the terminated elements, and the driving current in the center element. This array of 19 currents is

---

[1] H.K. Schuman, D.R. Pflug, and L.D. Thompson, Space-Based Radar Array System Simulation and Validation, First Technical Report, RADC-TR-80-294, Rome Air Development Center, September 1980.

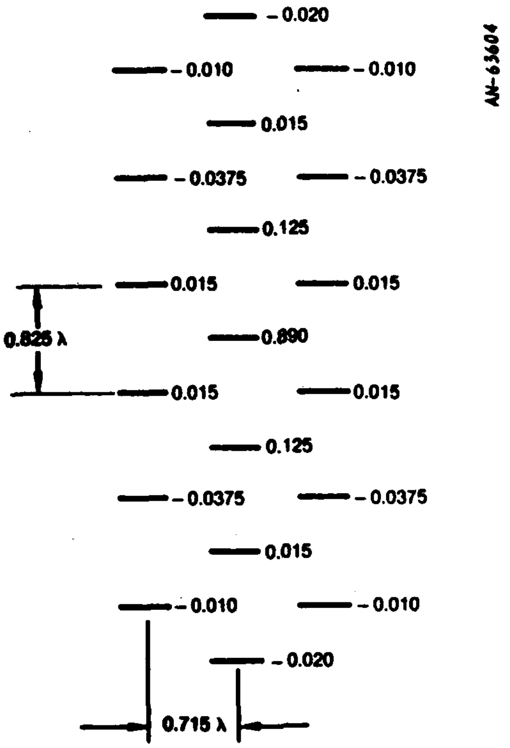

Figure 2.9. Grumman 19-Element Test Array

then defined as the current set for each source in the array. One such source is located at every element location in the array, so there is a large overlap between sources. This overlap provides the equivalent superposition that one would obtain with the alternate ARC approach.

The patterns resulting from this model are compared to the measured Grumman data[1] in Figs. 2.10 and 2.11. These figures clearly demonstrate that the model provides an excellent means for incorporating measured pattern data including the effect of mutual coupling. The principal polarization is matched very well over a large angular

---

[1] John Diglio, op. cit.

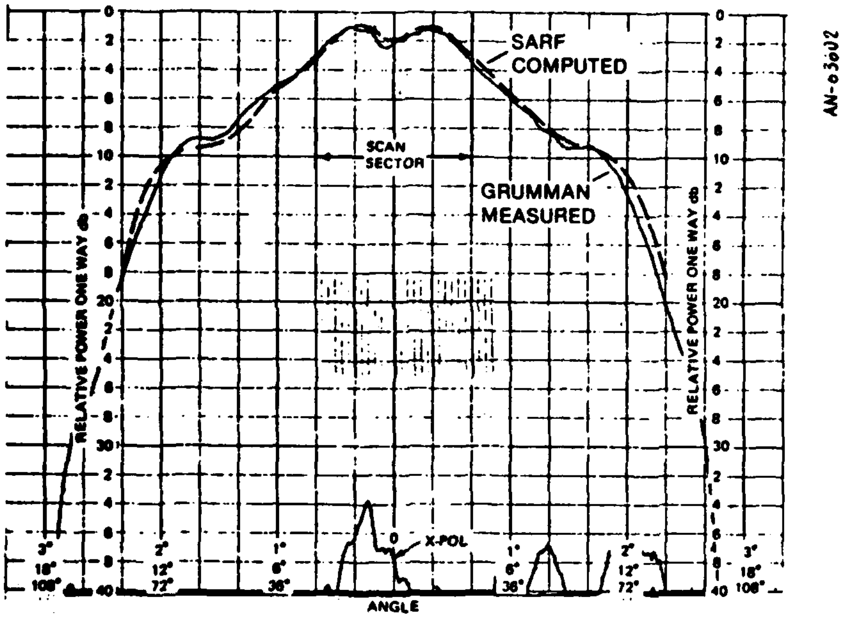

Figure 2.10. Measured and Modeled Embedded Element H-Plane Patterns

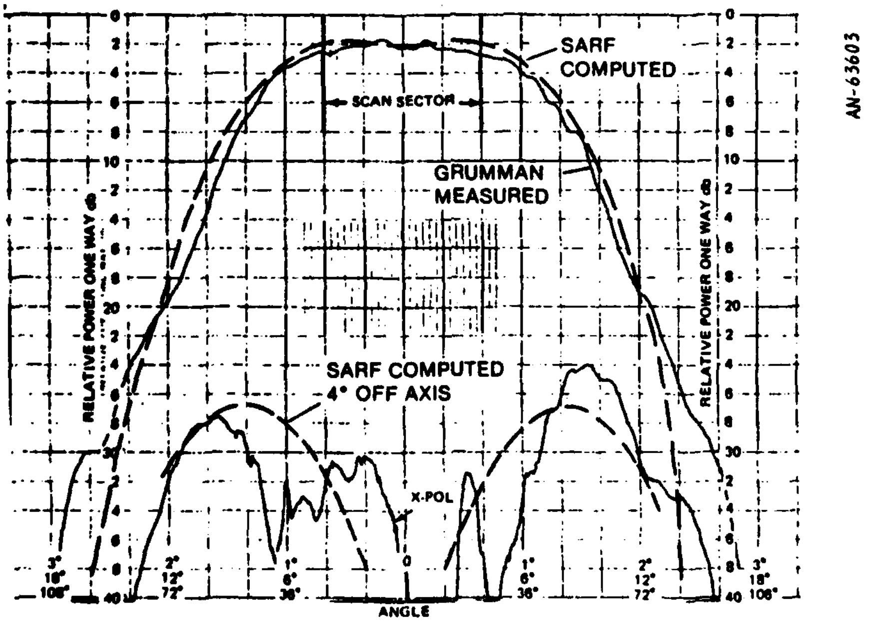

Figure 2.11. Measured and Modeled Embedded Element E-Plane Patterns

sector--much larger than the scan sector of an SBR. The only significant discrepancy is that the model has zero cross polarization, whereas the measured data cross polarization--particularly in the E-plane--is significant. Figures 2.12 and 2.13 show full 3D plots of the principal and cross polarization predicted by the model. It is seen that the cross polarization is zero only in the two principal planes; with even a slight deviation from the principal plane, the cross polarization predicted by the model is significant. In Fig. 2.11, the level of cross polarization is shown for a 4° off-axis cut through the pattern, which is roughly in agreement with the measured values. This suggests the possibility that there was a slight misalignment in the experimental setup.

<u>Multiple Types of Sources/Partial Failures</u>. The assumption that all sources in the array have the same radiation pattern is a common one since it greatly simplifies array analysis. There are cases in which this assumption is unsatisfactory, e.g.,

1. Edge elements which exhibit significantly different mutual coupling effects
2. Element failure modes other than total shutoff

The SARF simulation provides the capability of modeling up to ten different element types per array. For the mutual coupling modeling technique just discussed (for a uniform infinite array) one embedded element pattern would be sufficient to determine the pattern characteristics of the full active array. However, in general, patterns for edge elements (or any other element with a unique environment) should be measured individually, and each significantly different type assigned its own set of currents. This is analogous to the ARC HAM/FAM model, where the FAM analysis assumes all elements behave identically, and the HAM analysis corrects for edge elements, etc. If more than one embedded element pattern is measured, then it is important that phase be measured as well as amplitude, in order to correctly model the patterns. This is due to the

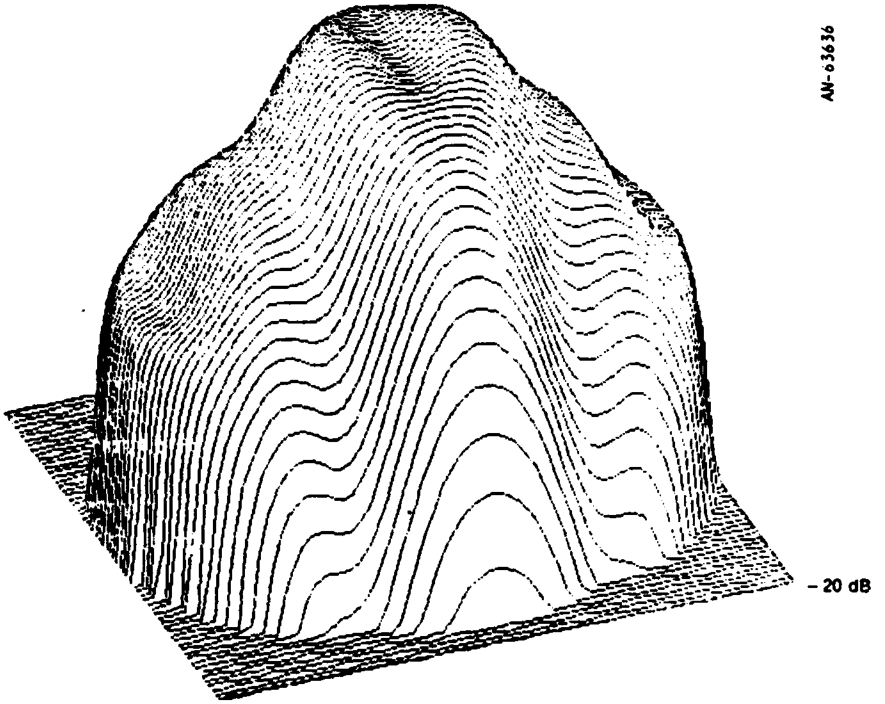

Figure 2.12. SARF Simulation of TA-2 Embedded Element Pattern, Principal Polarization

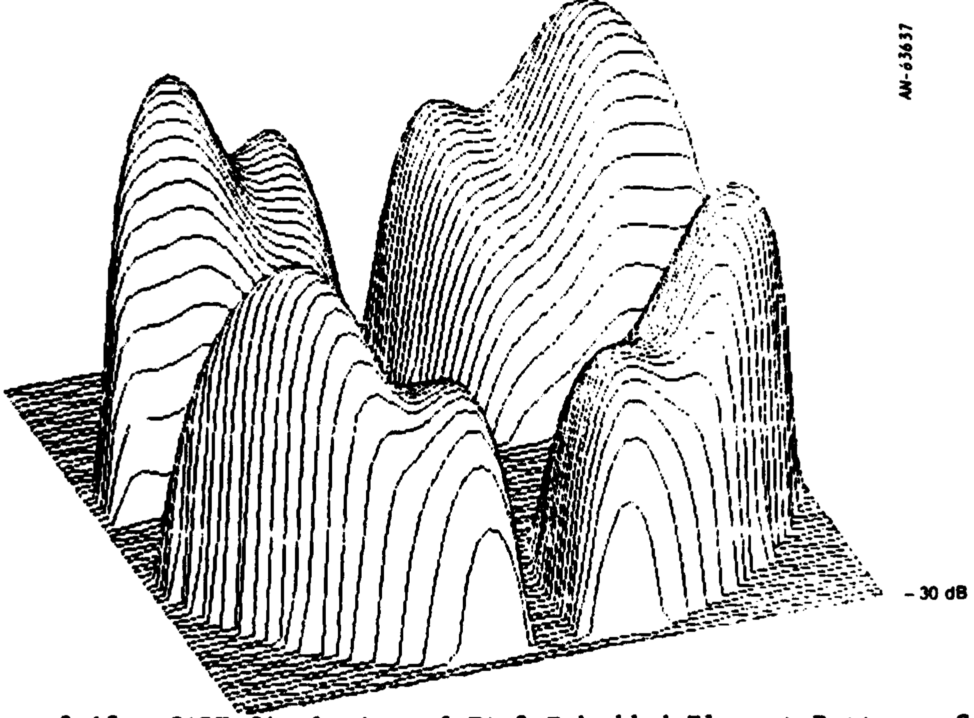

Figure 2.13. SARF Simulation of TA-2 Embedded Element Pattern, Cross Polarization

fact that the superposition of the patterns depends on the relative phase of the patterns themselves, as well as the relative phase of the element excitations.

Partial failures of elements can be modeled by defining a source type which, when superimposed on the nominal source, produces the failure mode. These failures may be distributed randomly over the aperture, or within specific areas, as discussed in Sec. 2.3.3.3. Several examples of partial failures are given in Fig. 2.14. The nominal source (a) is assumed to be a single unit current segment at the source coordinate origin. The source shown in (b) has a segment to exactly cancel the nominal segment, and a second segment displaced by a distance d ; the superposition of (a) and (b) is thus one segment displaced a distance d . The superposition of (a) and (c) is a unity amplitude current but at a phase of 22.5 degrees. The superposition of (a) and

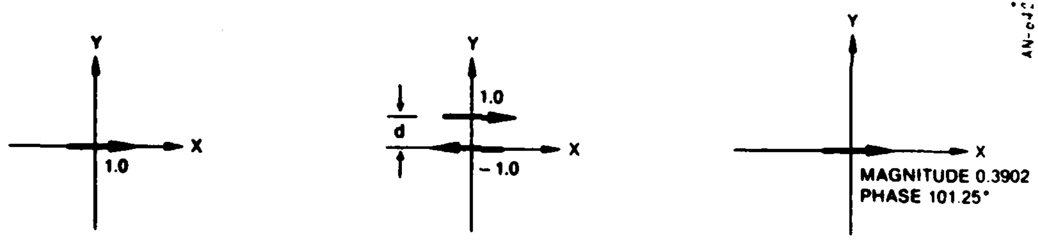

(A) NOMINAL SOURCE

(B) SYSTEMATIC DISPLACEMENT
BY A DISTANCE d

(C) ONE-BIT PHASE ERROR
OF 22.5°

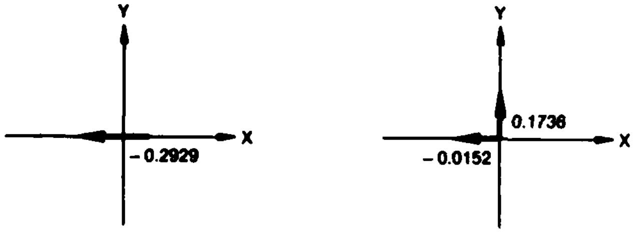

(D) 3 dB POWER LOSS

(E) 10 DEGREE ROTATION
IN THE X-Y PLANE

Figure 2.14. Partial Failure Examples

(d) represents an element with a 3 dB power loss, and (a) and (e) results in an element rotated 10 degrees in the x-y plane. As mentioned previously, an application is given in Sec. 2.1.3.6 which involves multiple partial failures as well as subarray modeling.

Random Pattern Deviations. Random deviations in the element patterns due to, say, manufacturing errors can also be modeled with the SARF simulation by specifying a statistical variance envelope for the patterns. This procedure is described in Sec. 2.3.3.2.

Source Element Pattern Summary. The SARF simulation source element pattern model is very general and allows a rich diversity of effects to be included, as the above discussion amply demonstrates. The range of options goes from the trivial isotropic radiator assumed in simple array models, to modeling mutual coupling effects of several element types. The burden on the user also ranges from trivial to substantial, and clearly the more complex models should only be used when they are really necessary. For cases involving simple dipole radiators where phase and polarization are not critical, an isotropic radiator or infinitesimal dipole will probably suffice. Cases requiring more complex models include:

1. Complex elements--e.g., microstrip radiators
2. Evaluation of vulnerability to jammers at wide angles
3. Nulling simulation and other problems sensitive to phase and polarization
4. Arrays utilizing subarrays
5. Incorporation of experimental data
6. Partial element failures

For such cases the flexibility of the model is essential, and it is precisely for such cases that a sophisticated simulation really shows its value.

2.1.1.3 Antenna Designs Modeled

A menu of potential antenna design variations is given in Table 2.2, along with SARF capabilities. All of these antenna options have been discussed in the previous section, with the exception of reflect arrays and the differences between active and passive lenses, which we will briefly cover here.

Reflect arrays have, to our knowledge, not been seriously proposed as a SBR option. Lens arrays are, to the first order, unaffected by structural deformations perpendicular to the array face, so they are relatively insensitive to mechanical errors. Reflect arrays, on the other hand, have the same sensitivity as reflectors to such deformations. In addition, reflect arrays have the same feed blockage problems as reflectors (and can also utilize offset feeds).

For these reasons, the SARF simulation was not designed with special provisions for modeling reflect arrays; however, they can be modeled by

1. Using the corporate-fed option
2. Doubling the true mechanical deformations, as discussed for reflectors
3. Blanking out regions blocked by the feed using the techniques discussed in Secs. 2.1.1.2.3 and 2.3.3.3

Active lenses have an amplifier following the module phase shifters, but are otherwise the same as passive lenses (see Sec. 4 in Vol. II). Beam scan and phase quantization are handled identically for the two cases. The difference between the two designs is modeled in the SARF simulation by the insertion amplitude and phase random polynomials given in Sec. 2.3.2.7. Specific differences would be:

1. The linear gain coefficient would be greater than one for an active lens, less than one for a passive lens to model phase

TABLE 2.2

SIMULATION SCOPE--ANTENNA DESIGNS

Active or Passive Space-Fed Lens, Reflect Arrays

- Raytheon Model of Space Feed
- Cluster Space Feed
- Lens Transfer Characteristics for N-Bit Phase Shifter With Random Polynomial Gain
- Full Feed Path Length Effects for Defocusing, Squint, Lens Distortions

Corporate-Fed Arrays

- Ideal Feed Network
- Lens Distortions in Any Dimension

Reflectors With Phased Array Feed

- Phased Array Feed is Modeled
- Reflector Segments Modeled as Array Elements

Wide Variety of Array Elements

- Very General Current Segment Model
- Infinitesimal Ideal Dipole
- Half-Wave and Bowtie Dipoles
- Turnstiles, Microstrip

Flexible Element Geometry

- Rectangular or Elliptical Aperture
- Rectangular or Triangular Element Grids
- Gore Designs

shifter losses, and the variance would reflect random gain variations and loss variations, respectively.

2. The square law and AM/PM terms would normally be zero for a passive design.

Active designs are also subject to gain variations due to the power distribution system, which can be modeled using the partial failure techniques discussed in the previous section.

2.1.1.4 SARF Simulation Outputs

The basic output of the SARF simulation is the full antenna pattern of the array. This data can be displayed in several formats:

- Three-dimensional plots
- Contour plots
- Histograms
- Pattern cuts
- Tabular data

An example of a 3-D plot is shown in Fig. 2.15, and a complete set of sample outputs is given in Appendix A.

The pattern cuts can be obtained along constant cuts in "sine space" coordinates

$$\begin{aligned} T_x &\equiv \sin\theta\cos\phi \\ T_y &\equiv \sin\theta\sin\phi \end{aligned} \qquad (2.1)$$

where θ and ϕ are the polar and azimuthal antenna pattern angles (also see Fig. 2.45). This pattern data provides the information listed in Fig. 2.15. The gain data is currently approximate, since mutual coupling effects are neglected; an improved gain calculation is being developed under another RADC contract, and the intent is to incorporate

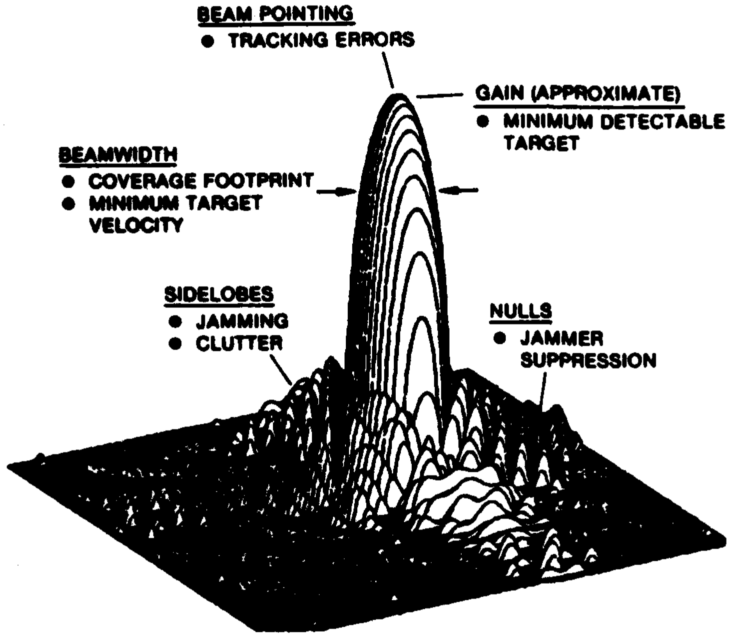

Figure 2.15. SARF Simulation 3-D Plot Output

the results in the SARF simulation when available. A similar set of parameters may be derived for monopulse patterns, as shown in Fig. 2.16.

It is important to note that the SARF simulation outputs the Cartesian field components E_x and E_y ; for far-field patterns with no radial component this may be converted to polar field components by

$$E_\theta = \frac{\cos\phi\, E_x + \sin\phi\, E_y}{\cos\theta}$$

$$E_\phi = -\sin\phi\, E_x + \cos\phi\, E_y \qquad (2.2)$$

Additional output data available include:

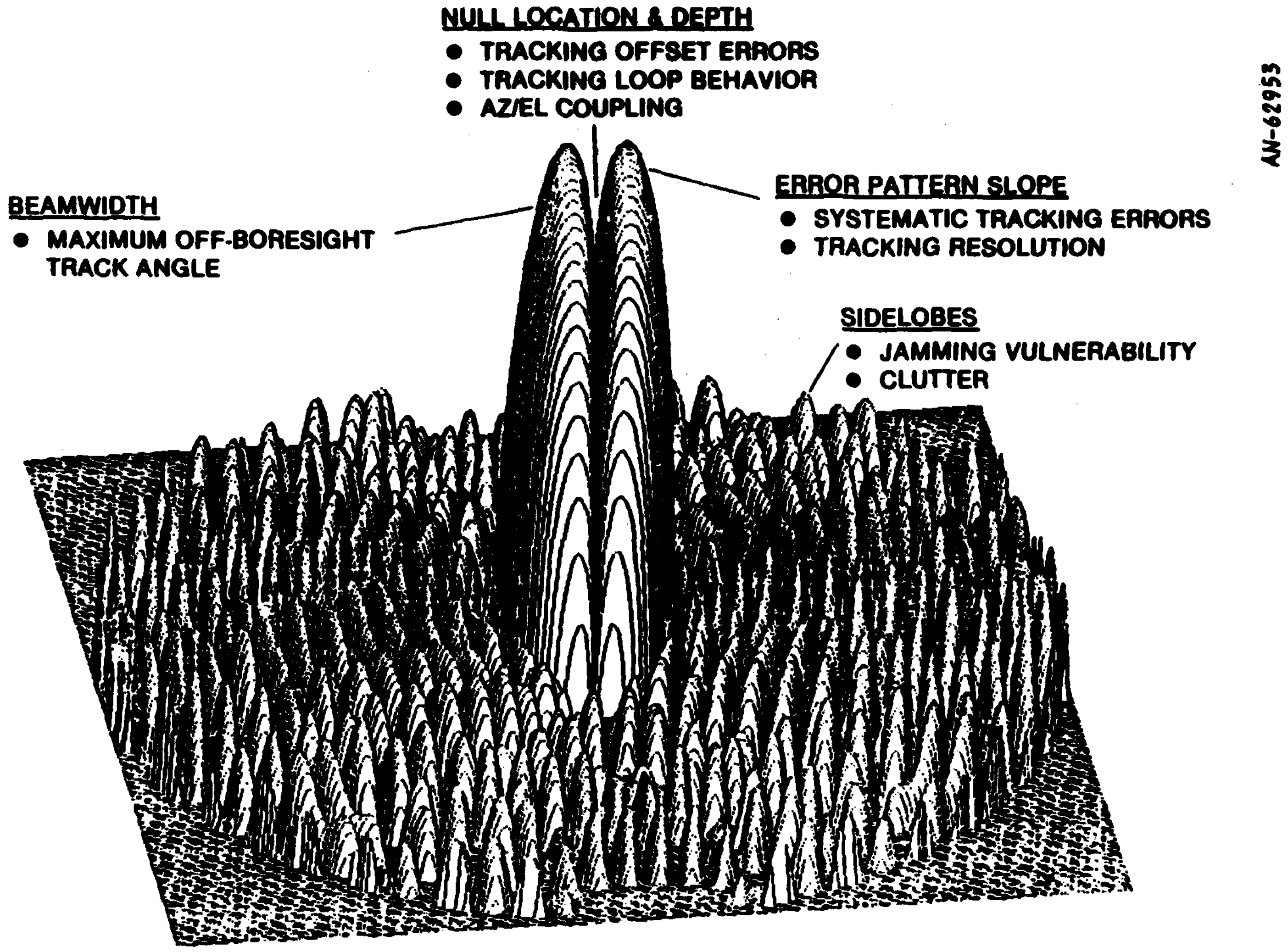

Figure 2.16. SARF Simulation 3-D Plot Output, Monopulse Pattern

- A printout of the input parameters
- An option to plot the aperture illumination
- An option to plot the element locations

Further information and output examples are given in Sec. 2.3.1.2.

2.1.1.5 Technology Results Incorporated

Prior RADC and DARPA technology programs provided a broad range of results relevant to the SARF simulation, and the last objective stated at the beginning of this section was to incorporate these results to the fullest extent. This not only avoids duplication of effort, but enhances compatibility of the simulation with other programs. The interfaces with other technology programs are shown in Fig. 2.17. Results incorporated into the SARF simulation include:

- RF Analysis. The ARC element model was adopted so that HAM/FAM model outputs could be written on tape and input to the SARF simulation. The Parametric Antenna Analysis System (PAAS) model developed by Simulation Technology, Inc. (STI) was incorporated as the basis for the efficient computation section of the simulation.

- Structural Analysis. The SARF simulation was designed to accept a tape written by the Draper Labs structural model. A case run with such a tape is discussed in Sec. 2.1.3.2.

- Membrane Development. The Grumman data on TA-2 was used in the incorporation of embedded element pattern data discussed in Sec. 2.1.1.2.3.

- Adaptive Nulling Techniques. Syracuse Research identified solar panel multipath as a primary potential problem area, and the multipath model discussed in Sec. 2.3.2.6 was designed particularly for this case.

- Ground-Based Validation. The Grumman TA-2 data was used as the basis for comparing measured and simulated array patterns, as discussed in Sec. 2.1.2.6.

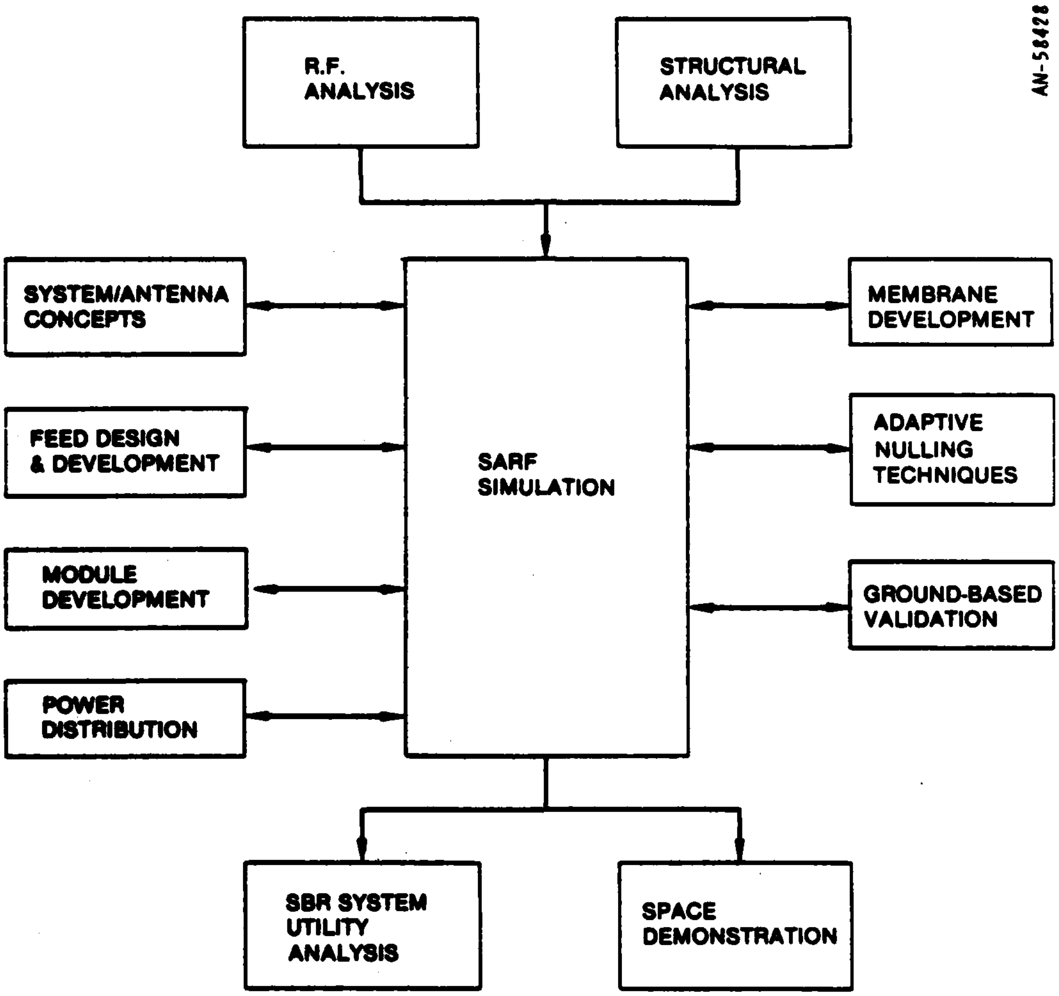

Figure 2.17. SARF Simulation Interfaces

- Space Demonstrations and Utility Analysis. These are future technology programs and interfaces are planned as part of a follow-on contract.
- Power Distribution. The simulation will model power variations in sections of the antenna, as discussed in Sec. 2.1.1.2.3.

- Module Development. Measured data from the STRAM module program was incorporated, and it is shown in Sec. 2.3.2.7 that the non-linear behavior is important and well modeled by the simulation.
- Feed Design and Development. The Raytheon multibeam feed program was incorporated as the basis for the space-feed section of the model, as discussed in Sec. 2.3.2.5.
- System/Antenna Concepts. One of the preliminary gore designs (#3) was simulated for a 37 m diameter circular aperture, as given in Sec. 2.1.3.3.

In addition to these specific items, there has been an on-going interaction with technology contractors, via visits and RADC program reviews, which has strongly influenced the development of the simulation.

2.1.1.6 Conclusions on SARF Simulation Development

The SARF Simulation has been developed in accordance with the statement of work, and the result is a powerful simulation with tremendous versatility. The simulation has already proved to be useful and adaptable to a wide range of problems. Inevitably, new problems will create new requirements, but the simulation has also demonstrated great flexibility: the modular file structure designed for ease of model additions and modifications has also proven to work well for the changes already incorporated.

2.1.2 Validation of the Simulation

As noted previously, model validation is at least as important as model design, since the ability to obtain a result is not worth much if you do not believe it after you get it. One major difficulty in validating a new powerful simulation is finding a benchmark to compare it to; almost by definition, nothing else exists with equivalent capability. The most satisfactory single answer is to use experimental data, but experiments also have their problems, and in the present case the available data is rather limited. A better answer is to draw on a wide variety of results, including experimental data, and to continue the process with each new application; e.g., for the feed defocusing data presented in Sec. 2.1.3.5, the beam shift can be checked against a simple analytical calculation, and some test cases with high sidelobes can be run for which published data is available. A related problem is that the SARF simulation is so broad in scope that the number of potential test cases is virtually limitless, and it is impossible to truly test it exhaustively.

The validation procedure that was designed to deal with these problems is as follows:

1. The SARF simulation has a built-in-test internal validation capability, for numerical accuracy checks.
2. Each major program module (e.g., the structural deformation code, or the source pattern model) was checked individually before interfacing it with the simulation. These checks consisted of a series of runs designed to exercise all parts of the code, with output checked numerically against the model equations.
3. The full model was checked against available analytical cases.
4. Comparisons were made with numerical data available from other models.
5. Comparisons were made with the measured TA-2 array data.

We will discuss each of these steps in the following sections. In most cases, a summary of the procedure will be given, but one detailed example regarding multibeam phase errors is included, and further detailed cases are given in Appendix A.

2.1.2.1 Internal Validation

As discussed previously, and shown in Figs. 2.1 and 2.2, the simulation is designed around the three data sets defining the source excitations, locations, and radiation patterns. These three data sets are then processed by the computational modules to compute the antenna pattern characteristics. As shown in Sec. 2.3.5, for large arrays it is essential to employ efficient computational techniques--otherwise literally years of computer time would be required. The SARF simulation employs a fast-Fourier transform (FFT) technique adopted from the PAAS model. This technique is approximate, and care must be taken to avoid numerical errors (see Sec. 2.2). To avoid any lingering doubts about numerical accuracy (and to also provide the capability of high-accuracy calculations over a wide dynamic range for null calculations), the simulation has an alternate brute-force calculation technique. Both the brute-force and FFT methods operate on the same three data sets, so this provides a means of directly spot-checking the numerical accuracy of the efficient technique. This capability was heavily utilized during the validation procedure, and may be exercised by a user on any computer run.

2.1.2.2 Program Module Validation

Appendix A contains detailed validation results on the element pattern model which will not be repeated here. An example of such data is provided by Fig. 2.6; these element patterns calculated by the SARF simulation can easily be checked against analytical results.

The surface deformation module was checked by making detailed numerical comparisons between output values and hand calculated values for off-line deformations input via tape. The on-line systematic deformations were tested by running canonical test cases, such as linear tilts and parabolic sags, for which results are known analytically.

Random deformations were tested by numerical spot checks, and by comparing with statistical tolerance theory.[1]

The excitation software was checked by comparison with the analytical cases discussed below, and by comparing with Raytheon results. A phase error test is described separately in more detail below.

The pattern calculation software was checked by the internal validation described above, and by the analytical test cases. The output routines are automatically checked as part of the other validation procedures.

2.1.2.3 Validation of Multibeam Phase Errors

In checking out the performance of the merged Raytheon multibeam feed software and the SARF software, we examined the effects of random phase errors on the main array as modeled in the multibeam software.

Two sets of test runs were made. One set introduced into the model random phase errors with a phase mean of zero and a standard deviation of 15° (0.2618 radians). The second run introduced phase errors characterized by a phase mean of zero and standard deviation of 6° (0.1047 radians).

Comparisons were made between the modeled test results and the expected results as described in the Radar Handbook.[2] To express the gain loss of the modeled runs, the ratio of the main beam E-field magnitude calculated in computer runs with and without the random errors was taken. This was compared to the Radar Handbook's expected gain loss, computed to be

---

[1] J. Ruze, "Antenna Tolerance Theory--A Review," Proc. IEEE, April 1966, pp. 633-640.

[2] M. Skolnik, Radar Handbook, McGraw-Hill, 1970, pp. 11-35 to 11-43.

$$e^{-(\sigma_\phi)^2}$$

where σ_ϕ = phase standard deviation (radians) of the errors introduced. The results of the comparison are shown in Table 2.3.

The RMS sidelobe level was also examined. Sidelobe levels were computed for the modeled runs and compared to the expected RMS sidelobe level computed by the Handbook equation:

$$\frac{(\sigma_\phi)^2}{\eta N}$$

where σ_ϕ = phase standard deviation (radians)
η = aperture efficiency
N = number of main array elements

Results are shown in Table 2.3.

TABLE 2.3
COMPARISON OF ACTUAL VERSUS HANDBOOK RANDOM PHASE ERROR EFFECTS

	Modeled Gain Loss	Handbook Gain Loss	Modeled RMS Sidelobe Level	Handbook RMS Sidelobe Level
Modeled Run 1				
σ_ϕ = 15° = 0.2618 rad Mean = 0	0.968 volts	0.966 volts	-34.78 dB	-34.33 dB
Modeled Run 2				
σ_ϕ = 6° = 0.1047 rad Mean = 0	0.995 volts	0.995 volts	-42.97 dB	-42.29 dB

We also examined the effects of varying the number of main array phase shifter bits and compared these to the expected results described in the Radar Handbook.

Test runs using a 5 × 5 beam configuration were made, varying the number of main array phase shifter bits from 10 to 4. The RMS sidelobe level of each run was calculated. Figure 2.18 shows a graph comparing the modeled results with the Handbook results.

The effects of reducing the number of phase shifter bits in the main array can be seen in Figs. 2.19 and 2.20. Here, a nominal 60 dB Taylor far field antenna pattern, generated from a 7 × 7 beam configuration, using 10 bits is compared with one in which 6 bits were used.

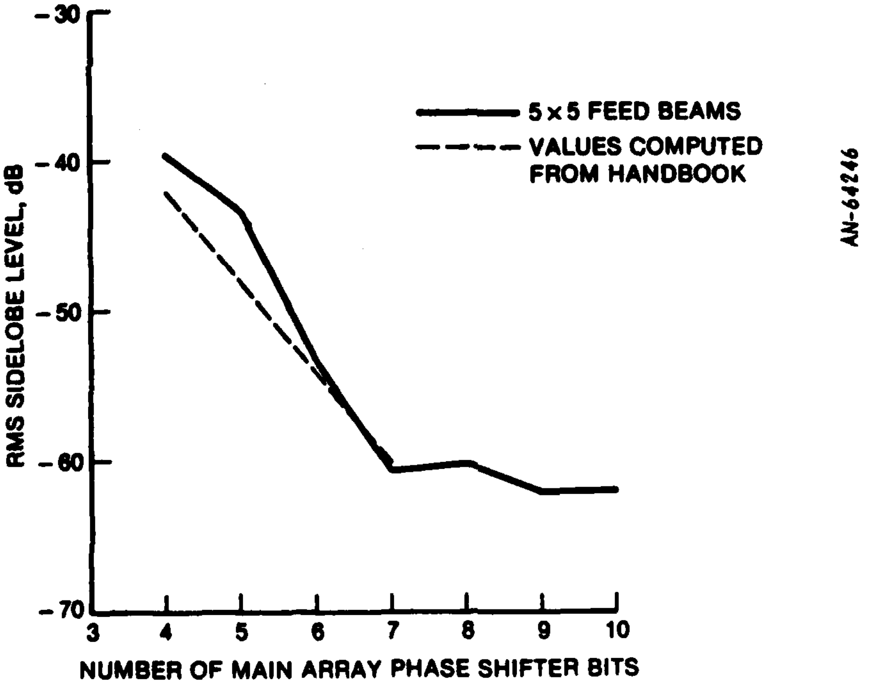

Figure 2.18. RMS Sidelobe Level as Function of Number of Main Array Phase Shifter Bits

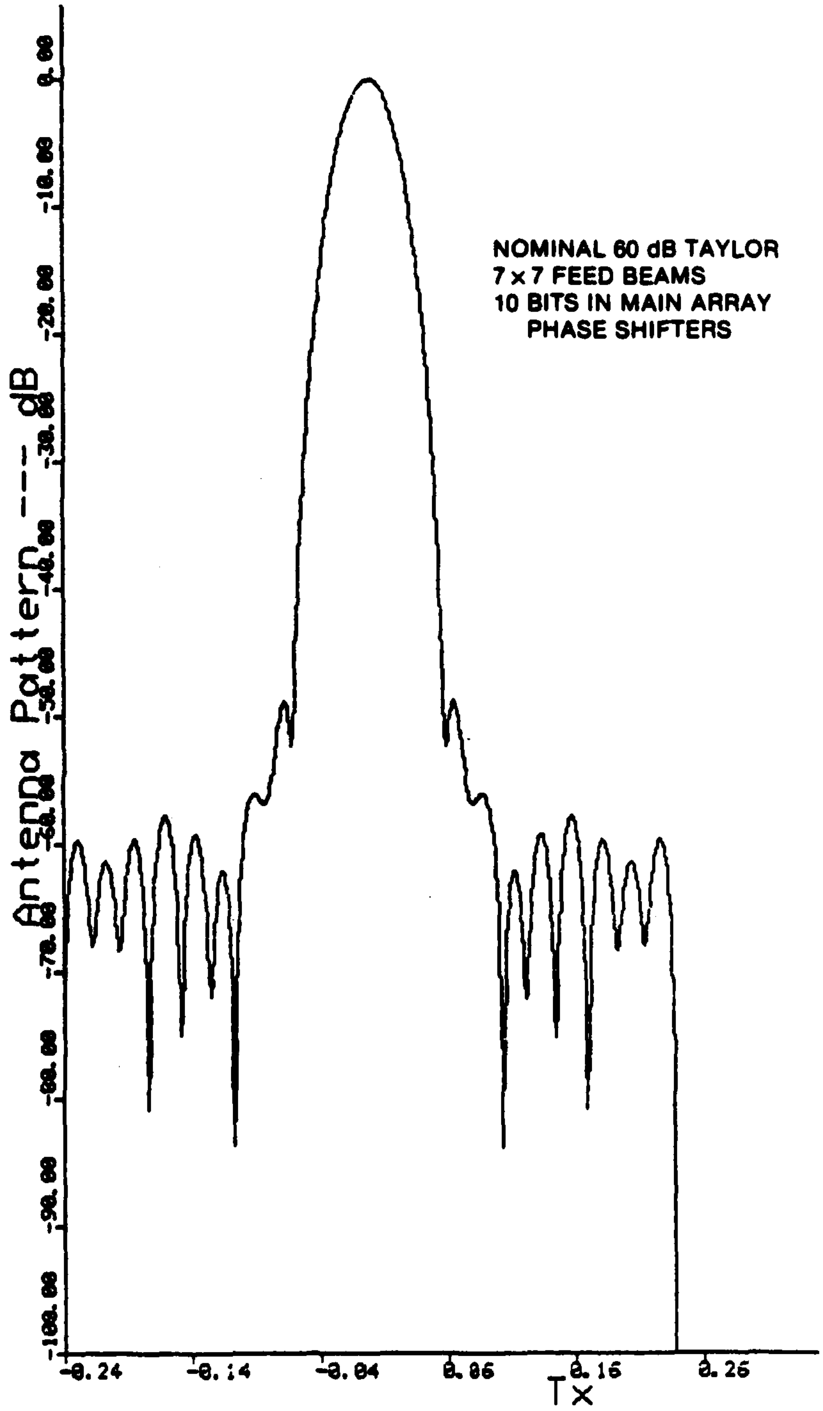

Figure 2.19. Antenna Pattern With Ten Phase Shifter Bits

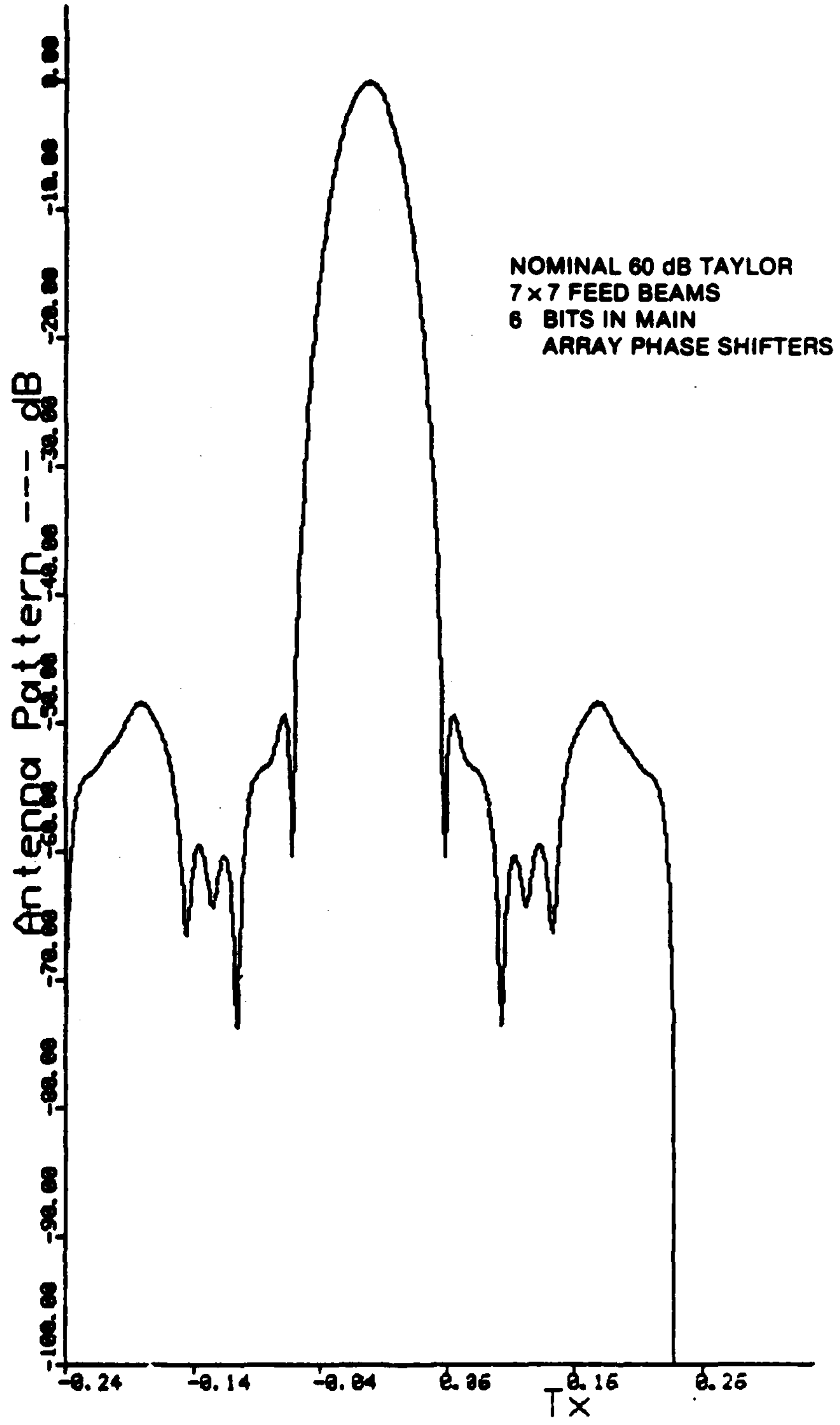

Figure 2.20. Antenna Pattern With Six Phase Shifter Bits

2.1.2.4 Analytical Pattern Tests

A series of comparisons with analytical cases is given in Appendix A, including:

- Uniform linear array of n-elements
- Binomial-weighted linear array
- Taylor and Bickmore-Spellmire circular distributions

The binomial distribution is particularly valuable for checking the brute-force technique, since it provides an exact analytical result over a dynamic range beyond the -120 dB capability of the program. The FFT and brute-force techniques were shown to have error levels 114 dB and 160 dB below the pattern peak, respectively.

Many other runs have been made in the course of applying the program, and all of the nominal aperture distributions listed in Table 2.1 have been run one or more times.

2.1.2.5 Comparison With Other Numerical Results

The feed defocusing cases given in Sec. 2.1.3.5 provided an opportunity to compare the SARF simulation with a linear array simulation developed by RADC. The data given in this report is for an elliptical array, which represents the actual design. For the design development, a simpler linear array model was used. The SARF simulation can calculate linear array patterns as a special case, and runs were made using a linear array feed also designed by RADC. Results were in close agreement with the RADC model.[1]

2.1.2.6 Validation Against Measured Data

The most gratifying validation test made was the excellent agreement obtained between the TA-2 patterns measured by Grumman,[2] and the SARF simulated patterns.

---

[1] D. Jacavanco, private communication, October 1982.

[2] J. Diglio, op. cit. The TA-2 element geometry is shown in Fig. 2.21.

The array was space-fed with a simple horn feed, which can be accurately modeled in the E-plane by a cosine-on-a-pedestal pattern with a 5.6 dB edge taper.[1] The lens was passive, employing 4-bit phase shifters. No information was available on the membrane contour, so a perfect planar lattice was assumed. The element pattern model shown in Figs. 2.10 through 2.13 was used, so mutual coupling effects are represented.

The total simulated array pattern is shown in Fig. 2.22. The only experimental data available was the E-plane pattern cut shown in Fig. 2.23, and the equivalent simulated pattern is superimposed for comparison. The first observation of the TA-2 pattern data comparison is that there is excellent agreement. The simulated and measured main beams are indistinguishable, and the sidelobe levels are within 1 to 4 dB.

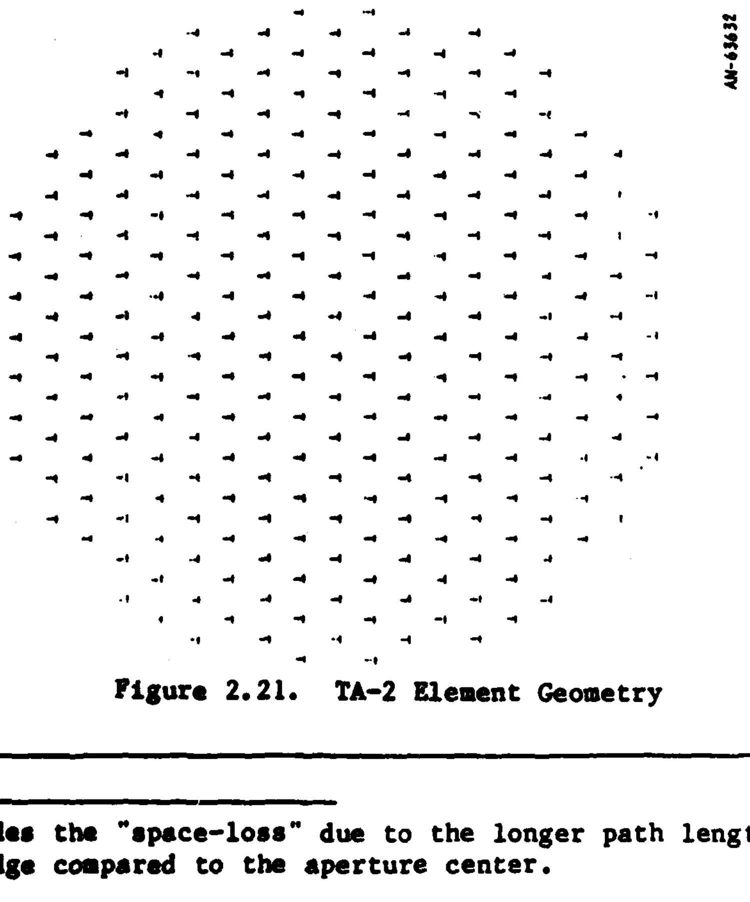

Figure 2.21. TA-2 Element Geometry

---

[1] This includes the "space-loss" due to the longer path length to the aperture edge compared to the aperture center.

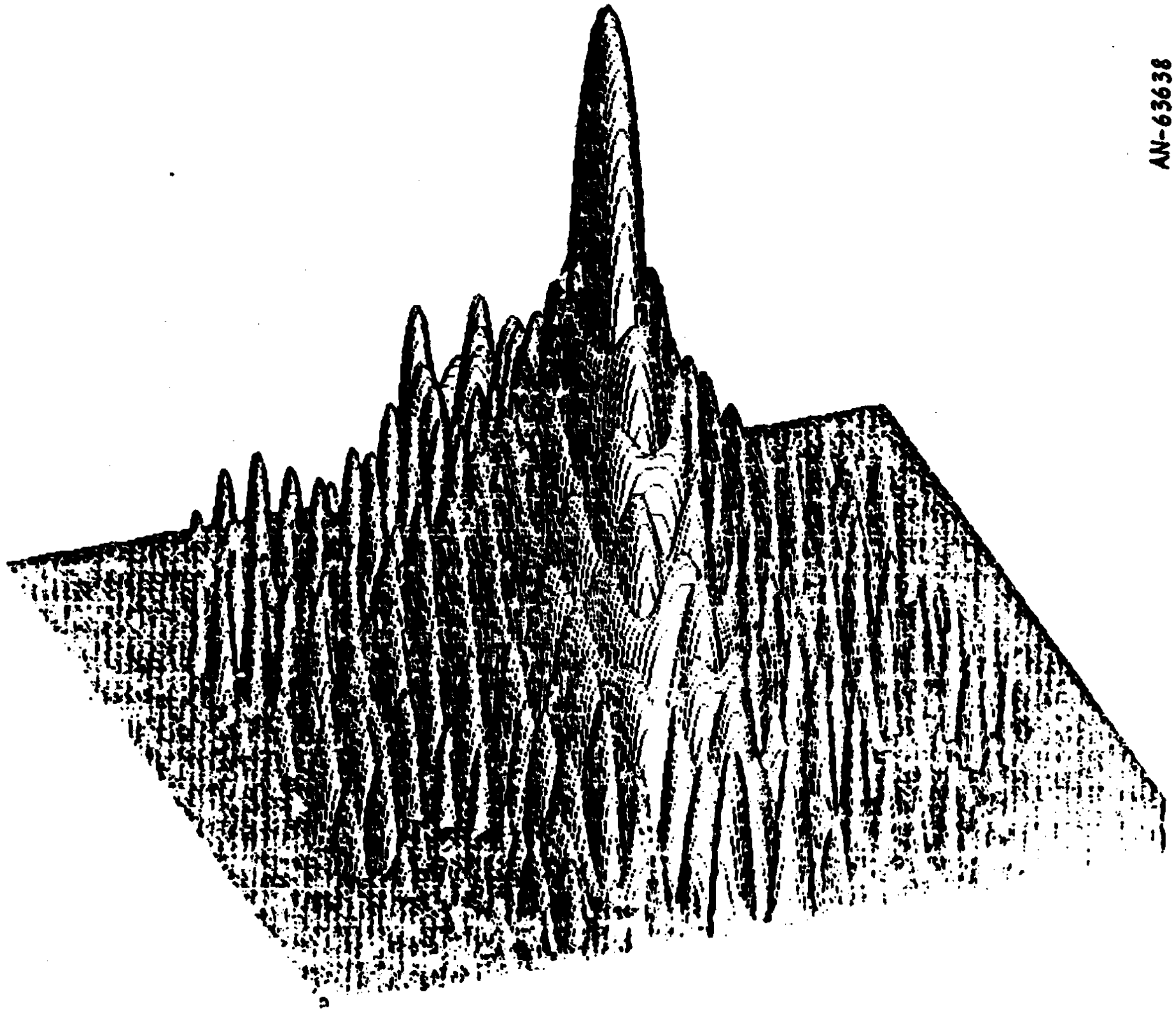

Figure 2.22. SARF 3-D Plots of TA-2 Pattern

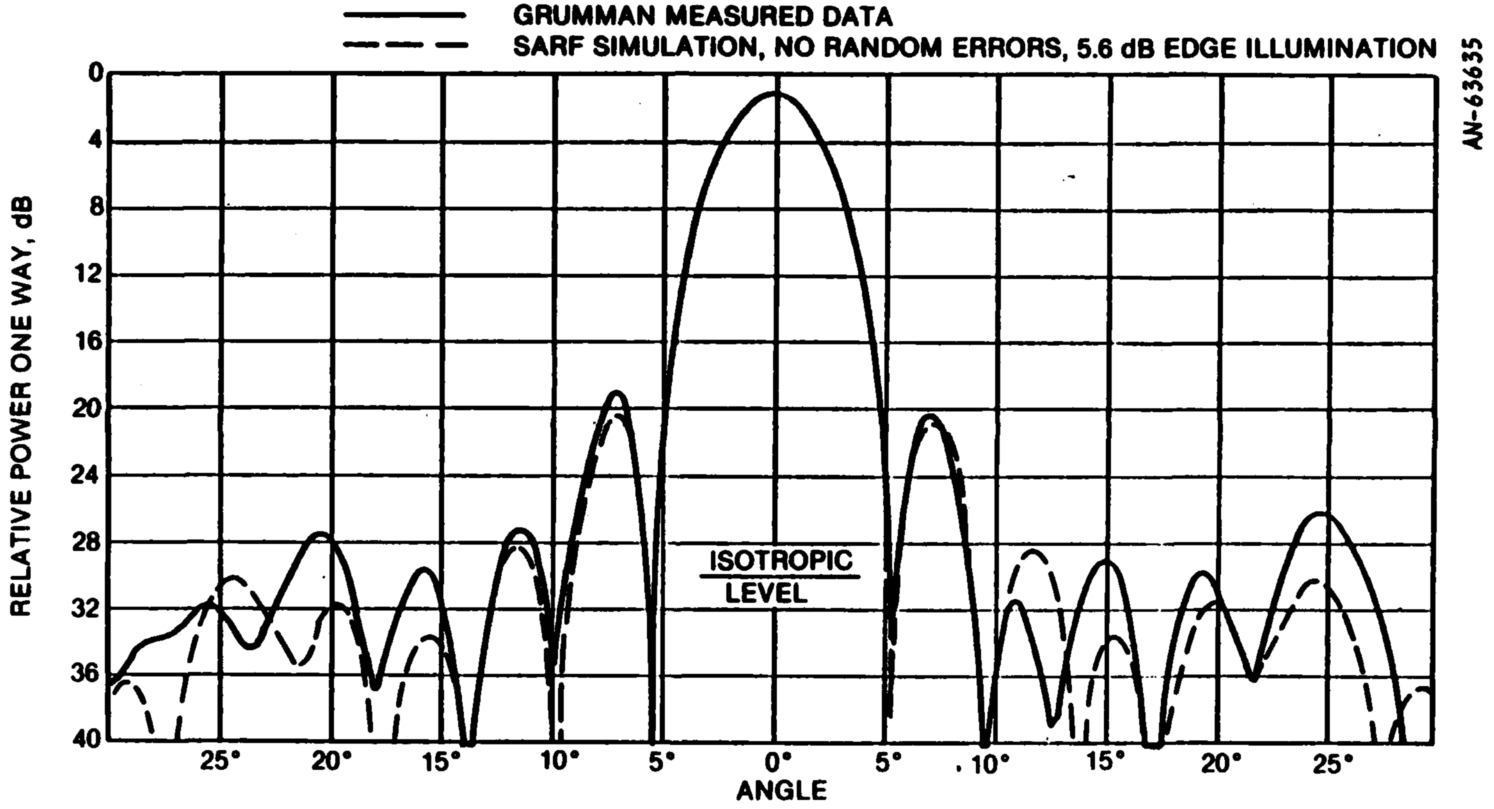

Figure 2.23. TA-2 E-Plane Pattern

A significant feature of the measured pattern is that the right and left hand sides differ between each other almost as much as they differ from the simulated pattern. This asymmetry is possibly due to (1) an asymmetric mechanical distortion of the membrane; (2) feed misalignment; or (3) range reflections. A review of the experimental procedure indicates that the feed was positioned quite carefully, and this possibility is virtually ruled out,[1] leaving mechanical distortion or range reflections as the primary possibilities. An obvious future refinement to the model would be to incorporate measured data on the mechanical distortion of the membrane (since measured embedded element patterns are already incorporated). It is also possible to incorporate data on the feed alignment, and any measured tolerances on the fixed phase shifters.

This type of iterative refinement of the model should certainly reduce the differences between the measured and simulated patterns, but it is worth emphasizing that the agreement is already quite good, and is in fact adequate for almost all system-level evaluations.

2.1.3 Initial Applications

In one's enthusiasm to develop, test, refine, and validate the software tools described in the above tasks, it is easy to lose sight of the fact that the ultimate goal of these efforts is to compare and evaluate alternative radar designs. This section reviews initial applications of the newly developed simulation to evaluate SBR design issues. The initial applications include:

- Grumman TA-2 modeling
- Grumman TA-3 modeling
- Draper structural data/circular gore design #2
- 36 m diameter circular gore design #3

---

[1] J. Diglio, op. cit., pp. 5-18.

- Multibeam feed sidelobe level study
- Feed defocusing study for 23 × 60 m low orbit elliptical aperture
- Defense suppression weapon study

The TA-2 modeling results have already been presented; the remaining applications are reviewed below.

2.1.3.1 Grumman TA-3 Modeling

TA-3 is similar to TA-2 except that:[1]

- The phase shifters are switchable instead of fixed
- There are 406 active elements instead of 258

There was little data available on TA-3 during this study other than the information given above, so the modeling effort was very preliminary. The element geometry is shown in Fig. 2.24, and simulated patterns in Figs. 2.25 and 2.26. An ideal planar lattice was assumed, infinitesimal dipole elements, and no errors. A cosine-on-a-pedestal feed illumination with 10 dB edge taper was used. The only non-ideal effect modeled was the 4-bit phase shifters. TA-3 will be subjected to detailed measurements in the future, and it is anticipated that the SARF simulation will be heavily utilized in modeling the data, in an interactive program with the measurement program.

2.1.3.2 Draper Structural Data/Circular Gore Design #2

The structural distortion modeling capability was applied to a data tape generated by Draper Labs.[2] A somewhat surprising result regarding the effect of the gore structure was discovered as a by-product. To clearly bring out the effect of structural distortions, a

---

[1] J. Diglio, op. cit.

[2] F. Ayer, Space Radar Large Aperture Simulation/Analysis--Interim Technical Report, Volume I, The Charles Stark Draper Laboratory, Inc., Report R-1413, October 1980.

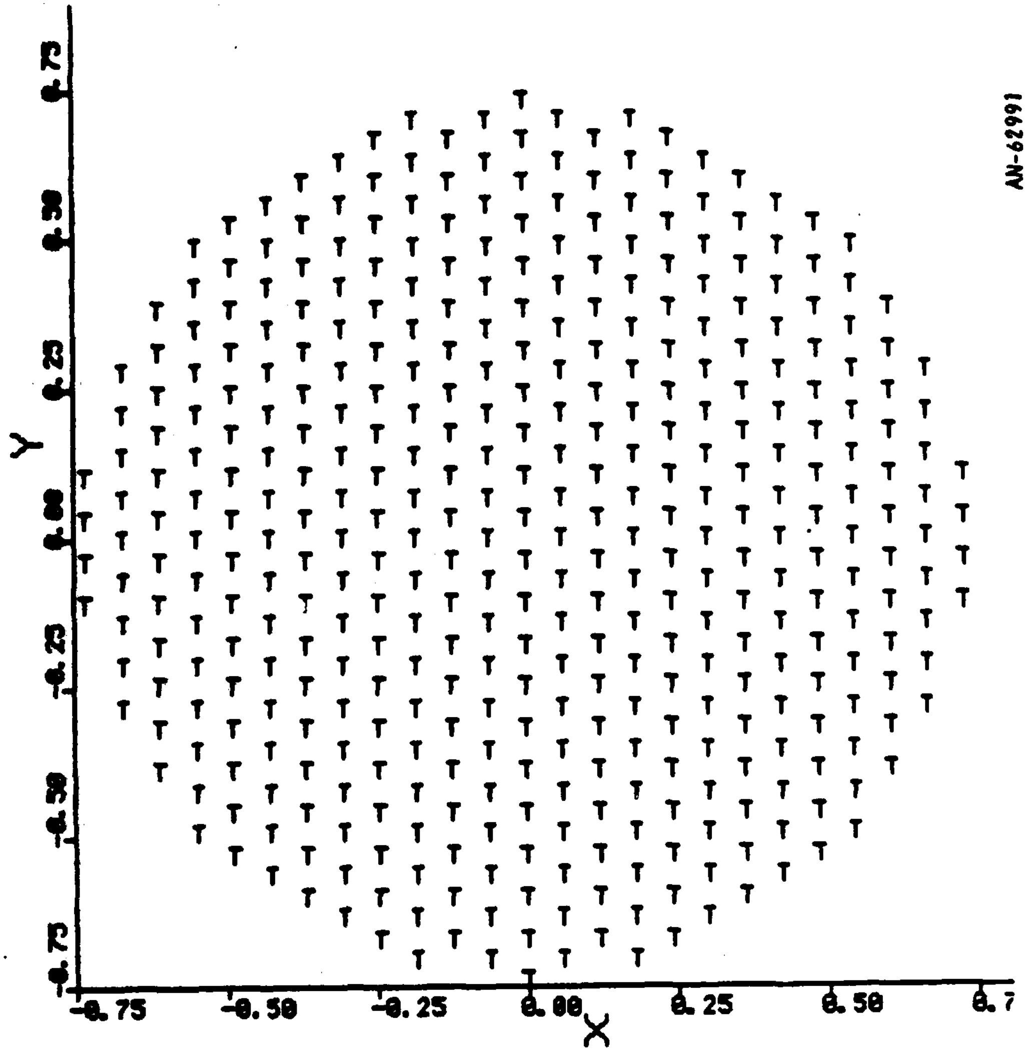

Figure 2.24. TA-3 Element Geometry

---

60 dB Taylor distribution was selected for the nominal aperture illumination. A 35 m diameter aperture operating at 1.25 GHz was selected to be representative of interesting designs. The Draper orbit position 5 was used for the distortions; the peak distortions in the x, y , and z directions are 0.045, -0.043, and 0.018 meters, respectively, for this

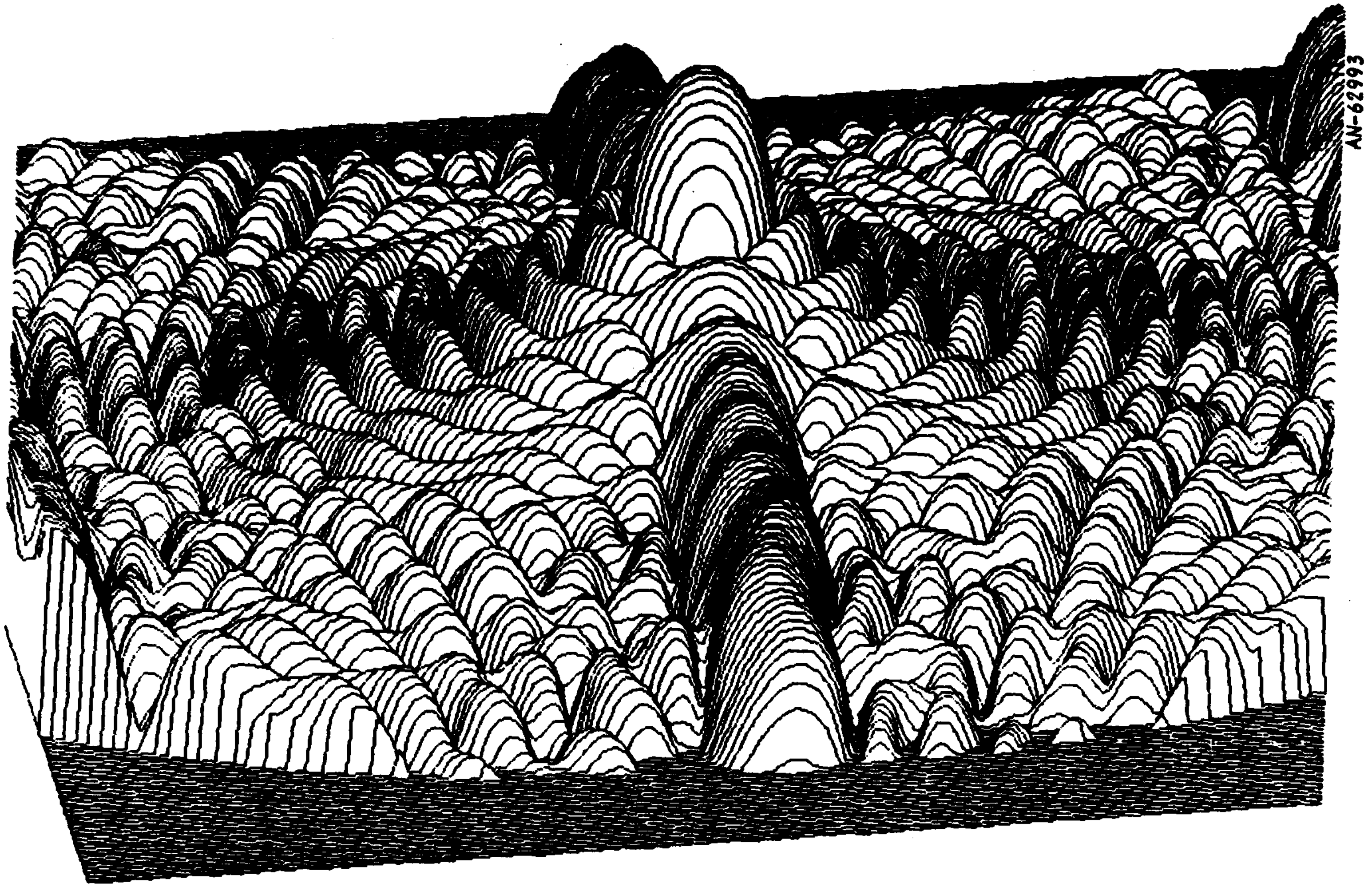

Figure 2.25. SARF 3-D Plot of TA-3 Pattern

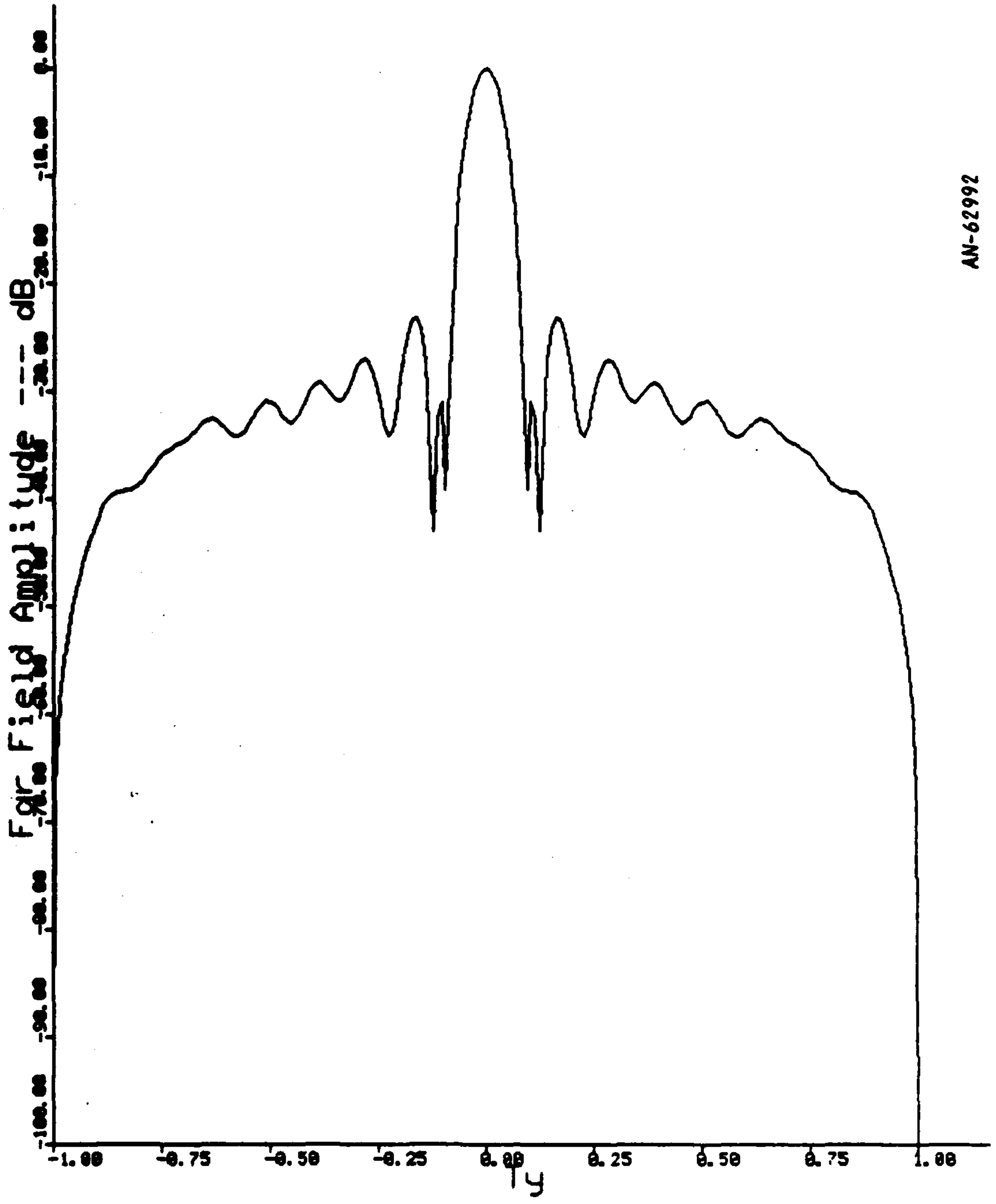

Figure 2.26. TA-3 Pattern Cut

case. The resulting pattern was computed with the SARF simulation for several cases with and without structural distortions. Figure 2.27 shows a case with no distortions, and elements located on a perfect, periodic, rectangular grid. The sidelobes are at -60 dB as expected.

Figure 2.28 shows the effect of distortions on this design. Two cases are shown: (1) a space-fed design where the excitation phases change due to the distortions, and (2) a corporate-fed design where the excitation phases do not change due to the distortions. It is seen that the sidelobe levels have risen from -60 dB to around -45 dB due to the distortions. The beamwidths appear to be quite different for the two cases, but actually what is happening is that the beam peak has shifted +0.025° for the corporate-fed case, and -0.012° for the space-fed case. The space-fed case sidelobes are roughly 5 dB lower than the corporate-fed--somewhat less of a difference than was anticipated.

Figure 2.29 shows the results when the elements are placed according to a "Hancock Design #2" gore geometry.[1] Gore Design #1 is based on a uniform rectangular lattice, and substantial gaps exist at the joints between gores. Gore Design #2 maintains a constant element spacing in the aperture radial direction, but a variable spacing in the azimuthal direction, to minimize these gaps. It is seen that even with no distortions gore Design #2 sidelobes are above -40 dB, and that the distortions have in fact a relatively small effect on the sidelobes. Hancock has previously shown that "Design #1" raised the sidelobes of a 40 dB Taylor distribution to -28 dB, and Design #2 lowered this total to -32 dB. The results shown here indicate that something around -35 dB is the best sidelobe level that can be obtained with Design #2 for a 73λ diameter aperture.

---

[1] R.J. Hancock, Space Antenna Far-Field Patterns (to be published).

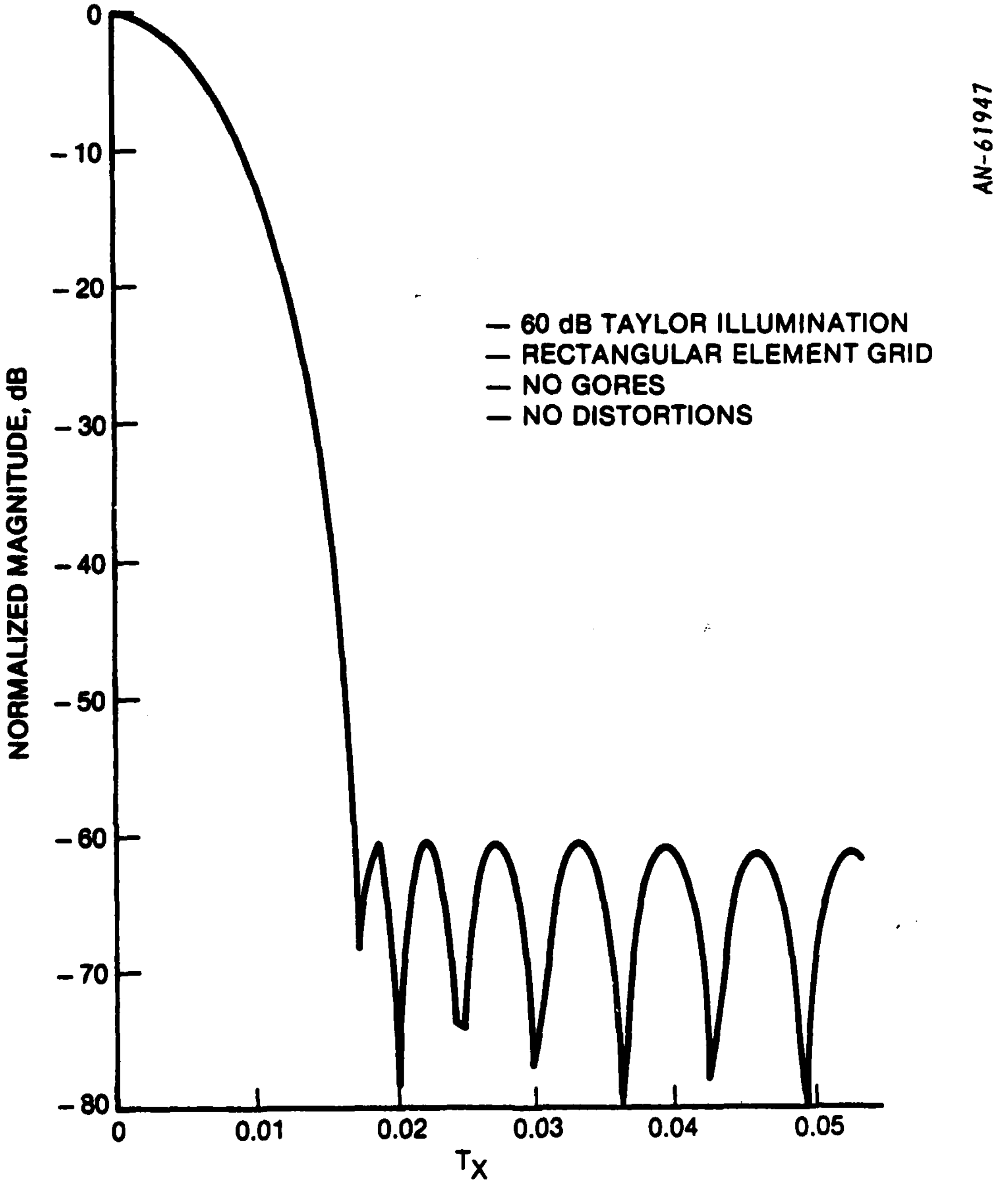

Figure 2.27. 35 m Diameter Circular Array, Ideal Case

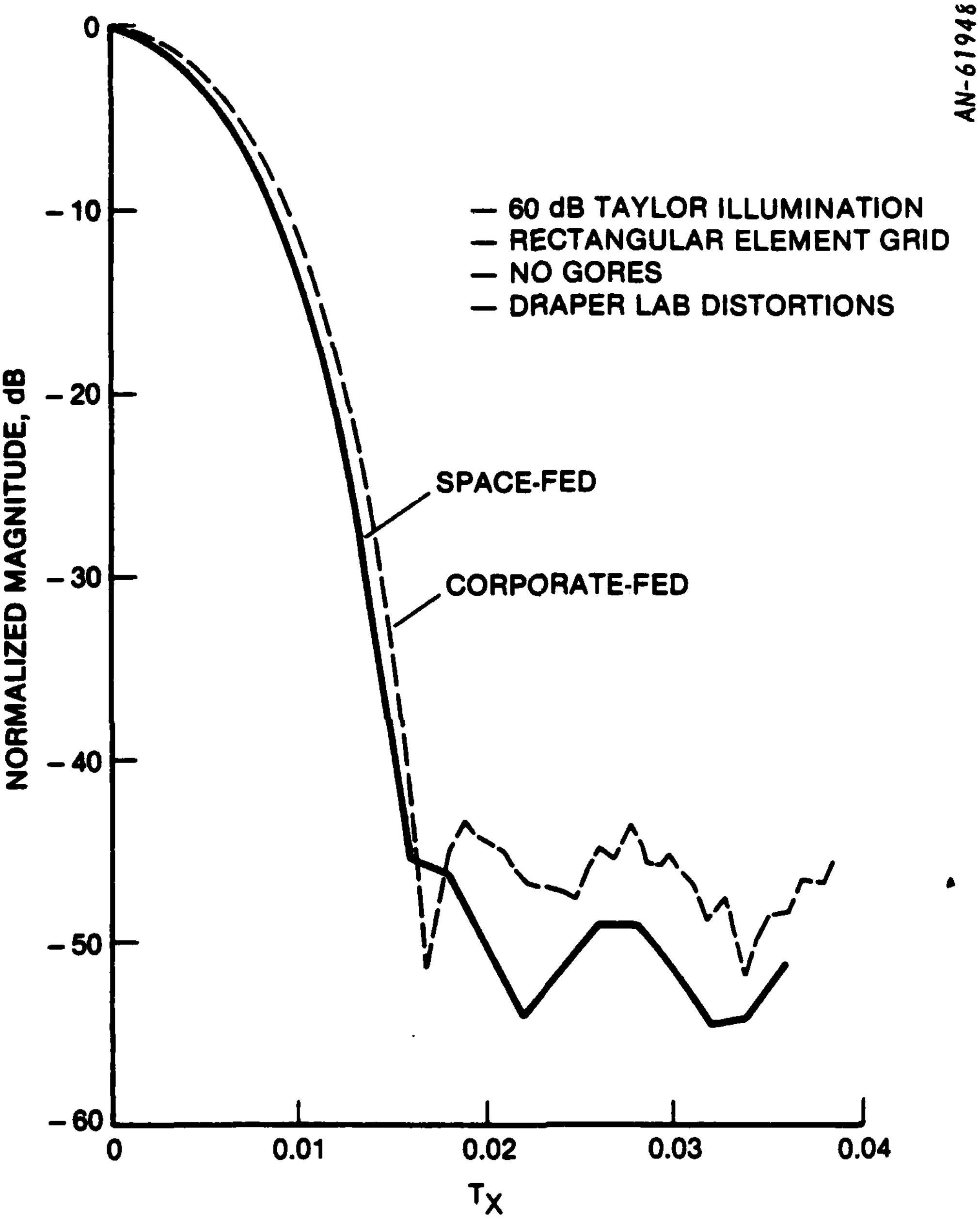

Figure 2.28. 35 m Diameter Circular Array, Draper Labs Distortions

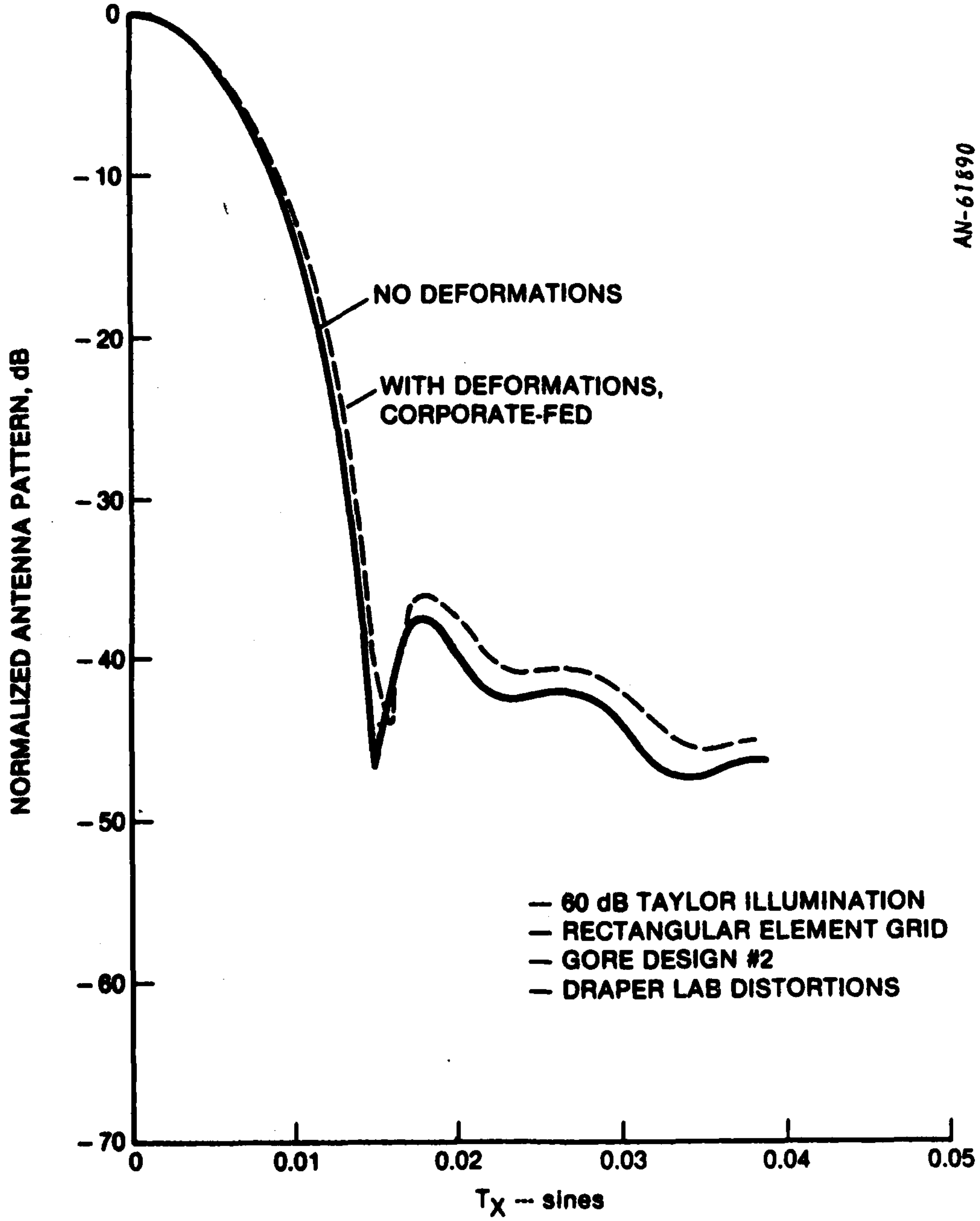

Figure 2.29. 35 m Diameter Circular Array, Gore Design #2

Doubling the diameter to 70 meters may improve the relative sidelobe level as much as 6 dB, but at best this is a marginal result, since there are many error sources which have not been modeled in the case shown in Fig. 2.28.

2.1.3.3 Circular Gore Design #3

The most recent gore design available during this study was "gore Design #3," which is illustrated in Fig. 2.30, showing two of the 32 gores. It is based on a uniform triangular element lattice, so it has gaps similar to Design #1.

The far-field pattern resulting from this design is shown in Figs. 2.31 and 2.32. The gore gaps produce 32 sidelobe "ridges" which can be seen in Fig. 2.31. Figure 2.32 is a cut through one of these ridges and it is seen that the sidelobes come up to roughly -35 dB due to the gaps, well above the nominal -60 dB level provided by the Taylor distribution.

These results and the results for gore Design #2 should not be interpreted to mean that low sidelobes cannot be achieved with a gore design, but rather that this has been identified as an issue that requires work in the future. The purpose of the SARF simulation is precisely to identify such issues, and to provide a tool for evolving solutions to problems identified.

2.1.3.4 Multibeam Feed Sidelobe Level Study

If a multibeam feed is employed in a space-fed array, a desired aperture distribution must be approximated by a summation of a finite set of feed beams. To determine the feed design tradeoffs and limitations, a series of runs were made with increasing numbers of feed beams, using a nominal 60 dB Taylor illumination. The results are shown in Fig. 2.33, indicating that there is a knee in the curve at four beams in each principal plane, and that even going to seven beams improves the results relatively little. Similar results have been published by

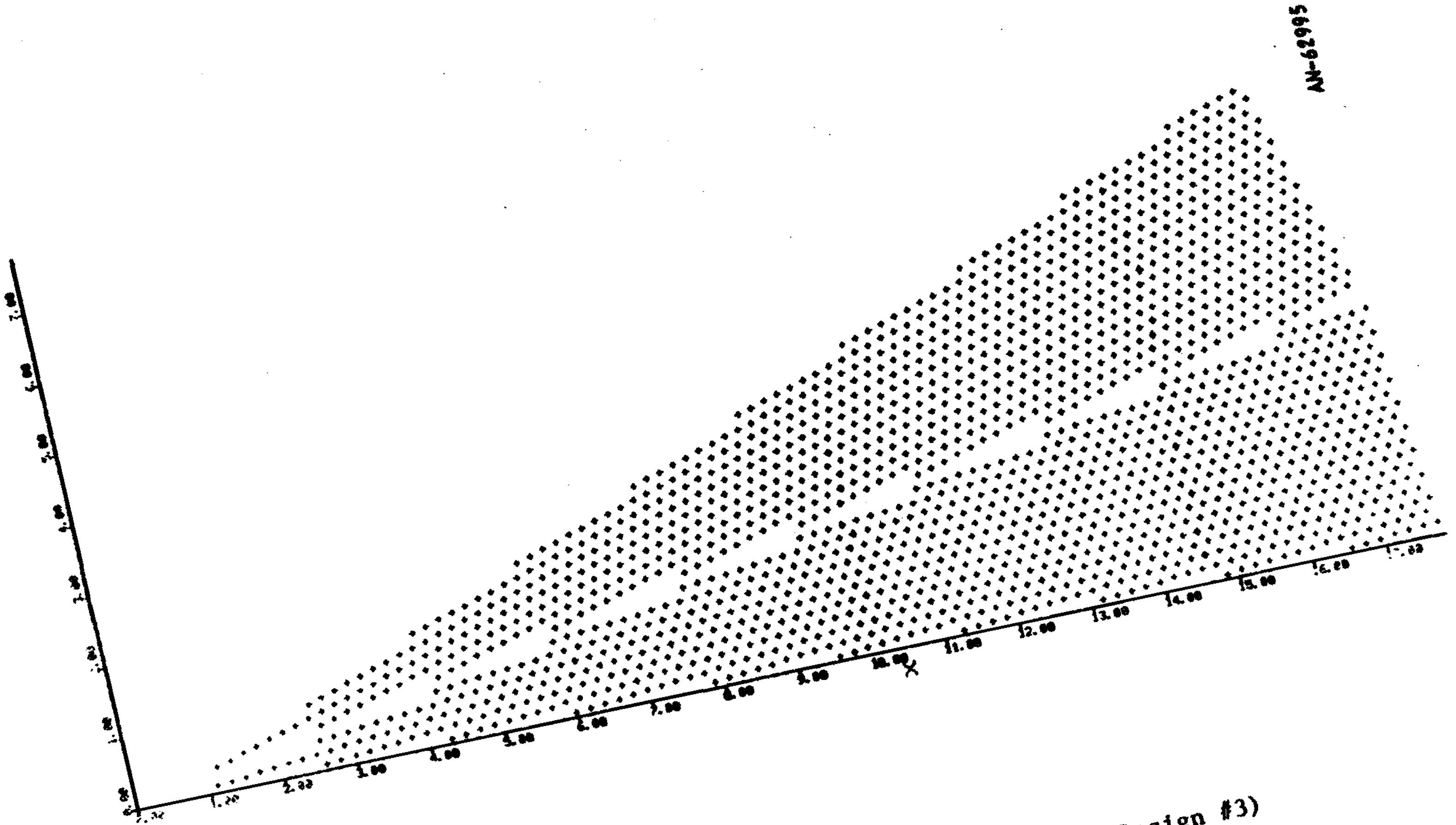

Figure 2.30. Element Position for Two Gores (Gore Design #3)

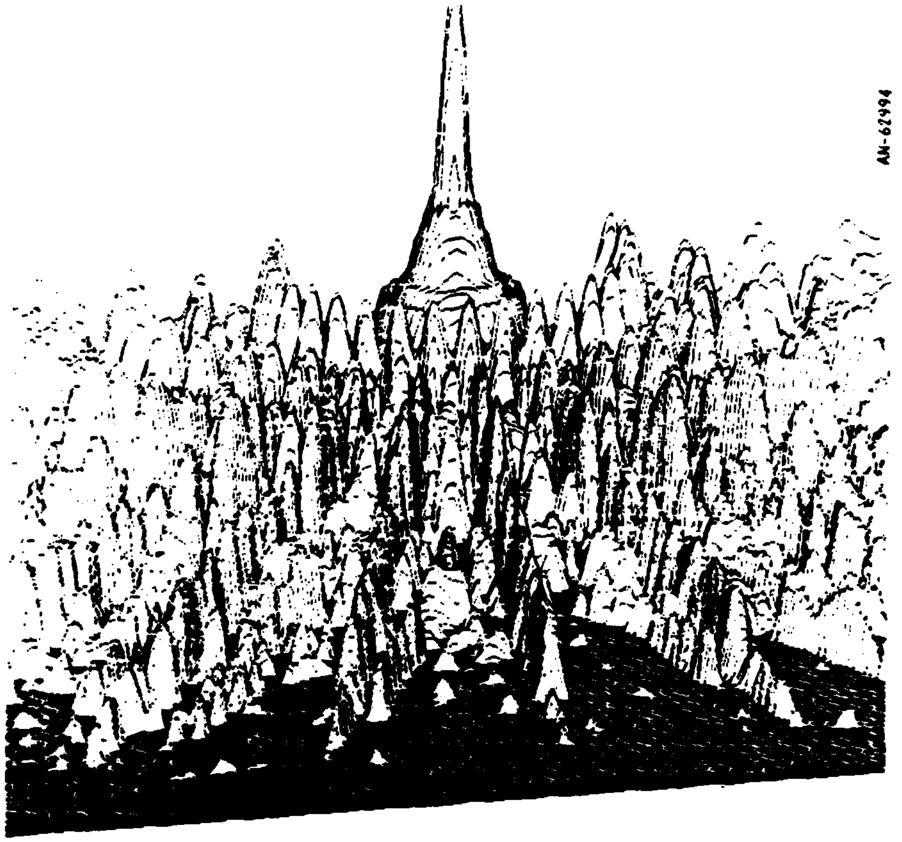

Figure 2.31. Far-Field Pattern for Gore Design #3

Raytheon.[1] The feed program developed by Raytheon determines the feed beam amplitudes (or weights) by sampling the desired illumination of the peak of each feed beam, and using the sampled value as the weight. This may not be the optimum method, and this is another potential area for future study.

---

[1] J.D. Hanfling and B.R. Herrick, Final Report for Low-Sidelobe Space-Fed Lens Antenna Transform Study, Raytheon Company, CDRL Seg No. 102, 29 January 1982.

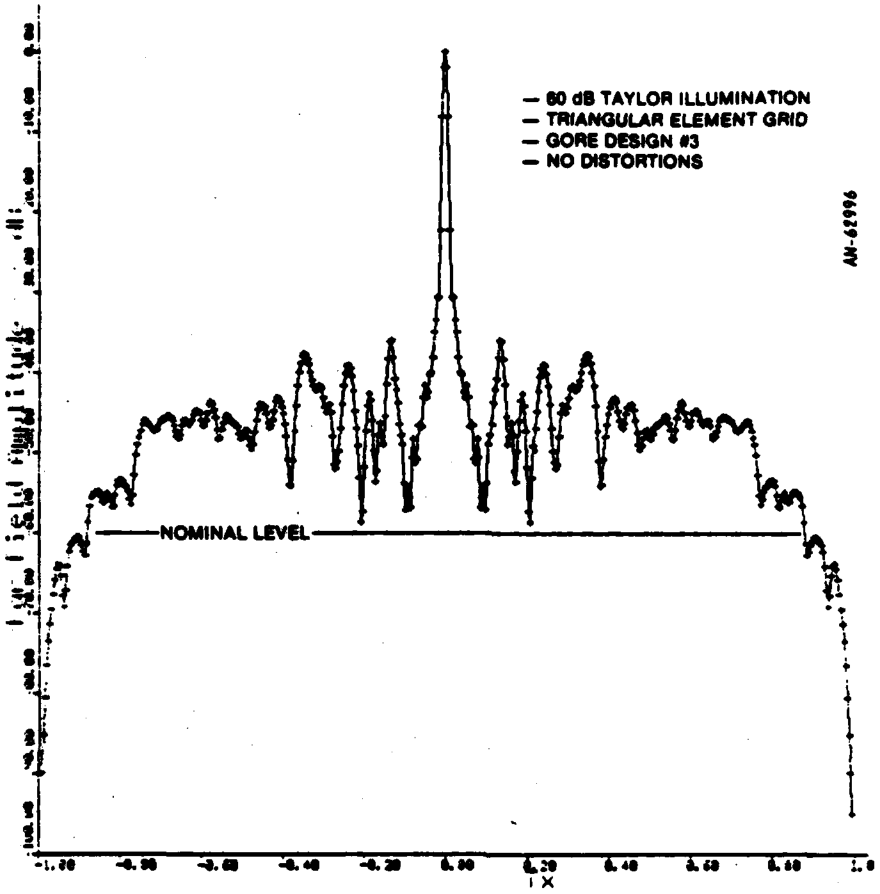

Figure 2.32. 35 m Diameter Circular Array, Gore Design #3

2.1.3.5 <u>Feed Defocusing Study--23 × 60 m Elliptical Aperture</u>

A low-orbit design is being considered which is illustrated in Fig. 2.34. It is a 23 × 60 m elliptical aperture, space-fed with an array feed at a focal length of 60 m. The issue under consideration is feed defocusing due to mechanical deformation of the supporting mast, and in particular, what specification should be used for the mechanical design.

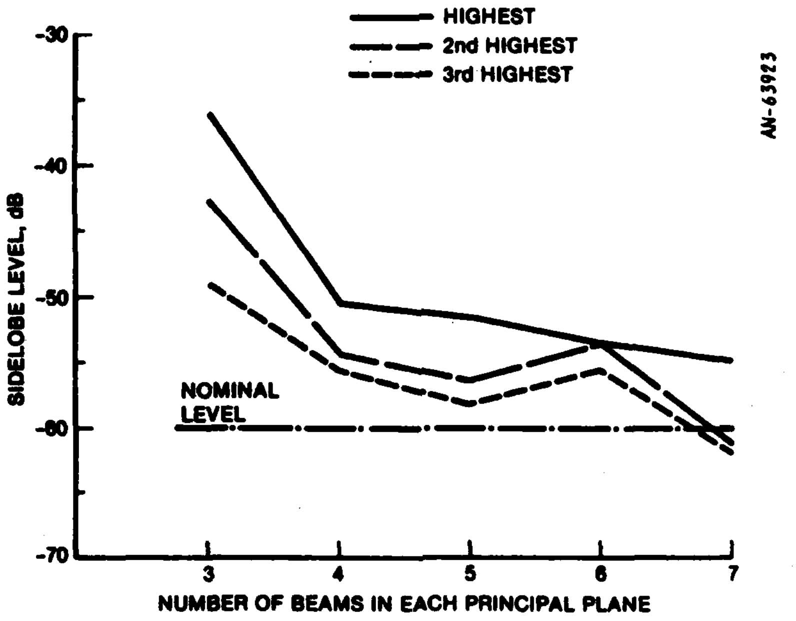

Figure 2.33. Multibeam Feed Sidelobe Levels

This study is being carried out by RADC using a linear-array model, and the SARF simulation was used to spot-check the results for the case of the two-dimensional array. A one-meter element spacing was used (instead of the actual 0.1716 meter spacing) since to the first order the results are not affected, and the computer time is reduced by a factor of 34, to about two minutes per case. The aperture illumination was provided by a 2-element array cluster feed, each element having a $e^{-11.23\theta^2}$ pattern. This gives an exponential illumination with a -22 dB edge taper across the long dimension of the ellipse (21 dB due to the exponential pattern and 1 dB due to space loss), and (approximately) cosine distribution, also with a -22 dB edge taper, across the short dimension.

The nominal pattern is shown in Fig. 2.35. For the same edge illumination, the exponential taper provides better sidelobes than the cosine taper, so there is a ridge of sidelobes along the principal plane

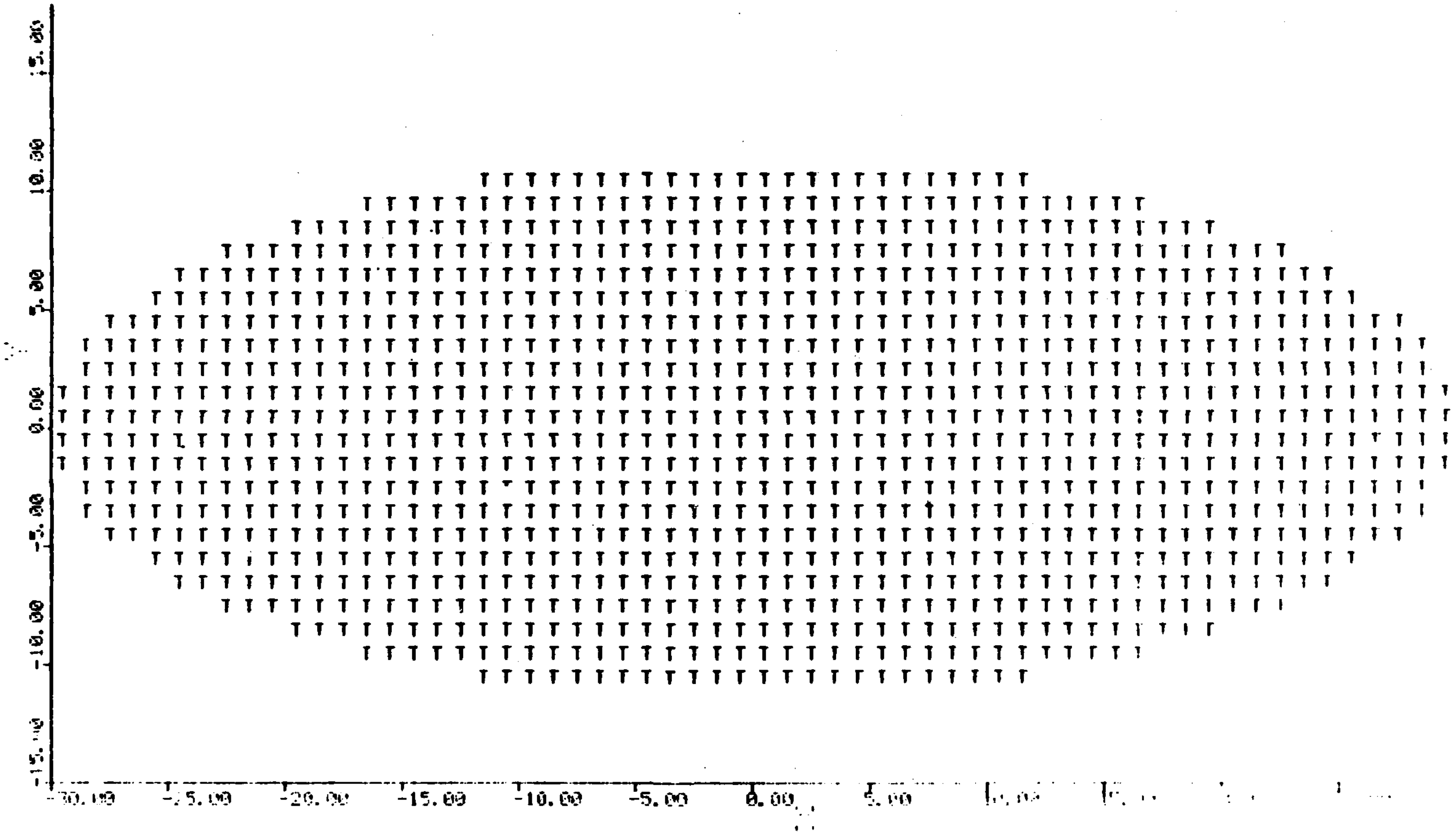

Figure 2.34. 23 × 60 m Elliptical Aperture

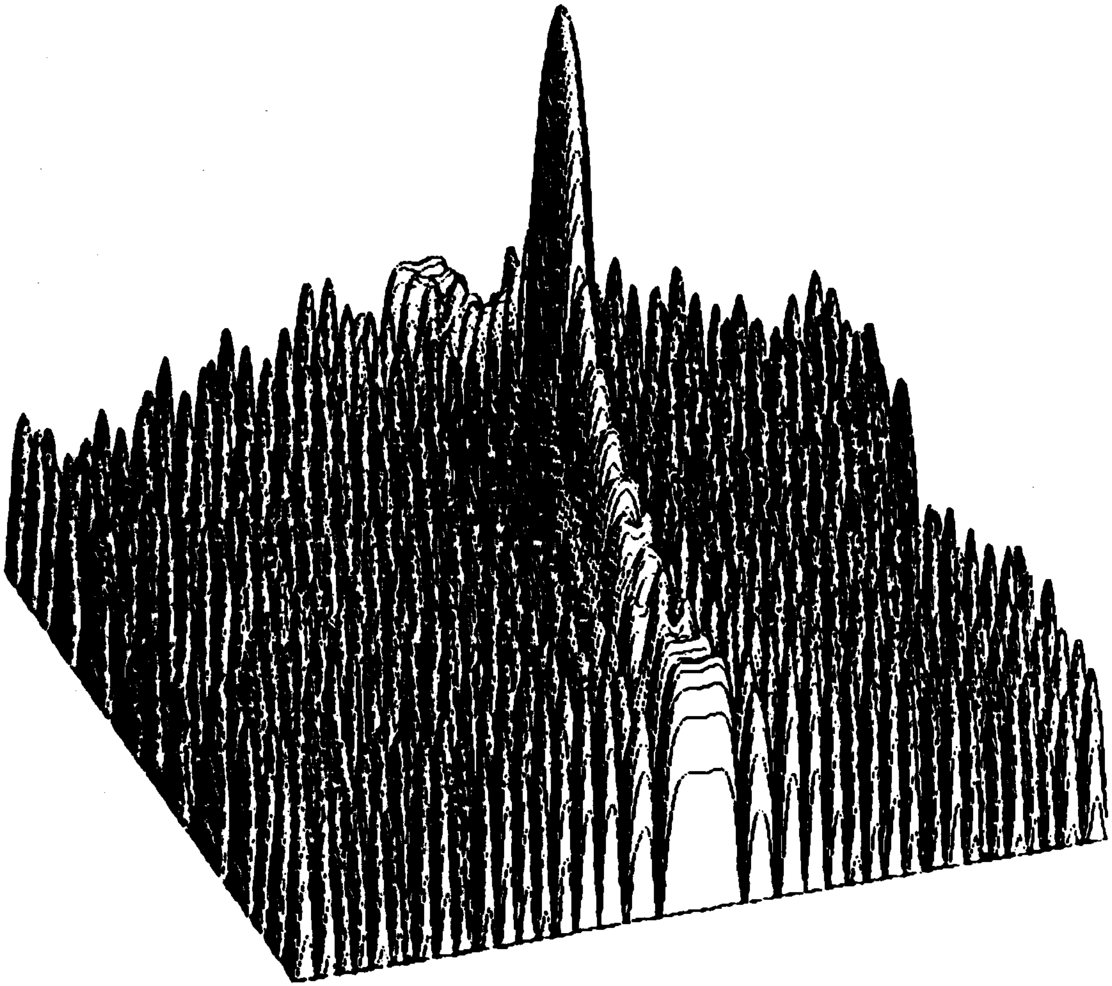

Figure 2.35. Elliptical Aperture Pattern

through the short aperture dimension (broad beamwidth plane), starting with a first sidelobe of -25.2 dB. In the orthogonal dimension, the first sidelobe is -39.2 dB. A pattern cut along the principal plane through the long aperture dimension is shown in Fig. 2.36. This is the plane in which a 0.05 m lateral feed translation was made, resulting in the pattern shown in Fig. 2.37. There is very little change in the pattern sidelobes; numerical data is given in Table 2.4 showing a negligible 0.2 dB increase in the highest first sidelobe. The beam scans over 0.05 degrees as a result of the feed translation, which is approximately equal to the angle between the feed and the array axis. The

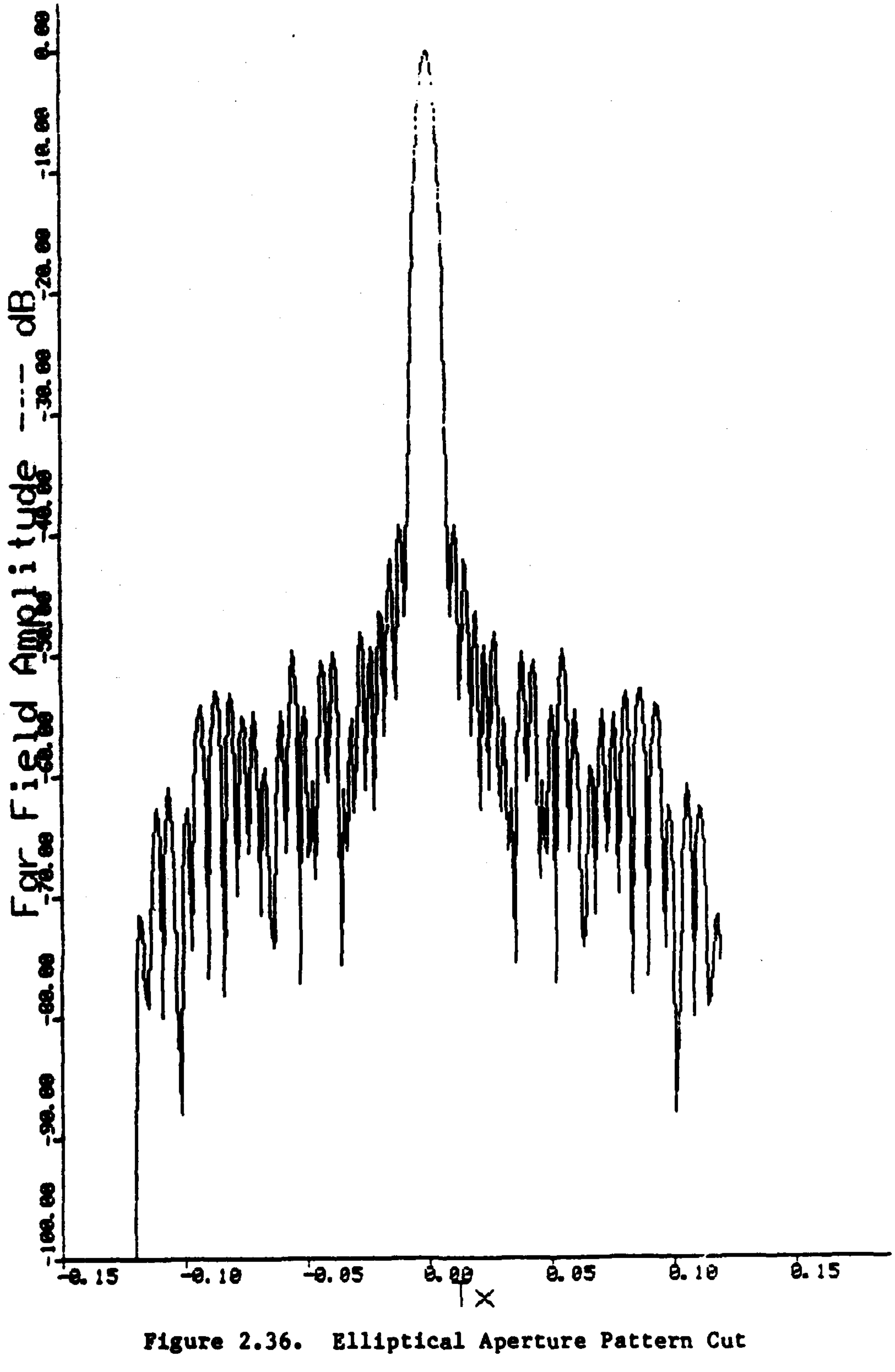

Figure 2.36. **Elliptical Aperture Pattern Cut**

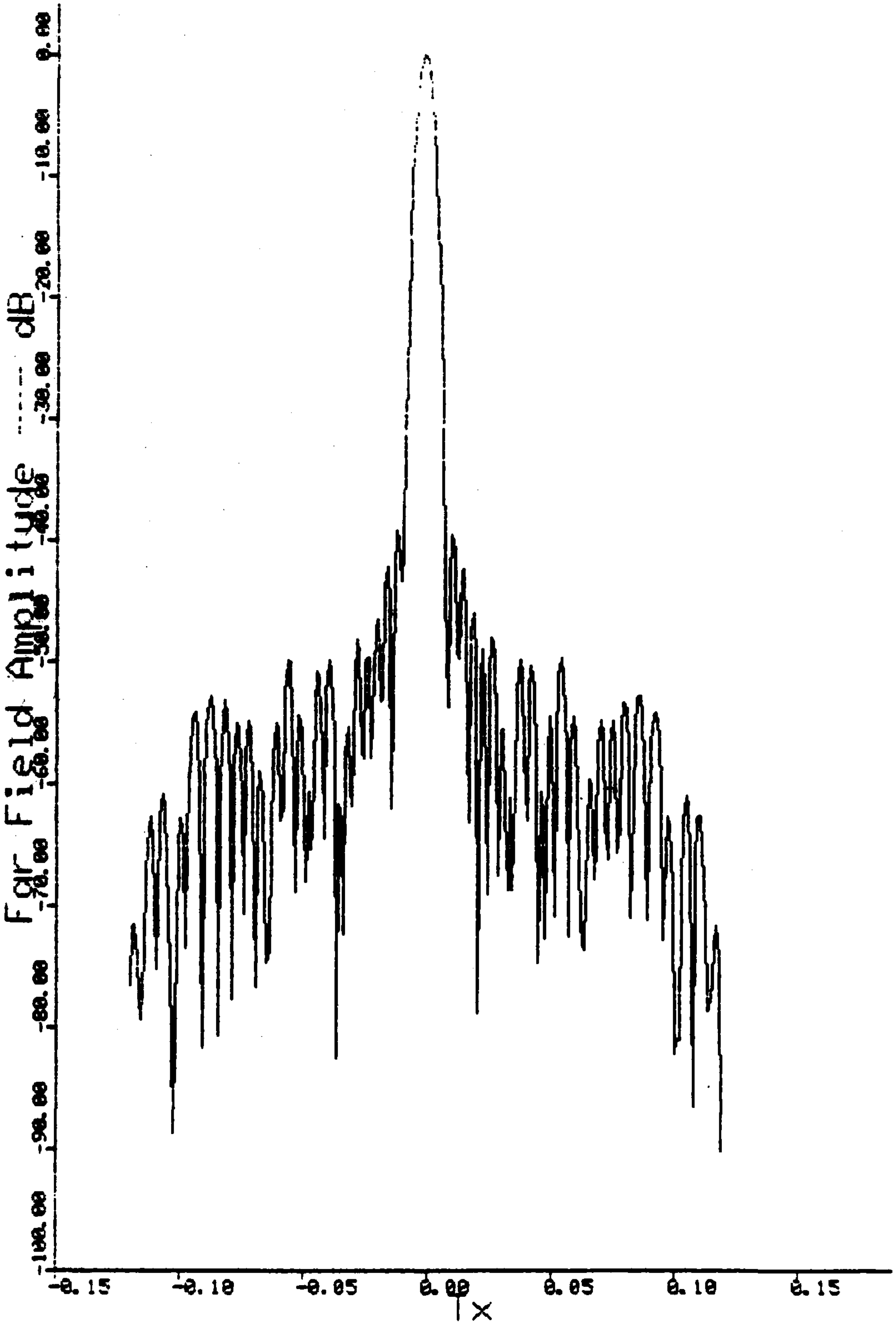

Figure 2.37. Effect of 0.05 m Feed Translation

TABLE 2.4

EFFECT OF FEED DEFOCUSING

	First Sidelobe, dB		
	Right Side	Left Side	Beamshift, deg
Nominal Case	39.21	39.21	0
0.05 m Lateral Translation	38.99	39.36	0.047
0.05 m Axial Translation	39.30	39.30	0
1° Feed Tilt	39.13	39.11	0

conclusion is that there must be compensation for the beam scan, but otherwise the effects are negligible. Similar runs were made for a 0.05 axial translation, and a feed tilt of one degree in the plane of the long aperture dimension. The feed tilt results in the aperture edge illumination becoming 1.5 dB higher on one side, and 1.5 dB lower on the other. However, this has a very minor impact on the sidelobes, and in all cases the effects are negligible. The conclusion is that displacements up to 0.05 m and tilts up to 1 degree are acceptable mechanical tolerances on the feed position.

2.1.3.6 Defense Suppression Weapon Study

The SARF simulation has also recently been applied on another Air Force contract.[1] Since the results demonstrate several capabilities of the SARF simulation not demonstrated in the other applications presented above, they are briefly reviewed here.

The Defense Suppression Weapon Study concept under investigation involves an anti-radiation missile (ARM) attacking a defensive bistatic radar. The receive antenna is a large array--roughly 20,000 dipole

---

[1] Mainbeam Precursor Jammer Study, Ballistic Missile Office (BMO), Norton Air Force Base, Contract F04704-82-C-0011.

elements--illustrated in Fig. 2.38, employing monopulse tracking. The transmit antenna is slightly smaller. The ARM is designed to spray shrapnel over the array face, to damage or destroy the dipole elements, or feed system components such as phase shifters. The array employs subarrays of two to eight elements, each fed with a 4-bit phase shifter, and hitting one phase shifter affects four elements on the average. The array was modeled as consisting of 2×2 subarrays, as illustrated in Fig. 2.39. The SARF simulation is well suited to this problem due to:

- The ability to handle large arrays
- The ability to model subarrays (see Sec. 2.1.1.2)
- The ability to model failures causing both total power shut-off or amplitude and phase changes
- The ability to model failures distributed randomly over the aperture or restricted to one or more sections of the aperture
- The ability to model both sum and difference patterns

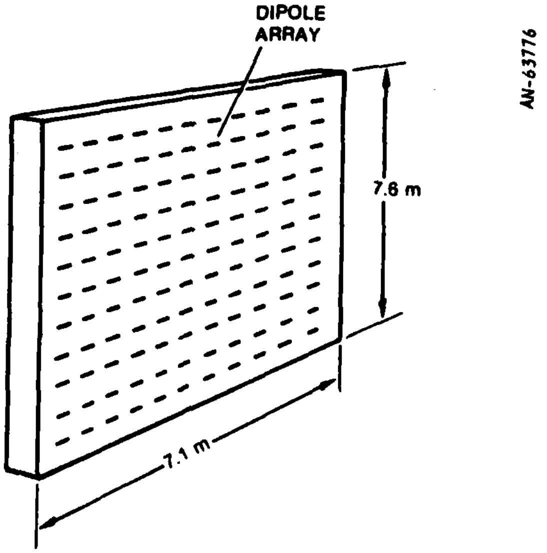

Figure 2.38. Receive Antenna

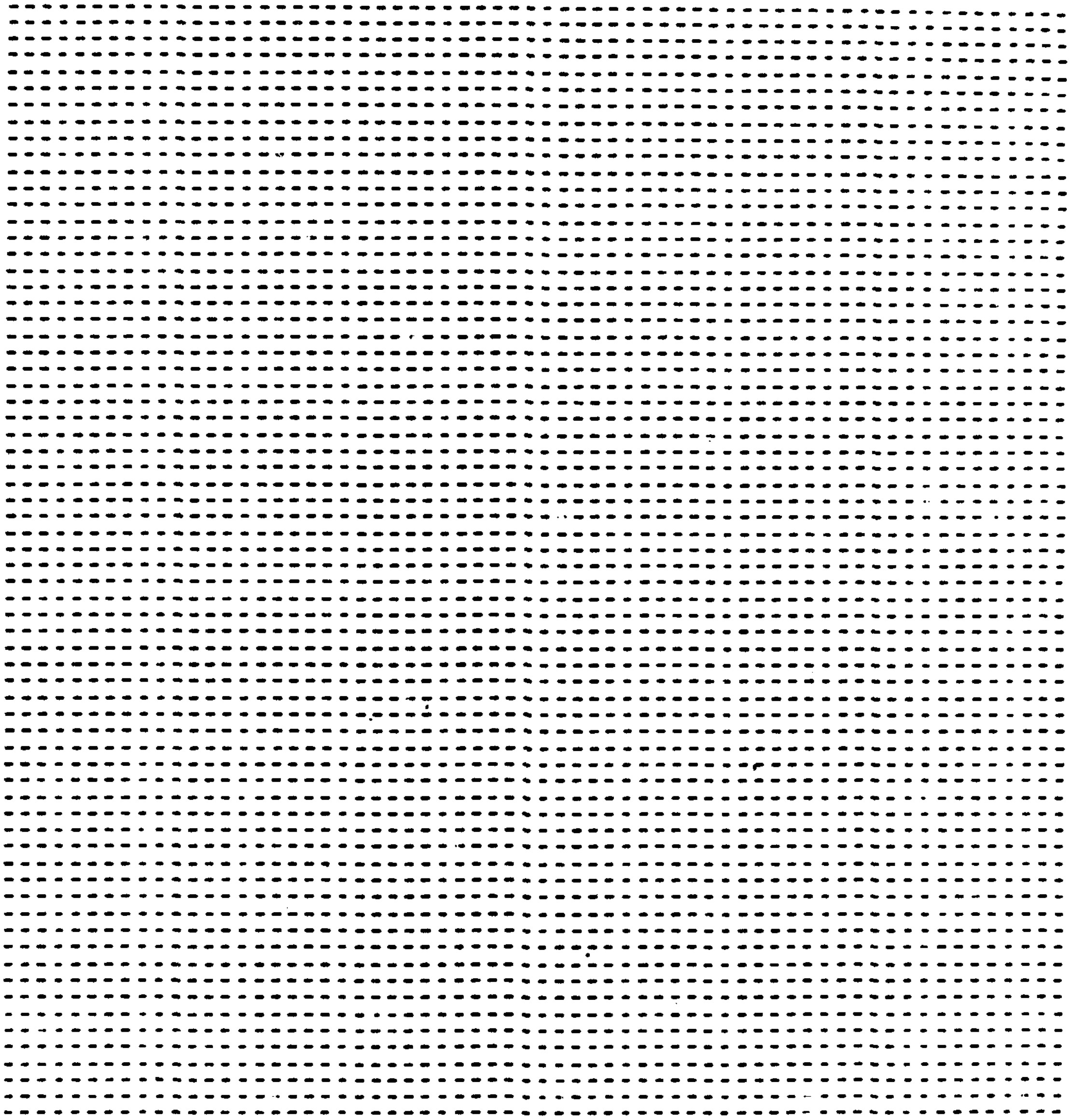

Figure 2.39. Nominal Locations, 2 × 2 Subarrays

The initial investigation involved a parametric study of a random distribution of shrapnel over the aperture, such as illustrated in Fig. 2.40. The percent failures ranged from 20% to 80%, and two failure modes were modeled:

- Total subarray power shutoff
- Random failure of one phase bit, causing a 22 1/2, 45, 90, or 180° phase error—with no power loss

A sample series of patterns with and without damage is shown in Figs. 2.41 through 2.44. A cosine on a 0.2 volt pedestal illumination was used for both the sum and difference patterns, the difference patterns obtained by phase-shifting half of the aperture 180 degrees. This results in rather high sidelobes in the tracking plane as shown in Fig. 2.43. The significant effects of the damage inflicted are summarized in Table 2.5 and 2.6.

For total subarray power loss, the gain loss is simply equal to

$$20 \log_{10}\left(\frac{\text{undamaged subarrays}}{\text{total subarrays}}\right)$$

which is of course what would be expected. For phase failures, the gain loss is much lower. The difference channel experienced a similar gain loss, and for the case of phase failures, very small shifts in the null position. There is <u>no</u> null shift for total failures. The tracking slope—difference channel divided by the sum channel—was also almost unchanged.

The conclusion from this initial study is that the uniform shrapnel pattern causes relatively minor disruptions to the radar, except for the gain loss associated with very high percentage of total damage. In the next phase of the study, non-uniform damage patterns will be studied. In particular, hitting a row feed affects a rectangular section of the aperture four elements high on one-half of the aperture.

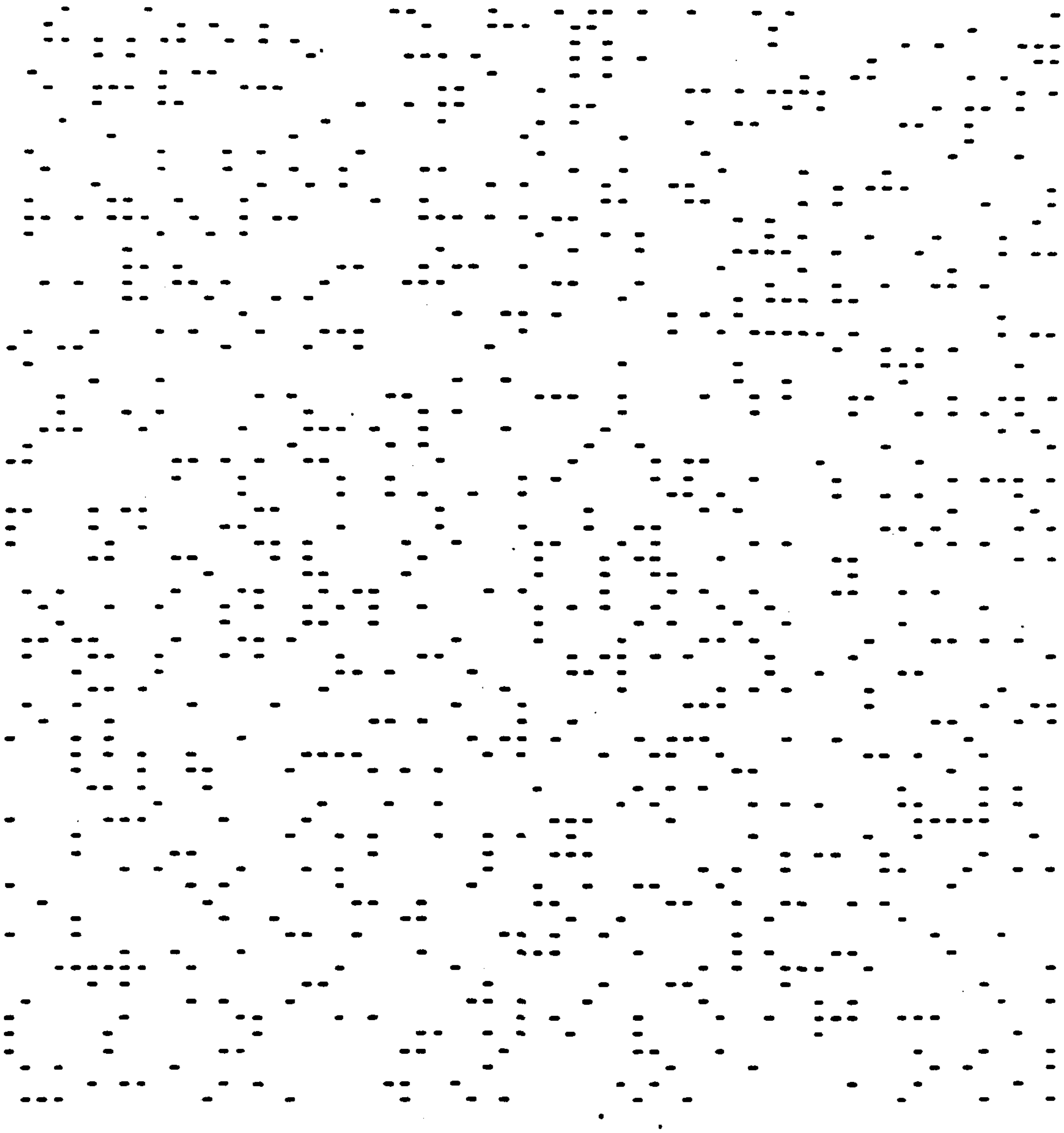

Figure 2.40. 20% Failed Subarrays

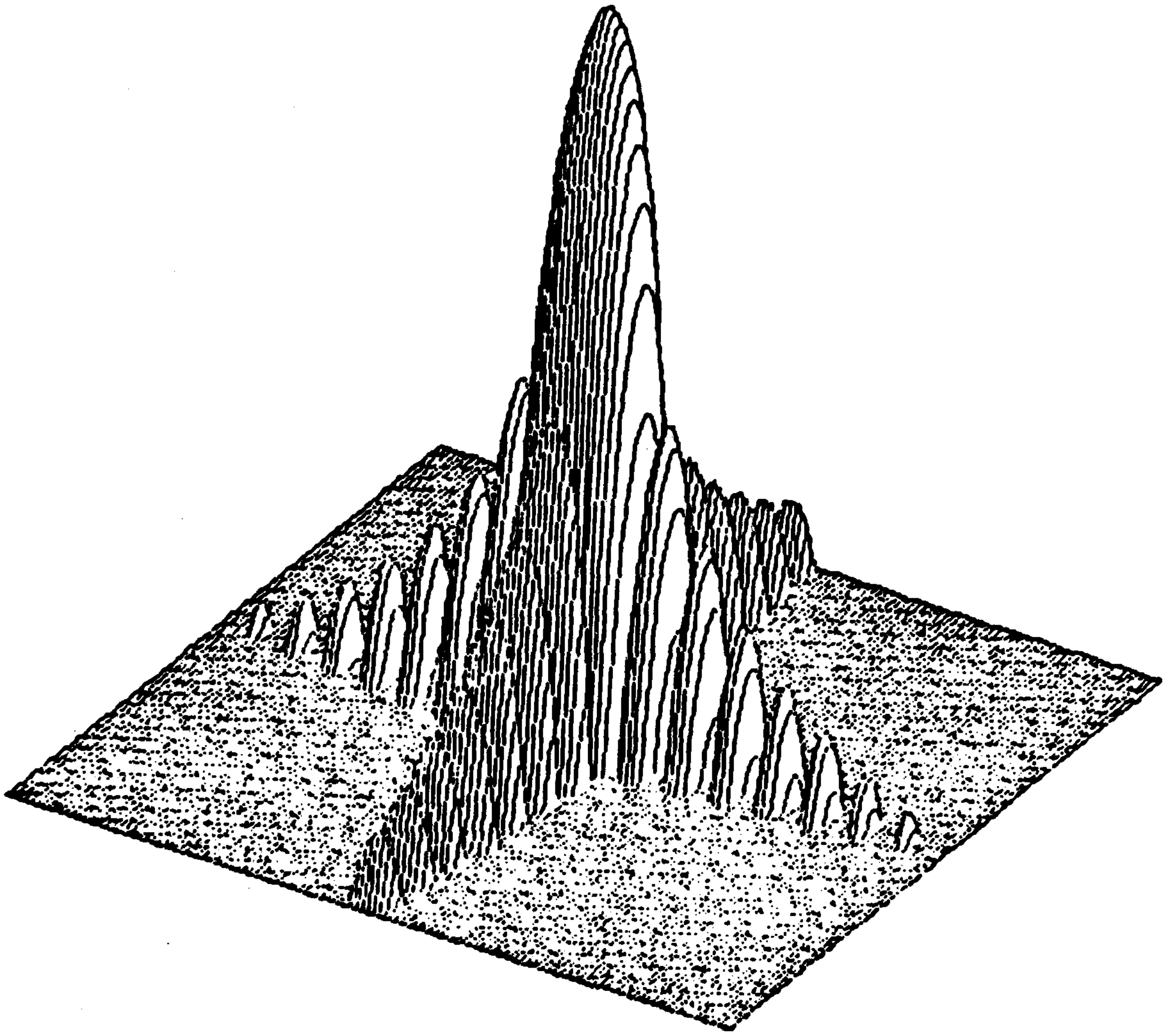

Figure 2.41. Nominal Sum Pattern

The SARF simulation will also handle this type of failure (see Sec. 2.3.3.3), again demonstrating the flexibility and wide range of applicability of the simulation.

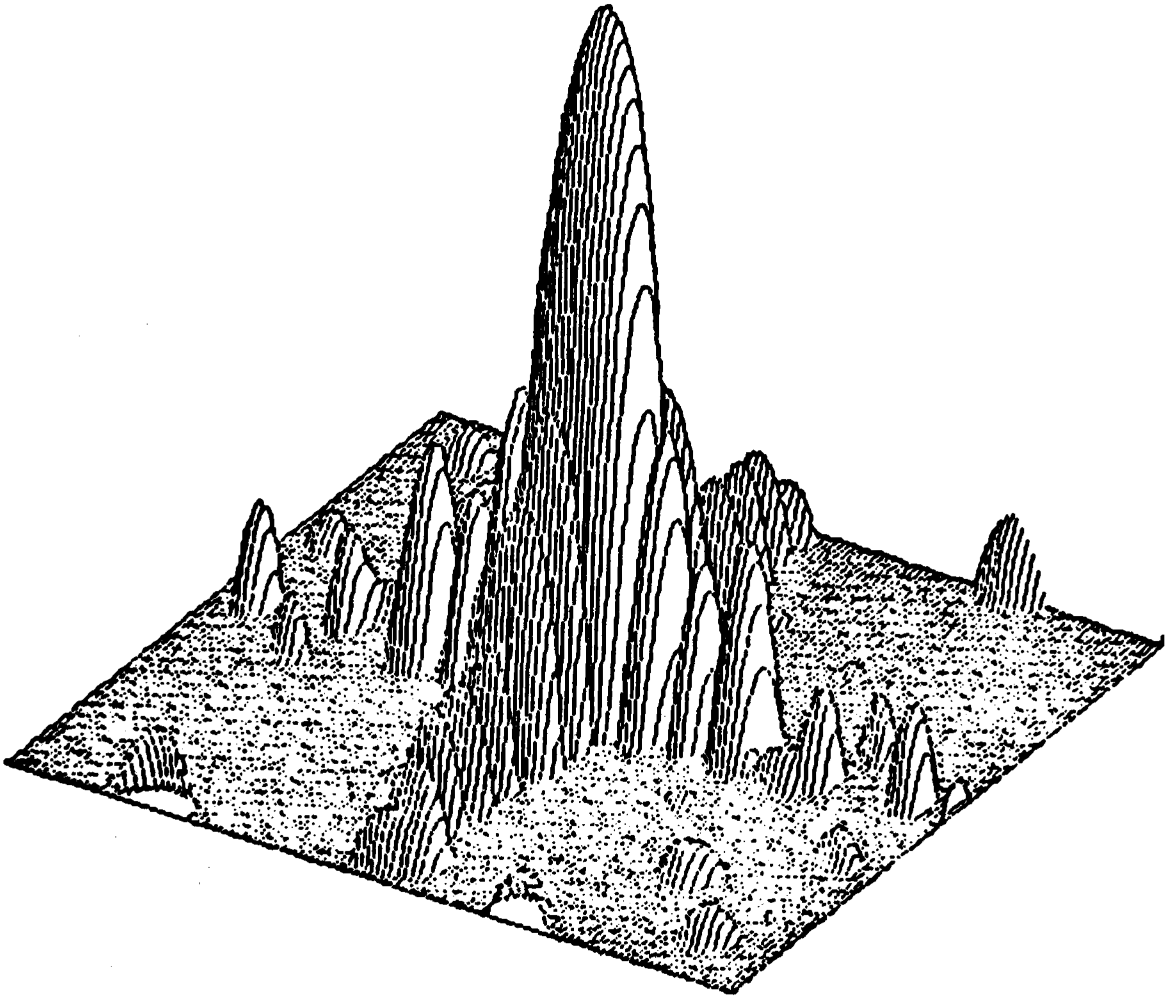

Figure 2.42. Sum Pattern--20% Failures

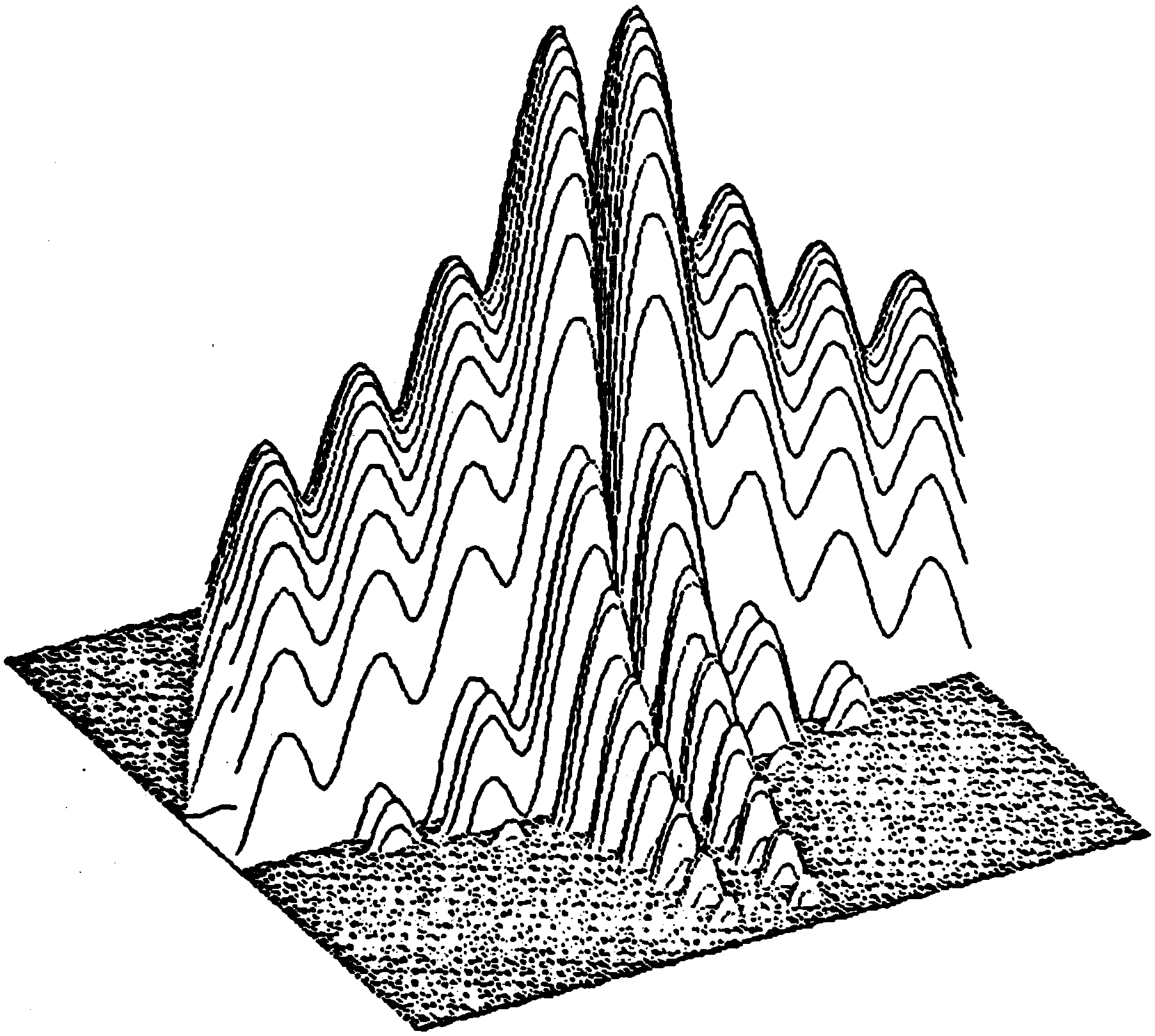

Figure 2.43. Nominal Difference Pattern

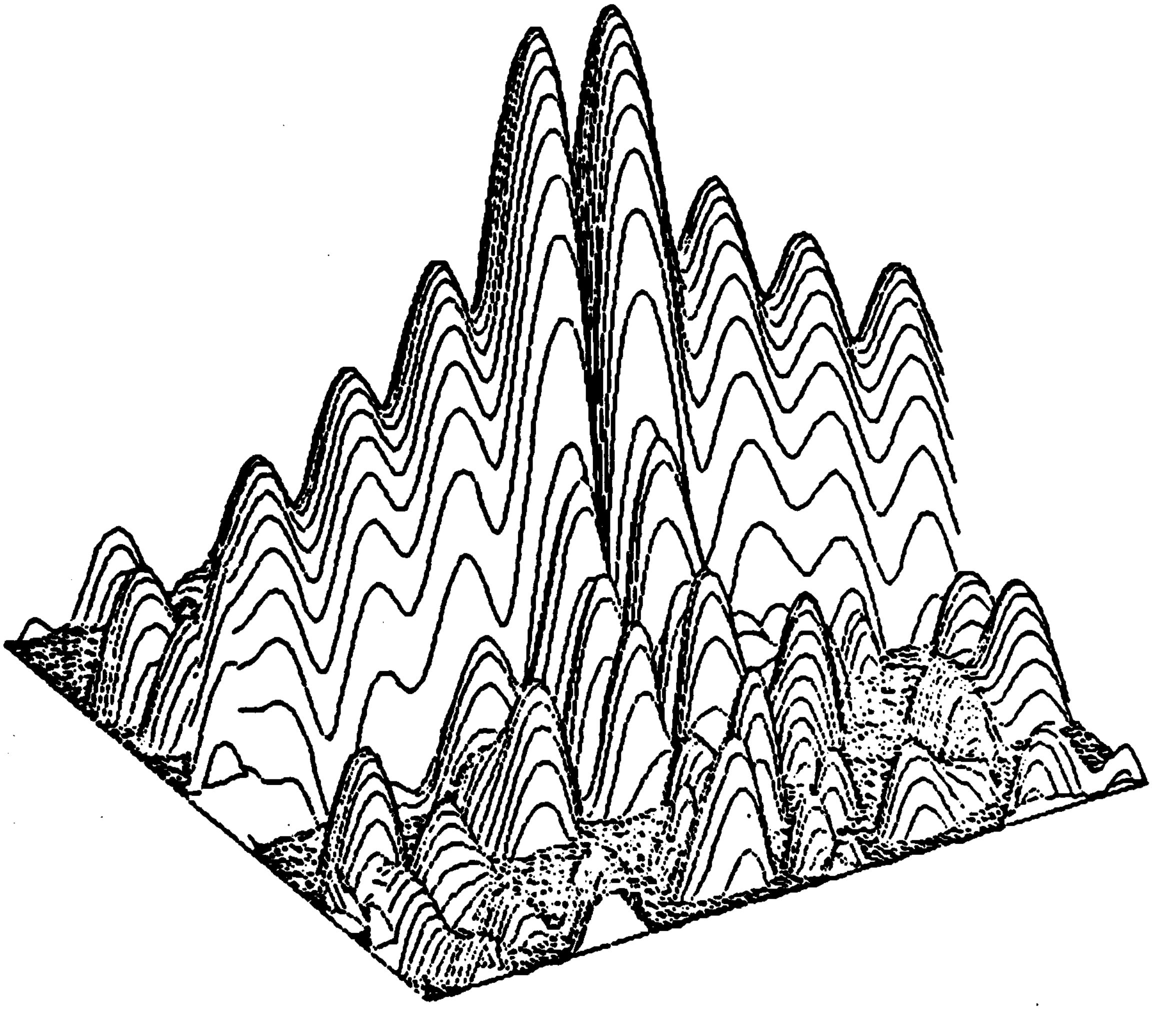

Figure 2.44. Difference Pattern--20% Failures

TABLE 2.5

SUM CHANNEL GAIN DEGRADATIONS

Damage Type	Gain Loss, dB
Total Loss of Power	
20% Damaged Elements	1.9
40% Damaged Elements	4.5
80% Damaged Elements	13.9
Phase-Bit Errors,* No Power Loss	
20% Damaged Elements	1.3
40% Damaged Elements	2.3
80% Damaged Elements	3.3

---

*Phase errors of 22-1/2°, 45°, 90°, and 180° with equal probability.

TABLE 2.6

DIFFERENCE CHANNEL DEGRADATIONS

Damage Type	Null Shift, degrees	Tracking Slope, Normalized by Nominal Value
Total Loss of Power		
20% Damaged Elements	0.0	0.9988
40% Damaged Elements	0.0	1.0032
80% Damaged Elements	0.0	0.9784
Phase-Bit Errors,* No Power Loss		
20% Damaged Elements	0.0002	0.9980
40% Damaged Elements	0.0020	1.0072
80% Damaged Elements	0.0035	0.9924

---

*Phase errors of 22-1/2°, 45°, 90°, and 180° with equal probability.

2.2 ANALYSIS

Nearly all the analysis concerning the SARF simulation was completed and documented in Appendix A. This analysis included the far-field approximations utilized as well as an evaluation of the errors incurred for a representative SBR scenario. The analysis also compared the cell model technique to that of the Fast Fourier Transform (FFT) for the implementation of an efficient computational method. A detailed analysis of the element pattern, with both random and systematic deviations, was also provided.

The remaining analysis (which was completed after the Interim Report) dealt with the errors obtained using an approximate technique when surface deformations exist. In the interest of brevity, the analysis reported in the Interim Report will not be duplicated. Therefore, the remainder of this section will present only the analysis relative to surface deformations.

2.2.1 Surface Deformation

Membrane surface deformation causes the elements in the array to be displaced from the ideal location on a planar lattice. This displacement can cause significant degradation in gain as well as a severe increase in the RMS sidelobe levels. Most of the literature treats surface deformation as a random phase error; however, they are not identical, since the illumination phase distortion, due to element displacement, is dependent (in general) on the position of the element as well as the direction of interest for pattern calculation.

Since the FFT does not provide an exact calculation of the antenna pattern for a deformed aperture, additional modifications must be incorporated to approximate the desired pattern. The remainder of this section is dedicated to determining the errors associated with the approximate pattern calculation techniques used in the SARF simulation. The arrangement of the following discussion starts with an analysis of the effects of out-of-plane random errors and then in-plane random errors. This analysis is performed first for corporate-fed arrays (since they are more easily described) and then for space-fed arrays. Next a brief intuitive discussion is presented for systematic deformation which includes both linear tilt and parabolic deformations. Finally, data obtained for several combinations of all of the above cases is presented along with the associated errors due to approximate technique.

2.2.1.1 Random Deformations--Corporate Feed

The FFT, in general, can only approximate the far-field pattern of a phased array. For the special case of a planar aperture with elements located on a rectangular or triangular grid it will give the exact answer. Not only is the above described array ideal for FFT modeling, it is also usually the desired array. Since it is desirable to have small deviations from the planar, regular grid array, the FFT input and output can be modified to give a very good approximation of arrays with non-negligible deformations.

To determine the error in the pattern calculation relative to the actual pattern, consider the equation for a corporate fed array with surface deformations $\bar{\delta}_{nm}$. (The associated coordinate system is shown in Fig. 2.45)

$$\bar{E}(T_x,T_y) = \sum_{nm} I_{nm} \exp\{jK(m\ d_xT_x + n\ d_yT_y + \bar{\delta}_{nm}\cdot\bar{T})\} \qquad (2.3)$$

where I_{nm} = illumination function of the nmth element

$K = 2\pi/\lambda$, λ = wavelength

d_x, d_y = the nominal element spacing in the x and y directions, respectively

$\bar{T} = T_x\hat{a}_x + T_y\hat{a}_y + T_z\hat{a}_z$

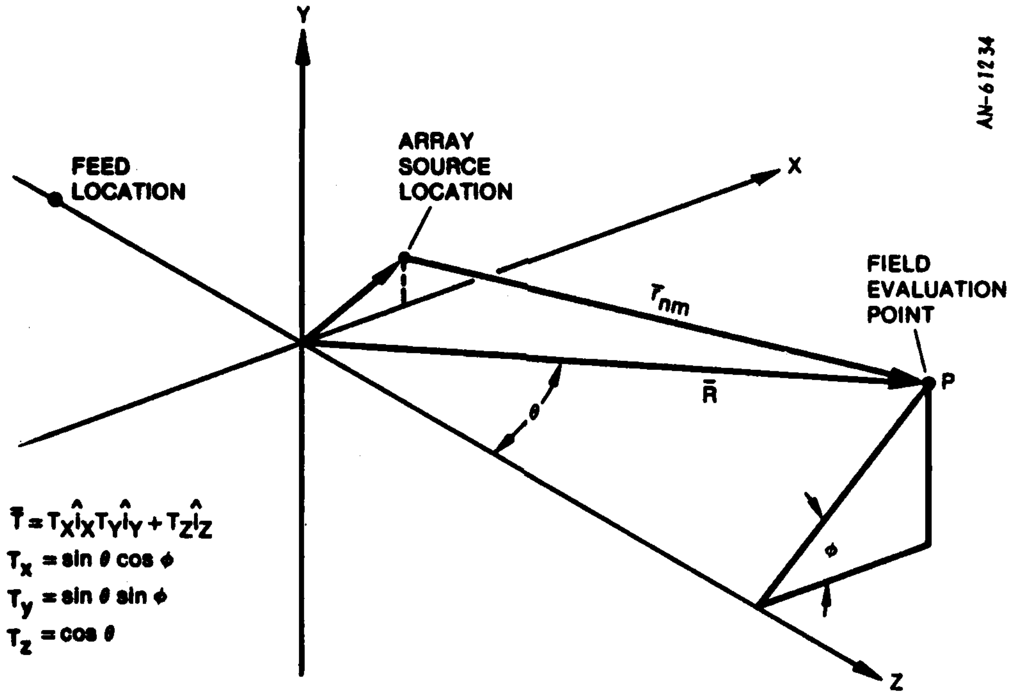

Figure 2.45. SARF Simulation Coordinate System

$\bar{\delta}_{nm} = \delta_{nmx}\hat{a}_x + \delta_{nmy}\hat{a}_y + \delta_{nmz}\hat{a}_z$, represents the displacement of the element in the x,y,z directions, respectively

The FFT can evaluate the above equation exactly if the term is zero $\bar{\delta}\cdot\bar{T}$.[1] However, for non-zero $\bar{\delta}\cdot\bar{T}$ an approximation must be made. (The components of $\bar{\delta}$ are shown in Fig. 2.46.)

In-Plane Deformations

Let's break the problem into two pieces. First, consider only in-plane deformations (i.e., δ_x and δ_y). To facilitate the analysis, assume that the in-plane deformations are random and normally distributed with zero mean and variance $\sigma^2 = \sigma_x^2 + \sigma_y^2$. Logically, one would assume that for small in-plane errors, the grid spacing of the FFT could

---

[1] When no confusion will result, the subscript nm will be dropped from the notation; therefore, $\delta_{nm} = \delta$.

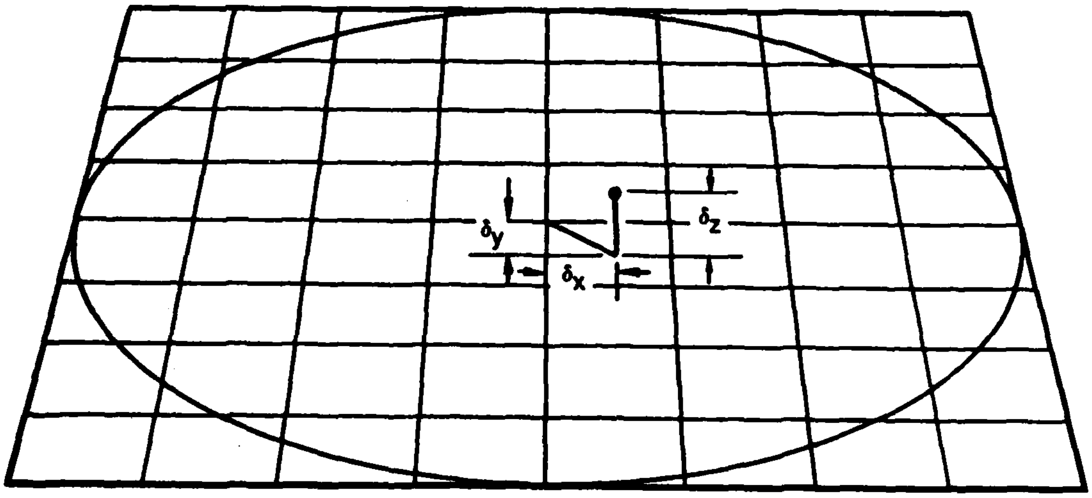

Figure 2.46. Components of Element Location Displacement

---

be reduced and the resultant errors in the FFT calculated pattern could be made negligible. But how small does the grid spacing have to be? The answer to the question can be obtained by considering a one-dimensional (x) random deformation, although the results of the subsequent analysis apply to the two-dimensional case as well.

Figure 2.47a shows a normally distributed random deformation $f(x)$, with some variance σ . If we use the FFT to model such a deformation, each element must be placed on the nearest grid center. Now consider the deformation that is approximated by this technique.

Let δ represent the true deformation and let the distance between grid lines equal d . We can now define a probability density function (p.d.f.) of the simulated deformation using the FFT by noting

AN-62342

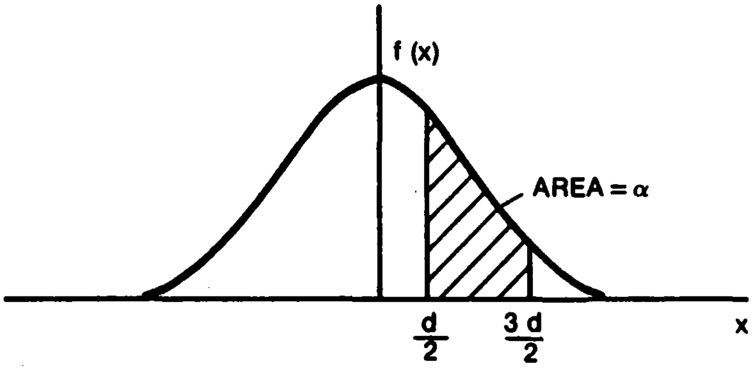

(a) Normally Distributed Random Deformation

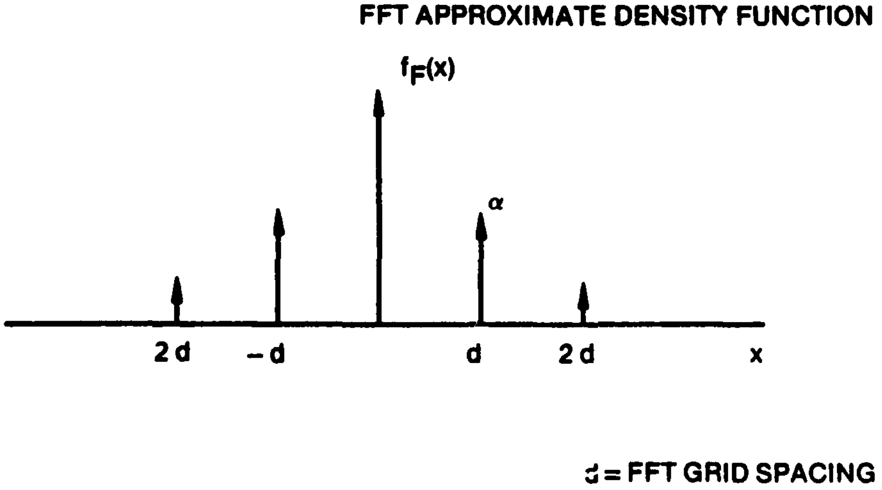

(b) Approximate Technique Density Function

Figure 2.47. Actual and Approximate Densities for Random Deformations

that the probability of a deformed element being on a grid line with value d is just the area under the p.d.f. of the true deformation between d $\pm$ d/2 , i.e.:

$$P(d) = \int_{d/2}^{3d/2} f(x)\, dx = \alpha = P(-d)$$

Likewise, the probability of a deformed element being at 2d is the area under the curve f(x) between 3d/2 and 5d/2 . Similar reasoning provides the rest of the p.d.f. for the simulated deformations. Figure 2.47b shows the resultant p.d.f.

Now the sampling theorem[1] states that any bandlimited function is uniquely determined by its values at uniform intervals less than $1/2f_s$ seconds apart, where f_s is the Nyquist sampling rate and is equal to the highest frequency component of the bandlimited function. Even though f(x) is not bandlimited, an excellent approximation can be made by neglecting its higher frequency components as shown below. The continuous Fourier Transform of f(x) is

$$F(\omega) = e^{-\sigma^2 \omega^2 /2}$$

By truncating this spectrum at some frequency f_s , nearly all the energy of the function f(x) can be retained and the sampling theorem now applies.

By choosing $f_s = 1/2\sigma$ we find 99.9% of the energy is contained in the frequency truncated version of f(x). Since our simulated p.d.f.

---

[1] M. Schwartz, Information Transmission, Modulation, and Noise, McGraw-Hill, 1959.

AD-A133 734 RF SYSTEMS IN SPACE VOLUME I SPACE ANTENNAS FREQUENCY 2/3
(SARF) SIMULATION(U) GENERAL RESEARCH CORP SANTA
BARBARA CA A C LUDWIG ET AL. APR 83
UNCLASSIFIED RADC-TR-83-91-VOL-1 F30602-81-C-0119 F/G 17/9 NL

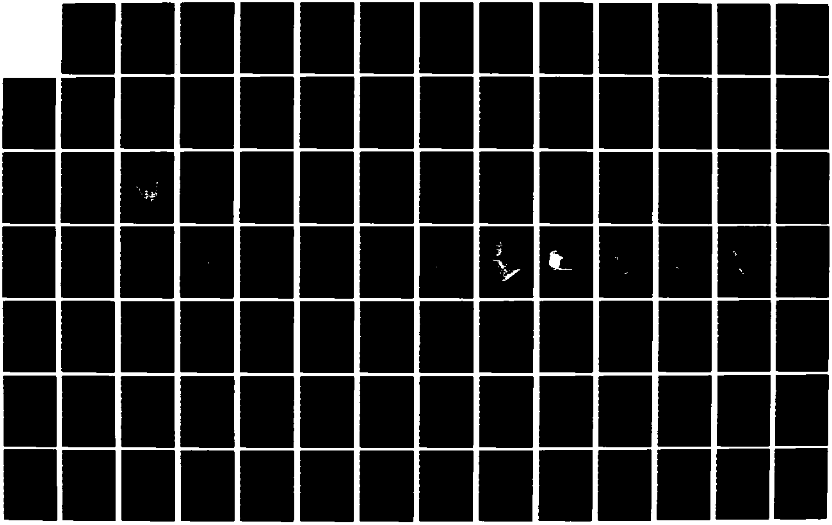

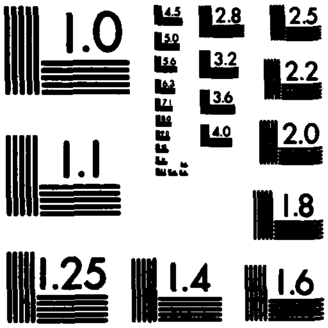

MICROCOPY RESOLUTION TEST CHART
NATIONAL BUREAU OF STANDARDS-1963-A

has impulses at nd $(n = 0,1,2,\ldots)$ and (by the sampling theorem), $d = 1/2f_s$, we obtain the result

$$d = \sigma$$

This establishes a lower bound for choosing the appropriate grid spacing in the presence of random, in-plane element displacements. It is a lower bound since very small displacements can be ignored and the grid spacing can be made equal to the nominal element spacing.

For example, consider a circular array with 130,000 elements spaced at a nominal distance of 0.7λ with a 60 dB Taylor tapered illumination. Assume some RMS in-plane deformations of $\sigma = \lambda/100$. This translates into an RMS phase distortion[1] of

$$\sigma_\phi = \left(\frac{2\pi}{\lambda}\right)\left(\frac{\lambda}{100}\right) = \frac{\pi}{50}$$

Then the sidelobe level relative to the peak of the main beam caused by these deformations is

$$SLL_N = \frac{\sigma_\phi^2}{G} = -72 \text{ dB relative to beam peak}$$

where

$$G = \frac{(\Sigma I_{nm})^2}{\Sigma I_{nm}^2}$$

---

[1] As was mentioned before, deformations produce phase distortions; and these phase distortions are a function of other parameters as well. However, for this example, equating deformations and phase distortions produces no significant errors in the analysis.

is the gain of the antenna. Obviously, in this example, the RMS sidelobe level caused by the surface deformations is negligible and the FFT grid spacing could be chosen as 0.7λ rather than σ, since the latter would cause extremely long processing time and storage requirements, without an improvement in the accuracy of the calculation.

Therefore, we can now choose our FFT grid spacing based on: the standard deviation of the displacements, the gain of the antenna, and the nominal level of the sidelobes without any surface distortion. A grid selection is shown in Fig. 2.48.

Several test cases have been performed using the SARF simulation and excellent results have been obtained using Fig. 2.48 for grid selection. In fact, test results indicate that Fig. 2.48 is conservative and

---

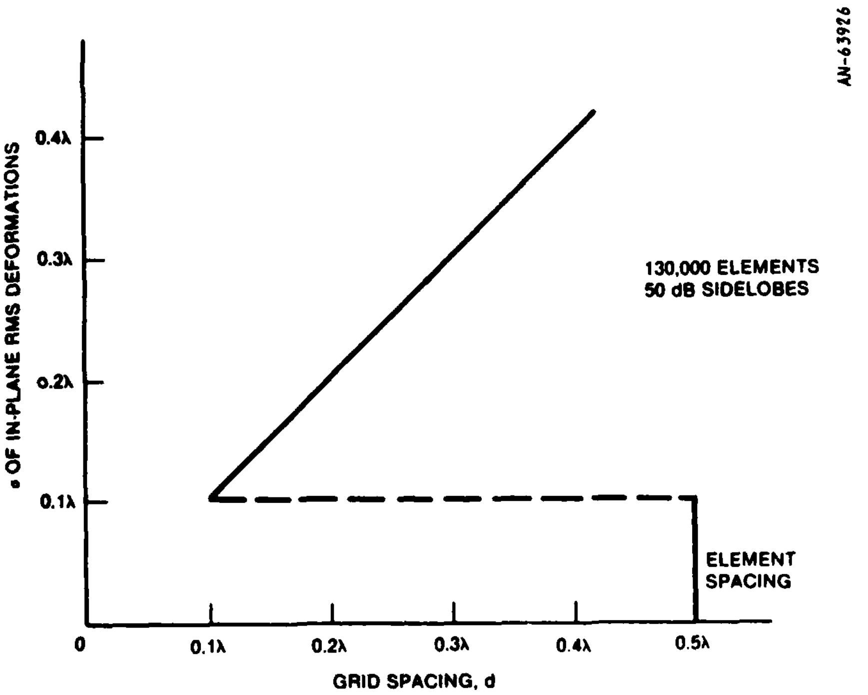

Figure 2.48. Selection of FFT Grid Spacing (Example)

larger grid spacing can be used for most cases. This is due to the choice of the highest frequency component in the spectrum of the actual deformations, and is also related to the threshold where errors are considered negligible.

Out-of-Plane Deformations

Now that we have established that the FFT (with the appropriate grid spacing) can provide an excellent approximation to in-plane deformations, let's discuss out-of-plane or z-directed deformations. Our term $\overline{\delta}_{nm} \cdot \overline{T}$ from Eq. 2.3 now becomes $\delta_{nmz} T_z$ where δ_{nmz} is the displacement of the nmth element in the z direction . Assume that the δ's are normally distributed with a standard deviation (RMS error) of σ_z . Then in order to use the FFT we need to approximate the term $e^{jk\sigma_z T_z}$. One method is obvious: use a 3-dimensional FFT and choose the grid spacing in the z direction based on the results of the previous subsection. While this seems like a reasonable approach, the cost (in computation time and storage) would be excessive for nearly all arrays of interest. In fact, the computation time would approach that of the brute-force technique, thus making the 3-dimensional FFT technique useless.

This leaves two alternatives to approximating out-of-plane deformations:

1. Elimination of the displacement dependence (n,m) by grouping elements with the same δ_z together and performing one FFT per group.
2. Elimination of the spatial dependence ($\overline{T}$) by modifying the illumination phase to provide an exact solution at some point in space T_o.

The first alternative was considered and rejected by estimating the number of FFT's necessary to implement the technique as well as the processing time needed to search the array and place groups of elements with the same δ together.

The second technique which was implemented in PAAS and has been adapted by SARF provides the most promising solution to the out-of-plane deformation problem.

How much error does the above-mentioned technique cause in the pattern calculation? Consider a corporate-fed array with normally distributed out-of-plane element displacements having a standard deviation of σ_z . This means that $\overline{\delta}_{nm} \cdot \overline{T}$ reduces to $\delta_{nmz} T_z$ or statistically to $\sigma_z T_z$. However, the FFT cannot model this term. So we approximate $\delta_{nmz} T_z$ by $\delta_{nmz} T_o$, where T_o is the point in space at which we will have an exact answer. Near the point T_o some error will exist and the error will increase as we move away from T_o , as shown in Fig. 2.49.

This figure shows the normalized phase distortion for the exact pattern and the approximate pattern generated by the modified FFT where the pattern is exact at $T_o = 0(T_z = 1; T_x = T_y = 0)$. Note that the approximate pattern is always conservative, i.e., the approximated phase distortion is greater than or equal to the true phase distortion. Hence, the approximate pattern RMS sidelobes will be greater than or equal to the actual sidelobe levels caused by the out-of-plane deformations.

Several test runs have been made verifying the above theory and the results indicate that the approximate technique provides negligible errors from boresight to about ±30°. The details of these empirical results are discussed in Sec. 2.2.2.4.

2.2.1.2 Random·Deformation--Space Feed

To this point, we have only discussed a corporate-fed array. Now we turn to a space-fed array. Figure 2.50 shows schematically a linear

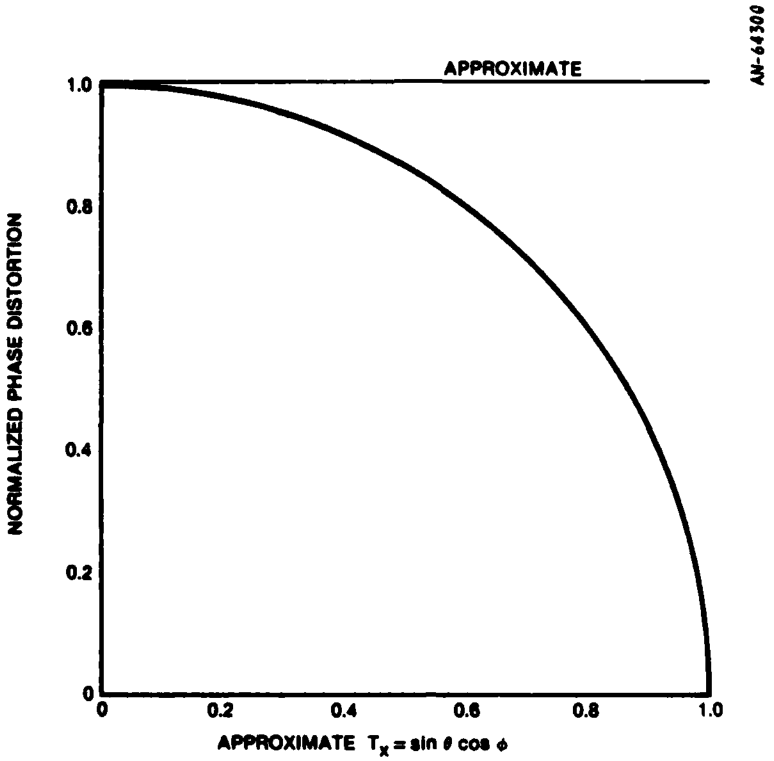

Figure 2.49. Comparison of Actual and Approximate Out-of-Plane Phase Distortions

---

array with an arbitrary random displacement of an element δ . The phase distortion for a particular element in this case can be divided into two parts: (a) in-plane (x-displacement), or (b) out-of-plane (z-displacement). The distortion is equal to the difference between the desired pathlength from the feed to the element and the actual pathlength plus the distortion due to the element displacement. Expressed mathematically,

$$\varepsilon_{n\phi x} = \left(\sqrt{F^2 + x_n^2} - \sqrt{F^2 + (x_n + \delta_{nx})^2} + \delta_{nx} \sin\theta\right)$$

$$\simeq \delta_{nx}\left(\sin\theta - x_n/\sqrt{F^2 + x_n^2}\right) \quad ; \quad \text{if} \quad F \gg |\delta|$$

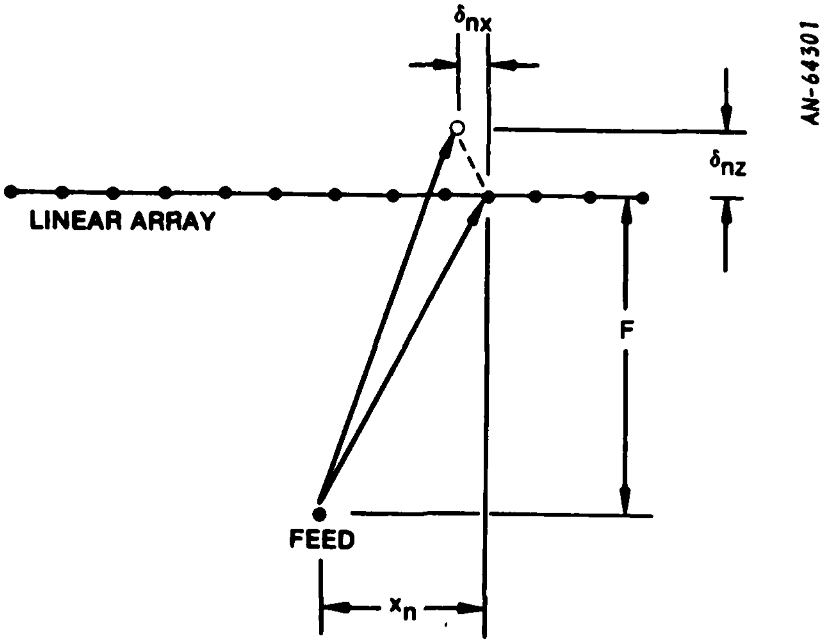

Figure 2.50. Linear Array With Displaced Element

Likewise

$$\varepsilon_{n\phi z} \approx \delta_{nz}\left(\cos\theta - F/\sqrt{F^2 + x_n^2}\right) \quad ; \quad \text{if} \quad F \gg |\delta|$$

where $\varepsilon_{n\phi x}, \varepsilon_{n\phi z}$ = the phase distortion of the nth element in the x and z directions, respectively

δ_{nx}, δ_{nz} = the displacement of the nth element in the x and z directions, respectively

F = distance from feed to array lens

x_n = the x coordinate of the nth element

θ = angle from boresight

If δ_x and δ_z are normally distributed with variances σ_x^2 and σ_y^2, respectively, then one can calculate the total mean square phase distortion as

$$\sigma^2_{\phi x} = \frac{\Sigma I^2_n \varepsilon^2_{n\phi x}}{\Sigma I^2_n}$$

and

$$\sigma^2_{\phi z} = \frac{\Sigma I^2_n \varepsilon^2_{n\phi z}}{\Sigma I^2_n}$$

where I_n = the illumination factor for the nth element.

Using a similar argument to that of Sec. 2.2.2.1, we can take care of the x distortion simply by choosing the appropriate grid spacing. Invoking the central limit theorem[1] and assuming the phase distortion to be sufficiently near a normal distribution, Fig. 2.49 can be used to determine the appropriate grid spacing.

Out-of-plane phase distortion for a space-fed array takes on a different nature than that for the corporate-fed array. Consider Fig. 2.51, which shows the normalized phase distortion of a corporate array and a space-fed array with focal length to diameter (f/D) ratio of 1.5 and a nearly uniform illumination function. Note that while the corporate-fed array has maximum phase distortion on boresight, the space fed array has no phase distortion. This is one of the very desirable features of the space-fed array in that it "corrects" for out-of-plane element displacements. Another difference between the two curves in this figure is that the space-fed array has a family of curves since the phase distortion is a function of the elements' position on the array (the figure only shows the envelope of distortions).

---

[1] The central limit theorem states that the sum of a large number of distributions approaches a normal distribution regardless of the shape of the individual distributions. See A. Papoulis, Probability, Random Variables and Stochastic Processes, McGraw-Hill, 1965.

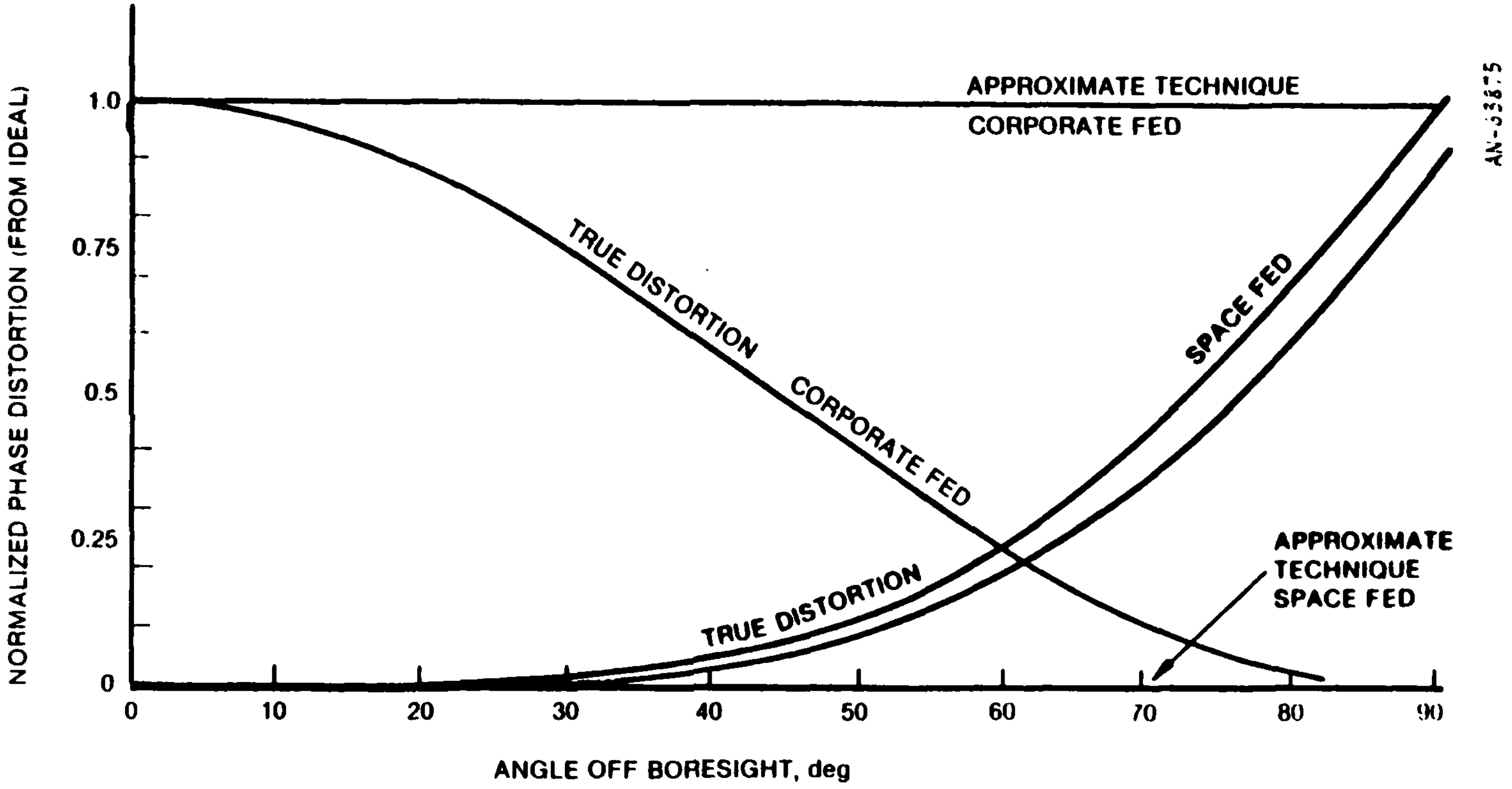

Figure 2.51. Phase Distortion for Corporate and Space-Fed Arrays Due to Out-of-Plane Deformations

If we use the same method (to modify the phase prior to performing the FFT) as before for the space-fed array we will approximate the actual phase distortions by a line coincidental with the abscissa in Fig. 2.51. The first examination of these curves indicates that the approximation for the space-fed array should be even better than that for the corporate-fed array. This is <u>not</u> true. To explain why, we will consider an example.

Assume that we wish to model an antenna pattern which has random phase distortions with an RMS value of 25°. Let us model this pattern using the same random set of numbers but all multiplied by 0.8. Hence, we are comparing the patterns of an array which has an RMS phase distortion of 25° to one of 20°. While the results will not be identical, they should be fairly close if the same set of random numbers are used.

Now let's do the same thing with another pattern that has a phase distortion of 3° and one which multiplies the random numbers by 0.0001. We are now comparing an essentially ideal pattern (σ_ϕ = 0.0003°) to one with non-negligible phase distortion (σ_ϕ = 3°). Even though the difference in phase distortion is less than the previous case (3° versus 5°), the first case will provide a much better approximation to the actual pattern.

This example illustrates why the curves in Fig. 2.51 are misleading. The important comparison when approximating errors is related to the ratio of the approximate to the actual RMS phase distortion, since this is the parameter which determines differences in RMS sidelobe levels. In other words, it is the relative error, not the absolute error which is important.

Figure 2.52 shows the expected error in RMS sidelobes due to out-of-plane distortions for both a corporate- and space-fed array. From these curves, it is obvious that the approximation technique works much

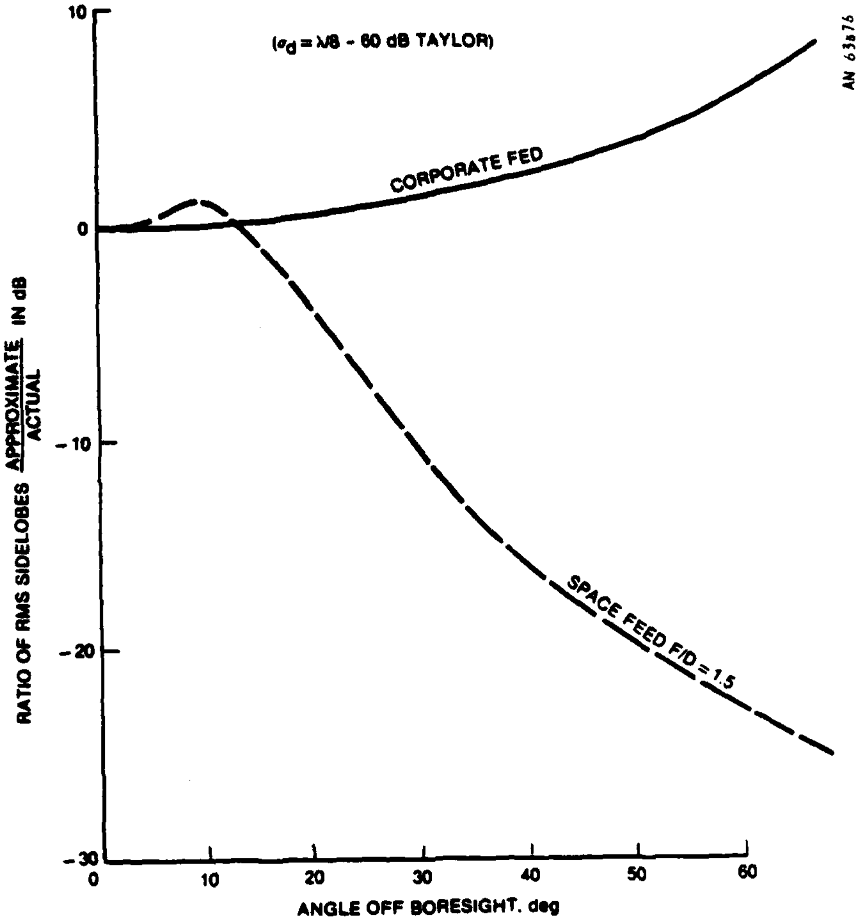

Figure 2.52. Comparison of Actual Mean Square Sidelobes to Approximate Technique

better for a corporate-fed array than for a space-fed array. However, test results covered in Sec. 2.2.2.4 show that the technique is adequate from boresight to ±25° when the phase modification is made on boresight.

What if the antenna designer is interested in the pattern at angles greater than 25°? There are two alternatives:

1. If only a few points are needed, the brute force technique can be used to give an exact solution at the desired points.

2. The phase adjustment for the approximate technique can be made at some point other than boresight.

Examples of the errors attributed to the second method are shown for a corporate feed in Fig. 2.53 where the phase is adjusted for $T_o = 0.6$ and $T_o = 0.8$ as well as $T_o = 0.0$ (boresight). The recommended approach would be to use a combination of both methods, using a few brute force points to verify the accuracy of the approximate technique.

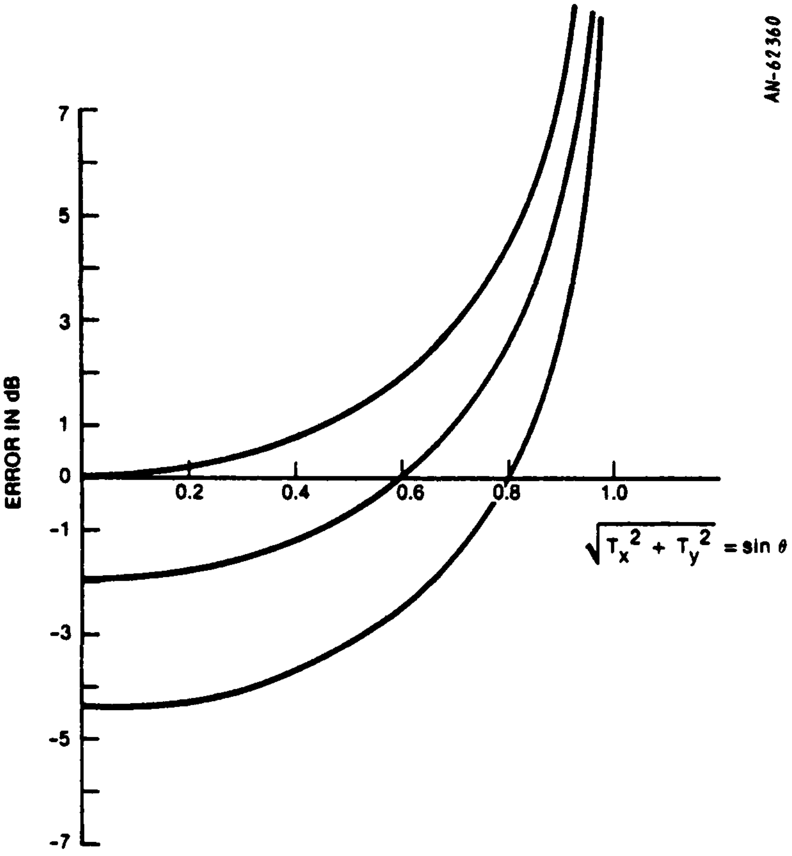

Figure 2.53. Approximate Technique Error When Phase Adjustment Made at $T_x = 0, 0.6, 0.8$

2.2.1.3 Systematic Deformations

So far we have only discussed random displacement of the elements. In this subsection we will briefly consider two systematic deformations: linear tilt and parabolic deformations. This discussion will be more of an intuitive explanation rather than a rigorous analysis. The errors in using the approximate technique will be determined by the empirical data presented in Sec. 2.2.1.4.

Linear Tilt

Consider a corporate-fed array which has been tilted by an angle of α. Without loss of generality, we can assume that α is in the same direction as the SARF coordinate θ (see Fig. 2.54). Then the resulting phase distortion will simply be equal to $\beta x \cos \theta$ where β is a constant dependent on the angle α and the size of the array. In

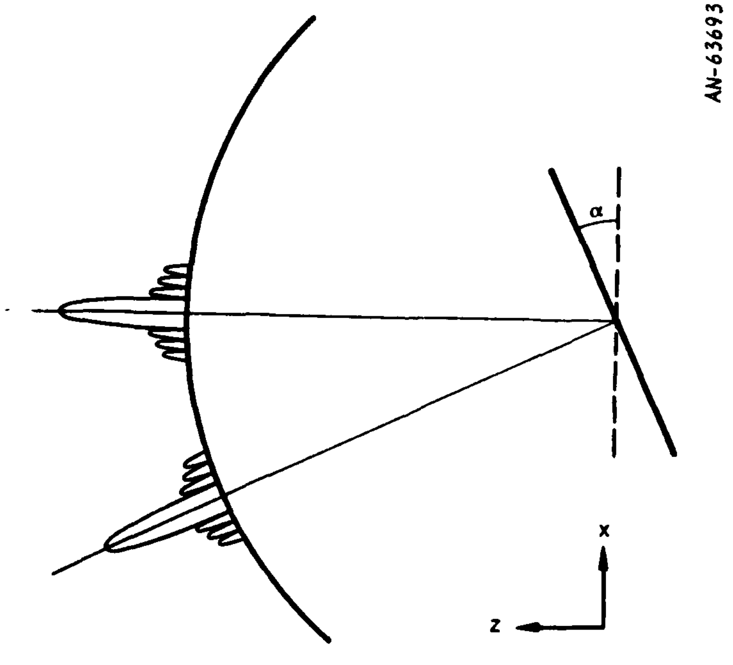

Figure 2.54. Tilted Corporate Fed Array

other words, the pattern is translated in angle space by an angle α. If we use the approximate technique (i.e., adjust the phase for zero error on boresight and select the appropriate FFT grid spacing), we get a phase distortion term approximately equal to βx. This corresponds exactly to a linear phase shift which scans the beam by an angle α. Therefore, the approximate technique can be thought of as a translation in sine space on $\sin \theta$. Therefore, if α is relatively small, then $\sin \alpha \approx \alpha$ and the approximation technique will provide a small error in the pattern.

Since a space-fed array tends to correct for element displacements, particularly out-of-plane displacements, a tilt of the aperture does not significantly translate the antenna pattern. Therefore, the approximate technique would be expected to provide a good match to the true pattern. This was verified and is shown in Sec. 2.2.1.4.

Parabolic Deformations

Parabolic deformations (as shown in Fig. 2.55) create a quadratic phase distortion and cause the maximum distortion of the antenna pattern near the boresight of the aperture. If the beam is not scanned, quadratic phase distortion essentially affects only the main beam and first sidelobe. Since the approximate technique models the antenna pattern exactly on boresight, one would expect the approximate technique to provide a very accurate representation of the actual pattern. This is exactly what the data show in the following subsection.

2.2.1.4 Empirical Error Data

To verify the preceding analyses and to determine the limits of accuracy of the approximate technique, many SARF simulation runs were performed with various types of deformations. The main parameters used for verification were:

1. Peak value of mainlobe
2. Location of pattern peak

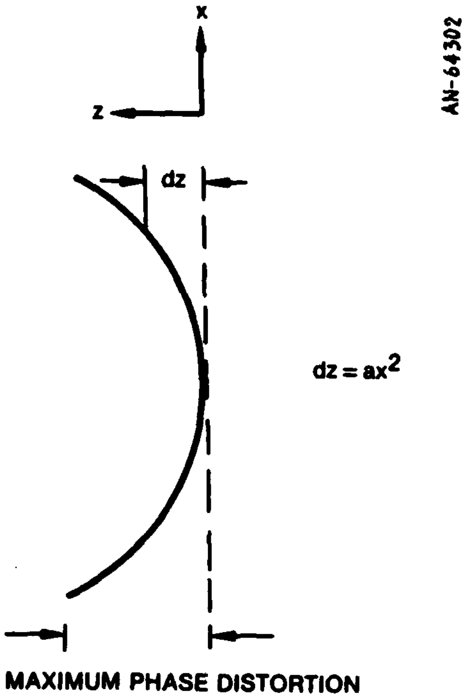

Figure 2.55. Parabolic Deformations

3. 3-dB beamwidth
4. RMS sidelobes (10°-20° and 20°-30°)
5. Location of pattern peak
6. First sidelobe peak
7. Location of first sidelobe peak

In addition to numerical comparison of the above parameters, additional visual comparison was performed to verify that the numerical data was being interpreted properly. For example, RMS sidelobes might agree quite closely for two patterns, but there could be extreme differences in the peaks and nulls.

Table 2.7 shows the results of eight of the many runs made to compare the approximate technique with the actual pattern. This table

TABLE 2.7

ERROR DUE TO APPROXIMATE TECHNIQUE PATTERN CALCULATION WITH SURFACE DEFORMATIONS

	Errors in						
	Peak of Main Lobe (Volts)	Location of Main Lobe (degrees)	3-dB Beamwidth (degrees)	RMS Sidelobes 10°-20° (dB)	RMS Sidelobes 20°-30° (dB)	First Sidelobe Peak [No Scan] (dB)	First Sidelobe Location [No Scan] (degrees)
<u>Corporate Feed</u>							
Random (Normal Distribution) Deformations, $\sigma = \lambda/8$	Accurate to six decimal places	*	0.010	0.11	0.72	0.05	0.020
Random Deformations, $\sigma = \lambda/4$	Accurate to six decimal places	0.001	0.008	0.21	0.10	0.05	0.020
Linear Tilt, 8°	Accurate to six decimal places	*	0.02	0.03	0.44	0.07	0.001
Parabolic Deformation (Maximum $\delta = \lambda/4$)	Accurate to six decimal places	0.001	0.006	0.01	0.02	0.24	0.007
<u>Space Feed</u>							
Random Deformations, $\sigma = \lambda/16$	Accurate to six decimal places	*	0.002	0.12	0.76	0.01	*
Random Deformations, $\sigma = \lambda/8$	Accurate to six decimal places	*	0.002	0.12	3.74	0.01	*
Linear Tilt, 8°	Accurate to six decimal places	0.01	0.015	0.15	0.30	0.03	0.030
Parabolic Deformations, (Maximum)	Accurate to six decimal places	0.001	0.002	0.01	0.01	0.26	0.030

---

*No error within resolution of the calculation.

represents a comparison of an 8.75 meter diameter circular aperture with a 42-dB Taylor taper. This antenna was chosen since it represents a scaled down version of a 70 meter, 60-dB tapered antenna (scaling factor = 1/8). By performing this scaling, considerable computer resources were saved while still acquiring the desired data.

The tests documented in Table 2.7 depict three types of deformations (random, linear tilt, and parabolic) for both a corporate-fed and space-fed (f/D = 1.5) antenna. The random errors represent relatively large displacement (up to $\sigma = \lambda/4$ for the space-fed case). The tilt used was 8° which would correspond to (same maximum phase distortion) a 1° tilt for a 70-meter aperture, which is considerably greater than would be expected for a space-based radar antenna. The parabolic deformation described by the table corresponds to a maximum deflection (at the edge of the array) of $\lambda/4$. Now we will review the tabular results, column by column.

The first column in the table represents the peak value of the main lobe of the pattern. In all cases, the error generated by the approximate technique was less than the accuracy of the machine (six decimal places). Obviously this is acceptable.

The second column shows the error in degrees of the location of the beam peak. In this column, an asterisk implies that the error in the technique is less than the error induced by the interpolation of the true location of the beam peak. (Since the FFT produces discrete location points, an interpolation of the exact beam peak was necessary.) The largest error in the column was produced by a large tilt in the aperture. Since the designer is free to use the brute force technique for the beam peak location to get an exact answer, these errors from the approximate technique are inconsequential.

The third column shows the error in the 3-dB beamwidth. The largest error in this case was 0.021°. Considering that the beamwidth for this antenna is 1.5°, this amounts to a 1.4% error in the beamwidth which, for most applications, would be acceptable. This error was generated by an 8° tilt which is not very realistic for normal applications. For the other tests, the error in the beamwidth was less than 0.5%. Also, if the antenna designer needs more accuracy in the beamwidth, it is a simple matter to use the brute-force technique.

The fourth column in Table 2.7 shows the RMS sidelobe level error between 10° and 20°. Since the largest error in this region is slightly greater than 0.2 dB, it should be acceptable in nearly every design evaluation. The RMS sidelobe levels of the next column are not nearly so desirable, particularly for random errors in a space-fed array.

These results are as expected, based on the analysis in Sec. 2.2.1.1. However, the 3.74 dB error for $\sigma = \lambda/8$ (space-fed array) is probably not acceptable for any reasonable design. Figure 2.56 shows the two patterns for this case. Obviously, the error is unacceptable for $T_x > 0.5$ $(\theta = 30°)$, but the error is not that bad for angles less than $T_x = 0.35$ $(\theta \approx 20°)$. The remaining errors in this column are most likely sufficient for most designs.

The last two columns deal with the first sidelobe peak (when the beam is not scanned). These two columns show that this peak has less than 0.3 dB error in all cases and has not been displaced by more than 0.03°. These seem like more than reasonable results for the details of the first sidelobe.

After considering the data in Table 2.7 and visually reviewing some of the other graphic results concerning the errors in the approximate technique, it seems reasonable to assume that the technique works quite well for all of the above mentioned deformations within ±25° off

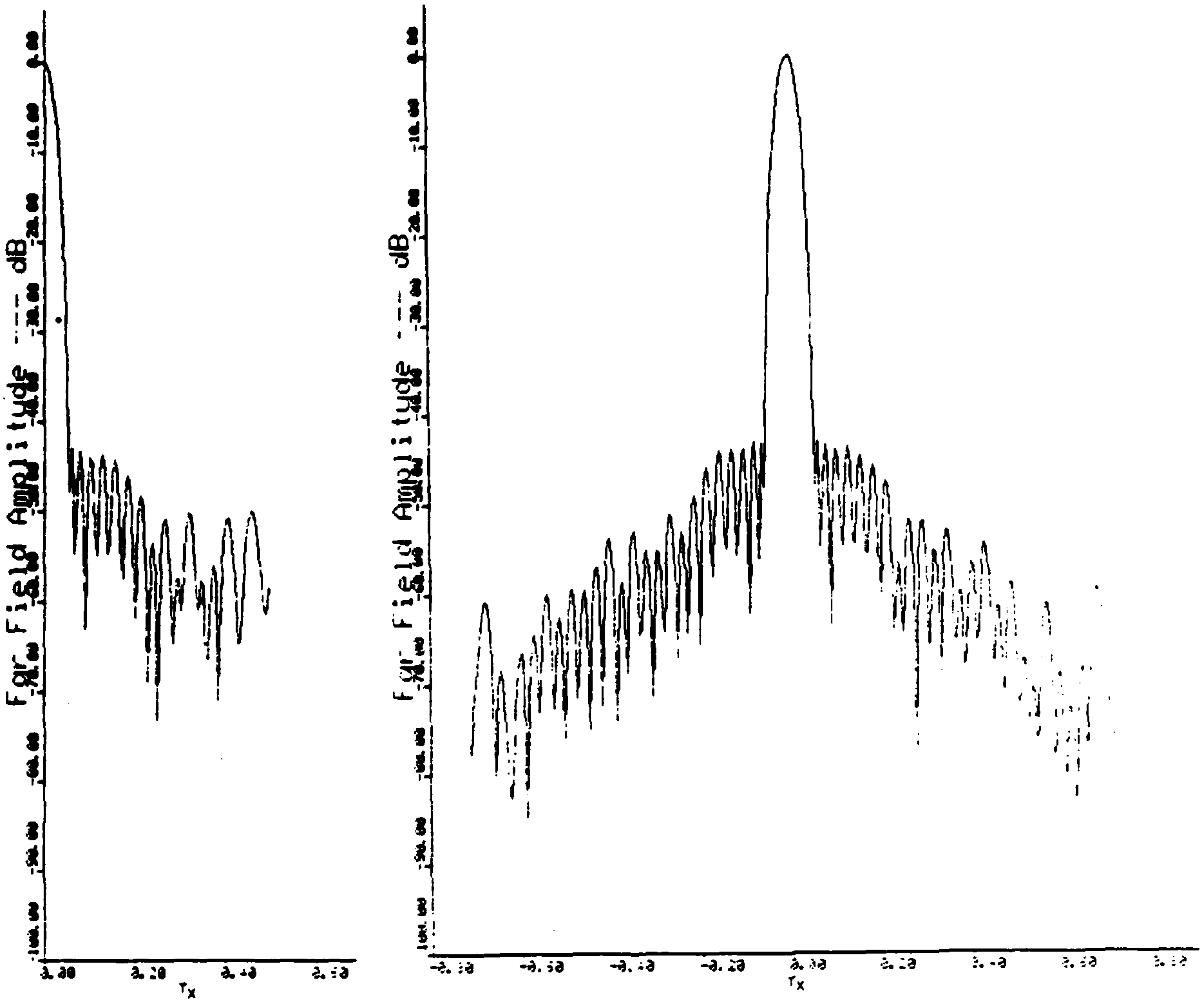

(a) Actual Pattern (b) Approximate Pattern

Figure 2.56. Space Feed Out-of-Plane Deformations

---

boresight. If the designer wishes information about the pattern at angles greater than |25°|, then he must either modify the phase to a correction point off boresight, or use the brute force calculation.

2.3 SOFTWARE DESCRIPTION

The SARF simulation contains three major models: the excitation model, the element pattern model, and the structural model. Each of these three models has been implemented somewhat differently but each was designed to provide maximum flexibility to the antenna designer as well as the programmer (for future modifications). This flexibility is produced by the modularity of the file structure of SARF. Each major model--excitation, element pattern, and location--is described by its own file. The structure of these files as well as a detailed description of each of the three major models is presented in the remainder of this section.

2.3.1 Overall Simulation Structure

The SARF simulation has two paths of information flow:

1. The efficient technique--which is implemented by means of a fast Fourier transform (FFT) along with various approximation techniques, which are described later in this section.
2. The brute-force technique--which takes the various input files and calculates the far-field pattern directly for the desired pattern angles.

This information flow can be observed from the block diagram of Fig. 2.57.

We will describe the efficient technique first. As is shown in Fig. 2.57, SARF first creates the nominal (or ideal) element location file and the nominal excitation (or illumination) file. These two files have a one-to-one correspondence, i.e., each complex illumination is tied directly to the appropriate location by its position in the file. These files can easily be modified by simply reading the existing value, adding an appropriate deviation to this value, then writing the resultant to a new file which possesses the identical file structure of the original file. In this manner, either file can easily be modified (either on-line or off-line) by the desired algorithm. For example, as can be seen from the block diagram, the location file can be deformed by thermal, systematic, or random distortions. As will be presented later, SARF currently handles thermal deformations off-line while it can handle

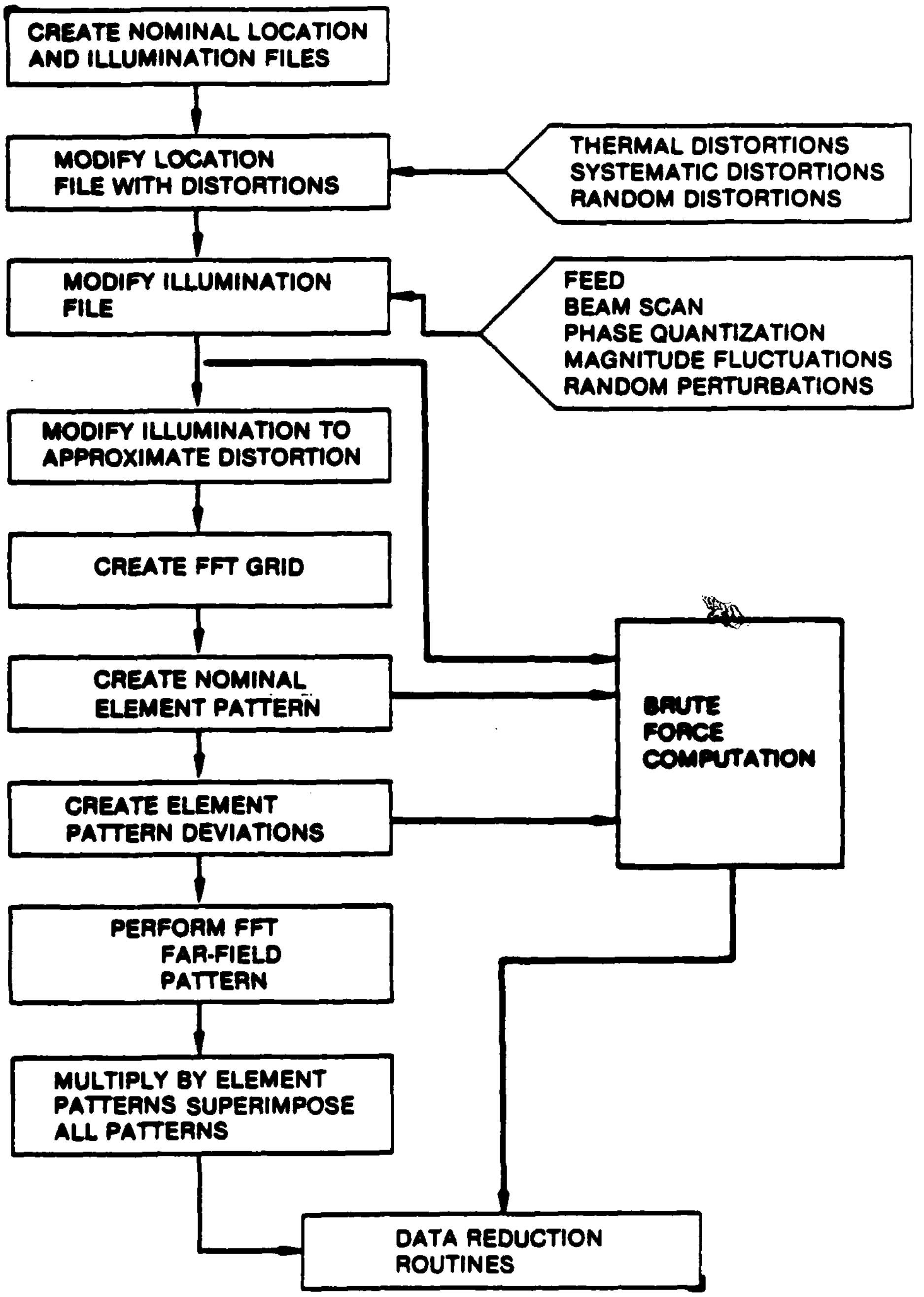

AN-62976

Figure 2.57. SARF Block/Flow Diagram

systematic and random distortions either on- or off-line (depending on the desired deformations).

The nominal illumination file can also be handled in the same manner since its file structure is identical to the location file. The (ideal) illuminations are modified by the feed characteristics. SARF currently has four feed configurations: (1) corporate feed, (2) point space feed, (3) cluster feed, and (4) multibeam feed. The multibeam feed model was originally designed by members of the Raytheon Company and has been incorporated and modified for SARF. It includes models of a Rotman lens and a Butler matrix feed. All of the feed models are described in Sec. 2.3.2.

In addition to modifications from the feed model, the illumination file can be modified by beam scanning capability, phase quantization, magnitude fluctuations (as might be due to module characteristics), and, of course, random perturbations. All of these excitation models are described in Sec. 2.3.2.

Mutual coupling can also be modeled by modifying the illumination file with the coefficients which are determined by such models as FAM and HAM developed by Atlantic Research Corporation.[1] SARF currently handles this in the off-line mode by reading appropriate magnetic tapes containing the mutual coupling data and then modifying the illumination file appropriately. Mutual coupling can also be handled by the proper choice of element pattern parameters, as shown in the block diagram. This method of modeling mutual coupling is described in detail in Sec. 2.4.

Lastly, the illumination file can be modified to approximate the effect of displacements in the location of elements. This technique is described in detail in Sec. 2.2.

---

[1] H.K. Schuman and D.R. Pflug, Space-Based Radar Array System Simulation and Validation, RADC-TR-81-366, December 1981.

Once the illumination and location files have been modified by the desired processes, SARF creates an FFT grid based on the inputs of the antenna designer. This grid is a rectangular spaced planar lattice, each grid point representing some physical point on the antenna aperture. The illumination of each grid point is determined by the corresponding point in the illumination file. Any grid point that does not have a specific complex illumination associated with it is given the value of zero (0.0 + j0.0).

Once the input FFT grid has been created, it represents a very good approximation to the desired aperture design. This grid is now fast Fourier transformed and the output is a similar grid which now provides a very good approximation (in many cases it is exact) to the far-field pattern of the designed antenna with one exception--it is the pattern due to an ideal isotropic element pattern.

To rectify this ideal representation, the appropriate element pattern is calculated and each output point of the FFT is multiplied by the appropriate complex number (determined by the element pattern calculation). In addition, several deviations in element patterns are created by performing additional FFT's on a subset of elements in the array. These additional element pattern capabilities are described in detail in Sec. 2.3.3.

With the inclusion of the various element patterns, the output file is now ready to be processed by the various data reduction routines. These routines include the output capabilities of PAAS (RTI, EDISYN) as well as numerical output, pattern cuts, and pattern plots (including three-dimensional plotting) of both the principal and cross polarization.

The brute-force technique is much easier to describe than the efficient technique, since it performs the pattern calculation directly on the same input files as used for the efficient technique. This is an important point because it insures that the input data for both techniques is identical, hence providing the user as well as the programmer with a built-in test.

Since the brute-force technique uses the same illumination and location files, all the modifications to these files explained in the preceding paragraphs apply equally to the brute-force technique. In addition, the element patterns are calculated using the same subroutine as used by the efficient technique. Therefore, the brute-force merely takes all of the above mentioned input data and performs the applicable complex multiplications and summations to provide the output. The only problem with this approach is that the brute-force technique can be three to four magnitudes slower than the efficient technique--but it always gives the exact value for a far-field pattern.

2.3.1.2 Support Program Structure

In addition to the main (on-line) program, SARF also contains several (off-line) support programs which operate as pre- or post-processors to create, modify, or reduce data stored on the input, output, and data files of SARF.

The most important of the pre-processors is the program DATAFILE. DATAFILE is an interactive program which helps the user specify all the input parameters for the files which make up the data base for the on-line program. This data base consists of input data files:

1. Element pattern
2. Element pattern variance coefficients
3. On-line systematic deformations
4. Brute-force output point
5. Multibeam and cluster feed input data

Each of these files is described in detail in the SARF Users Manual.[1] However, a brief description will be provided here for the convenience of the reader.

The element pattern file contains the coefficients and the location coordinates for all current segments in the nominal element pattern as well as the deviation to the desired elements. It also contains the parameters which define the desired subset of deviated elements.

The element pattern variance file contains the coefficients of the variance (as a function of space) for the random deviations to the element pattern.

The systematic deformation file contains the coefficients which deform the aperture in all three dimensions according to a quadratic in x and y (with cross product terms).

The brute-force file contains the points in sine-space which the user wishes to calculate during the on-line run. These points can be overridden during on-line interactive processing.

The multibeam and cluster feed file contains all the parameters necessary for the design of a Rotman lens, Butler matrix, or a cluster space feed. This file includes such parameters as feed element spacing, number of ports, quantization levels, design bandwidth, etc.

After using the program DATAFILE to create all of these input data files, the user can proceed with an on-line run. Once these files have been created, they can be used over and over. Any one (or any subset) of the files can be modified by using DATAFILE, leaving the remaining

---

[1] J.R. Feeman and J.D. Capps, SARF Users Manual, General Research Corporation CR-2-1048, Vol. II (Preliminary Release), October 1982.

files as previously created. In addition, since all five are sequential, formatted files, any of them can be modified by using the text editor (assuming the user is intimately familiar with the file structure).

One additional pre-processing step is necessary if SARF is to be run in the BATCH (as opposed to INTERACTIVE) mode. The batch input data file must be altered using the text editor. This file contains all the input parameters that the user would supply if he were running on-line interactively. The file is structured with the alpha-numeric data on the right and a brief description of the parameter on the left. A detailed explanation and listing of the batch data file is contained in the SARF Users Manual.[1]

The support program which processes deformations due to thermal effects or systematic deviations is also essentially a pre-processor. There are two reasons why this capability was not incorporated directly into the on-line program. First, it usually requires considerable processing time (for input supplied by Draper Labs), and secondly, once a particular set of deformations is created, it can be used over and over by the on-line program.

The deformation program consists of three routines: G2, G3, and DEFORM. G2 performs a two-dimensional interpolation on a nominal or ideal set of element locations based on a set of ideal structural locations along with the deformed structural locations. G3 performs the same function as G2 but in three dimensions. DEFORM takes the nominal structural data and displaces it according to the (user supplied) input polynomials. Each of the gores can be distorted according to a different polynomial. The details of these three routines are presented in Sec. 2.3.4.

---

[1] J.R. Feeman and J.D. Capps, op. cit.

In addition to the above pre-processors, SARF uses three post-processing routines for plotting data. Only a cursory explanation of each of these routines will be presented here since they are detailed in the Users Manual.

PLOTXY plots the element location in the x-y plane. Each element is represented by a character selected by the user. The scale is in meters and the length and increment are selected by the user. (See Fig. 2.58 for an example.)

PLOTPATT is used for plotting a cut through the antenna pattern or the aperture illumination. The increment, maximum and minimum values of both the abscissa and ordinate are user-selected. A sample output from this routine is shown in Fig. 2.59.

PLOT3D provides the capability of plotting either the entire pattern or aperture illumination in three dimensions. The maximum value of all three coordinates along with their increment is selected by the user. A sample 3-D plot is shown in Fig. 2.60.

The SARF on-line program, along with the pre- and post-processors, provides the antenna designer with a very flexible tool. The modularity of the file structure allows additional capability to be incorporated relatively easily. This allows the incorporation of the latest results from the various technology contractors as this data becomes available.

Now that we have discussed the overall structure of SARF, we will proceed to detail each of the three major models in the following order: excitation, element pattern, and structural.

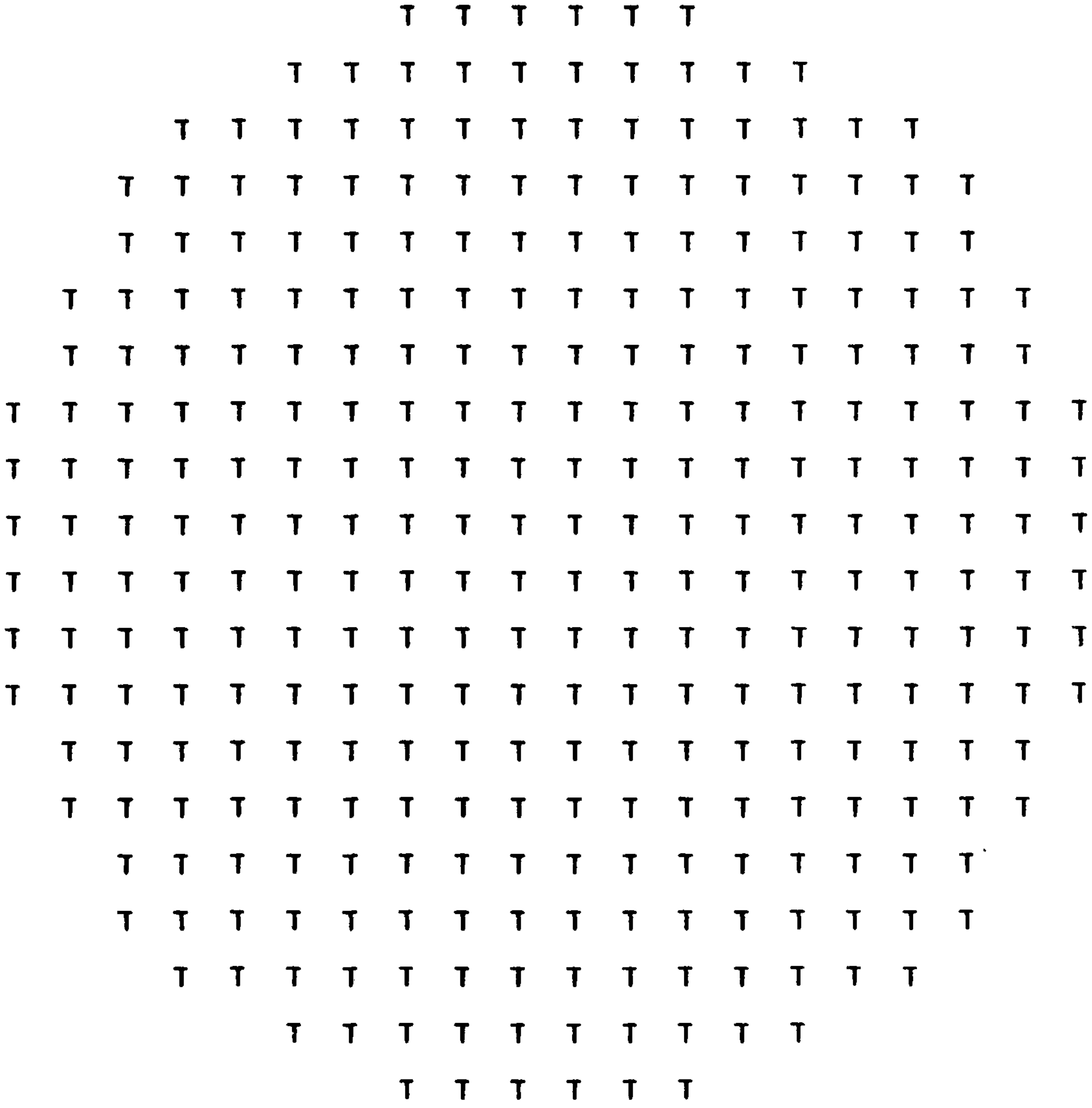

Figure 2.58. Output From PLOTXY--Element Locations for Circular Aperture

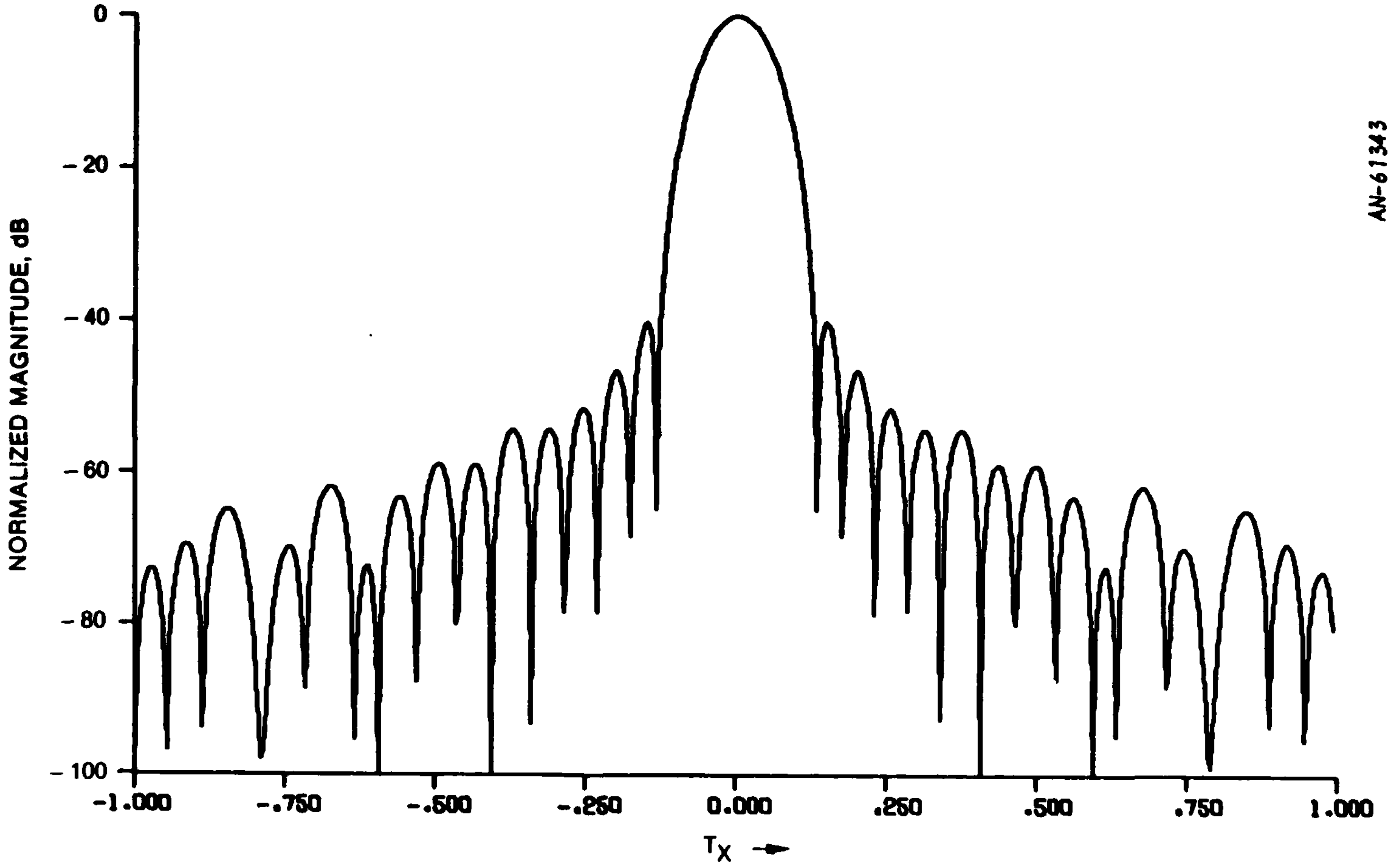

Figure 2.59. Output From PLOTPATT--Linear Pattern Plot

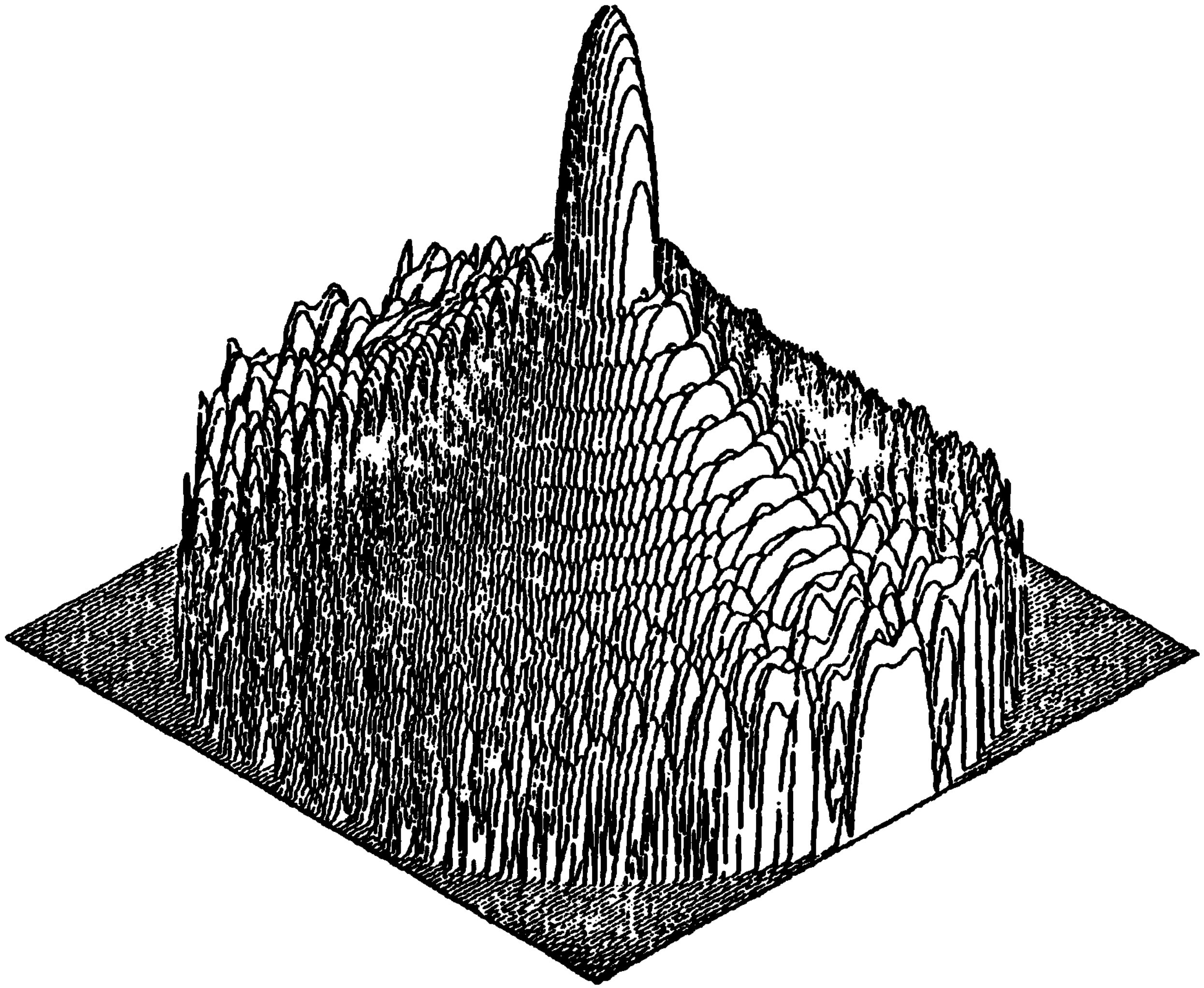

Figure 2.60. Output From PLOT3D--Three-Dimensional Antenna Pattern

2.3.2 Excitation Model

2.3.2.1 Introduction--Overview

The body of software which makes up the excitation model has the sole purpose of creating a file of source excitations for the main array. For each main array element, a corresponding complex illumination value is computed, stored in a file, and used within the SARF simulation.

These excitation values are a result of varying degrees of detailed modeling. Excitations may, on one hand, be obtained from a set of ideal distributions, such as an ideal Taylor or Gaussian distribution. They may, on the other hand, reflect deviations from the ideal due to a variety or combination of factors, such as beam steering, or random element failures, or different feed designs. The user may select from a menu those features he wishes to model.

The excitation model has two sections: (1) the feed system, and (2) the lens. The feed system models the excitations produced at the feed side of the lens modules (see Fig. 2.61). The excitation may be produced by a corporate feed system, as described in Sec. 2.3.2.2, or a space feed system, as described in Secs. 2.3.2.3 through 2.3.2.6. The feed-side excitations are then transformed through the lens, as described in Sec. 2.3.2.7, to become the target-side excitations, which are the final outputs of the excitation model.

2.3.2.2 Corporate Feed

The software for the corporate feed models a near-ideal configuration. The nominal amplitude is derived by sampling a perfect aperture distribution, and the phase for beam-scan is perfectly linear, except for quantization introduced by a n-bit phase shifter. Errors due to internal reflections, etc., are modeled as random Gaussian noise as discussed below.

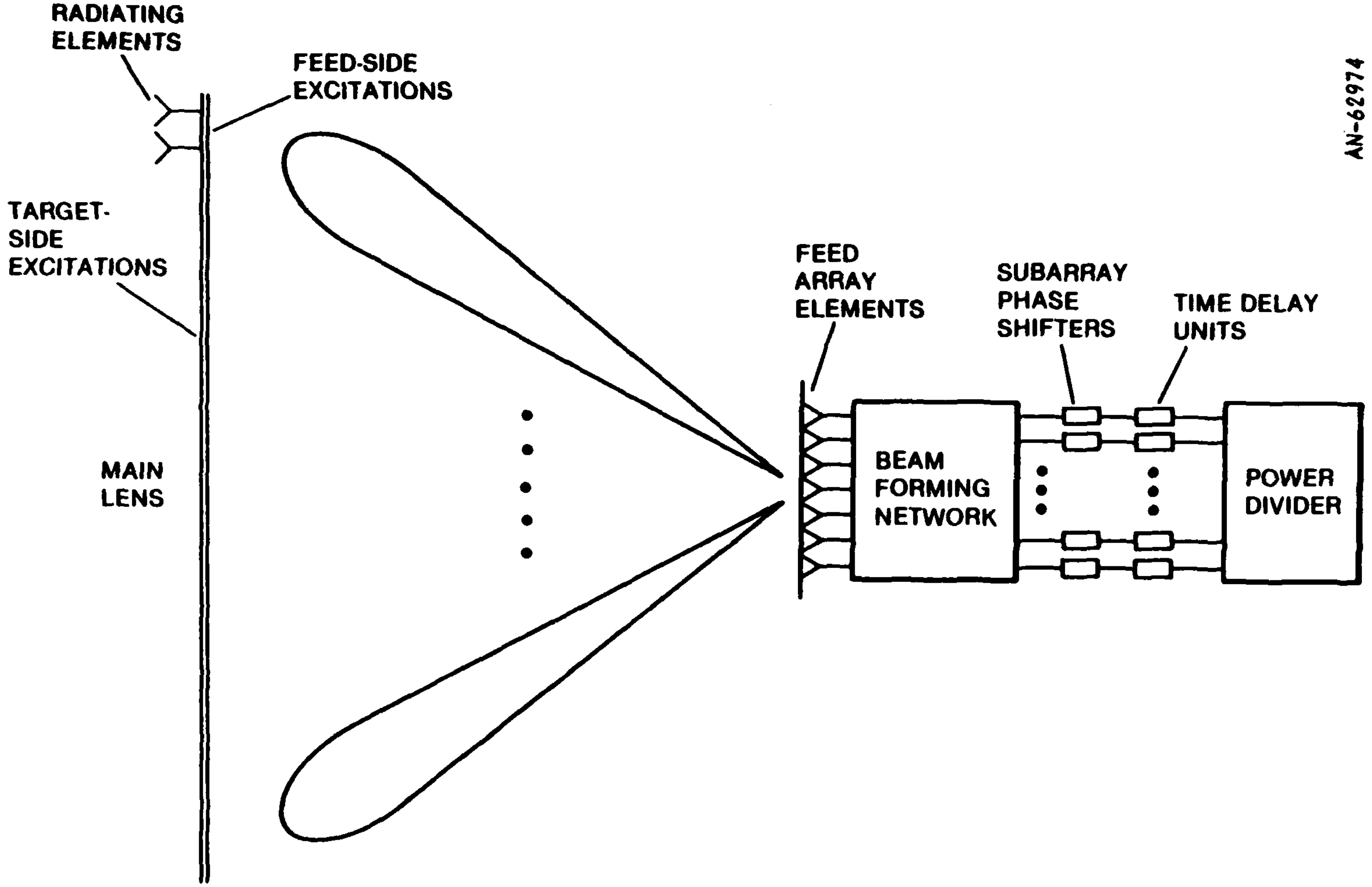

Figure 2.61. Block Diagram of Space-Fed Multibeam Array

2.3.2.3 Point Feed for Space-Fed Array

A point feed can actually be modeled by the simulation in two ways. Each has its advantages. In one instance, the simulation models a single, ideal, spherically radiating point located anywhere behind the main array. Phase differences due to varying path lengths to the main array are taken into account. This method of modeling a point feed has the advantage of being executed very easily and quickly in the software.

A point feed might also be modeled as a single-element cluster feed, which is the next option we discuss.

2.3.2.4 Cluster Feed

The cluster feed models the excitations from a group, or cluster, of at most 10 radiating elements. These feed elements may be positioned anywhere behind the main lens. Each feed element has a Gaussian pattern of $e^{-\alpha\theta^2}$ where α is a user-defined constant, and θ is the angle measured with respect to the z-axis. Each feed element has a complex excitation value associated with it.

The illumination at a particular main array element location, $E(\ell,m,)$, is the sum of the illumination contributions from each cluster feed element.

$$E(\ell,m) = \sum_{k=1}^{N_{fe}} Amp(k)e^{phase(k)}$$

where

N_{fe} = number of cluster feed elements

k = kth feed element

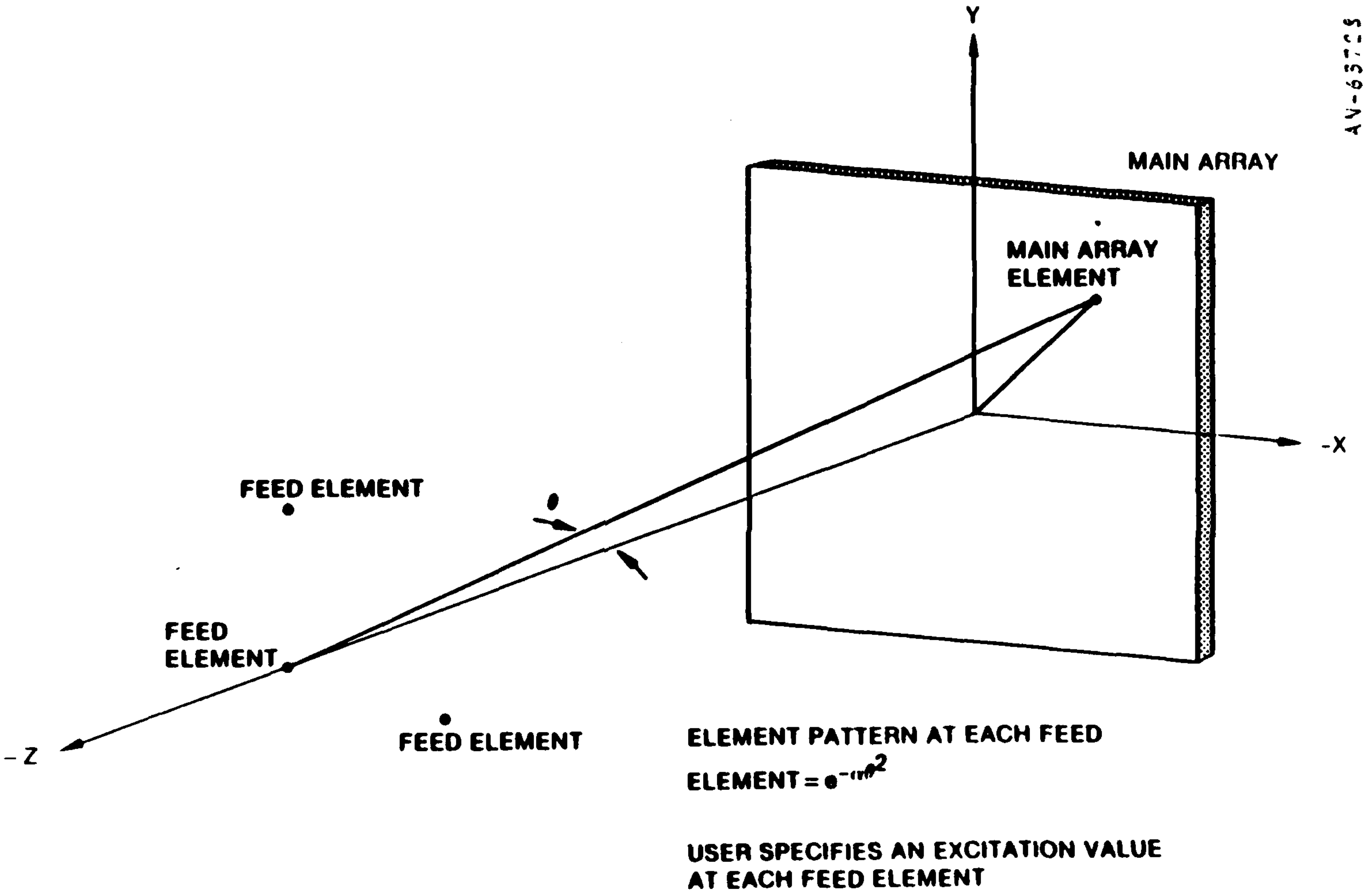

Figure 2 62. Cluster Feed

$$\text{Amp} = \frac{\sqrt{a_k^2 + b_k^2}}{\rho} e^{-\alpha\theta^2}$$

$$\text{phase} = \tan^{-1}\left(\frac{b_k}{a_k}\right) - \rho \frac{2\pi}{\lambda}$$

ρ = distance between feed element k and main array element (l,m)

$$= \sqrt{(x_{ma} - x_{fe})^2 + (y_{ma} - y_{fe})^2 + (z_{ma} - z_{fe})^2}$$

(x_{ma}, y_{ma}, z_{ma}) = location coordinates of main array element (l,m)

(x_{fe}, y_{fe}, z_{fe}) = location coordinates of cluster feed element (k)

$(a_k + jb_k)$ = complex excitation value at cluster feed element (k)

$$\theta = \cos^{-1}\left(\frac{z_{ma} - z_{fe}}{\rho}\right)$$

λ = wavelength

α = feed constant, specified by user prior to simulation

The cluster feed has the capability of including multipath effects in the modeling.

2.3.2.5 Multibeam Feed for Space-Fed Array

The core of the multibeam software was acquired from Raytheon.[1] Parts of the original code have been altered and parts have been deleted in merging this software into the SARF simulation. Several new parts have been added in order to expand the modeling capabilities. The SARF simulation User's Manual[2] specifically lists the modifications made to each Raytheon routine, as well as documenting the new software which has been added.

2.3.2.5.1 Types of Multibeam Beamforming Networks

Two types of beamforming networks can be modeled with the multibeam software. First is the Rotman lens, two versions: an ideal Rotman lens, and a more detailed, software designed, Rotman lens that takes into account actual cable lengths and focal points. Raytheon's final report discusses the Rotman lens, so it will not be repeated here.

The second type of beamforming network is the Butler matrix.

A Butler matrix feed consists of $m = 2^n$ (n an integer) elements fed by a network that produces a phase increment from element to element of

$$\delta_M = (N + 1 - 2I)\pi/m$$

where $I = 1,\ldots,N$ is the beam number. For an interelement spacing d the resulting far-field feed pattern is

$$E_I = \frac{1}{m}\,\frac{\sin m\{(kd/2)\sin\theta - [(2I - 1)/m](\pi/2)\}}{\sin\{(kd/2)\sin\theta - [(2I - 1)/m](\pi/2)\}}$$

---

[1] J.D. Hanfling and B.R. Herrick, Final Report for Low-Sidelobe Space-Fed Lens Antenna Transform Feed Study, Raytheon Company, Equipment Division, Contract No. F19628-79-C-0157, 29 January 1982.

[1] J.R. Feeman and J.D. Capps, SARF User's Manual, op. cit.

The beam peaks are located at (neglecting grating lobes)

$$\sin \theta_I = \frac{\lambda}{md}\left(I - \frac{1}{2}\right)$$

All other beams have nulls at the peak of any given beam, and the beams span an angular region between $\sin \theta = -\lambda/2d$ and $\sin \theta = \lambda/2d$, as shown in Fig. 2.63.

The phase increment, P_I, in the Raytheon feed model is (for one dimension)

$$P_I = \frac{\left(\frac{m+1}{2} - p\right) Y_{I,J} \cdot F_h \cdot F_c \cdot 2\pi}{m \cdot c}$$

where $Y_{I,J} = B(N + 0.5 - J)$

= sine space y coordinate of feed beam 1,m

$F_h = \frac{C \cdot B}{F_c}$ = feed height

B = one half the beamwidth to the first null

F_c = center frequency, GHz

c = speed of light × 10^{-9}

I,J = feed beam indices in x and y directions, respectively

N = number of beams

m = number of feed elements

p = feed element index

Substituting for Y and F_h

$$P_I = \left(\frac{m+1}{2} - p\right)(N + 1 - 2I)\frac{\pi}{m}$$

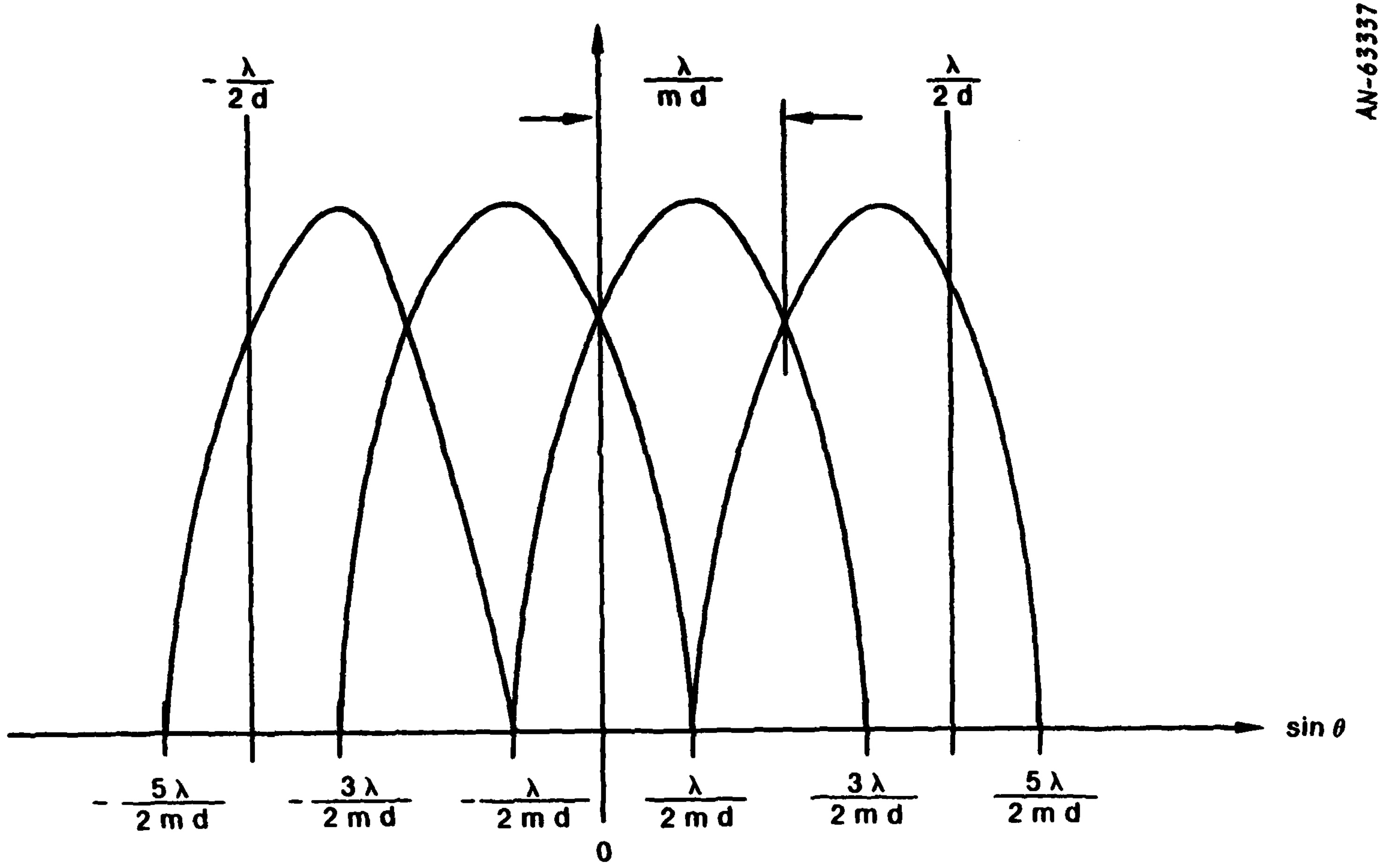

Figure 2.63. Butler Matrix Feed Beams

This provides the desired Butler matrix phasing. However, the ideal Butler matrix option in the Raytheon feed program does not explicitly constrain the feed to have 2^n elements. The program has been modified so the user may override the value selected by the model to enforce this condition.

The number of beams should be less than or equal to the number of elements; if fewer beams are selected, they will correspond to the innermost beams, and will span the angular region subtended by the aperture. The feed element spacing may also be entered manually to provide other coverage if desired.

The Raytheon feed program designs the feed as follows:

1. Feed beamwidth is determined such that N beams span angle subtended by aperture.
2. Feed size is determined to provide desired beamwidth at center frequency.
3. Element spacing

$$d = \frac{c}{F_B}\left\{1.0 + \sin\left[\tan^{-1}\left(\frac{D_F}{A_L/2}\right)\right]\right\}$$

where c = speed of light × 10^{-9}

F_B = highest frequency in the band

D_F = distance of feed from main array

A_L = main array length

is determined to prevent grating lobes at high frequency.

4. Number of elements m is derived by dividing feed size by element spacing.

Manual override for real Butler matrix should proceed as follows:

1. Redefine $m = 2^n$, n an integer.
2. Redefine d to provide desired feed beamwidth.

3. Check that coverage provided by N beams is the desired range. The coverage in sine space at the beam crossover level is given by

$$-\frac{N\lambda}{m\,2d} \leq \sin\theta \leq \frac{N\lambda}{m\,2d}$$

4. Check that the grating lobe is outside of the scan range; first grating lobe is at $\sin\theta_g = \lambda/d - \sin\theta$.

5. Iterate if coverage or grating lobe is not as desired, by altering n, d , or N.

2.3.2.5.2 Modeled Multibeam Feed Effects

There are several effects which can be modeled at the multibeam feed array.

The original code allowed the user to "turn on" either all beams or a single beam. GRC has made program modifications to allow any subset of feed beams to be turned on.

The power divider weightings in Raytheon's software were computed for either a circular Taylor distribution, a uniform distribution, or a Gaussian distribution. The SARF simulation had a larger menu of weighting distributions which could be used. Rather than duplicating the SARF code in the multibeam code to provide these additional weightings, the multibeam software was modified. The software now reads a nominal weighting file and an element location file. From these, the software interpolates an appropriate illumination weight at each beam center projected onto the main array. With this modification, the multibeam feed model can weight itself with respect to any given illumination file.

The ability for the user to manually override the power divider weights which have been computed by the model has been added.

The capability of overriding the number of feed elements and their spacing as determined by the feed model was added primarily for modifying the Butler matrix beamforming network.

For a batch run, these values are to be specified prior to program execution. In the interactive mode, the user is shown the computed feed element number, the spacing, the resulting beam coverage region, and the grating lobe location. The beam coverage region is computed by

$$C = \frac{M\lambda}{2dm}$$

where
M = number of feed beams, y-direction
m = number of feed elements, y-direction
λ = wavelength
d = element spacing

The location of the grating lobe, if it exists, is found by

$$G = \frac{\lambda}{d} - C$$

Knowing this information, the user can alter the element number, or spacing, or both. The resulting coverage and grating lobe location are recalculated for the user with each spacing or element number alteration he makes. When the user is satisfied with the changes he has implemented, the simulation then proceeds. With the current software, the user may not have different element spacing in the y-direction than in the x-direction.

The Raytheon software has the capability to add Gaussian distributed amplitude and phase errors to the feed. GRC has slightly modified the manner in which this was handled. It now is a user option, specified through a data file, whereas before the user would have needed to recompile the software to include or exclude this option.

The same is true for random feed element failures. GRC has made this effect an option through the user's data file. If the user selects this option, he must specify a desired probability of element failure. For every element, the simulation generates a uniformly distributed pseudo-random number. If the number is less than the specified probability of failure, the element is "failed" by setting its excitation to zero.

After integrating the Raytheon feed routine into the SARF software, we began to look at its execution time. We were greatly concerned when we estimated that the feed simulation, alone, for a 7 × 7 feed beam configuration and 132,000 array elements would require roughly 10 hours of CPU time. Using in-house software evaluation programs, we examined how the code was executing on the VAX 11/780. We found that the largest amount of CPU time was spent in calculating the illumination. In fact, nearly 90% of the time was spent within a 4-line nested loop. By streamlining computations and sorting procedures and by redefining array variables and looping indices to reduce page faulting, we were able to reduce the CPU time substantially (see Fig. 2.64). We have since introduced modifications which will have changed these timing estimates to some extent. All modifications have, however, been made with consideration of their effect on execution time and we have tried to keep the code as time efficient as possible.

In implementing the multibeam feed, we took a look at the sidelobe levels versus the number of feed beams in each of the principal planes, as discussed in Sec. 2.1.3.4. Figure 2.33, shown previously, compares the three highest sidelobes for the case of a 60 dB Taylor. Figures 2.65 and 2.66 compare the aperture and far-field patterns of a multibeam feed with a corporate (ideal) feed for the specific case of 5 × 5 beams and a nominal 40 dB Taylor.

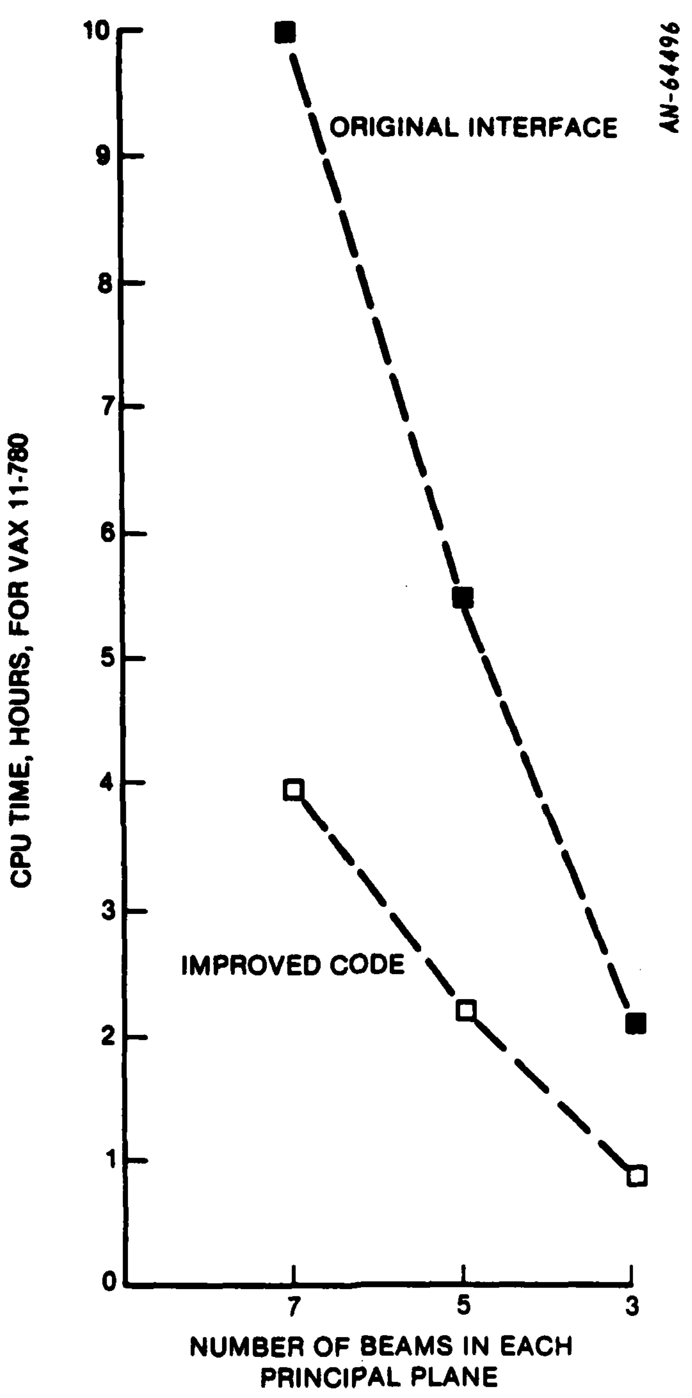

Figure 2.64. CPU Time Requirements for Feed Simulation (Intermediate Study)

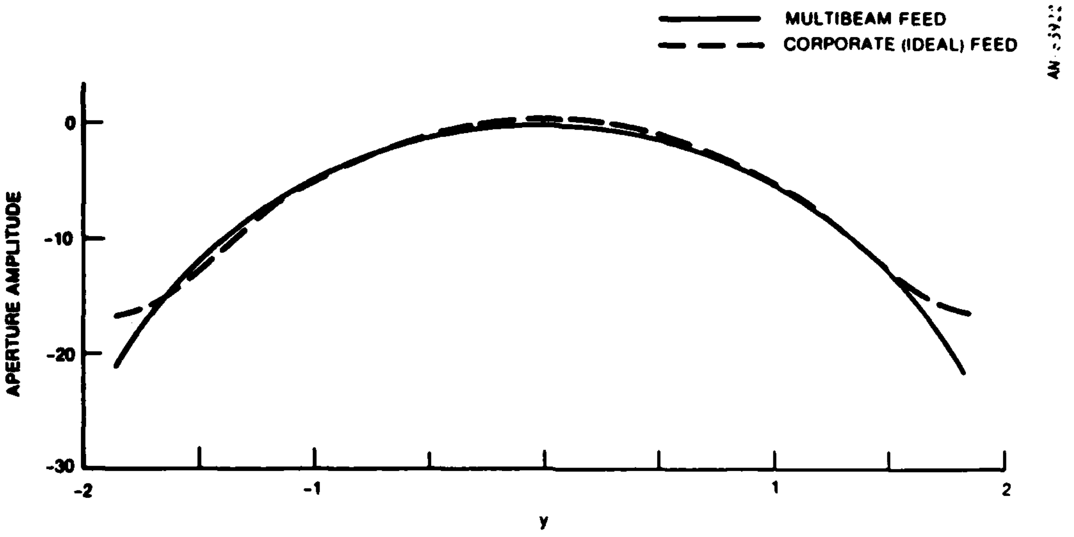

Figure 2.65. Comparison of Multibeam Feed and Corporate (Ideal) Feed

---

2.3.2.6 Multipath

The SARF simulation can model multipath effects for the space-fed arrays. Figure 2.67 shows the physical situation being modeled and the coordinate system used. The user must specify the location of a primary feed source. This would be the location from which all energy is initially radiated. The user also must specify location coordinates for at most ten scattering points. These are points of reflection, which are presently modeled as isotropic scatterers. Energy from the primary feed source reflects from the rear face of the lens, back to the scattering points, and is then reflected back to the lens. Each scattering point has a complex excitation value which describes how the energy from that point is reflected to the lens. The coordinate system which is used has its origin at the center of the main array. The x axis is the horizontal plane, the y axis is the vertical, and the -z axis extends from the main array to the feed.

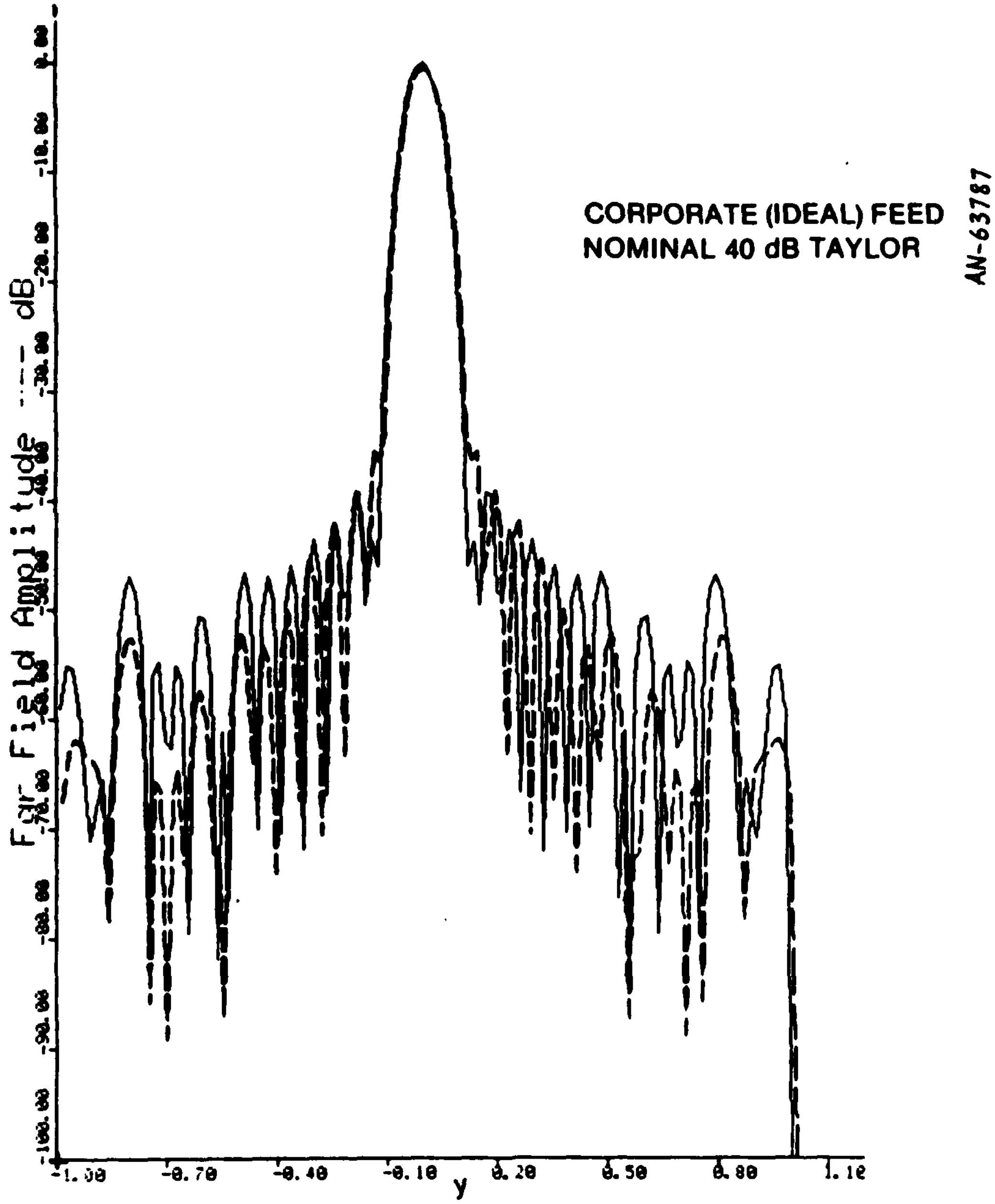

Figure 2.66. Far-Field Patterns, Multibeam Feed and Corporate (Ideal) Feed

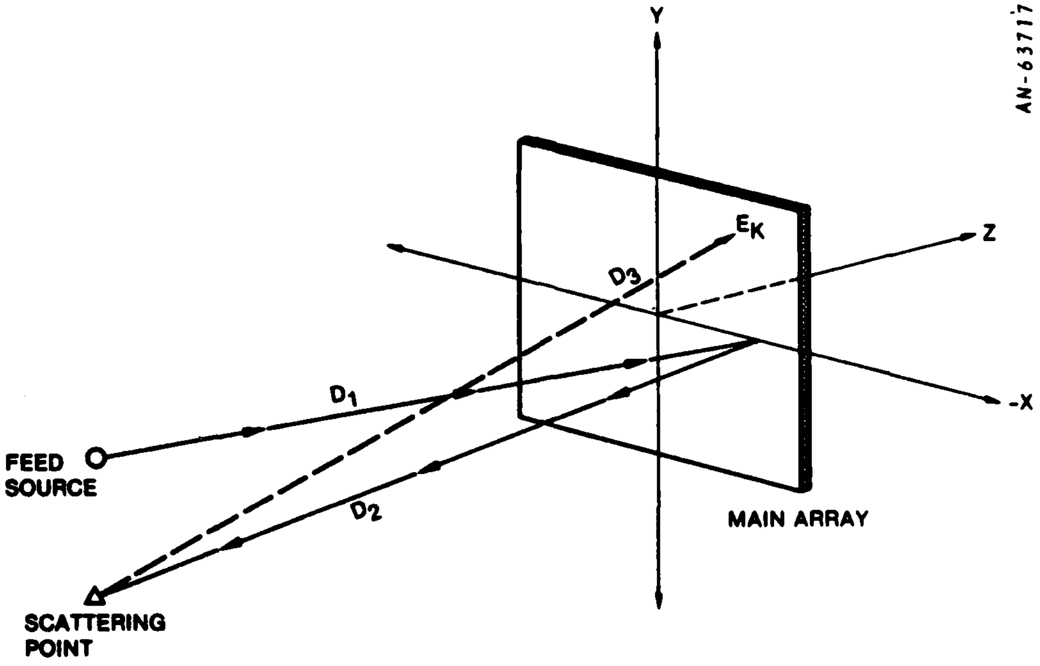

Figure 2.67. Multipath Model

When the illumination contribution from each feed element is being summed at each element in the main array, the software also sums in the amplitude and phase contribution from each scattering point. The contributions are computed to be

$$\text{Amplitude} = \frac{\sqrt{a^2 + b^2}}{\rho}$$

$$\text{Phase} = \tan^{-1}\left(\frac{b}{a}\right) - \frac{\rho 2\pi}{\lambda}$$

where

(a + jb) = excitation at scattering point whose contributions are being computed

$$\rho = \sqrt{(x_{ma} - x_{sp})^2 + (y_{ma} - y_{sp})^2 + (z_{ma} - z_{sp})^2}$$
$$+ \sqrt{(x_{ps} - x_{sp})^2 + (y_{ps} - y_{sp})^2 + (z_{ps} - z_{sp})^2}$$

(x_{ma}, y_{ma}, z_{ma}) = location coordinates of main array element at which illumination is being computed

(x_{sp}, y_{sp}, z_{sp}) = location coordinates of scattering point whose contributions are being computed

(x_{ps}, y_{ps}, z_{ps}) = location coordinates

λ = wavelength

The software normally sums the feed effects and the multipath effects together. However, the software does have a user option to calculate only multipath effects and to ignore all other effects, including the feed.

As an example of how the simulation might be used to study the effects of multipath, an example was run introducing two reflection points (Fig. 2.68). The aperture illumination and far-field patterns can be acquired for cases without the multipath effects (Figs. 2.69 and 2.70), with only the multipath effects (Figs. 2.71 and 2.72), and with both multipath and nominal effects (Figs. 2.73 and 2.74).

2.3.2.7 Lens Model

Lens transmit/receive (T/R) modules are one of the critical technologies of a space-based radar, due to the requirements of low cost, light weight, and high performance. The module parameters have a very significant impact on the radar's performance, and an important feature of the SARF simulation is that it is designed to incorporate measured module data into the model. This use of measured data insures high fidelity and credibility in the modeling of lens effects.

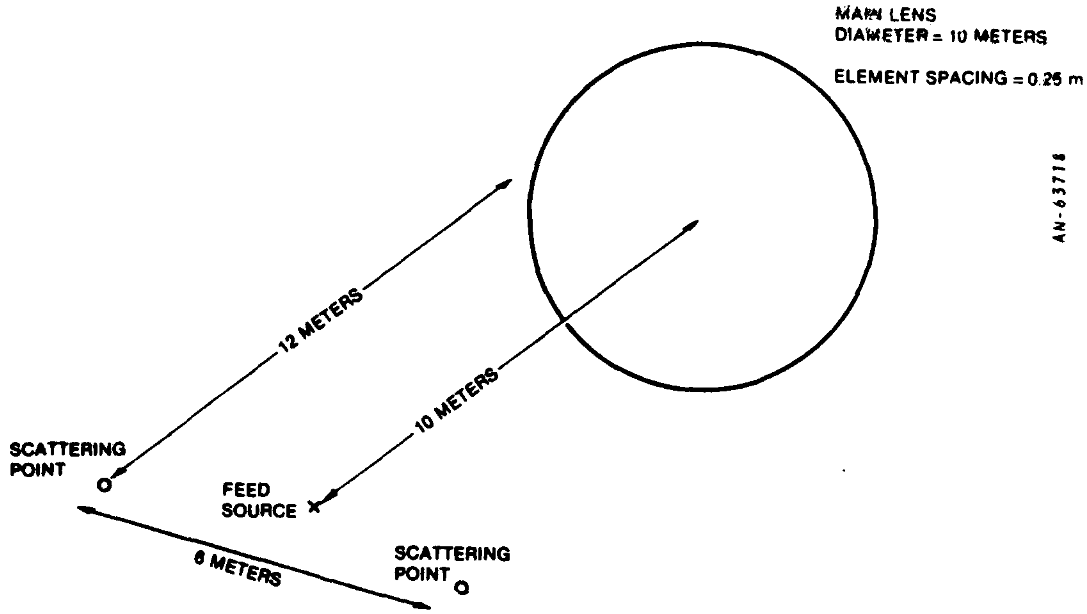

Figure 2.68. Multipath Example

The module characteristics affect the source excitation file of the SARF simulation (see Fig. 2.1). The source excitations can be obtained either by:

1. The ARC FAM/HAM model, run off line
2. The SARF on line feed/lens model

The ARC model computes the currents in the target-side array elements, including the effects of mutual coupling, ground plane feedthrough, and edges. It is designed to provide a very accurate model of these effects. However, it assumes a linear network parameter model for the module, and is not appropriate for modeling experimental module data, as shown below. The SARF on-line model is capable of modeling measured data. Which of the two options should then be selected depends on the problem being simulated:

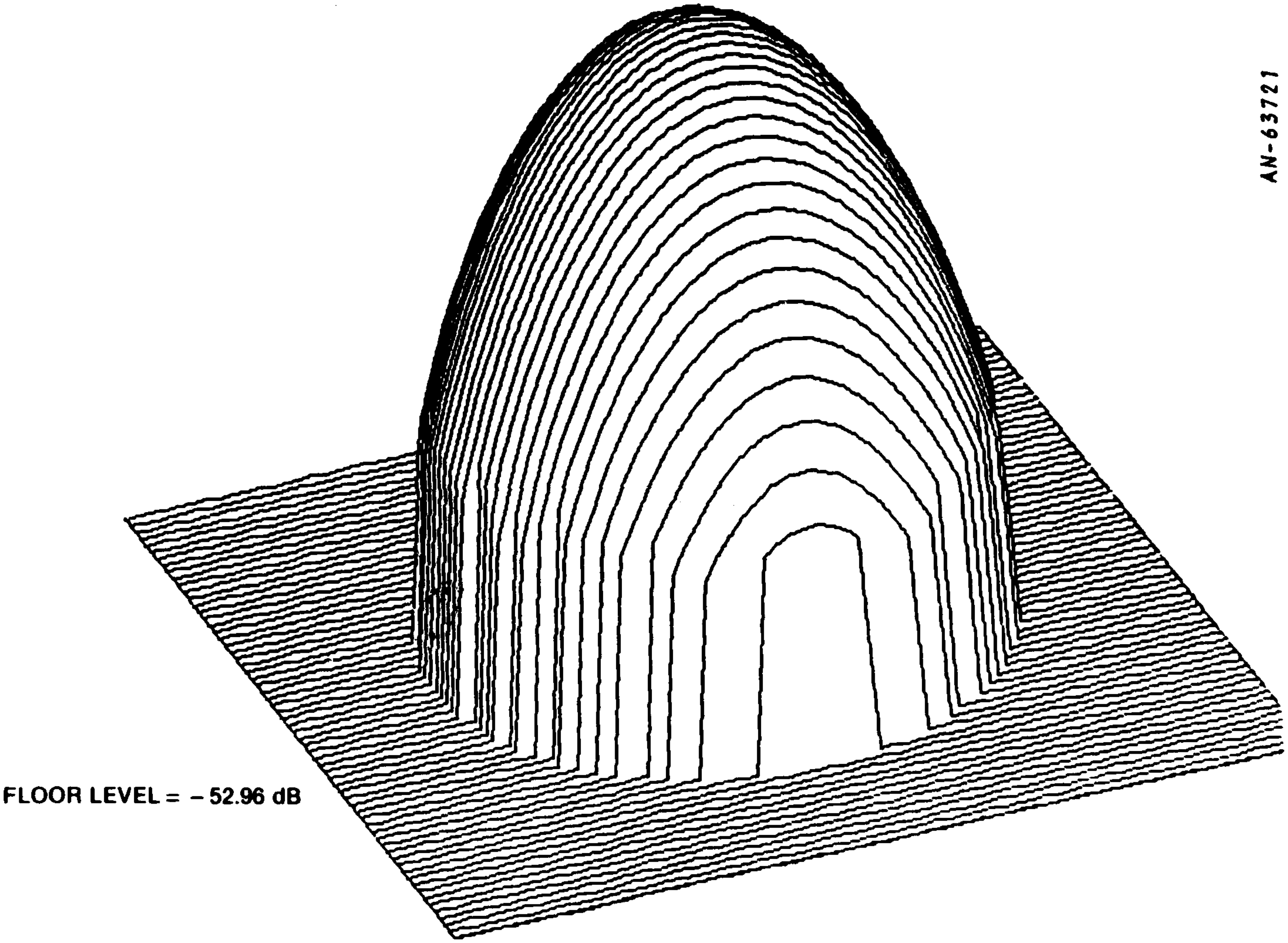

Figure 2.69. Nominal 60 dB Taylor Aperture Illumination

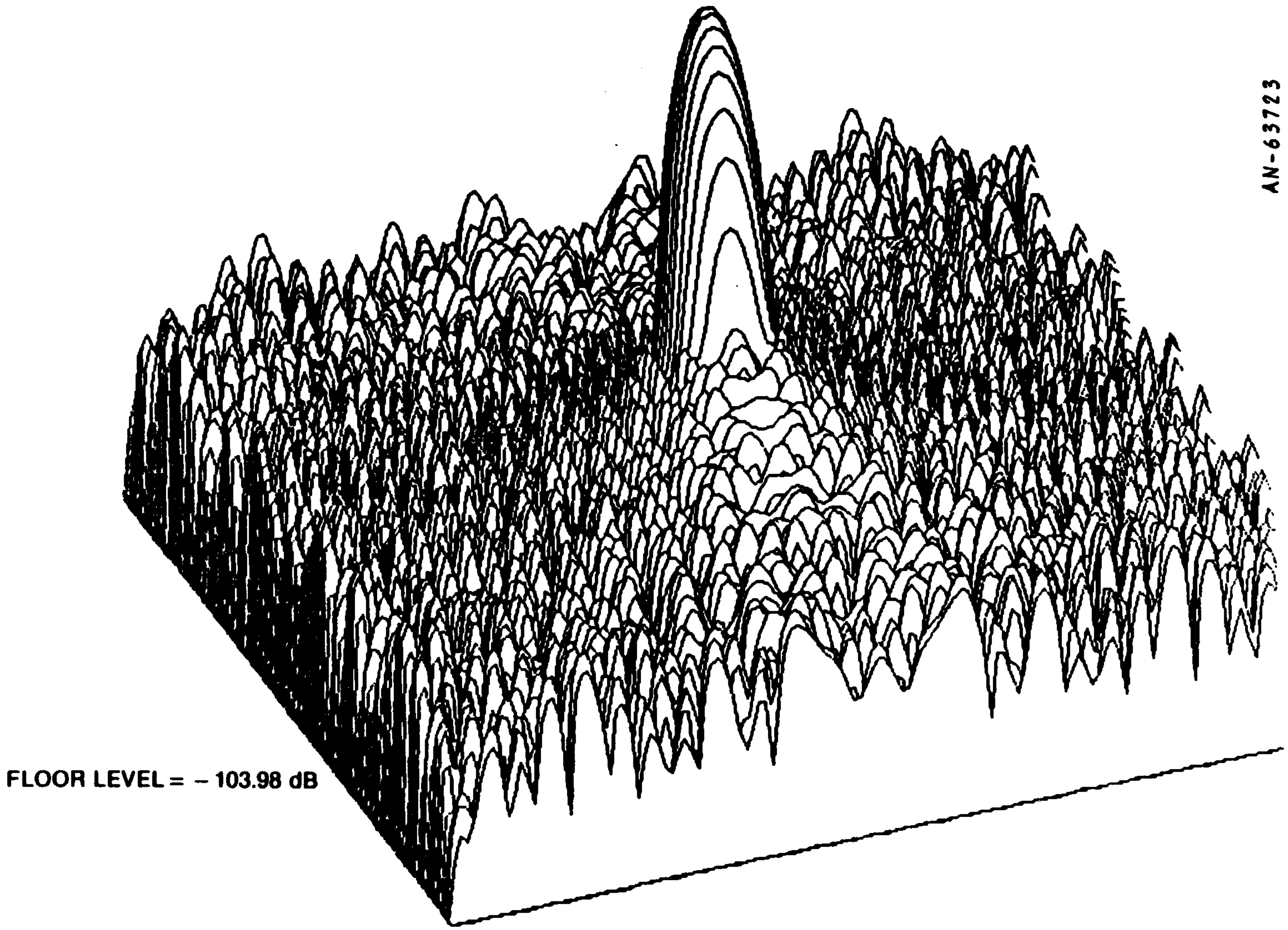

Figure 2.70. Nominal 60 dB Taylor Far-Field Pattern

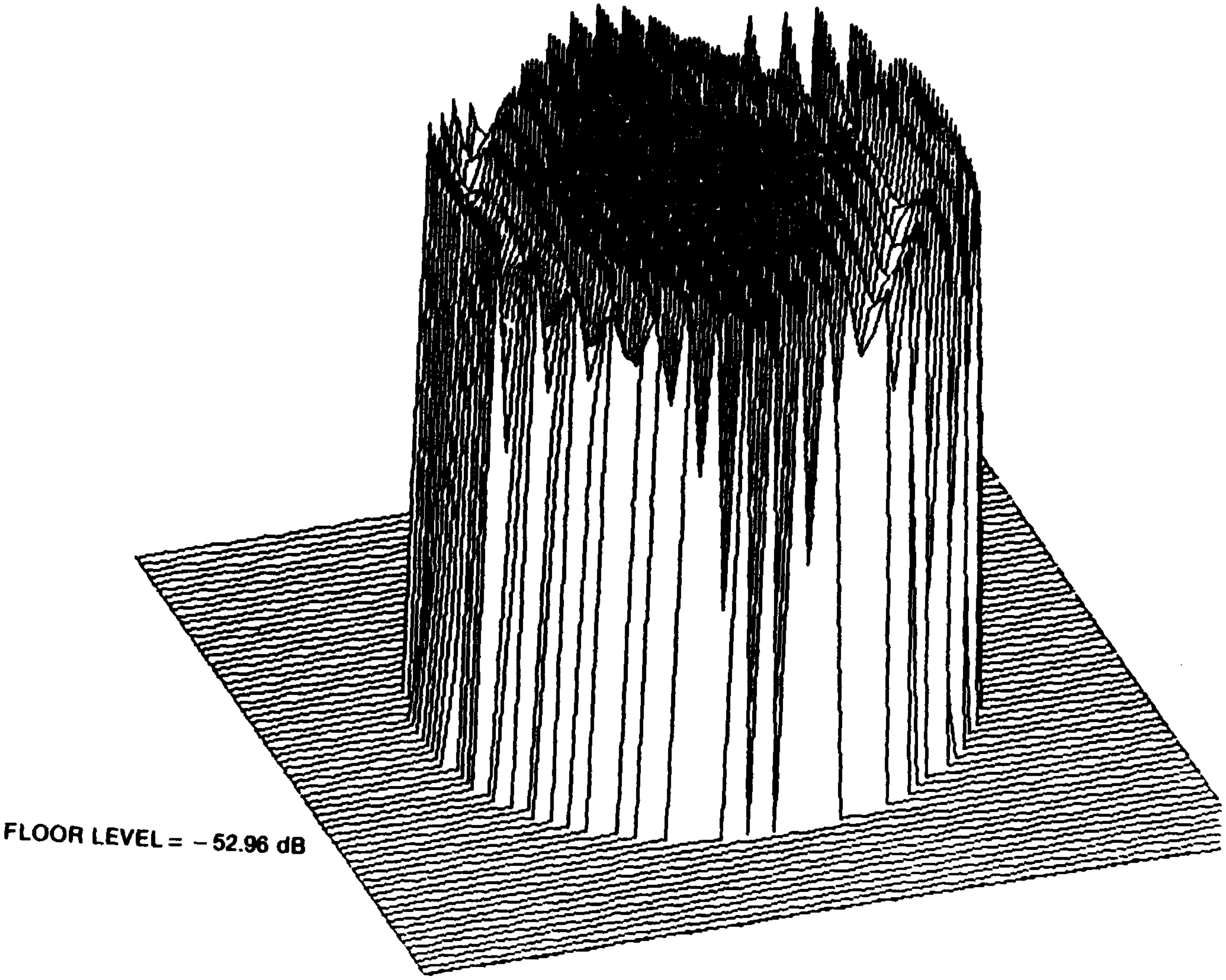

Figure 2.71. Aperture Illumination With Multipath Effects Only

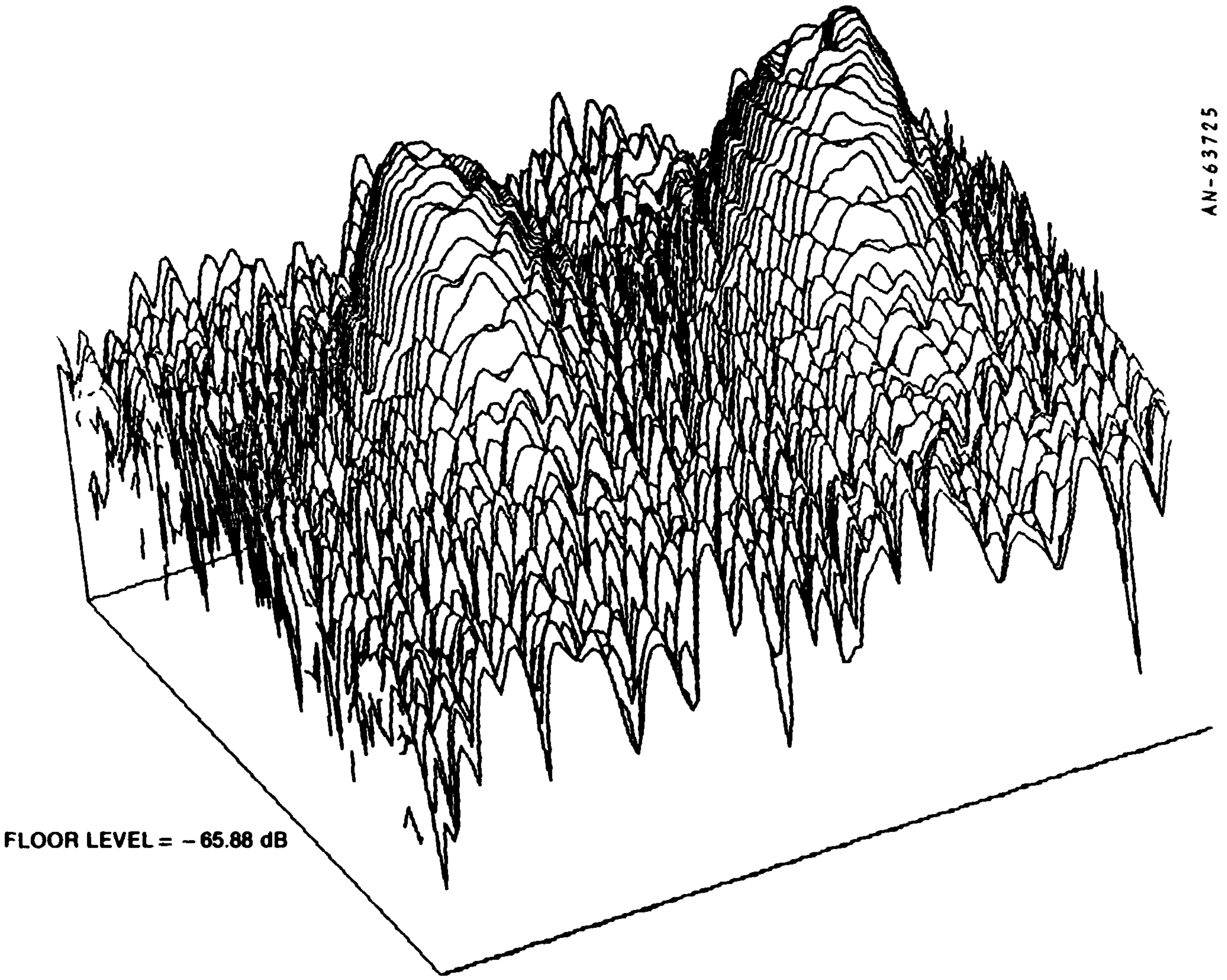

Figure 2.72. Far-Field Pattern With Multipath Effects Only

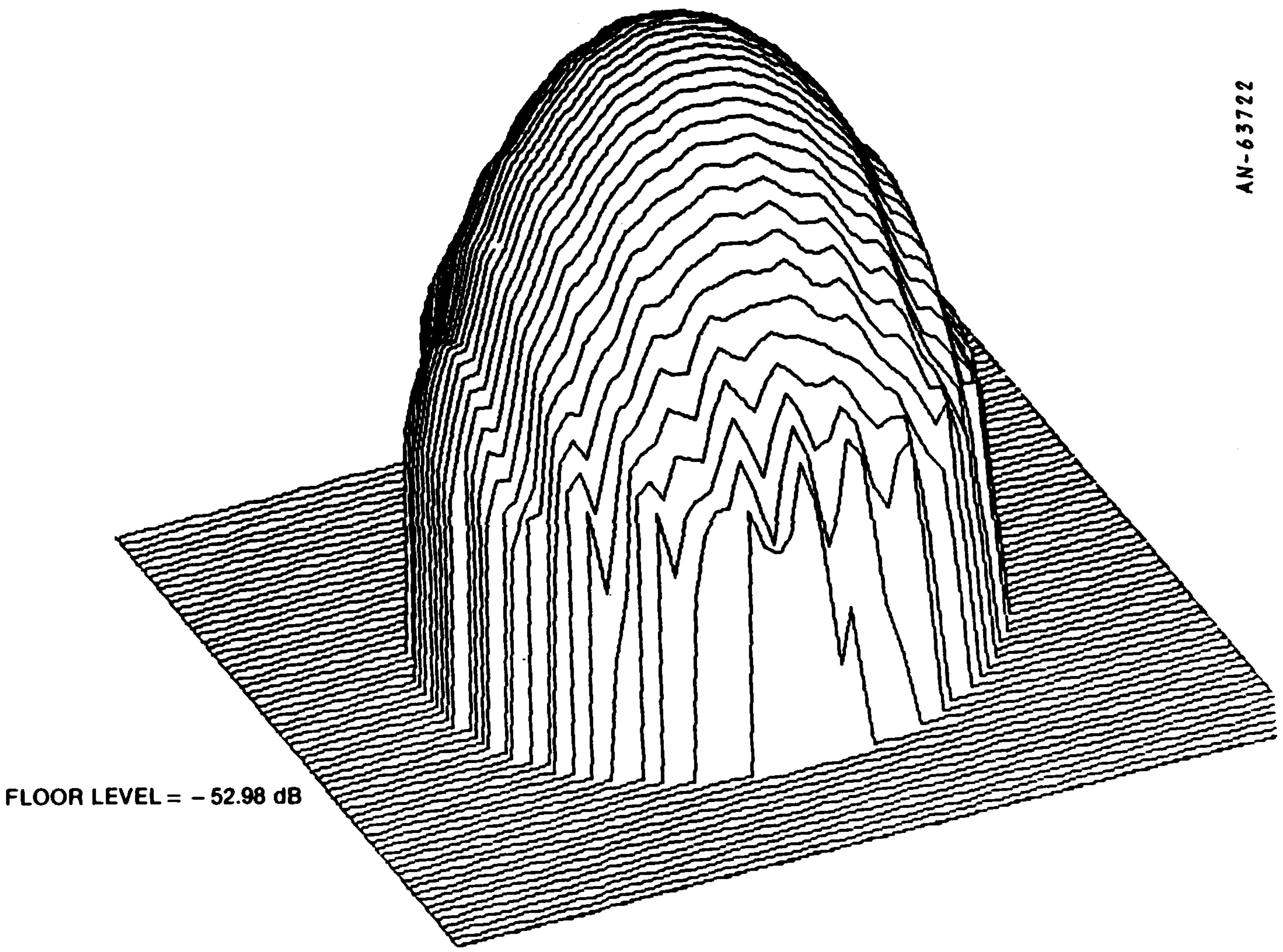

Figure 2.73. Aperture Illumination With 60 dB Taylor Plus Multipath Effects

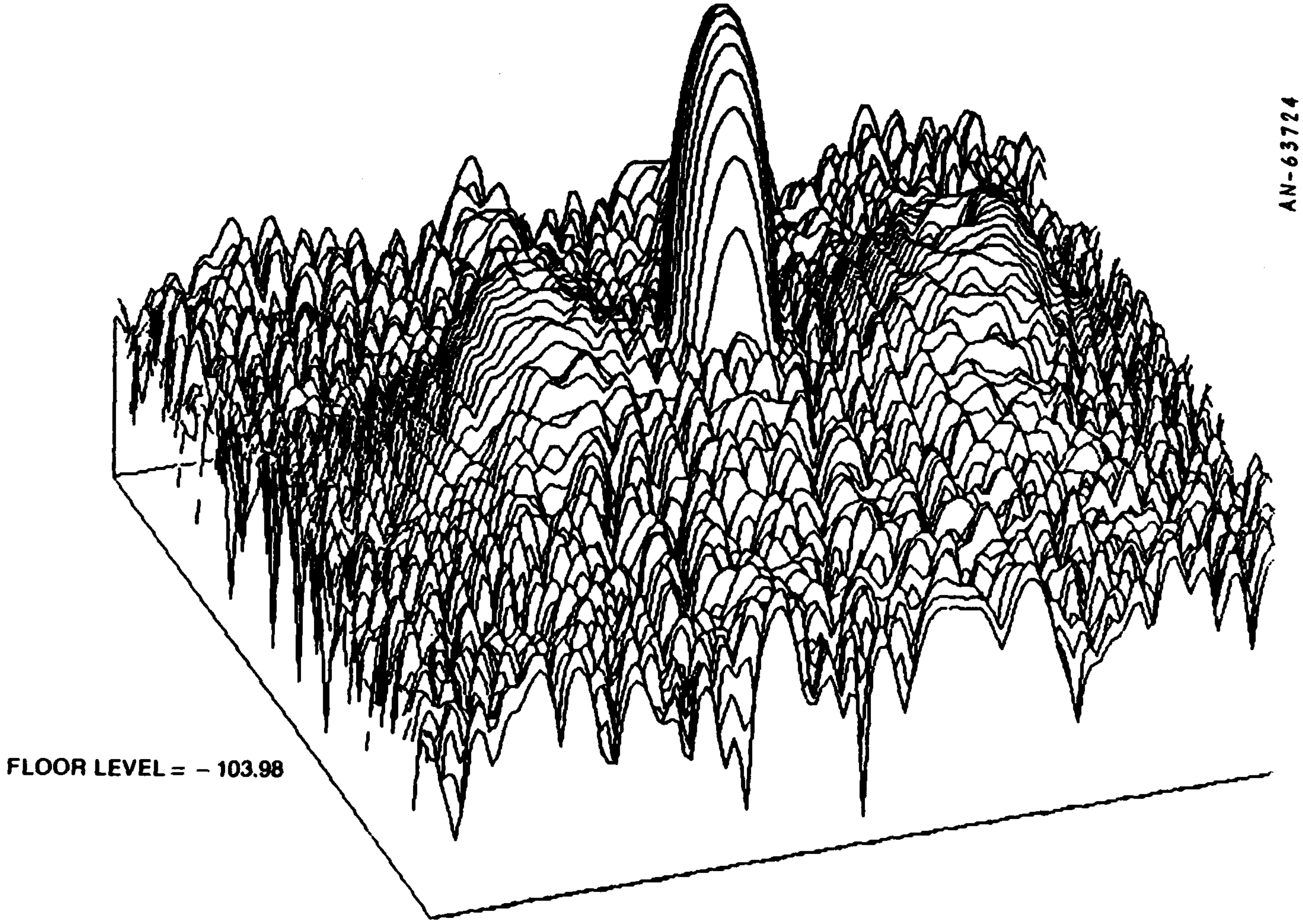

Figure 2.74. Far-Field Pattern With 60 dB Taylor Plus Multipath Effects

1. Mutual coupling differences between different element designs, edge geometries, etc., are best handled using the ARC off-line lens model.
2. Incorporation of measured module data is best handled using the SARF on-line lens model.

The ARC model is described in their reports.[1-3] Here we will focus on the SARF on-line model.

In the SARF model the amplitude and phase transfer functions of the lens are defined by

$$V_{out} = a_0 + a_1 V_{in} + a_2 V_{in}^2$$

$$\phi_{out} = \phi_{in} + [\phi_s]_{quantized} + \phi_0 + \alpha V_{in}$$

where V_{in} = amplitude at lens feed-side elements

Vout = amplitude at lens target-side elements

ϕ_{in} = phase at lens feed-side elements

ϕ_{out} = phase at lens target-side elements

a_0 = Gaussian amplitude noise random variable

a_1 = Gaussian gain factor random variable

a_2 = Gaussian square law factor random variable

---

[1] H.K. Schuman, D.R. Pflug, and L.D. Thompson, <u>Space-Based Radar Array System Simulation and Validation, First Technical Report</u>, RADC-TR-80-294, Rome Air Development Center, September 1980.

[2] H.K. Schuman, D.R. Pflug, and L.D. Thompson, <u>Space-Based Radar Array System Simulation and Validation, Final Technical Report</u>, RADC-TR-81-215, Rome Air Development Center, August 1981.

[3] H.K. Schuman and D.R. Pflug, <u>Space-Based Radar Array System Simulation and Validation, Final Technical Report</u>, RADC-TR-81-366, Rome Air Development Center, December 1981.

ϕ_s = nominal phase for lens focusing and beam scan

ϕ_0 = Gaussian phase noise random variable

α = amplitude modulation/phase modulation (AM/PM) factor random variable

$[\,]_{quantized}$ = the phase quantization due to an n-bit phase shifter

For a space-fed lens, beam focusing is achieved by calculating the path lengths from the feed to the lens elements and adjusting ϕ_s to make all target-side elements have the same phase. Beam scanning is then obtained by superimposing a linear phase shift across the aperture. For a corporate-fed design it is assumed that the feed network provides equal phase at the module inputs, and a linear phase shift is imposed for beam scan. The resulting value of ϕ_s is then quantized to reflect the specified number of phase shift bits.

The user must be aware that V_{in} is not normalized. The reason for this is that the amplitudes are being computed at the same time the random errors are being computed. To normalize the amplitudes would require all amplitudes to be computed and written to a file. This file would then be reread and the amplitudes normalized. These two passes through the file, which can be quite large, would be very time-consuming.

As stated above, this SARF on-line model has sufficient generality to include virtually all experimentally measured data. The specific procedure for including measured data in the model is as follows:

1. Obtain measured data for insertion and phase as a function of the input amplitude and phase, for several modules, and under varying load and thermal conditions.
2. Select the mean values of the Gaussian random variables a_0, a_1, a_2, ϕ_0, and γ to fit the mean measured data. Thermal

effects can be treated systematically by repeating this procedure for each thermal case, or they can be lumped in with the random variations from module to module.

3. Select the variance of the Gaussian random variables to match the variations from module to module and/or variations of load and thermal conditions.

An example of the results of this procedure is illustrated in Fig. 2.75, using STRAM module data measured by Ed Jones.[1] The triangles represent measured data points, and the solid line shows that the SARF model provides an excellent fit to the data.

A linear network parameter model, such as used in the ARC HAM/FAM model, is shown by the dashed line in Fig. 2.75. It is evident that the simple linear model does not fit the data well, but the real question of course concerns the effect on the antenna pattern. To illustrate this, we will compare a feed illumination with an ideal linear gain module, and the illumination that would result with the non-linear gain of the real module. The aperture illumination is shown in Fig. 2.76 for the case of an ideal 50 dB Taylor distribution and a multibeam feed. The dashed line shows the illumination for the ideal linear gain module, and the solid line the illumination for the real non-linear gain. Finally, the resulting antenna patterns are compared in Fig. 2.77. The first sidelobes are very different between the two cases, and it is evident that the non-linear effects are important. It should be emphasized that a proper design will compensate for the module non-linearity by adjusting the feed illumination, so good sidelobes will be obtained. A major function of the simulation is precisely to provide a tool for such design optimization.

The example above involved amplitude data from a single module, and the variables a_0, a_1, and a_2 were selected with the mean values

---

[1] RADC TD meeting, 23 February 1982.

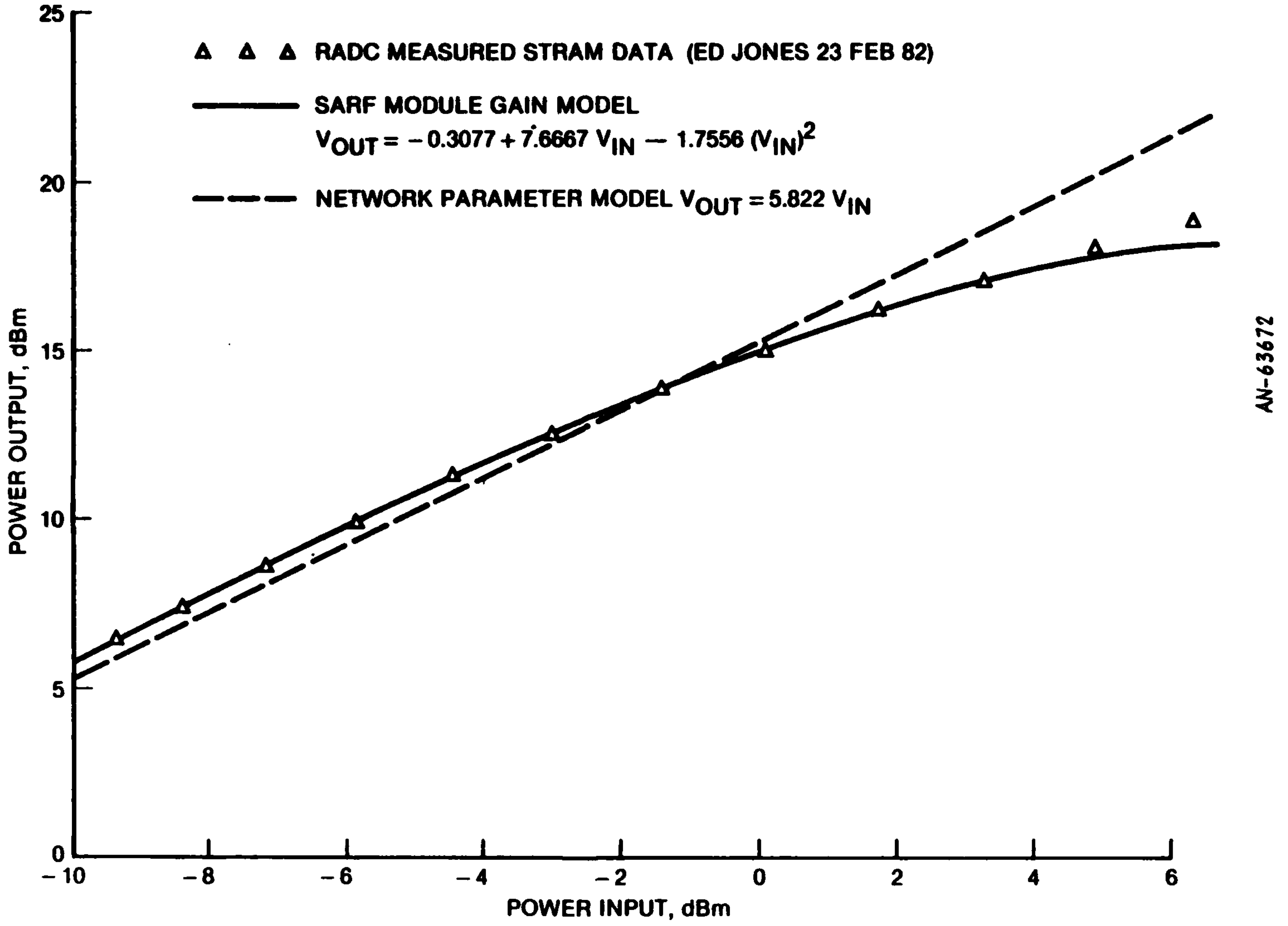

Figure 2.75. Module Gain--Model of RADC Measured Data

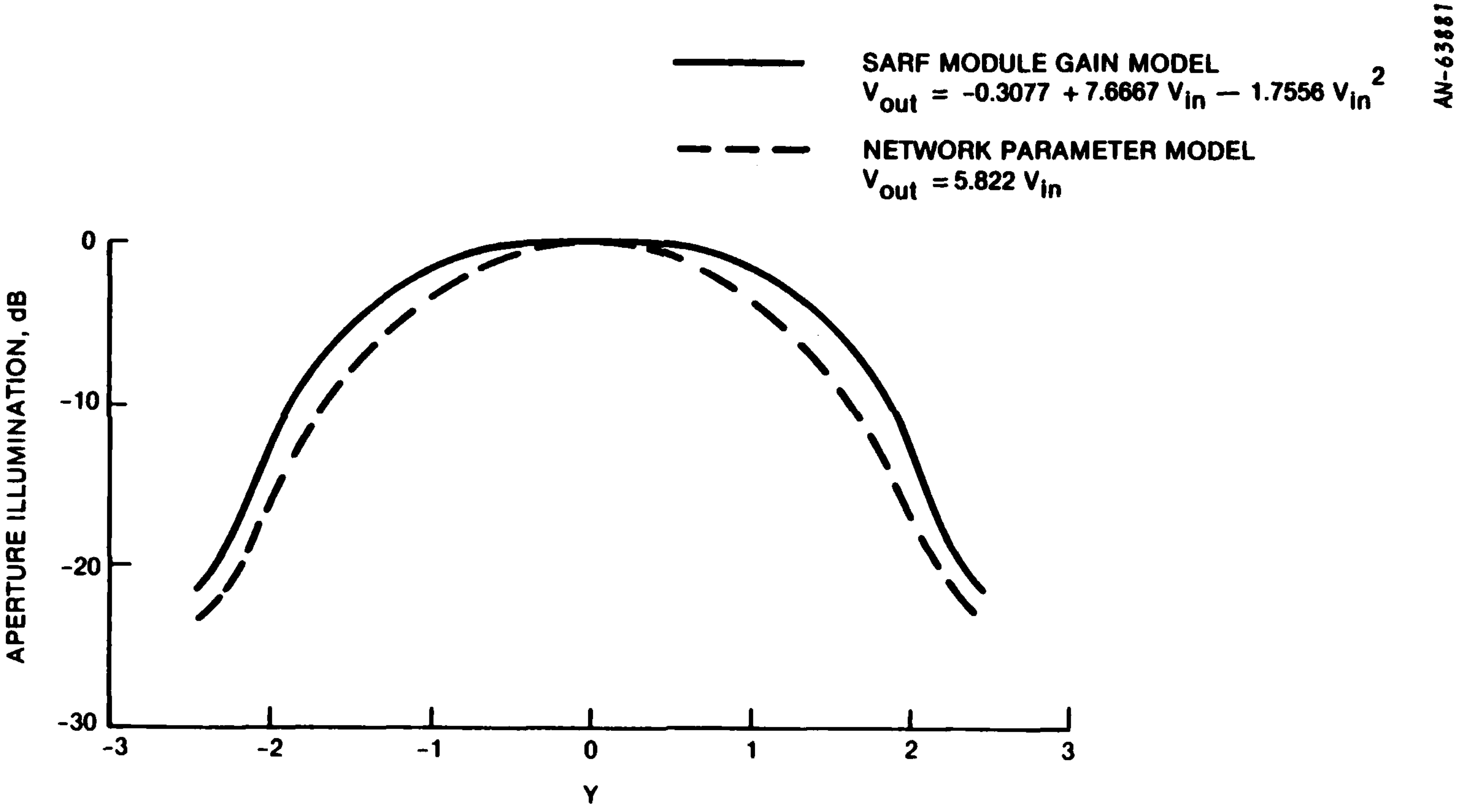

Figure 2.76. Active Lens Effect on Aperture Illumination

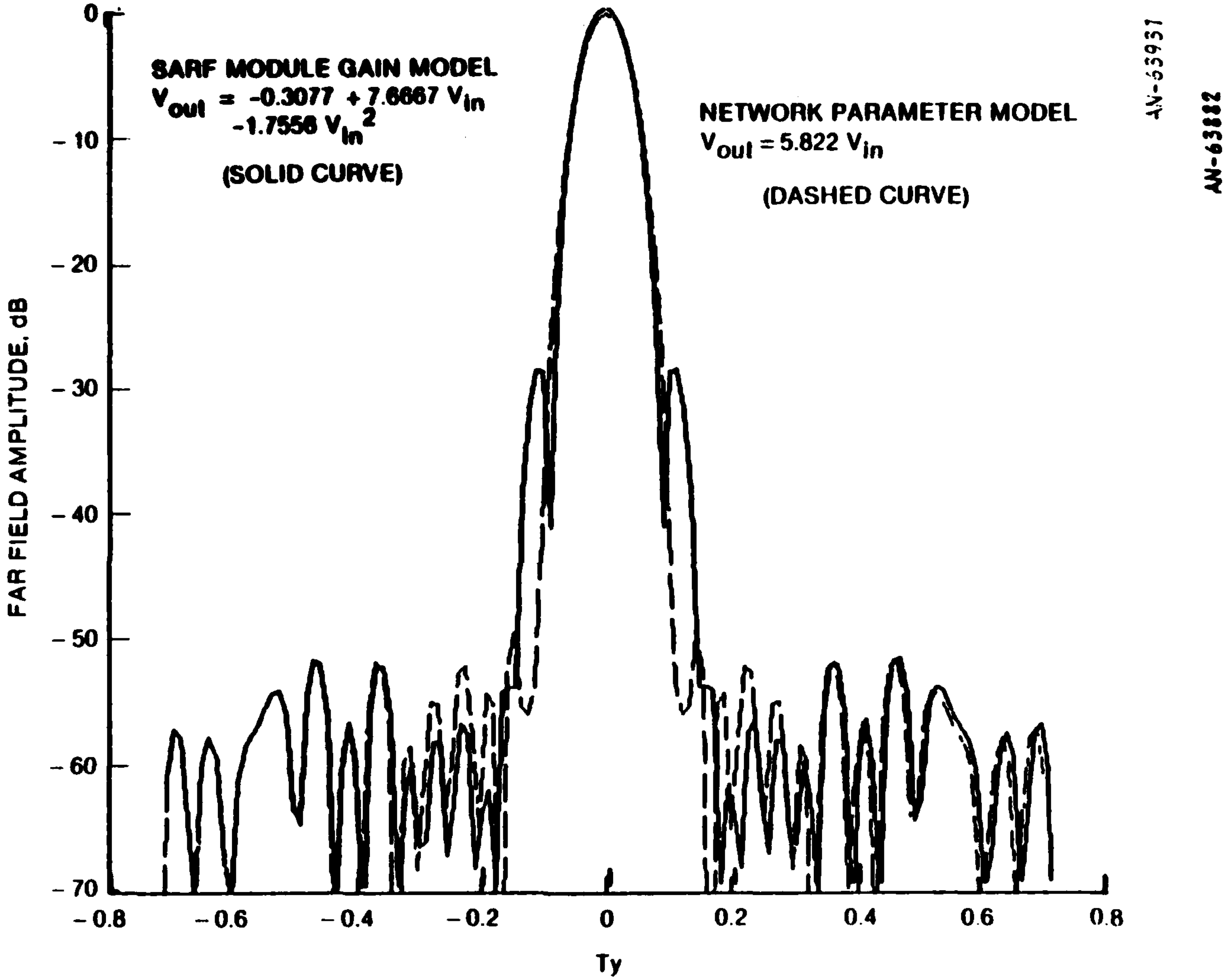

Figure 2.77. Calculated Antenna Patterns With Linear and Non-Linear Module Gain

shown in Fig. 2.77, and zero variance; therefore, they are in fact constants and not random variables in this particular case. If data from several modules were available, the incorporation of randomness by inputting non-zero variances would be straightforward. It should be noted that the ARC HAM/FAM model and the Raytheon feed model also have the capability of adding random effects, but only additive noise corresponding to the a_0 and ϕ_0 factors in the SARF model. Random variations in gain, which are represented by the a_1 term in the SARF model, are not included in the ARC or Raytheon models. These other models are also lacking the AM/PM factor α as well as the square law factor a_2.

2.3.3 Element Pattern Model

The SARF element pattern model is based on the sum of infinitesimal current segments which can be placed anywhere on the main array by the user. Each element (or subarray) on the membrane is represented by up to 50 current segments. Therefore, straight or bent dipoles, turnstiles, bowtie microstrips or any other device that can be modeled by a set of current segments are easily simulated. Also, since the current segment model can calculate vector patterns, SARF models the cross polarized pattern as well as the principal polarization.

Due to its flexibility, the element pattern model provides the capability of modeling mutual coupling and empirical data obtained on antenna ranges. An example of this capability is shown for the Grumman Test Article-2 (TA-2) in Sec. 2.1.1.2.3.

In addition to simulating each element in the main array, the SARF element pattern model also allows the antenna designer to model various types of degradation in the element patterns. Random deviations are easily included and can be modeled using either uniform, Gaussian, or Rayleigh densities. Major deviations can also be simulated with up to nine different types of degradations, or failures, to a particular subset of the elements. The details of the entire element pattern model are described in the remainder of this section.

2.3.3.1 Nominal Element Pattern

The nominal element pattern is modeled by a vector sum of up to 50 current segments which simulate some particular element type. The nominal pattern applies to every element in the array that is "turned on" (an element may be "turned off" if an element failure is being simulated).

Figure 2.78 shows a simplified block diagram of the implementation of the nominal element pattern (the associated paths for random and major deviations are shown as well). The diagram indicates that after reading the element pattern data file, SARF tags each element with the

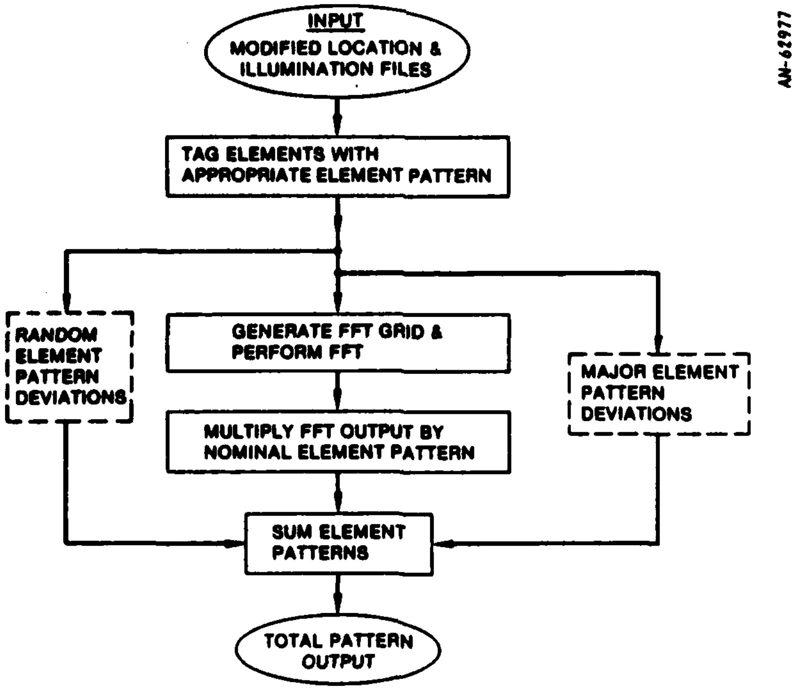

Figure 2.78. Block Diagram of Element Pattern Calculation

appropriate element pattern (for the nominal pattern all elements are tagged). Next, the model generates an FFT grid, determined by the illumination and location files, and performs the transform operation. Each point in the $T_x - T_y$ plane (sine space) is then multiplied by the appropriate value of the nominal element pattern for both the principal and cross polarization. The resulting pattern is stored on a file for future summation, if applicable, with the random and/or major element pattern deviation output files.

2.3.3.2 Random Element Pattern Deviations

If a group of element patterns are each measured in an anechoic chamber, no two of them will be identical but will have random deviation around some "nominal" pattern. Figure 2.79 shows a fictitious example of this phenomenon for three element patterns. If a very large number of these patterns were measured, a statistical variance could be calculated for the envelope of element patterns. This variance would be a

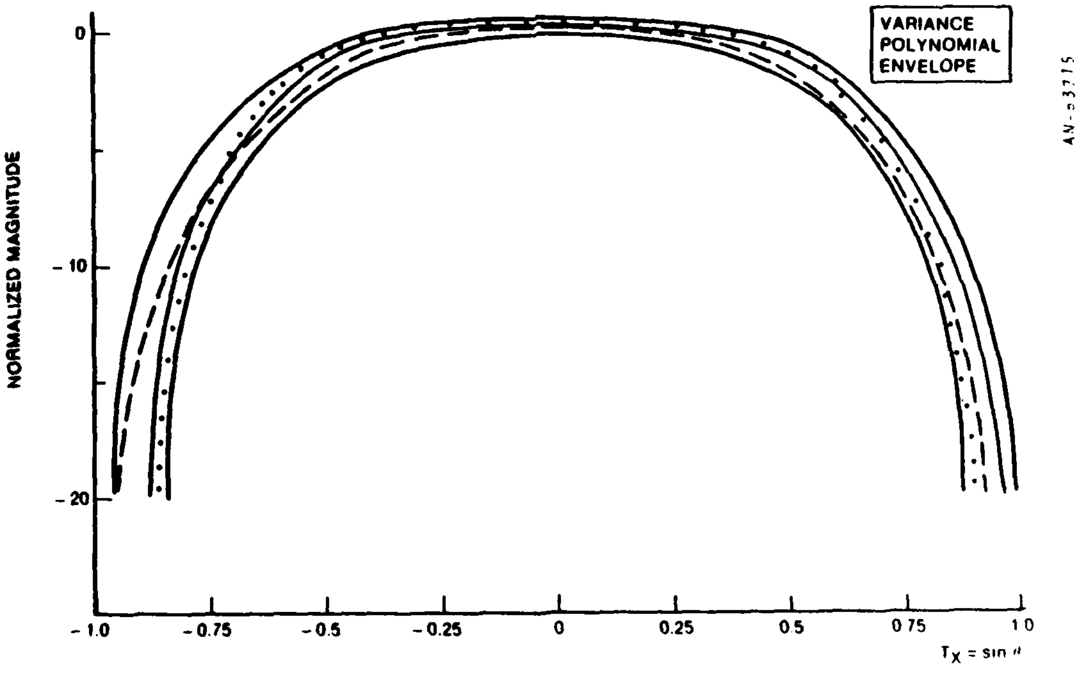

Figure 2.79. Random Element Pattern Samples With Variance Envelope

function of the measurement angle (as seen in the figure) since there is less variation in the pattern near boresight than at the edges. The SARF element pattern model simulates this random pattern variation by an envelope variance for each of the two polarizations. These envelopes are described by the equation:

$$\sigma^2(T_x,T_y) = a_0 + a_1T_x + a_2T_y + a_3T_xT_y + a_4T_x^2 + a_5T_y^2$$

where σ^2 = the variance of the random element pattern

a_n = the user-defined coefficients which describe the variance function

Each polarization has its own variance equation with separate coefficients, to reflect the typical case of larger variation in the principal polarization than in the cross polarization pattern.

Figure 2.80 provides a simple block diagram of the random element pattern model. First, each illumination is multiplied by a random number with unit variance. These modified illuminations are stored in a temporary file so that a new FFT grid can be generated. This new grid is then fast Fourier transformed and the output is multiplied by the proper variance quadratic. The resultant output file is now summed with the nominal element pattern file to obtain a nominal far-field pattern along with random variations.

2.3.3.3 Major Element Pattern Deviations

Deployment of a space-based radar may result in some damage to the membrane and the elements. In addition, failures may occur during the operating life of the radar. As examples, consider power supply failure, disabling many of the elements in a particular region; or a random set of elements might change characteristics due to thermal effects. It

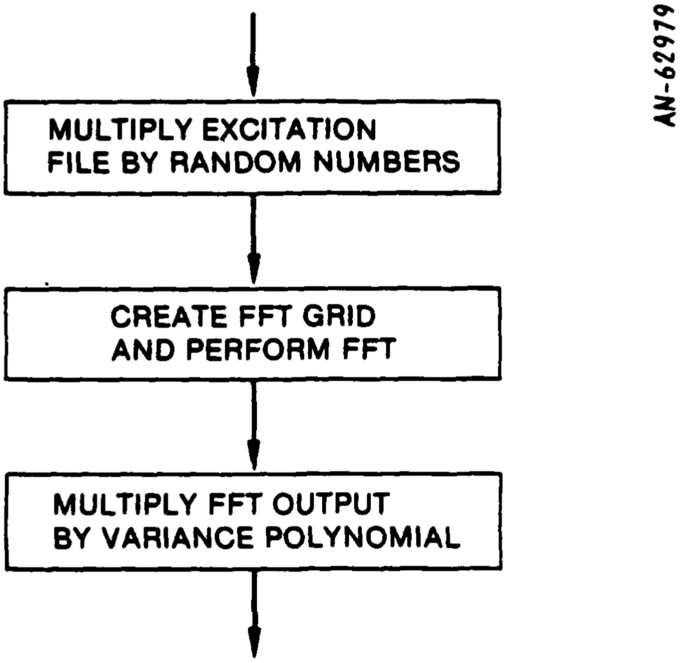

Figure 2.80. Random Element Pattern Diagram

is with these types of element pattern degradation in mind that the major element pattern deviation (MEPD) model was incorporated into SARF.

The MEPD allows for nine types of element pattern degradations. Each of these nine types may affect from one to all of the elements on the membrane. Which elements a particular type of deviation will affect is determined in two ways: (1) A percentage of the elements can be selected and this percentage will be chosen randomly from the entire array. (2) A rectangular patch of elements can be selected by defining the maximum and minimum coordinates (X and Y) on the aperture face.

An example of each of these two means of element selection is shown in Fig. 2.81. Figure 2.81a graphically shows the entire set of elements in the main array while Fig. 2.81b shows 30% of the elements randomly selected, and Fig. 2.81c shows a rectangular patch of elements

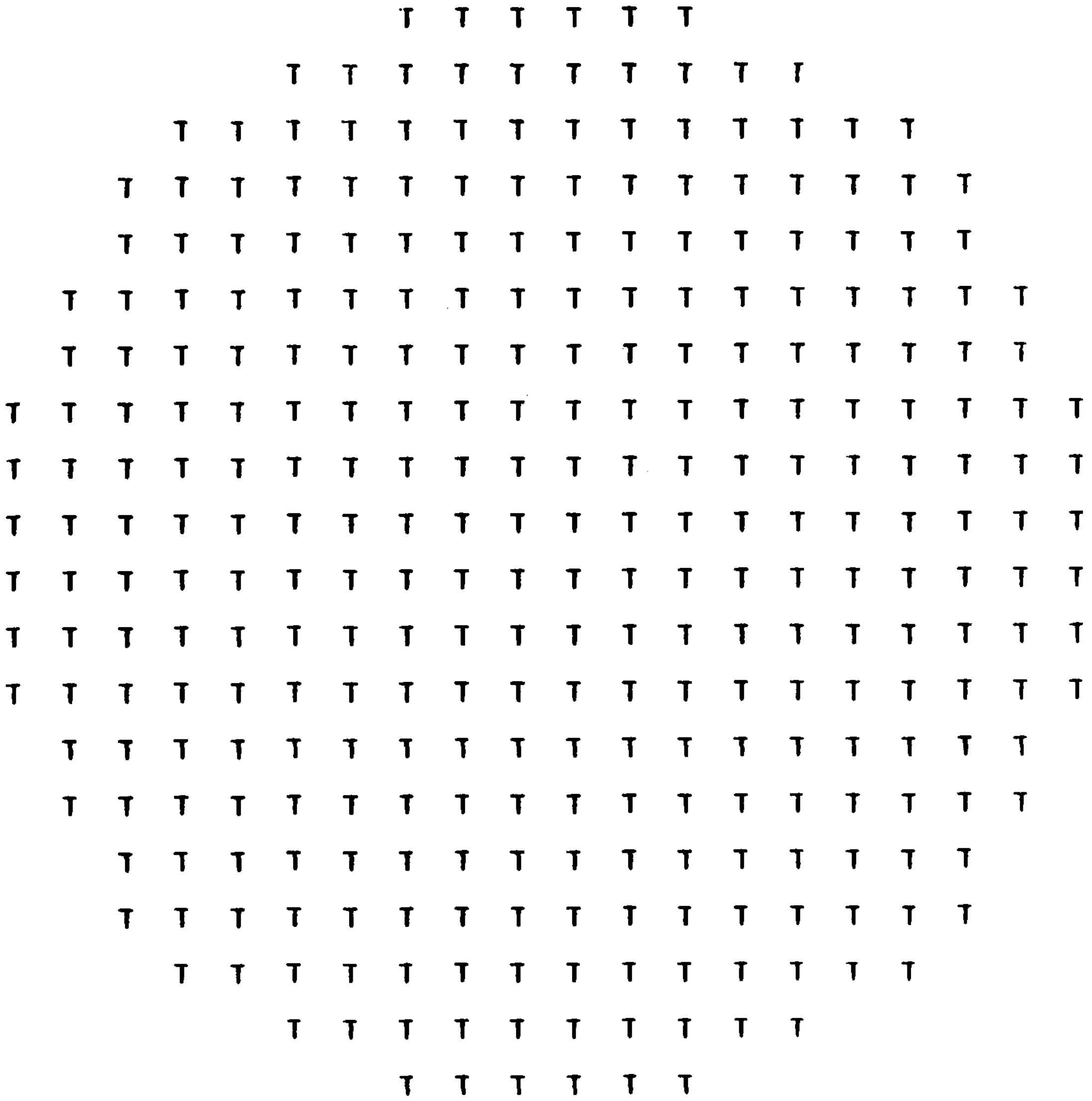

Figure 2.81. Nominal Element Pattern Locations

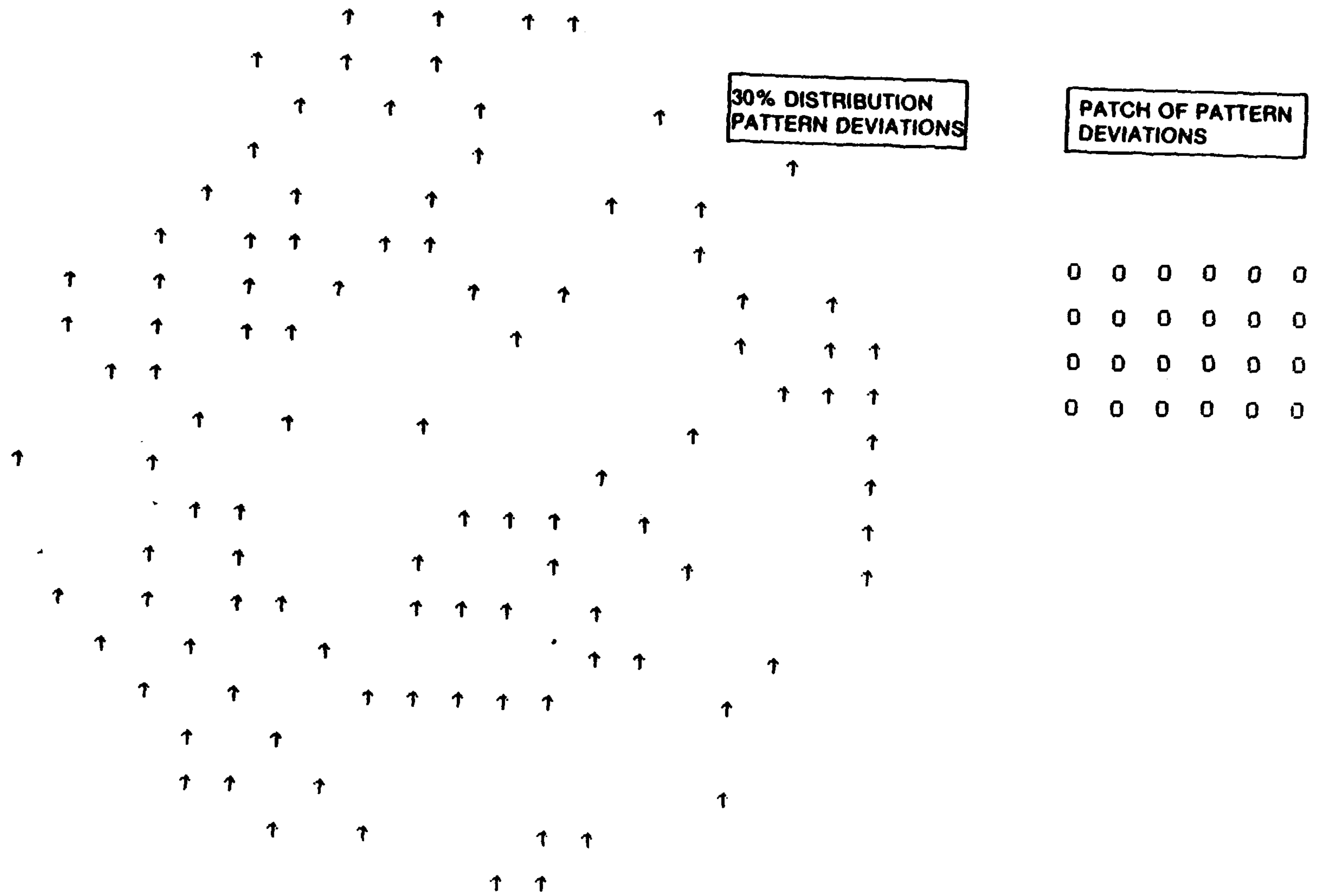

Figure 2.81 (Concl.)

chosen in the upper right of the array. This figure could represent an example of element pattern calculation with (a) representing the elements' nominal pattern, (b) showing a slight degradation in the elements due to a deployment mishap (e.g., bending of dipole elements), and (c) might be a small group of elements which completely failed due to a power supply line failure. Several examples of models for different types of partial failures were shown previously in Fig. 2.14.

Figure 2.82 shows the implementation of the MEPD model. The left side of this diagram shows the implementation using the efficient technique while the right side shows the mini-brute force technique.[1] Major deviations are handled by the efficient technique essentially the same as the nominal element pattern with the exception of the elements being considered. These identified elements are used to create the FFT grid and an FFT is executed. Then the FFT output is multiplied by the appropriate element pattern. All of the resultant patterns are then summed together with the nominal output pattern (and random deviation, if applicable) to provide the total far-field pattern. The mini-brute force technique simply calculates the exact pattern using the same input files as the efficient technique and adds the result to the nominal element pattern.

With the capability of nine major deviations, SARF provides a sufficiently flexible element pattern model for any desired pattern calculation.

2.3.4 Structural Model

The SARF structural model starts with a file containing the nominal element locations. These locations are then perturbed (according to

---

[1] This is referred to as the mini-brute force technique since it is implemented the same as a brute-force calculation, but deals with only a small amount of input (element) points.

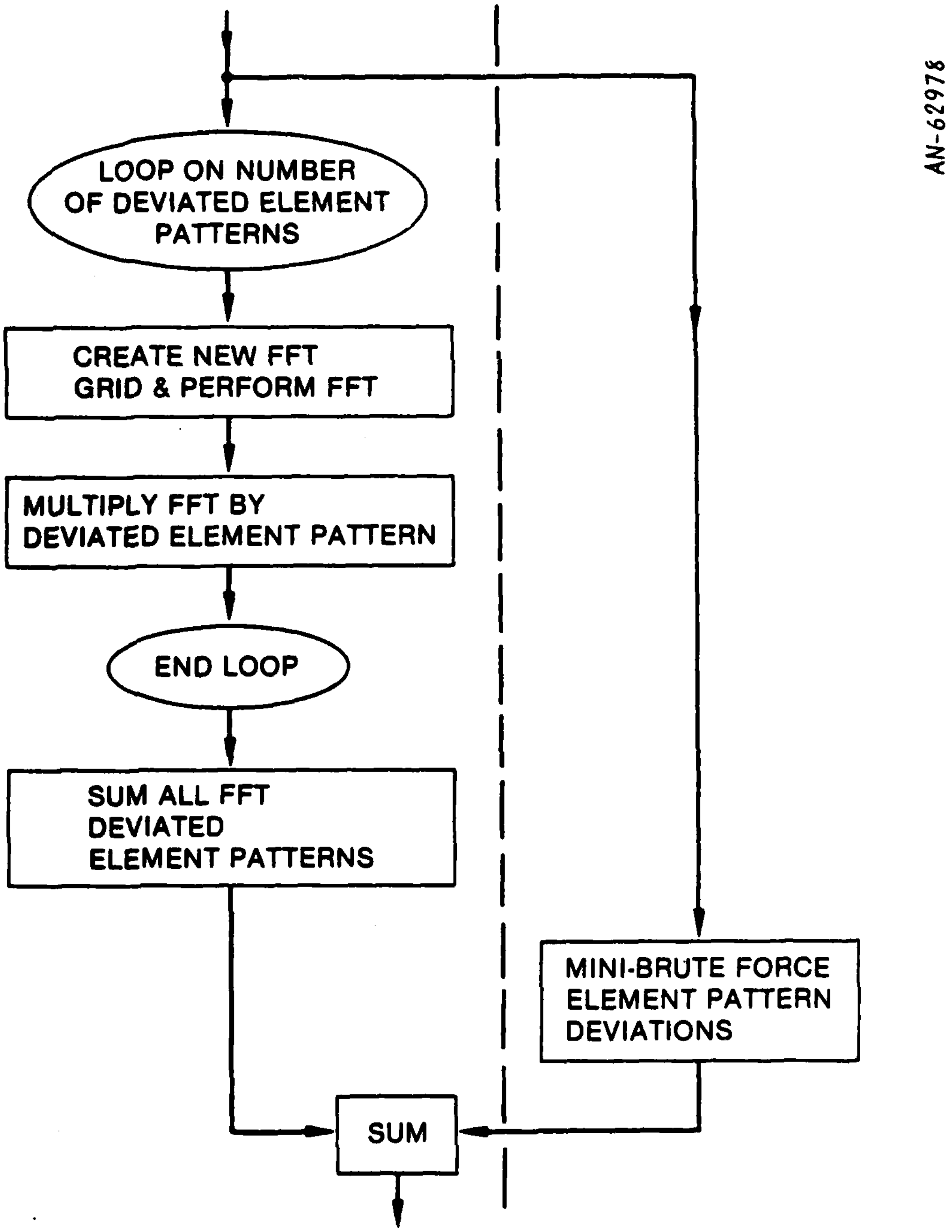

Figure 2.82. Major Element Pattern Deviations

the designer's inputs) and a new file is created which contains the true element locations.

The antenna designer has three options for the nominal aperture shape: (1) circular, (2) rectangular, and (3) elliptical. The designer selects the aperture radius (circular); the height and width (rectangular); or the major and minor axis lengths (elliptical) along with the desired element spacing. The nominal location file is then created as specified. The element spacing can be chosen to be on a rectangular lattice, a triangular lattice, or one of three circular gore designs. (Examples of triangular, rectangular, and gore lattices are shown in Figs. 2.24, 2.30, and 2.34, respectively.)

The three circular "gore" designs emulate structures originally proposed by Grumman. The first design used pie-shaped gores with the elements spaced on radial lines. Investigation of this design indicated that the gaps between gores caused a high sidelobe level in the pattern. This led to design number two proposed by Bob Hancock (Simulation Technology Inc.). The second design reduced the gaps and the sidelobe levels, but still provided sidelobes greater than desired. The third design utilizes a triangular element spacing and includes additional parameters (such as space for d.c. power distribution) to provide a more realistic simulation of the expected hardware configuration.

The structural deformation model is divided into an on-line processor and an off-line processor. The on-line model allows the antenna designer to create the ideal or nominal element location file and then distort these locations randomly or systematically. The off-line model provides the designer with the capability of distorting the aperture based on empirical deformation data. The off-line model also provides local systematic distortion capability.

The deformation model was divided into two modes of operation for three reasons. First, complex deformations such as provided by Draper Laboratories[1] can take a considerable amount of computer resources to process. Secondly, this type of data needs to be created only once and then can be stored on a tape or a disk. By providing the off-line capability, a deformed set of element locations can be generated and stored for future use. Thirdly, the off-line capability allows for easier reformatting of additional distortion data obtained from technology contractors in the future.

Therefore, SARF provides the on-line structural model for the (everyday) majority of design evaluations with the off-line model adding the necessary complexity for modeling empirical data.

2.3.4.1 On-Line Deformation Model

The on-line structural deformation model allows the user to displace elements in the array either randomly or systematically. The random displacements can assume one of three probability density functions: uniform, Gaussian, or Rayleigh. The user simply selects the desired mean and standard deviation for each of the three location coordinates (x,y,z) and SARF perturbs each element according to the input statistics.

The systematic deformations provide element displacement (for the entire aperture) according to the following equations:

$$dx = a_0 + a_1x + a_2y + a_3xy + a_4x^2 + a_5y^2$$

$$dy = b_0 + b_1x + b_2y + b_3xy + b_4x^2 + b_5y^2$$

$$dz = c_0 + c_1x + c_2y + c_3xy + c_4x^2 + c_5y^2$$

---

[1] F. Ayer, op. cit.

where dx,dy,dz = the differential between the nominal and the perturbed location in the x,y,z directions, respectively

a_n, b_n, c_n = the user selected coefficients for the desired deformation

As an example, assume the user wishes to linearly tilt the aperture by some angle α.

Then, as shown in Fig. 2.83

$$dx = -x_i(1 - \cos \alpha)$$

$$dz = x_i \sin \alpha$$

Therefore, the coefficients in the deformation equations would be defined by:

$$a_1 = 1 - \cos \alpha$$

$$c_1 = \sin \alpha$$

and the remaining coefficients would all equal zero.

Therefore, the on-line model allows the user to model relatively complex structural deformations which can be composed of systematic and random distortions. However, if the antenna designer has "real" data obtained through a thermal analysis or some empirical process, the off-line structural model is needed.

2.3.4.2 Off-Line Deformation Model

The off-line deformation model has two major modes of operation. The first provides the capability of interpolating the proper element

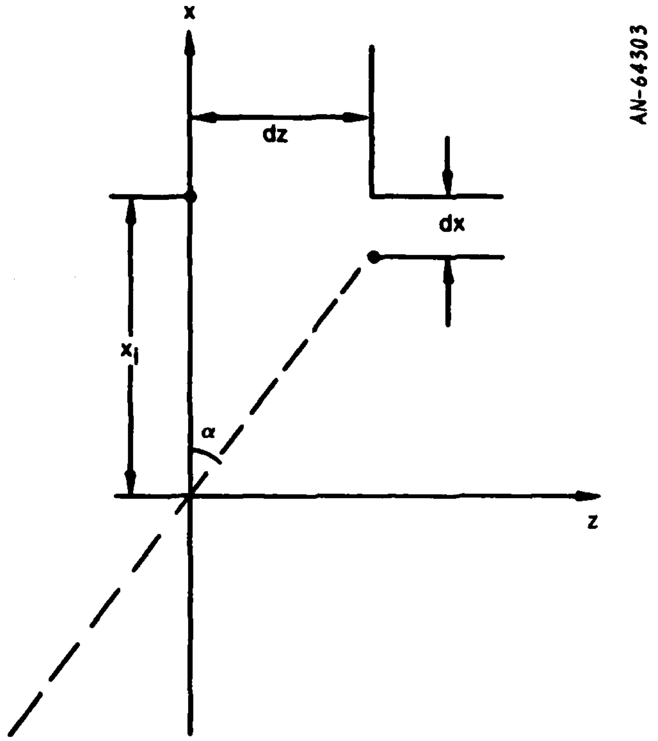

Figure 2.83. Linear Tilt Example

displacement from discrete structural deformation data. The second method allows the user to deform each "gore"[1] of the aperture according to quadratic equations in all three dimensions.

The first mode of operation is depicted in Fig. 2.84. The diagram shows how SARF manipulates the data files to obtain the correct displacements in the element locations. First the on-line program is used to create the ideal or nominal element locations, which are stored in the element location file. Now, the off-line program G2 or G3 is used

---

[1] "Gore" in this context implies a fundamental piece of the antenna such as a pie-shaped wedge used in the Grumman design. It can, however, be of any shape such as a rectangle or square, but the entire aperture must be described by all of the "gores."

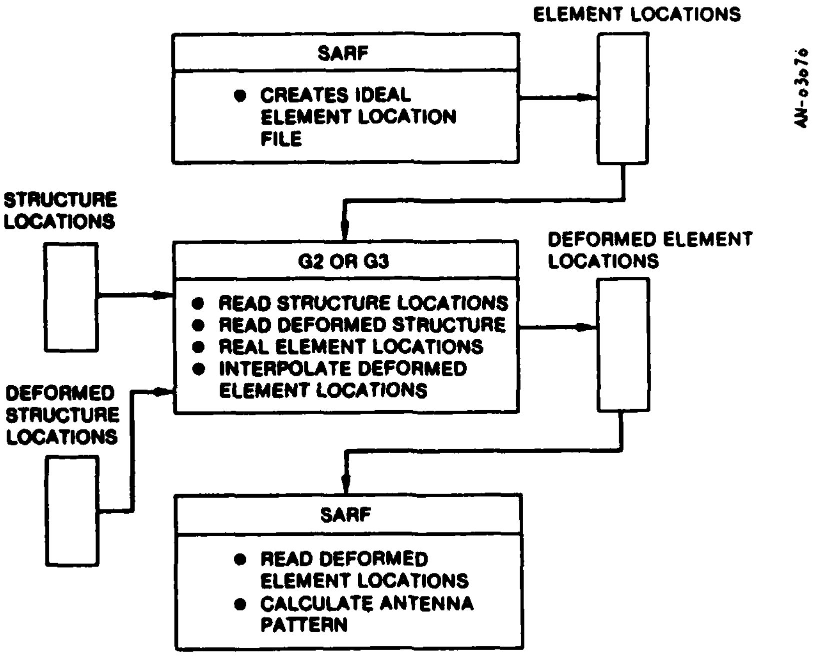

Figure 2.84. Offline Structural Deformation Data Flow (Empirical Data)

to interpolate the element displacements as follows.[1] The three nearest non-colinear structural locations are found for the element location of interest. Next, the three corresponding deformed points are located. The element in question is displaced to the plane determined by the three structural deformation points through a linear interpolation. (The details of the mathematics and the algorithm for this interpolation are documented in Appendix A.) Once the interpolation is complete, G2 writes the coordinates of the displaced element to a file which is identical in format to the element location file. This new file is now compatible with the on-line simulation and the antenna pattern associated with it can now be evaluated.

---

[1] The off-line model consists of two interpolation programs, G2 and G3. G2 performs a two-dimensional interpolation, while G3 performs an interpolation in three dimensions. The two are essentially interchangeable in structure. The use of G2 rather than G3 depends on the deformation data.

If the user needs to model localized systematic deformations, he merely needs to utilize another off-line pre-processor prior to using G2 or G3. This additional pre-processor is named DEFORM and it operates in the following manner (as shown in Fig. 2.85). DEFORM reads the ideal element location file along with the desired structural locations and creates a file of structural deformations according to the input coefficients (for the deformation equations) which are defined by the user. These equations are identical to those described in subsection 2.3.4.1 except that each "gore" is defined by its own unique set of equations.

Once DEFORM has written a structural deformation file, G2 (or G3) can perform the desired interpolation on the element location file. As before, the deformed element location file can be used in the on-line program to determine the far-field pattern.

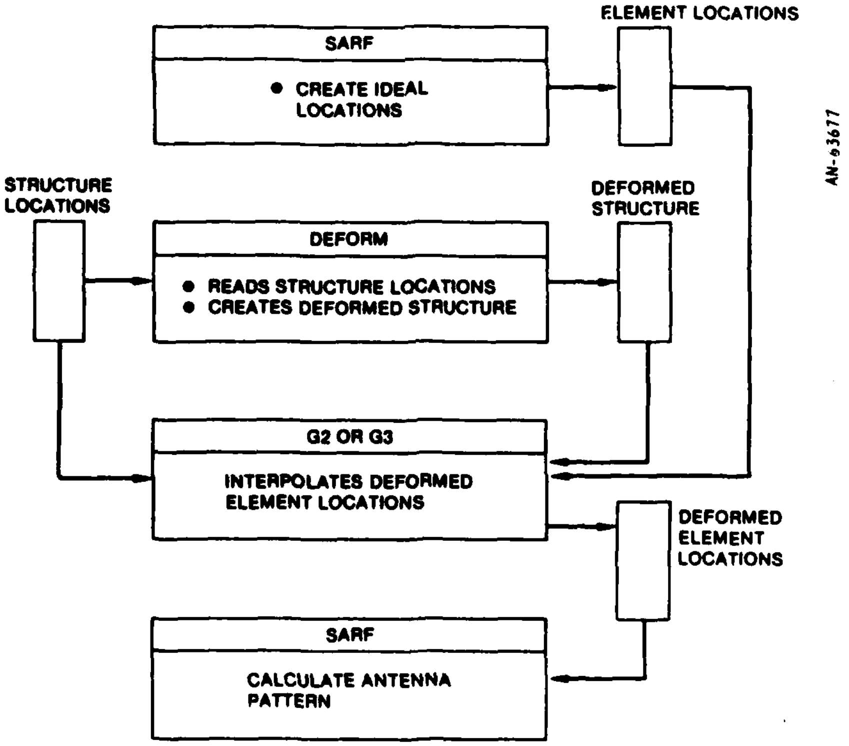

Figure 2.85. Offline Systematic Distortions

One further capability, not yet mentioned, is available to the user in the off-line mode, which consists of manual modification of the element location file. This can be done simply (but tediously) by searching the location file for the elements of interest and changing their current coordinates to the desired deformed values. Obviously, this technique is useful only for a small number of element displacements; however, it is a capability that should not be overlooked for certain types of evaluation.

2.3.5 Computational Techniques

The two computational techniques employed by SARF are: the efficient technique, which utilizes a fast Fourier transform, and the brute-force technique, which implements the far-field computation directly and thereby exactly (within machine accuracy and far-field assumptions).

This section discusses the salient features of each of these two techniques.

2.3.5.1 Efficient Technique (FFT)

The heart of the efficient technique is the two-dimensional FFT which was adopted from the Parametric Antenna Analysis Simulation (PAAS).[1] The FFT provides a very fast computation of the approximate far-field pattern of a phased array antenna. This difference in computational speed is depicted in Fig. 2.86, which shows the difference in central processing time between the efficient technique and the brute-force technique (both with isotropic element patterns). For large arrays, this difference can approach four orders of magnitude.

In addition to its speed, the PAAS FFT is structured to allow partial processing of the output array. That is, a piece of the far-field

---

[1] R.J. Hancock, Parametric Antenna Analysis Software, Simulation Technology, Inc., December 1978.

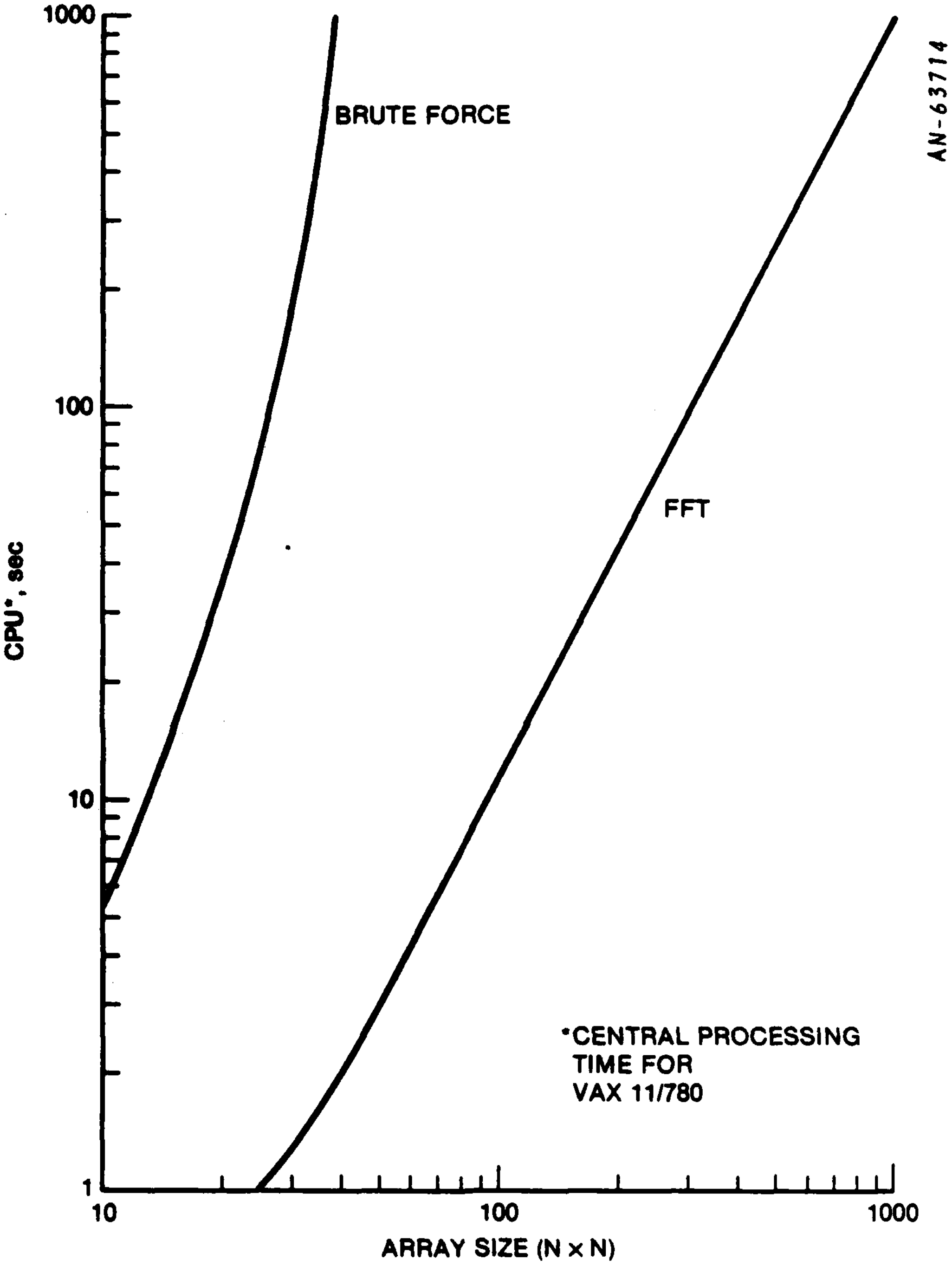

Figure 2.86. Computation Time, FFT Versus Brute-Force

pattern can be calculated without transforming the whole FFT array, thus saving computational time and storage requirements.

Despite its great speed and flexibility, the FFT has two disadvantages for the calculation of antenna patterns. First it does not, in general, give an exact answer for the pattern unless the elements of the array lie on a rectangular planar grid. Secondly, it does not provide the pattern at every point in space but is limited to points located on a rectangular plane in sine space ($T_x - T_y$).

Both of these drawbacks can be overcome by the prudent designer. The inaccuracies due to the elements not lying on a rectangular planar grid can be compensated for with good results as documented in Sec. 2.2. Also, by an appropriate selection of the output grid points, the resolution of the FFT can be small enough that a linear interpolation will provide an excellent fit to the true pattern at any point in space.

Therefore, the efficient technique can provide a good approximation for nearly every case desirable to the antenna designer and at a considerable saving in computational resources compared to other techniques.

2.3.5.2 Brute-Force Technique

The brute-force technique is simply what its name implies--a brute force computation of the equation:

$$\bar{E}(\bar{T}) = \sum_{\ell} F_{\ell} \sum_{nm} I_{nm} \exp\{jK(\bar{\rho}\cdot\bar{T})\}$$

where $\bar{E}$ = the electric field vector

F_{ℓ} = the nominal plus deviated element patterns

I_{nm} = the illumination of the nmth element

$K = 2\pi/\text{wavelength}$

$\bar{\rho}$ = the location vector

$\bar{T}$ = the sine space vector

The brute-force technique provides three important advantages:

1. It provides an exact pattern calculation.
2. Since the algorithm uses double precision arithmetic, the dynamic range is increased from 120 dB to 140 dB.
3. It provides an internal check on the efficient technique.

The brute-force computation has only one drawback--but this can be a very major drawback--speed. As was shown in Fig. 2.86, the brute-force algorithm is typically three orders of magnitude slower than the efficient technique. Hence, for most applications, it is prohibitively slow. However, if the designer wishes only to obtain a few pattern points, then the speed of the brute-force technique is more than sufficient to provide the desired data.

2.3.5.3 Computational Techniques Block Diagram

Figure 2.87 shows a block diagram of the two computational techniques used in SARF. The efficient technique is shown on the left-hand side of the figure, while the brute-force technique is shown on the right.

The efficient technique implements the following path in the block diagram. First, the illumination and location files are created and modified by the desired algorithms. Next, the illumination file is modified to provide approximations to the deformations (as described in Sec. 2.2). The FFT grid is created and the array is fast Fourier transformed. Now the output of the FFT is multiplied by the nominal element pattern. The resultant is added to both the random and major element

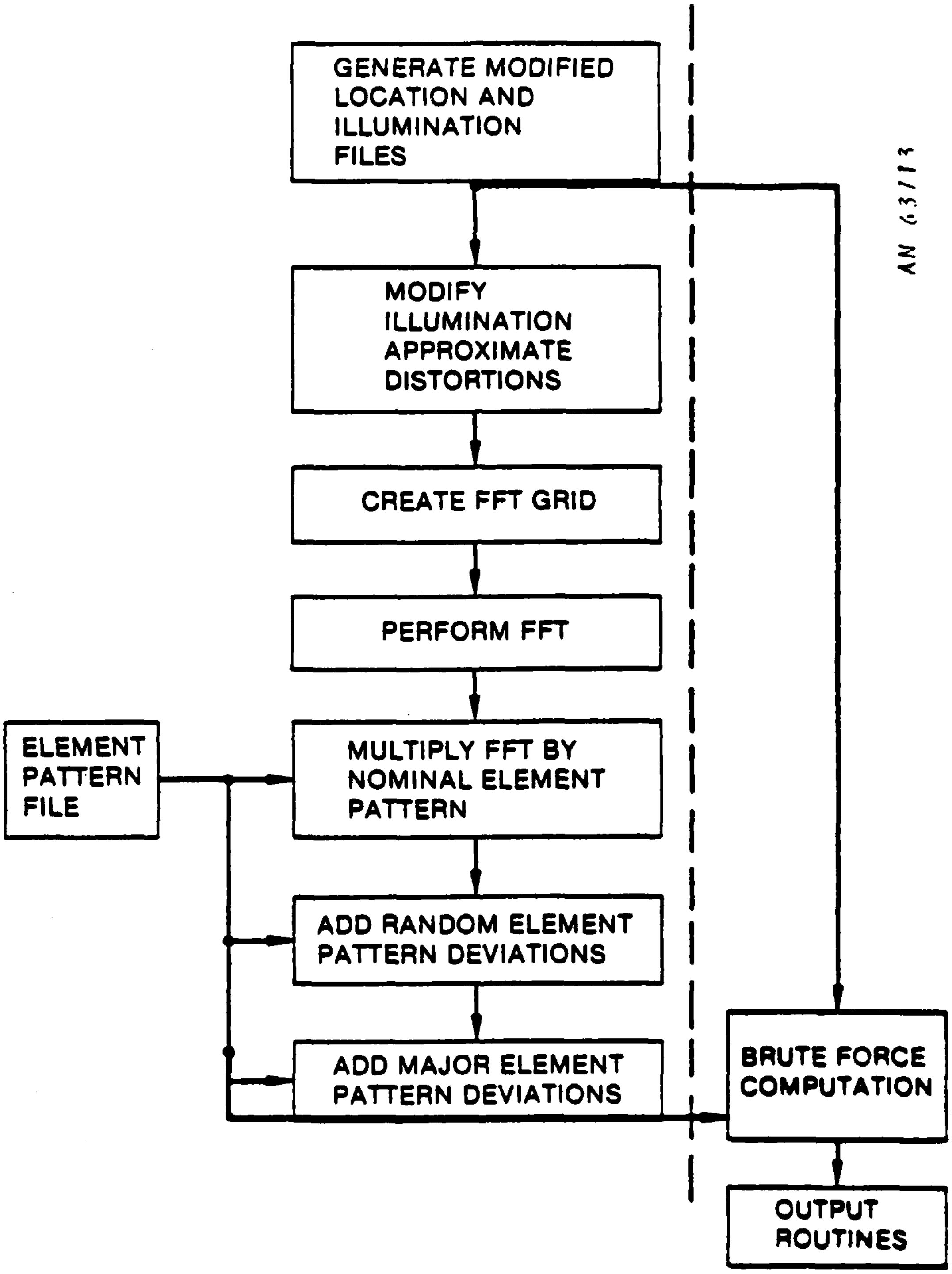

Figure 2.87. Computational Techniques Block Diagram

pattern deviations and the output of this summation is then available for the output routine.

The brute-force technique functions as follows: First the same illumination and location files serve as two of the inputs to the brute-force computation subroutine. Also, the element pattern file provides the same information to the brute-force algorithm as was supplied to the efficient technique. Therefore, all inputs are identical for both techniques. Once the inputs are set up for the brute-force routine, it can "grind away" on the answer. The output is then also available for the SARF output routine.

The combination of the two techniques allows the antenna designer the capability of calculating an approximate antenna pattern for the entire $T_x - T_y$ plane. He can also verify that the approximations are sufficiently accurate by calculating a few scattered points using the brute-force technique. Therefore, by using discretion, the designer can obtain the optimum selection of computer resources, versus the amount and accuracy needed.

2.4 CONCLUSIONS

The SARF simulation has been developed to meet the requirements of broad scope, flexibility, and modular adaptability, to meet the needs of the RADC space-based radar program. Results have been drawn from virtually all of the prior technology programs to take full advantage of existing computer models, analysis, and measurements. The validation procedure has been designed to exercise the code from the program module level, to very complex full scale models, and to utilize available analytical, numerical, and experimental data for comparison.

Initial applications demonstrate the broad range of applicability of the simulation, and have provided several interesting results, which would be difficult or impossible to obtain without the simulation. A number of fruitful future applications have been discussed in the Introduction (Sec. 2.1), and we believe that the simulation is ready to be utilized for design optimization, concept evaluation, and interaction with experimental programs in support of the RADC SBR programs.

APPENDIX A

ARRAY ANALYSIS AND SOFTWARE DEVELOPMENT (FROM INTERIM REPORT)

A.1 ARRAY ANALYSIS

We begin the analysis with an exact, general equation. Let the field radiated by the nmth source be $\overline{F}_{nm}(\overline{R})$.[1] The source excitation is I_{nm}, and the location is ρ_{nm}. These are the basic array data sets shown in Fig. 2.1. The coordinate system is shown in Fig. A.1. The source field is defined under the conditions that the excitation I_{nm} of the nmth source is unity, and the excitation of all other sources is zero. Then, by superposition, the field radiated by the full array of sources is

$$\overline{E}(\overline{R}) = \sum_{nm} I_{nm}\overline{F}_{nm}(\overline{R}) \tag{A.1}$$

A.1.1 Far-Field Approximations

Although Eq. A.1 appears simple, $\overline{F}_{nm}(\overline{R})$ is a very complicated function if all near-field effects are included. This equation may be greatly simplified using the conventional far-field approximations.[2] The first approximation (for the source patterns) assumes that the field point P is many wavelengths away from the source, so that we can use the far-field form

$$\overline{F}_{nm}(\overline{R}) \cong \overline{F}_{nm}(T_x,T_y)\,\frac{e^{-jkr_{nm}}}{r_{nm}} \tag{A.2}$$

---

[1] A source may be an array element, a segment of an element, or an induced current in an object blocking the aperture.

[2] S. Silver, Microwave Antenna Theory and Design, McGraw-Hill, 1949.

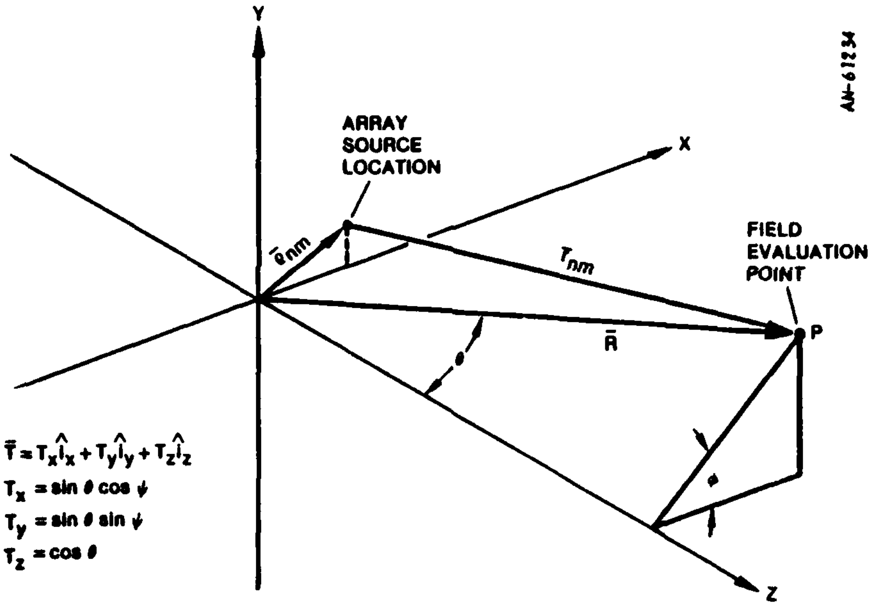

Figure A.1. SARF Simulation Coordinate System

---

where $j = \sqrt{-1}$

$k = 2\pi/\lambda$

λ = wavelength

T_x, T_y = components of a sine space vector defined in Fig. A.1

r_{nm} = the distance from the source to the field point

This equation basically makes the approximation $1 - j/kr_{nm} \cong 1$. For $\lambda = 0.1$ m, and a distance 10 m away from the source, this introduces a negligible phase error of less than 0.1 degree, and an even less significant amplitude error. This is an excellent approximation except under extreme near-field conditions.

The second far-field approximation assumes the conventional "$2D^2/\lambda$" for the overall array, where D is the maximum dimension of the array aperture, and concerns r_{nm}. The exact equation is

$$r_{nm} = R\left[1 - 2(\bar{\rho}_{nm} \cdot \bar{T})/R + (\rho_{nm}/R)^2\right]^{1/2} \tag{A.3}$$

which can be approximated by

$$r_{nm} \cong R\left[1 - (\bar{\rho}_{nm} \cdot \bar{T})/R\right] \tag{A.4}$$

It can be shown that if $r_{nm} > 2D^2/\lambda$, where $D \geq 2\rho_{nm}$, then the error in the approximation is less than $\lambda/16$. This introduces a maximum phase error of 22.5 degrees in Eq. A.2. For example, for an array diameter $D = 20$ m, and $\lambda = 0.1$ m, the "far field" distance $2D^2/\lambda = 8$ km. This is much smaller than a typical SBR operating range, and at a representative range of 1,600 km, the maximum phase error is 0.1 degree. Therefore, Eq. A.4 is an excellent approximation under typical operating conditions, but even at a "far-field" range, the 22.5 degree phase error is <u>not</u> negligible.

For the $1/r_{nm}$ amplitude factor the approximation is $r_{nm} \cong R$, which would introduce an error less than 0.05 dB at $r_{nm} > 100D$ (2 km for the example above). This almost always introduces negligible error compared to the prior approximation.

The end result of these approximations is that Eq. A.1 can be written in the far-field form

$$\bar{E}(T_x, T_y) = \frac{e^{-jkR}}{R} \sum_{nm} I_{nm} \bar{F}_{nm}(T_x, T_y) e^{jk\bar{\rho}_{nm} \cdot \bar{T}} \tag{A.5}$$

For the typical SBR deployments, the difference between Eqs. A.5 and A.1 will be negligible, and Eq. A.5 is taken as the basic equation to be evaluated by the SARF simulation. For testing purposes, where the range may be much smaller, the far-field approximation may introduce significant errors, and a different or modified simulation may be required.

A.1.2 *Evaluation of the Far-Field Equation*

Even with the far-field simplifications, Eq. A.5 is impractical for the analysis of large arrays. For 10^5 elements, a Digital Equipment VAX-11/780 requires about 4 minutes of computer time per output point to evaluate this equation.[1] Since the number of output points may range up to 10^6, this is prohibitive.

The approaches considered to alleviate this situation include:

1. A faster computer
2. More efficient numerical techniques
3. Fewer output points
4. Alternative analyses

At this time, using a faster computer is being held in reserve, and it is hoped that it will not be required. All of the remaining approaches are incorporated in the current program development plan. Efficient numerical techniques and alternative analyses are discussed below. Preliminary work has been done on reducing the number of output points, but is in a very early stage, and will be described in a future report.

A.1.2.1 Efficient Numerical Techniques

Two candidate techniques have been considered for efficiently evaluating Eq. A.5: (1) a "cell model" similar to the one employed by

---

[1] This is the double precision vector version, with full I/O, implemented in the present code as described in Sec. A.2. A bare-bones evaluation would be about 20 times faster, but still prohibitive.

Atlantic Research Corp. (ARC),[1] and (2) the fast-Fourier transform (FFT) such as developed by Hancock and Fricke under a prior RADC contract.[2] The FFT technique is preferred for incorporation into the SARF simulation.

A.1.2.1.1 Cell Model

The cell model technique involves three steps: (1) the array aperture, containing up to 10^6 elements, is divided into a few hundred cells; (2) the pattern of each cell is calculated by a fast technique--e.g., an analytic equation; and (3) the pattern results for the cells are superimposed. In the ARC model the incident field amplitude and phase distribution for each cell is approximated by a series of plane waves; for a single plane wave the amplitude is uniform and the phase varies linearly. As more plane waves are added, more complex distributions can be modeled.

For the purposes of the SARF simulation, the critical question is how the cell model impacts the antenna pattern. To evaluate this, a series of test cases was run with various models of the amplitude distribution across a cell. Phase was not varied, and was always assumed to be uniform. The selected nominal test case was a -70 dB circular Taylor distribution, to clearly illustrate the effect on low sidelobes. Nominally 8 radial rings were assumed. Each radial ring would normally be subdivided into azimuthal divisions, leading to a total of about 200 cells. However, in this case circular symmetry is assumed, and the number of azimuthal divisions is irrelevant.

Figure A.2 illustrates the antenna pattern resulting from the cell model. The reference perfect case is shown in Fig. A.2a. If a uniform amplitude model across the cell is used, corresponding to a single plane

---

[1] H.K. Schuman, D.R. Pflug, and L.D. Thompson, op. cit.

[2] R.J. Hancock and J.R. Fricke, op. cit.

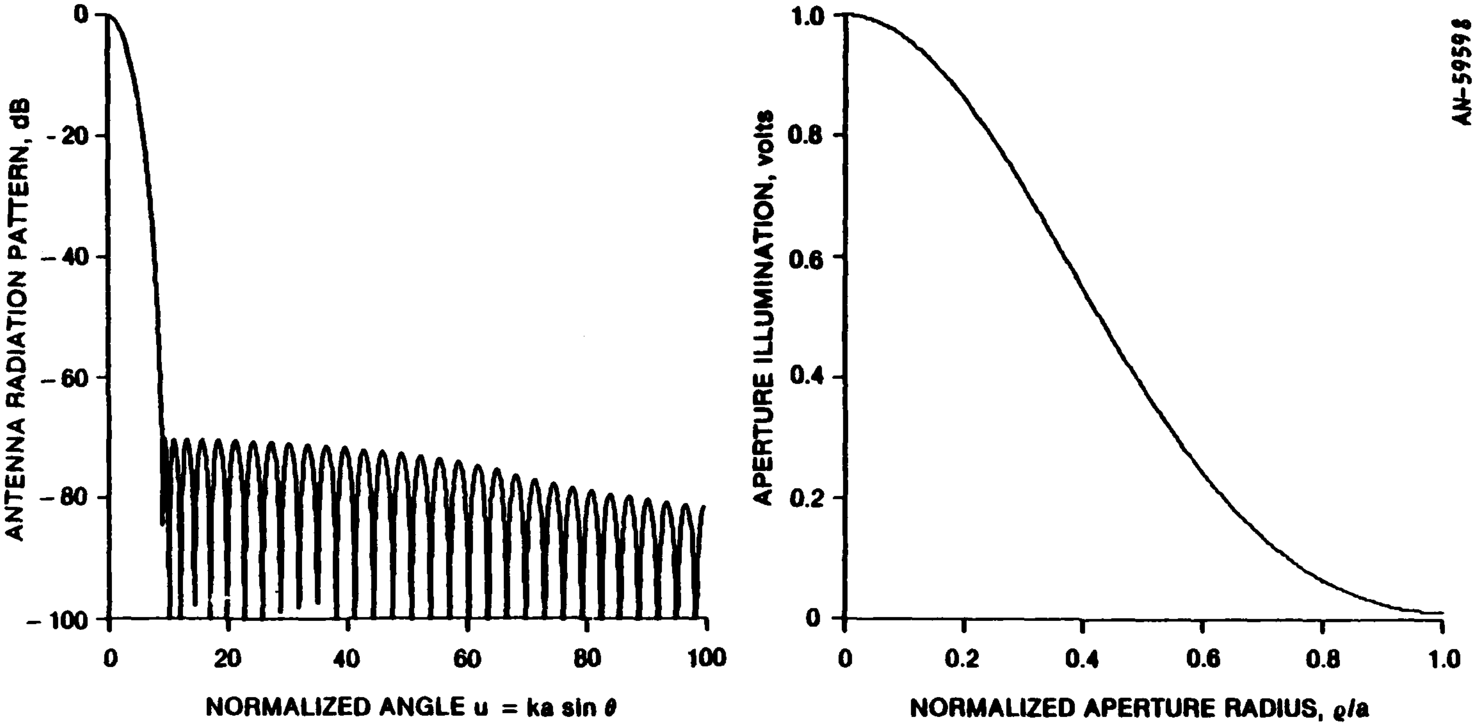

(a) Reference Perfect Case

Figure A.2. Models of 70-dB Circular Taylor Distribution

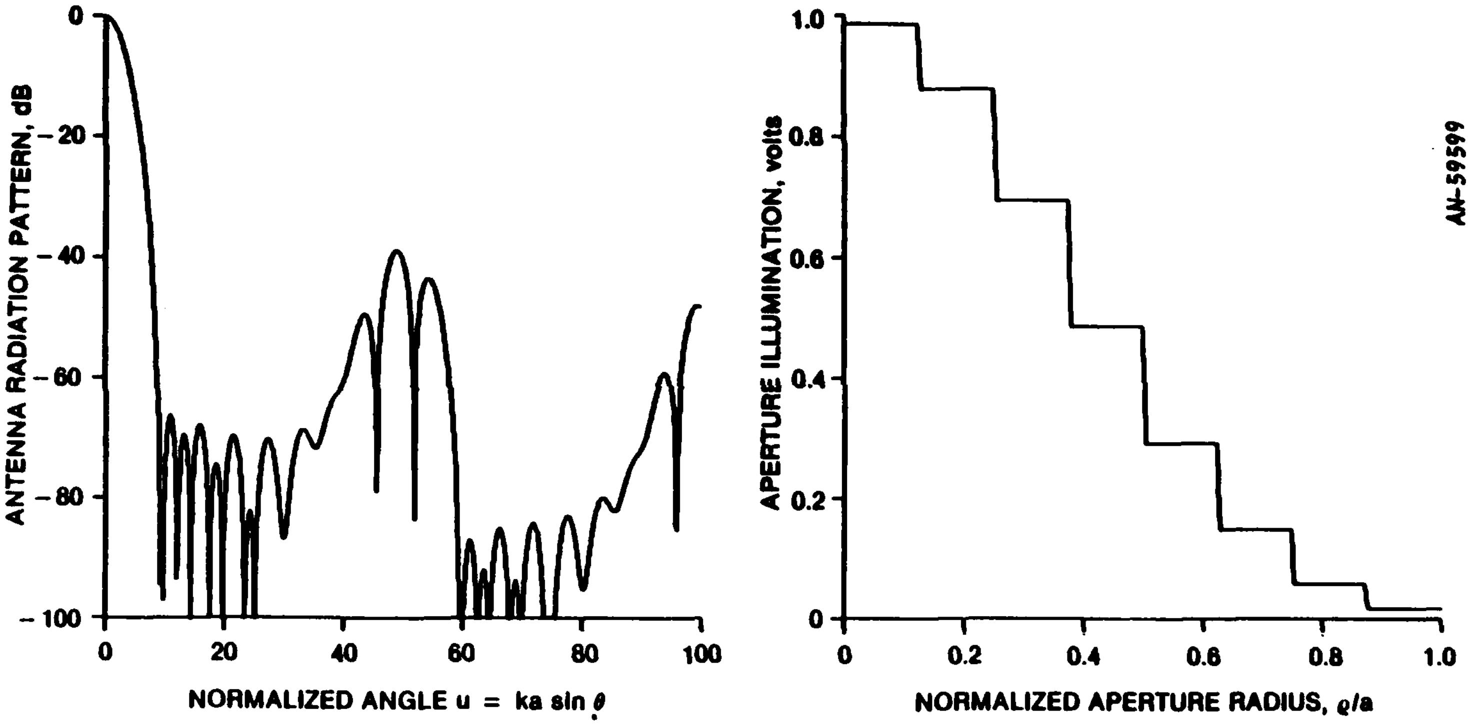

(b) Eight Cells, Step Amplitude

Figure A.2 (Cont)

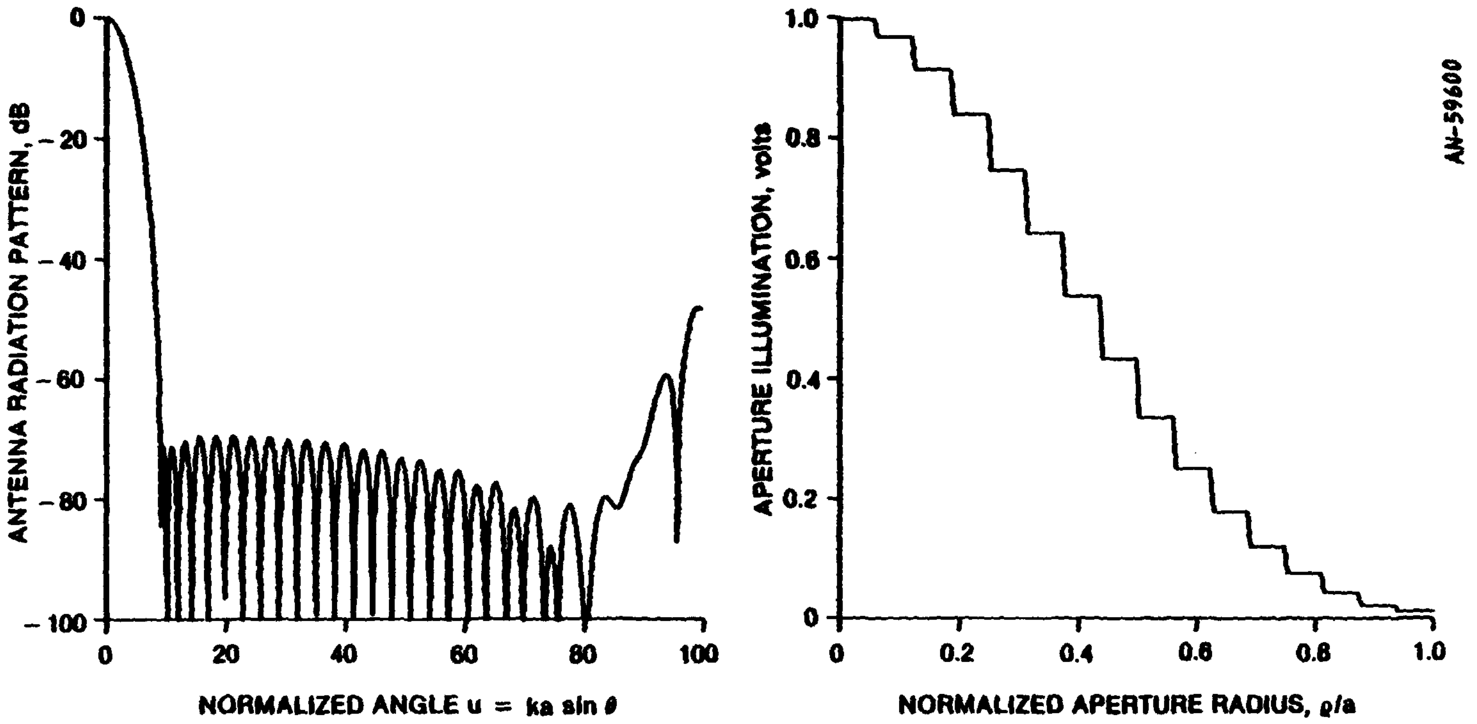

(c) 16 Cells, Step Amplitude

Figure A.2 (Cont.)

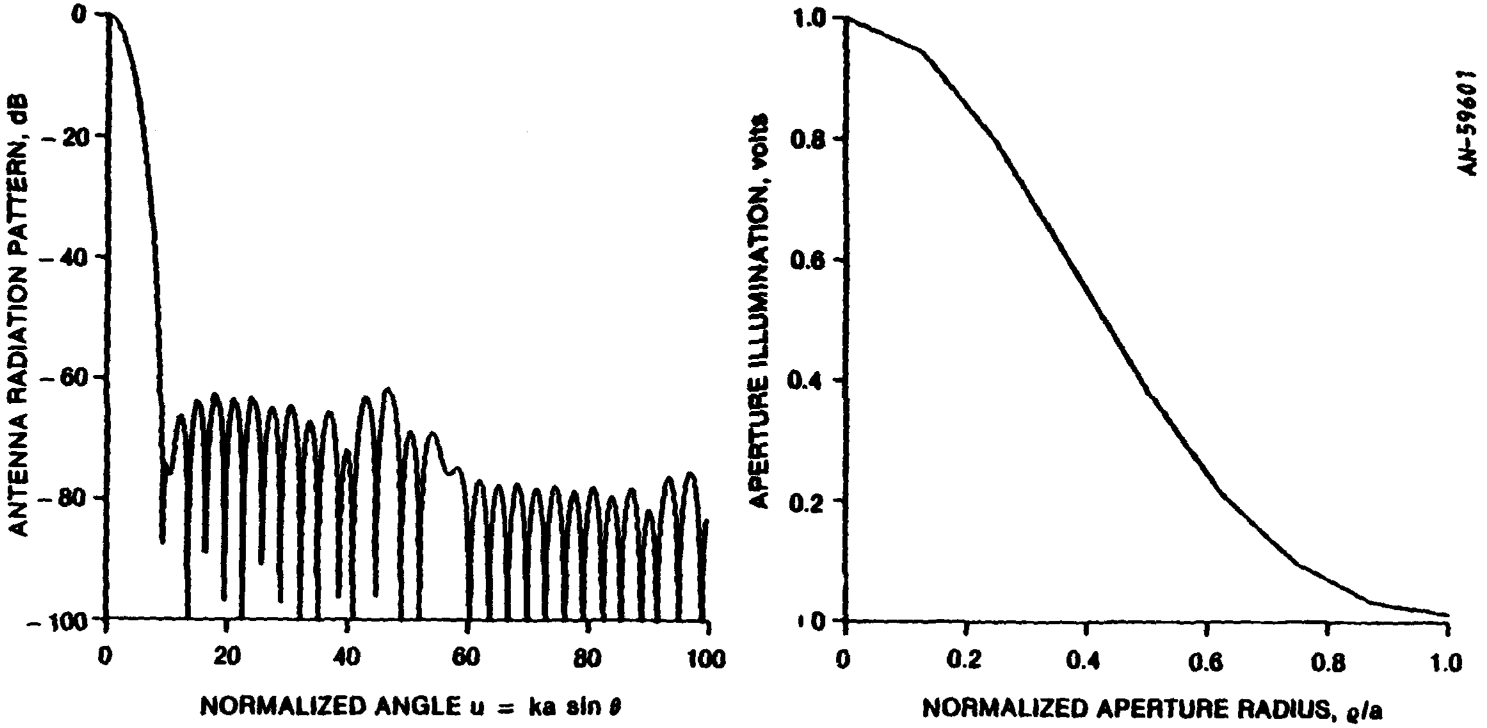

(d) 8 Cells, Linear Amplitude

Figure A.2 (Cont.)

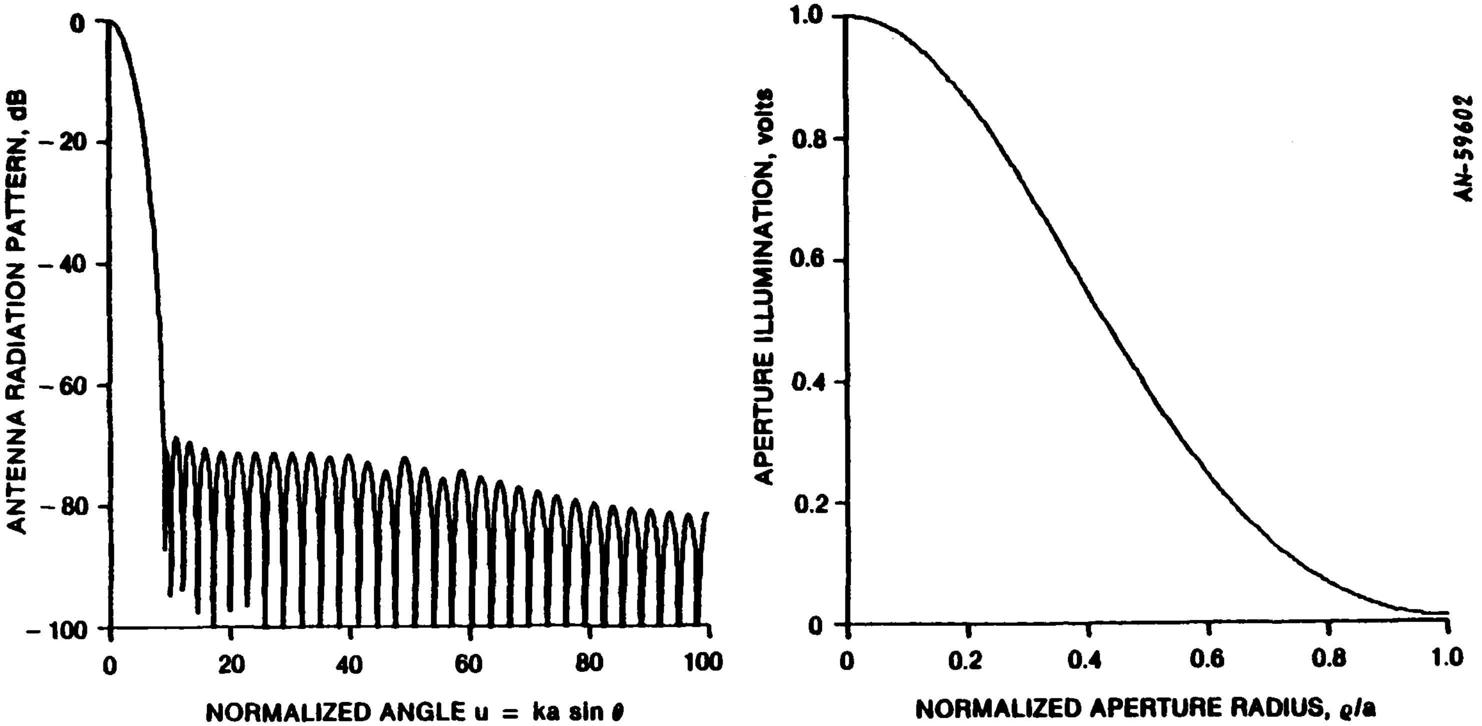

(e) Eight Cells, Quadratic Amplitude

Figure A.2 (Concl.)

wave, Fig. A.2b results--which is clearly unacceptable. Doubling the number of radial rings to 16 helps, as shown in Fig. A.2c, but is still unacceptable. Alternatively, the amplitude model can be improved. Results for a linear amplitude model and a quadratic amplitude model are shown in Fig. A.2d and A.2e, respectively. Clearly, at least a quadratic model is required.

The cell model is generally inappropriate for fine-grain variations--e.g., between adjacent elements, since many more terms would be required to represent the field. Combined with the sensitivity illustrated in Fig. A.2, it was decided to pursue the FFT alternative instead.

A.1.2.1.2 Fast-Fourier Transform

The FFT is a well-known technique that is dramatically faster than the brute-force summation of Eq. A.5. In addition to this, the FFT has been applied to the large array problem by Hancock and Fricke under a previous RADC contract, so a considerable amount of useful software is available. This makes the FFT technique highly attractive since it is not only numerically efficient, but also efficient in the use of contractual resources.

The primary problem is that Eq. A.5 is not quite in the form solvable by a FFT. The approach taken by Hancock and Fricke[1] was to approximate Eq. A.5 with an equation in the form of a FFT, by assuming

$$\overline{F}_{nm}(T_x,T_y) \cong \text{a constant scalar} \qquad \text{(A.6)}$$

$$\bar{\rho}_{nm} \cong n\, d_x\, \hat{i}_x + m\, d_y\, \hat{i}_y \qquad \text{(A.7)}$$

---

[1] R.J. Hancock and J.R. Fricke, op. cit.

The FFT grid spacings d_x and d_y are taken smaller than the spacing between array elements, and the array element location approximated by the nearest FFT grid point.

Here we take an alternative approach: To avoid the error introduced by this approximation, we rearrange Eq. A.5 to be the sum of three terms, one of which is in the form of a FFT, and the other two which can be considered to be perturbations.

To accomplish this we define

$$\bar{F}_{nm}(T_x,T_y) \equiv \bar{F}_o(T_x,T_y) + \bar{f}_{nm}(T_x,T_y) \tag{A.8}$$

$$\bar{\rho}_{nm} \equiv n\, d_x\, \hat{i}_x + m\, d_y\, \hat{i}_y + \bar{\delta}_{nm} \tag{A.9}$$

$\bar{F}_o(T_x,T_y)$ is the nominal source radiation pattern, and $\bar{f}_{nm}(T_x,T_y)$ is defined to be the <u>deviation</u> of the <u>nmth</u> source pattern from the nominal, due to failures, manufacturing errors, edge effects, etc. In cases of interest $\bar{f}_{nm}(T_x,T_y)$ will be much smaller than $\bar{F}_o(T_x,T_y)$, except for catastrophic failures, which will be restricted to a relatively small number of elements (if not, the array is not functional).

The location deviations $\bar{\delta}_{nm}$ are defined with respect to a rectangular grid rather than the nominal element locations, so they include both structural deformations, and the difference between the grid location and the nominal element location. However, we still expect that $\bar{\delta}_{nm}$ will be smaller than d_x or d_y.

Using the definitions above, Eq. A.5 becomes

$$\overline{E}(T_x,T_y) = \frac{e^{-jkR}}{R}\sum_{nm} I_{nm}\left[\overline{F}_o(T_x,T_y) + \overline{f}_{nm}(T_x,T_y)\right]$$

$$\cdot e^{jk[n\, d_x\, T_x + m\, d_y\, T_y]}\, e^{jk\overline{\delta}_{nm}\cdot\overline{T}} \tag{A.10}$$

This may be rearranged into three terms

$$\overline{E}(T_x,T_y) = \frac{e^{-jkR}}{R}\left\{\overline{E}_1(T_x,T_y) + \overline{E}_2(T_x,T_y) + \overline{E}_3(T_x,T_y)\right\} \tag{A.11}$$

where

$$\overline{E}_1(T_x,T_y) \equiv \overline{F}_o(T_x,T_y)\sum_{nm} I_{nm} e^{jk[n\, d_x\, T_x + m\, d_y\, T_y]} \tag{A.12}$$

$$\overline{E}_2(T_x,T_y) \equiv \sum_{nm} I_{nm}\overline{f}_{nm}(T_x,T_y) e^{jk\overline{\delta}_{nm}\cdot\overline{T}}\, e^{jk[n\, d_x\, T_x + m\, d_y\, T_y]} \tag{A.13}$$

$$\overline{E}_3(T_x,T_y) \equiv \overline{F}_o(T_x,T_y)\sum_{nm} I_{nm}\left(e^{jk\overline{\delta}_{nm}\cdot\overline{T}} - 1\right) e^{jk[n\, d_x\, T_x + m\, d_y\, T_y]} \tag{A.14}$$

This rearrangement of Eq. A.5 is (at this point) exact, and no additional approximations have been made. The advantage gained is that the dominant term is $\overline{E}_1$, and the summation factor of Eq. A.12 is precisely in the form desired for a FFT, which can be evaluated using the PAAS software. The additional factor $\overline{F}_o(T_x,T_y)$ in Eq. A.12 adds the effect of the nominal source pattern, including polarization, and only involves a multiplication for each output point.

The two remaining terms, $\overline{E}_2$ and $\overline{E}_3$, are complicated, but are always small compared to $\overline{E}_1$ in cases of interest. Therefore, it is possible to evaluate these two equations using approximate techniques, and still achieve high accuracy in the overall result. For example, if $\overline{E}_2$ is always 40 dB or more below $\overline{E}_1$, and the calculation for $\overline{E}_2$ is accurate within ±1 dB, the total field will be accurate within ±0.01 dB, which is totally satisfactory for the intended application (note that the brute-force technique is used in the vicinity of deep nulls).

A.1.2.1.3 Pattern Deviation Term

Pattern deviations will be subdivided into two categories: (1) catastrophic or other substantial deviations, and (2) small widespread deviations. Category 1 covers the deployment failure of pop-up elements, meteorite penetration of a membrane, severe mutual coupling edge effects, etc. Category 2 covers manufacturing tolerances, variations in feedline deployments, etc. The basic assumptions made are that category 1 involves at most a few thousand elements, and that category 2 involves random errors that may be analyzed statistically. Category 1 can then be handled with a brute-force technique, and category 2 handled analytically, avoiding excessive computer time.

Category 1: Large Systematic Deviations

The category 1 deviations are evaluated directly by Eq. A.13, the only change being that the summation ranges over a limited number of elements.

Category 2: Small Random Deviations

The category 2 deviations require further analysis. The deviations are assumed to be statistically characterized by

$$EV\{\overline{f}_{nm}(T_x,T_y)\} = 0 \qquad \text{(A.15a)}$$

$$EV\left\{\bar{f}_{nm}(T_{1x},T_{1y})\cdot\bar{f}^{*}_{ij}(T_{2x},T_{2y})\right\} = \begin{cases} 0 & i \neq n \text{ or } j \neq m \\ |\bar{\sigma}_f(T_{1x},T_{1y},T_{2x},T_{2y})|^2 & \begin{matrix} i = n \\ \text{and} \\ j = m \end{matrix} \end{cases} \qquad \text{(A.15b)}$$

where EV denotes expected value,[1] * denotes the complex conjugate, and the subscripts 1 and 2 correspond to two field point directions $\bar{T}_1$ and $\bar{T}_2$. Then assuming all other variables in Eq. A.13 are deterministic

$$EV\{\bar{E}_2(T_x,T_y)\} = 0 \qquad \text{(A.16a)}$$

$$EV\left\{\bar{E}_2(T_{1x},T_{1y})\cdot\bar{E}^{*}_2(T_{2x},T_{2y})\right\} = |\bar{\sigma}_f(T_{1x},T_{1y},T_{2x},T_{2y})|^2 \sum_{nm} |I_{nm}|^2 e^{jk\bar{\rho}_{nm}\cdot(\bar{T}_1-\bar{T}_2)}$$

$$\text{(A.16b)}$$

This equation is very similar to the array pattern equation, with a peak at $\bar{T}_1 = \bar{T}_2$, and sidelobes and nulls roughly similar to the array pattern.

Since the element deviation pattern $\bar{f}_{nm}(T_x,T_y)$ physically arises from a small source, like the typical element pattern factor, it will be highly correlated (slowly varying) over a substantial increment in T_x or T_y ; i.e., $\bar{\sigma}(T_{1x},T_{1y},T_{2x},T_{2y})$ will be nearly constant for small differences $T_{1x} - T_{2x}$ or $T_{1y} - T_{2y}$. Conversely, the summation term in Eq. A.16b, corresponding to the array pattern factor, will change very rapidly for small differences between $\bar{T}_1$ and $\bar{T}_2$. Therefore,

---

[1] A good general reference for the statistical analysis applied here is A. Papoulis, Probability, Random Variables, and Stochastic Processes, McGraw-Hill, 1965.

AD-A133 734 RF SYSTEMS IN SPACE VOLUME I SPACE ANTENNAS FREQUENCY 3/3
(SARF) SIMULATION(U) GENERAL RESEARCH CORP SANTA
BARBARA CA A C LUDWIG ET AL. APR 83
UNCLASSIFIED RADC-TR-83-91-VOL-1 F30602-81-C-0119 F/G 17/9 NL

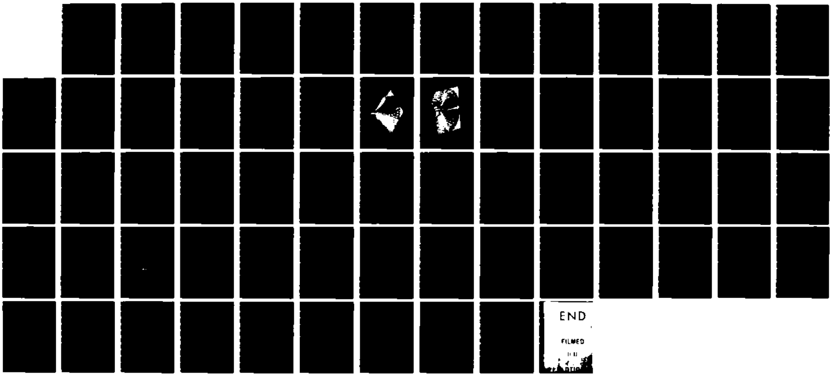

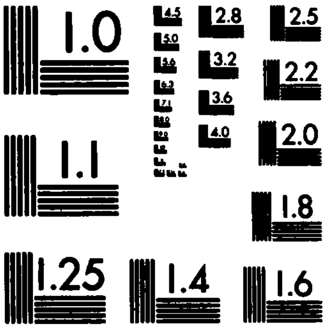

MICROCOPY RESOLUTION TEST CHART
NATIONAL BUREAU OF STANDARDS-1963-A

the behavior of the summation term will totally dominate, and we can assume

$$|\bar{\sigma}_f(T_{1x},T_{1y},T_{2x},T_{2y})|^2 \cong EV\{|\bar{f}_{nm}(T_{1x},T_{1y})|^2\} \qquad (A.17)$$

Referring to Eq. A.13, it is clear that the assumption that $\bar{f}_{nm}(T_x,T_y)$ is slowly varying means it is essentially interchangeable with I_{nm}. In other words, a random pattern and a deterministic excitation will provide the same result as a deterministic pattern and a random excitation. Therefore, we can model the random pattern deviation by[1]

$$\bar{E}_{2R}(T_x,T_y) = \bar{\sigma}_f(T_x,T_y)\sum_{nm} a_{nm}I_{nm}e^{jk\bar{\delta}\cdot\bar{T}}e^{jk[n\,d_x\,T_x+m\,d_y\,T_y]} \qquad (A.18)$$

where

$$|\bar{\sigma}_f(T_x,T_y)|^2 \equiv EV\{|\bar{f}_{nm}(T_x,T_y)|^2\} \qquad (A.19)$$

and a_{nm} is a complex random scalar satisfying

$$EV\{a_{nm}\} = 0 \qquad (A.20a)$$

$$EV\{a_{nm}a^*_{ij}\} = \begin{cases} 0 & \text{if } i \neq n \text{ or } j \neq m \\ 1 & \text{if } i = n \text{ and } j = m \end{cases} \qquad (A.20b)$$

The final step is to neglect $\bar{\delta}_{nm}$ in Eq. A.18 so it can be evaluated using the FFT. Note that the PAAS software always neglects $\bar{\delta}_{nm}$ and still gets good results, so neglecting it in this small remainder

---

[1] It is not difficult to replace this heuristic argument with a mathematical derivation, but it is omitted for brevity, and to focus on the underlying physics.

term, where the impact is much smaller, is acceptable. (This can be verified on a case-by-case basis using the brute force spot check.)

The bottom line is that random pattern effects are modeled by a Monte Carlo procedure, as follows:

1. A random number generator is used to provide a set of values a_{nm}, which are multiplied by I_{nm} to obtain a set of random excitations.
2. PAAS is used to compute the array pattern of these excitations.
3. The resulting pattern is multiplied by $\bar{\sigma}_f(T_x,T_y)$ (which is determined from input specifications on the pattern deviation), and superimposed with the other pattern terms.

A.1.2.1.4 Position Deviation Term

The position deviation term, Eq. A.14, poses a special problem. Like the pattern deviation term, it contains a factor within the summation that is a function of T_x and T_y so the FFT is not directly applicable. A procedure similar to that used for the pattern deviation term can be developed, but there is one new category of potential deviations, where the errors are significant, systematic, and widespread. For example, such errors can arise from a global warping of the surface. The plan is to generate errors of this type, and calculate their effects, before attempting to select a final method of calculation. This effort will be initiated in the immediate future.

A.1.3 Analysis Summary

The far-field equation (Eq. A.5) is the basic equation to be evaluated by the SARF simulation. This equation has been rearranged into three major terms: (1) a dominant term in a form solvable by a FFT, (2) a residual term due to deviations from a nominal element pattern, and (3) a residual term due to element location deviations from a planar rectangular grid. No approximations or errors are introduced by the rearrangement itself, but the purpose is to allow approximate methods to be applied to the residual terms while still maintaining high accuracy in the overall result.

Explicit equations have been developed for the evaluation of the dominant term and the residual pattern deviation term. Methods for evaluating the residual location deviation term will be developed in the immediate future.

A.2 SOFTWARE DEVELOPMENT

The SARF Simulation accurately models the RF performance of a large SBR system. The development of this simulation to date entailed three steps:

1. Development of the simulation core
2. Incorporation of PAAS and addition of new capabilities
3. Validation and computer timing tests

The development of the simulation core consisted of designing and implementing a main "driver" program to control subroutine execution as well as file manipulation and input/output functions. The core was developed to be compatible with PAAS and was designed with sufficient flexibility to readily allow assimilation of additional technology program results. The core also includes the new capability of an optional brute-force calculation technique. The majority of the core software is contained in the main program (EXPAAS).

PAAS incorporation primarily consisted of modifying the existing software so that it could be transported from the RADC computing system to the GRC computer. The details of this effort are described in Sec. A.2.1.

After PAAS was installed at GRC, various new analysis capabilities were added including:

- Additional aperture weighting functions
- Additional data reduction techniques
- Internal test capability
- "Brute-force" calculation
- Element pattern generation
- Polarization effects

These capabilities are discussed in Secs. A.2.2, A.2.3, and A.2.4.

Lastly, both validation and computer time tests were performed to ensure proper implementation of the software. These tests are explained in Secs. A.2.5 and A.2.6.

A.2.1 Incorporation of PAAS

The PAAS package allows a user to model a wide variety of planar antenna arrays and compute their approximate far-field radiation patterns. PAAS uses an inverse Fast Fourier Transform technique to perform this calculation. While this provides a large saving in computer resources, it has the disadvantage of introducing error unless the elements (in the aperture array) lie on a rectangular grid within a plane. Also the vector characteristics of the pattern are not calculated, and effects such as mutual coupling are not modeled.

Formerly, PAAS resided only on the Honeywell G6180 GCOS computing system at RADC. Since a considerable portion of PAAS is directly applicable to the analysis of SBR, PAAS has been incorporated into the SARF simulation. This installation required a non-trivial effort due to the differences in operating systems between the RADC computer and the GRC computing system (DEC VAX 11/780).

In order to minimize modifications to existing PAAS code (during the installation of PAAS at GRC) some Honeywell operating system routines were emulated first. Therefore, the changes to the existing modules were minor with the following exceptions:

1. The routines ILAPTR, LAPTUR, and GRMELE have been extensively modified, and now generate rectangular arrays as well as the Grumman designs.
2. The routines INPLARY and PLARY are not used for array generation (even though they are functional on the GRC VAX system).
3. The routines IWFUNC and WEIGHT were modified to include additional weighting functions.
4. The routine RRAND was replaced.

The reasons for modifications 1 and 2 above go hand-in-hand. PAAS uses the routines INPLARY and PLARY to generate symmetrical rectangular, circular, and elliptical aperture arrays, while ILAPTR, LAPTUR and GRMELE are used to generate the GRUMMAN "gore" structured aperture arrays. While this is a reasonable approach for FFT processing, it is not the desired approach for a comparison of FFT processing with "brute-force" calculation.

To alleviate this situation, the INPLARY, PLARY sequence was eliminated and the ILAPTR, LAPTUR, GRMELE sequence was modified so that all aperture arrays are created from a single input file which contains <u>all locations</u> of the radiating elements in Cartesian coordinates. This file is then used directly, either to generate a file for FFT processing (by filling in the remaining equally spaced grid with zeros) or, as the input for a "brute-force" calculation. Therefore, regardless of which processing technique is used, the input data is (initially) identical.[1]

---

[1] The FFT input file will, in general, have some errors in location due to the required equal spacing of grid points. In the PAAS code this introduces an error, but in the SARF simulation code this is corrected as discussed in Sec. A.1.

The third change was necessary to provide the additional weighting functions for future antenna evaluation. The new weighting includes: Bickmore-Spellmire ($p = 0, 1$), generalized circular Taylor ($p = 1$), rectangular Taylor, Hamming, and Blackman-Harris.[1]

The last major change deals with the routine RRAND. RRAND provides random numbers which possess a uniform, normal (Gaussian) or Rayleigh distribution. This routine was completely rewritten since it is dependent upon a 36-bit machine, and the VAX-11 is a 32-bit machine.

A.2.2 Input Options

PAAS has the capability of modeling four aperture shapes:

1. Rectangular antenna (rectangular grid)
2. Circular antenna (rectangular grid)
3. Elliptical antenna (rectangular grid)
4. Circular gore antenna (rectangular grid)

PAAS also models ten aperture weighting functions:

1. Uniform (no weighting)
2. Cosine on a pedestal
3. Blackman
4. Kaiser
5. Triangular
6. Circular Taylor ($p = 0$)
7. Bessel
8. Cubic
9. Bayliss
10. Gaussian

---

[1] These weights are described in A.C. Ludwig, Low Sidelobe Aperture Distribution for Blocked and Unblocked Circular Aperture, General Research Corporation RM-2367, April 1981.

The SARF simulation contains all PAAS aperture shapes and weighting functions as well as providing additional capability. While the SARF simulation uses the same basic shapes as PAAS it allows for deviation in the shape in two important ways: (1) the elements are not forced to lie in a plane (i.e., deformation in the Z-direction), and (2) the elements need not occupy points on a rectangular grid.[1]

Furthermore, seven other weighting functions are available in the SARF simulation. They are:

1. Generalized circular Taylor ($p = 1$)
2. Rectangular Taylor
3. Bickmore-Spellmire
4. Hamming
5. Blackman-Harris
6. Binomial
7. Impulse (single element at origin)

The generalized circular Taylor weighting function is similar to the classical Taylor weighting function but provides much lower wide angle sidelobes.[2]

Rectangular Taylor weighting produces essentially the same antenna pattern as circular Taylor weighting except that it applies to a rectangular rather than a circular aperture, and therefore produces a pattern with rectangular rather than circular symmetry.

Bickmore-Spellmire weighting represents a class which generalizes the $(1 - r^2)^P$ distributions. Their performance is near optimum in the sense of maximizing energy within a given area of the T_x,T_y-plane.

---

[1] Both of these additional capabilities are currently only applicable to the "brute-force" calculation and not the inverse FFT processing.

[2] A.C. Ludwig, op. cit.

The Hamming distribution is a classical cosine-type distribution which has been included for completeness.

The Blackman-Harris weighting function is a sum of cosines which provide a maximum sidelobe level of -92 dB from the peak of the main lobe.

The Binomial weighting function was installed primarily for simulation validation and is described in more detail in subsection A.2.3.6.

The Impulse weighting function provides a uniform antenna pattern (in the T_x,T_y-plane). It is used primarily for element pattern test cases.

The implementation of all the above weighting functions was straightforward with the exception of the generalized Taylor ($p = 1$), since this function requires a numerical integration to obtain the correct weight.[1] To avoid a numerical integration each time a weight is to be assigned to an element, the SARF simulation performs a single integration over the entire aperture and then generates a "look-up" table. A quadratic interpolation is then used in assigning the correct weight to a given element.

Evaluation of the above interpolation technique indicated that weights are interpolated with precision of at least five decimal places. Since this was easily accomplished, the interpolation technique was also applied to the classical circular Taylor distribution with equal precision and a considerable reduction in computing time.

While this interpolation scheme reduces computing time and provides very good precision, it has one restriction. The value of $\bar{n}$

---

[1] A.C. Ludwig, op. cit.

must not exceed the suggested values listed in Table A.1. The reason for this restriction is simply explained. As $\bar{n}$ increases beyond the recommended value, the aperture weighting function develops a "spike" at the edge of the aperture. This spike is far removed from the smooth curve expected by the interpolation scheme and thereby causes excessive errors near the aperture's edge. This restriction is really no problem since a distribution with a spike is not used in practice.

A.2.3 Output Options

PAAS (as delivered to GRC) contains two output routines named RTI and EDISYN. As PAAS has already been documented in detail,[1] only a brief description of these routines is provided below.

Subroutine RTI is used to represent either the array weighting function or the antenna pattern as a discrete contour plot. It contains

TABLE A.1

SIDELOBE LEVEL VERSUS PARAMETER $\bar{n}$ FOR TAYLOR (p = 0, 1) DISTRIBUTIONS

Sidelobe Level dB	$\bar{n}$ (p = 0)	$\bar{n}$ (p = 1)
-20	2	2
-30	4	2
-40	7	2
-50	11	3
-60	16	4
-70	21	5
-80	27	7

---

[1] R.J. Hancock and J.R. Fricke, op. cit.

40 quantization levels which are represented by alpha-numeric characters. The floor level is selected in dB as are the quantization levels. The RTI plot has been modified for the SARF simulation so that both the E_x and E_y (Ref. 1) components of the far-field patterns are graphed. An example of this output option is shown in Figs. A.3 and A.3b for a Bickmore-Spellmire (p = 1), 60-dB antenna pattern.

The EDISYN routine generates a synopsis of the energy distribution of the far-field pattern in histogram form. The plot is generated by determining the amount of energy in concentric circles of the antenna pattern. The amplitude of the energy is represented by its position along the ordinate axis. The energy quantization levels are represented by one of forty alpha-numeric characters. A sample of the EDISYN plot is shown in Figs. A.4a and A.4b.

The SARF simulation contains four additional output options:

1. Numerical antenna pattern cut
2. Histogram pattern cut
3. Linear pattern plot
4. Three-dimensional (3-D) antenna pattern or array weighting function

The numerical pattern cut allows the user to take a cut along any horizontal or vertical line as well as at a 45° diagonal through the antenna pattern. The output from this cut provides the magnitude and phase of the pattern points, the position in the T_x, T_y-plane , and the normalized magnitude (relative to the antenna peak) in both volts and dB.

---

[1] The SARF simulation provides polarization effects while PAAS does not.

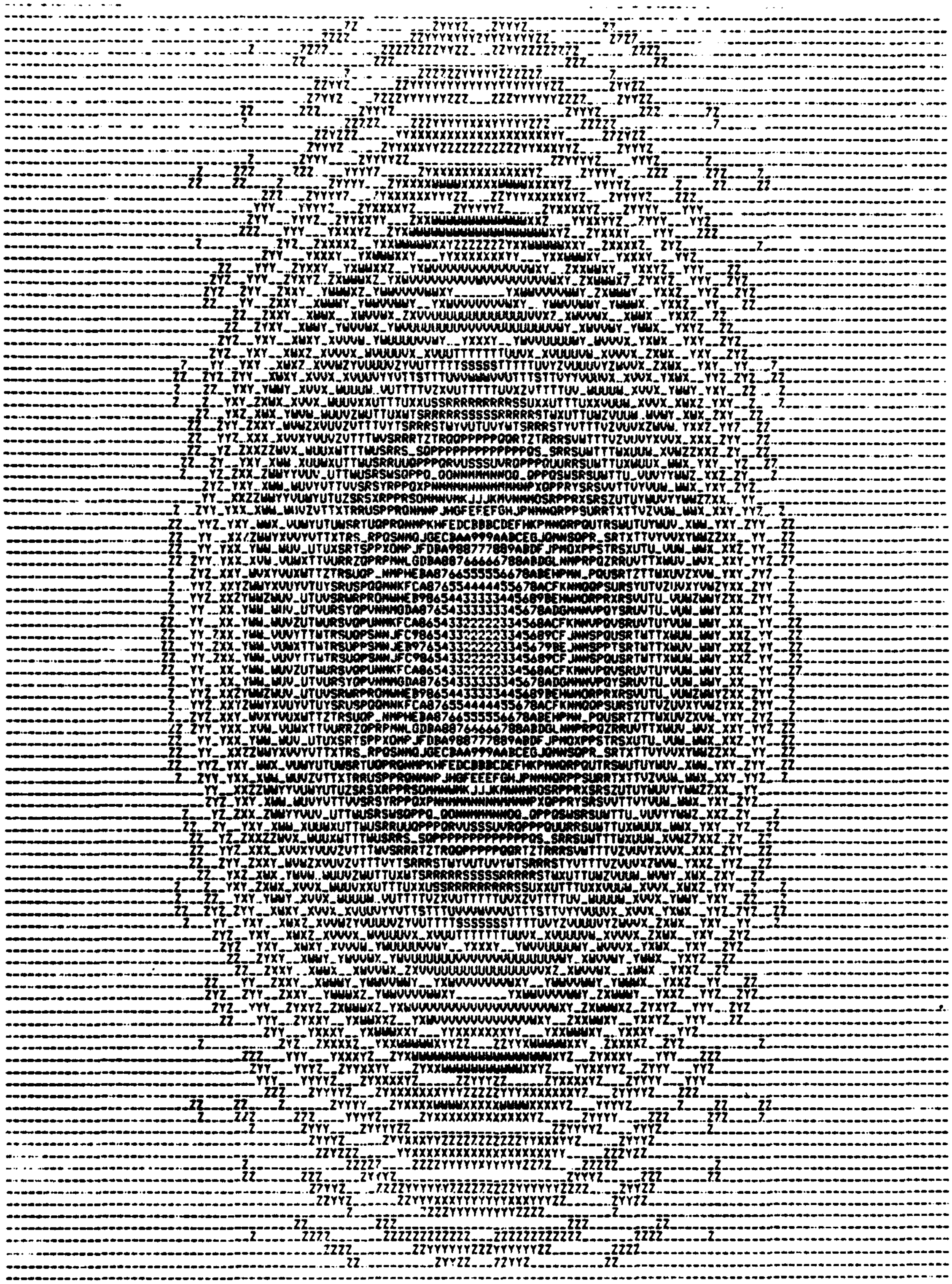

Figure A.3a. E_x-Field RTI-Plot

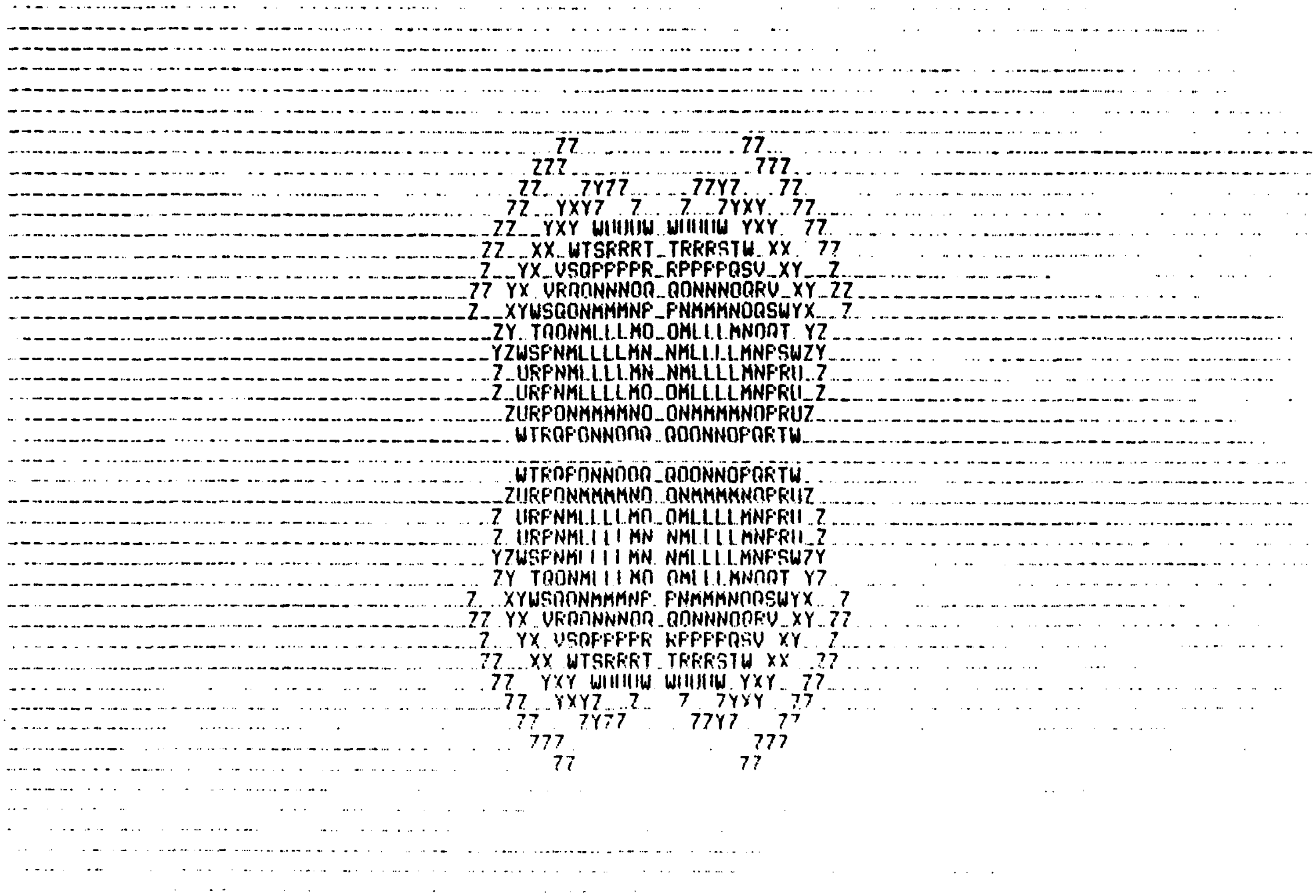

```
       ZZ             ZZ
     ZZZ               ZZZ
    ZZ   ZYZZ     ZZYZ   ZZ
   ZZ  YXYZ  Z   Z  ZYXY  ZZ
  ZZ  YXY WUUUW WUUUW YXY  ZZ
 ZZ  XX WTSRRRT TRRRSTW XX  ZZ
 Z  YX VSQPPPPR RPPPPQSV XY  Z
ZZ YX VRQQNNNOQ QONNNOQRV XY ZZ
Z  XYWSQONMMMNP PNMMMNOQSWYX  Z
  ZY TQONMLLLMO OMLLLMNOQT YZ
  YZWSPNMLLLLMN NMLLLLMNPSWZY
  Z URPNMLLLLMN NMLLLLMNPRU Z
  Z URPNMLLLLMO OMLLLLMNPRU Z
   ZURPONMMMMNO ONMMMMNOPRUZ
    WTRQPONNOOQ QOONNOPQRTW

    WTRQPONNOOQ QOONNOPQRTW
   ZURPONMMMMNO ONMMMMNOPRUZ
  Z URPNMLLLLMO OMLLLLMNPRU Z
  Z URPNMLLLLMN NMLLLLMNPRU Z
  YZWSPNMLLLLMN NMLLLLMNPSWZY
  ZY TQONMLLLMO OMLLLMNOQT YZ
Z  XYWSQONMMMNP PNMMMNOQSWYX  Z
ZZ YX VRQQNNNOQ QONNNOQRV XY ZZ
 Z  YX VSQPPPPR RPPPPQSV XY  Z
 ZZ  XX WTSRRRT TRRRSTW XX  ZZ
  ZZ  YXY WUUUW WUUUW YXY  ZZ
   ZZ  YXYZ  Z   Z  ZYXY  ZZ
    ZZ   ZYZZ     ZZYZ   ZZ
     ZZZ               ZZZ
       ZZ             ZZ
```

Figure A.3b. E_y-Field RTI-Plot

```
GRDSPX,GRDSPY =   0.15625E-01  0.15625E-01
APERTURE ENERGY, FARFIELD ENERGY:   0.00000E+00   0.14922E+03
KPEAK=   65 JPEAK=   65 PEAKDB=   48.55 FLOOR=  -49.45
T-PLANE MAXIMUM RADIUS=  0.98438E+00


AWNDO,EWNDO,XMSSL =  0.61074E+01  0.59763E+03  0.92036E-02
THE ARRAY FACTOR ISOTROPIC REFERENCE LEVEL IS:    19.7825 DB
 28.77 ______________________________________________________________
 26.77 _YW___________________________________________________________
 24.77 __ZW__________________________________________________________
 22.77 ___Y__________________________________________________________
 20.77 ____S_________________________________________________________
 18.77 ______________________________________________________________
 16.77 _____U________________________________________________________
 14.77 _____W________________________________________________________
 12.77 _____Y7_______________________________________________________
 10.77 ______V_______________________________________________________
  8.77 ______Y_______________________________________________________
  6.77       Y                ________________________________________
  4.77       _7     ___________________________________________________
  2.77       _U_____________________________________________________
  0.77        Y      _______________________________________________
 -1.23      ________________________________________________________
 -3.23       _Y ______________________________________________________
 -5.23 _______Y______________________________________________________
 -7.23 ______________________________________________________________
 -9.23 ________Z_____________________________________________________
-11.23 ________V_____________________________________________________
-13.23 _________JU___________________________________________________
-15.23 ________YZV___________________________________________________
-17.23 ________Y_Y___________________________________________________
-19.23 __________Y_MQ________________________________________________
-21.23 __________V_QN________________________________________________
-23.23 _______Y____Y_Y4______________________________________________
-25.23 ___________U_YWQ_LYQ__________________________________________
-27.23 __________Y  WV S GR  VU______________________________________
-29.23        Y     YV SYMYV RR  QV__________________________________
-31.23           V   YY MUKUWII7I YTII  Q__V_UY______Y_______________
-33.23        Y  YU YY  UR NQSMNYU+M KCU UISYSEU UV__NE_ZUZ__YZ__Y
-35.23      _V  V  YV  SY  SK QUKNIWNTG_IKQUUIQYMKY_VIUYUCUUSQ_US
-37.23 __________Y______Y___V___V_VQN_SYNGE_KEQ_MNQYC2RYKVEQMCEVEVU_7
-39.23 ______________Y__YY__YS__RY_QSSWKWIGECSVGKIIIYCSNRESSYIIVGE
-41.23 ________Z_________W__YZ__V___WU_VQV__QSVVQSGNWSSSKNVVNSNNSN7SS_
-43.23 ______________Y___Y__UV_YYM__NY_SSWYYVQS_ISWGYVNWNKNQAF_QTS
-45.23 ___________V___V___V__VY_____YYQ_YQVYSQ_QVVY_KQQVWQV_QNYEQCU
-47.23 ______________Y___Y__Y___V___S__WSY_YSY_QS__QSRYYSSVINVNQIE
-49.23 ______________Y__YV___Y__VY__V___Q__WVVYVVYYSMYYSS__RGY_QVV
-51.23 _____________________Y_______V___S___QV__VY_YS_VVNSEVNSVSYY
-53.23 _____________________Y___V___YV__S__YYV__YVV_N_SSV_YVUV_VVY
-55.23 ___________Z______Z__Y____Y__Y______YV__VY__SY__Y_YS_VY_YV_VY_
-57.23 _________________Y_____Y_________________Y__VYW____ZYY_Y__V_SVY
-59.23 ___________________________Y____7_______Y_YY__Y_YYYYVY_SV__VY_
-61.23                      ___7___Y___W___Y__YY__Y_____Y_YYV_Y____V_Y
-63.23                      ___Z___Z_____________Y_____YYZYY________YY
-65.23                            Y _______________W__YS__VY_Y____VV_
-67.23                       Y ____________________Y___Y_______YY____Y
-69.23                  _____Y___ ____________________YY_Y____Z______Y_____
```

Figure A.4a. EDYSIN Output

```
IRING   T-RAD    ANGL   SAMPLES    MEAN SQ        RMEAN          VAR        MSQDBI   CMSQDBI  MSQDBML,   CMSQDBML

 63   0.96875  75.6385    392   0.13216E-01   0.97955E-01   0.36210E-02  -38.5715   0.0000  -67.3377  -67.3377
 62   0.95313  72.3876    388   0.54969E-02   0.62839E-01   0.15482E-02  -42.3813   0.0000  -71.1475  -68.8284
 61   0.93750  69.4359    392   0.47997E-02   0.56545E-01   0.16023E-02  -42.9704   0.0000  -71.7366  -69.6025
 60   0.92188  67.2018    368   0.10872E-01   0.94823E-01   0.18802E-02  -39.4196   0.0000  -68.1858  -69.2196
 59   0.90625  64.9922    364   0.11890E-01   0.95330E-01   0.28019E-02  -39.0308   0.0000  -67.7970  -68.9091
 58   0.89063  62.9519    360   0.59853E-02   0.63999E-01   0.18894E-02  -42.0117   0.0000  -70.7779  -69.1576
 57   0.87500  61.0450    344   0.67962E-02   0.66928E-01   0.23169E-02  -41.4599   0.0000  -70.2260  -69.2844
 56   0.85938  59.2465    376   0.15783E-01   0.11293E+00   0.30288E-02  -37.8007   0.0000  -66.5668  -68.8328
 55   0.84375  57.5383    324   0.12782E-01   0.95441E-01   0.36734E-02  -38.7164   0.0000  -67.4826  -68.6804
 54   0.82813  55.9066    344   0.69132E-02   0.67275E-01   0.23872E-02  -41.3858   0.0000  -70.1519  -68.7996
 53   0.81250  54.3409    312   0.93821E-02   0.76296E-01   0.35610E-02  -40.0595   0.0000  -68.8257  -68.8016
 52   0.79688  52.8327    324   0.22010E-01   0.12419E+00   0.65873E-02  -36.3564   0.0000  -65.1226  -68.3849
 51   0.78125  51.3752    336   0.15704E-01   0.10841E+00   0.39509E-02  -37.8223   0.0000  -66.5885  -68.2261
 50   0.76563  49.9627    304   0.35677E-02   0.47102E-01   0.13491E-02  -44.2587   0.0000  -73.0248  -68.4091
 49   0.75000  48.5904    312   0.78898E-02   0.78704E-01   0.16955E-02  -40.8119   0.0000  -69.5781  -68.4706
 48   0.73438  47.2545    292   0.20202E-01   0.13267E+00   0.25994E-02  -36.7287   0.0000  -65.4948  -68.2506
 47   0.71875  45.9514    296   0.17716E-01   0.11946E+00   0.34440E-02  -37.2990   0.0000  -66.0652  -68.1087
 46   0.70313  44.6783    272   0.61328E-02   0.64675E-01   0.19499E-02  -41.9059   0.0000  -70.6721  -68.1959
 45   0.68750  43.4326    276   0.14441E-01   0.97589E-01   0.49173E-02  -38.1866   0.0000  -66.9528  -68.1340
 44   0.67188  42.2120    288   0.29079E-01   0.15321E+00   0.56045E-02  -35.1467   0.0000  -63.9129  -67.8361
 43   0.65625  41.0145    264   0.20251E-01   0.11621E+00   0.67453E-02  -36.7182   0.0000  -65.4844  -67.7188
 42   0.64063  39.8385    272   0.80191E-02   0.70291E-01   0.30782E-02  -40.7413   0.0000  -69.5075  -67.7745
 41   0.62500  38.6822    236   0.18657E-01   0.12217E+00   0.37320E-02  -37.0740   0.0000  -65.8402  -67.6979
 40   0.60938  37.5443    248   0.34474E-01   0.17702E+00   0.31389E-02  -34.4077   0.0000  -63.1739  -67.4481
 39   0.59375  36.4236    256   0.19813E-01   0.12907E+00   0.31541E-02  -36.8130   0.0000  -65.5792  -67.3735
 38   0.57813  35.3188    228   0.36470E-02   0.52538E-01   0.88674E-03  -44.1632   0.0000  -72.9294  -67.4619
 37   0.56250  34.2289    232   0.22736E-01   0.14269E+00   0.23767E-02  -36.2154   0.0000  -64.9816  -67.3704
 36   0.54688  33.1529    208   0.47629E-01   0.21255E+00   0.24538E-02  -33.0038   0.0000  -61.7700  -67.1027
 35   0.53125  32.0900    228   0.24929E-01   0.14208E+00   0.47429E-02  -35.8155   0.0000  -64.5817  -67.0154
 34   0.51563  31.0392    208   0.74760E-02   0.73940E-01   0.20089E-02  -41.0459   0.0000  -69.8121  -67.0631
 33   0.50000  30.0000    200   0.36767E-01   0.18173E+00   0.37405E-02  -34.1279   0.0000  -62.8941  -66.9143
 32   0.48438  28.9715    208   0.62163E-01   0.24711E+00   0.10987E-02  -31.8472   0.0000  -60.6134  -66.6128
 31   0.46875  27.9532    188   0.26187E-01   0.14891E+00   0.40133E-02  -35.6017   0.0000  -64.3679  -66.5558
 30   0.45313  26.9444    192   0.12393E-01   0.90364E-01   0.42274E-02  -38.8508   0.0000  -67.6170  -66.5743
 29   0.43750  25.9445    168   0.67143E-01   0.24849E+00   0.53958E-02  -31.5126   0.0000  -60.2787  -66.3426
 28   0.42188  24.9530    164   0.90851E-01   0.29798E+00   0.20603E-02  -30.1992   0.0000  -58.9654  -66.0404
 27   0.40625  23.9695    176   0.32757E-01   0.16198E+00   0.65179E-02  -34.6296   0.0000  -63.3958  -65.9788
 26   0.39063  22.9934    168   0.24542E-01   0.12869E+00   0.79815E-02  -35.8834   0.0000  -64.6496  -65.9540
 25   0.37500  22.0243    152   0.12544E+00   0.34689E+00   0.51004E-02  -28.7983   0.0000  -57.5645  -65.6031
 24   0.35938  21.0618    140   0.13565E+00   0.36449E+00   0.27998E-02  -28.4582   0.0000  -57.2244  -65.2839
 23   0.34375  20.1055    136   0.30014E-01   0.14356E+00   0.94044E-02  -35.0093   0.0000  -63.7755  -65.2615
 22   0.32813  19.1550    144   0.60111E-01   0.21728E+00   0.12899E-01  -31.9930   0.0000  -60.7592  -65.1600
 21   0.31250  18.2100    124   0.25038E+00   0.49753E+00   0.28461E-02  -25.7966   0.0000  -54.5628  -64.6836
 20   0.29688  17.2700    120   0.20435E+00   0.44673E+00   0.47826E-02  -26.6788   0.0000  -55.4450  -64.3561
 19   0.28125  16.3348    120   0.28101E-01   0.13334E+00   0.10323E-01  -35.2953   0.0000  -64.0615  -64.3529
 18   0.26563  15.4041    116   0.23877E+00   0.46883E+00   0.18964E-01  -26.0028   0.0000  -54.7690  -64.0141
 17   0.25000  14.4775     96   0.55739E+00   0.74534E+00   0.18665E-02  -22.3209   0.0000  -51.0871  -63.3944
 16   0.23438  13.5548     96   0.27115E+00   0.49289E+00   0.28203E-01  -25.4505   0.0000  -54.2167  -63.1437
 15   0.21875  12.6356     88   0.11544E+00   0.29611E+00   0.27763E-01  -29.1589   0.0000  -57.9251  -63.0693
 14   0.20313  11.7198     92   0.10508E+01   0.10071E+01   0.36616E-01  -19.5674   0.0000  -48.3336  -62.1996
 13   0.18750  10.8069     80   0.12071E+01   0.10917E+01   0.15230E-01  -18.9652   0.0000  -47.7314  -61.4820
 12   0.17188   9.8969     64   0.14439E+00   0.32803E+00   0.36785E-01  -28.1872   0.0000  -56.9533  -61.4399
 11   0.15625   8.9893     68   0.30087E+01   0.16541E+01   0.27261E+00  -14.9987   0.0000  -43.7649  -60.2268
 10   0.14063   8.0840     56   0.58145E+01   0.24056E+01   0.27628E-01  -12.1374   0.0000  -40.9036  -58.8023
  9   0.12500   7.1808     56   0.43726E+01   0.17508E+01   0.13073E+01  -13.3751   0.0000  -42.1413  -57.9844
  8   0.10938   6.2793     48   0.17648E+03   0.12524E+02   0.19617E+02    2.6844   0.0000  -26.0818  -49.5075
  7   0.09375   5.3794     36   0.12551E+04   0.34764E+02   0.46560E+02   11.2041   0.0000  -17.5621  -42.0544
  6   0.07813   4.4808     40   0.50496E+04   0.69894E+02   0.16436E+03   17.2500   0.0000  -11.5162  -35.3761
  5   0.06250   3.5833     24   0.14201E 05   0.11884E+03   0.77185E+02   21.7405   0.0000   -7.0257  -31.7184
```

Figure A.4b. EDYSIN Numerical Output

The histogram pattern cut plots a histogram (in dB) of the normalized magnitude which represents the numerical pattern cut. An example of the numerical and histogram pattern cuts is shown in Figs. A.5a and A.5b.

The linear pattern plot is performed by a CALCOMP 53 drum plotter interfaced to the GRC CDC 6400 computer. This plot is derived from a cut identical to the numerical pattern cut. The output is a continuous line plot representing the magnitude of the pattern in dB. The amplitude range can be selected between 0.0 and -200 dB and the T_x- or T_y-axis can be adjusted anywhere in the range of -1.0 to +1.0. A sample of such a plot is shown in Fig. A.6.

The SARF simulation can provide the user with a three-dimensional plot of either the antenna pattern or the aperture array weighting. The floor level (in dB) is selectable as are the angles of tilt. That is. the pattern can be rotated about the T_x- or the T_z-axis . A portion of the pattern can be plotted as well as the entire pattern. An example of three-dimensional plots is shown in Figs. A.7a and A.7b.

A.2.4 New Analysis Capabilities

Analysis of space-based radars requires capabilities not supplied by PAAS. At this point two major additions have been made to the SARF simulation to provide some of these additional capabilities. Also, several minor additions have been installed to improve simulation fidelity.

The addition of a "brute-force" computation algorithm provides a major capability increase in the SARF simulation. This method allows the calculation of far-field patterns for various cases not possible with the inverse FFT method. It also provides a built-in test validation technique.

```
MAX AMPLITUDE =  0.41107074E+03ROW-COL-BIAS =        33         0         0
Tx/Tw Location       E-FIELD MAGNITUDE      PHASE           Normalized Pattern Magnitude               (dB)

  -1.00000            0.00000000E+00      0.00000             0.00000000E+00                        -200.00
  -0.96875            0.12255287E+01     -1.61988             0.29813084E-02                         -50.51
  -0.93750            0.54655516E+00      1.47263             0.13295891E-02                         -57.53
  -0.90625            0.17732557E+01      1.42354             0.43137483E-02                         -47.30
  -0.87500            0.58357835E+00     -1.76714             0.14196543E-02                         -56.96
  -0.84375            0.26463239E+01     -1.81623             0.64862897E-02                         -43.76
  -0.81250            0.11635525E+01     -1.86532             0.28305408E-02                         -50.96
  -0.78125            0.37900847E+00      1.22719             0.92200306E-03                         -60.71
  -0.75000            0.79467869E+00     -1.96349             0.19331920E-02                         -54.27
  -0.71875            0.89119756E+00     -2.01257             0.21679907E-02                         -53.28
  -0.68750            0.20588381E+01      1.07993             0.50084763E-02                         -46.01
  -0.65625            0.30749061E+01      1.03084             0.74802358E-02                         -42.52
  -0.62500            0.88025972E-01      0.98172             0.21413826E-03                         -73.39
  -0.59375            0.10711598E+01     -2.20893             0.26057798E-02                         -51.68
  -0.56250            0.16984768E+01      0.88360             0.41318359E-02                         -47.68
  -0.53125            0.16840235E+01      0.83456             0.40966757E-02                         -47.75
  -0.50000            0.27877998E+01     -2.35619             0.67818007E-02                         -43.37
  -0.46875            0.30633104E+01     -2.40528             0.74520274E-02                         -42.55
  -0.43750            0.26562419E+01      0.68723             0.64617633E-02                         -43.79
  -0.40625            0.29764910E+01      0.63815             0.72408244E-02                         -42.80
  -0.37500            0.49267497E+01     -2.55254             0.11985162E-01                         -38.43
  -0.34375            0.62374525E+01     -2.60163             0.15173672E-01                         -36.38
  -0.31250            0.42699041E+01      0.49088             0.10387274E-01                         -39.67
  -0.28125            0.81006708E+01      0.44180             0.19706270E-01                         -34.11
  -0.25000            0.37874703E+01     -2.74889             0.92136702E-02                         -40.71
  -0.21875            0.92892971E+01     -2.79798             0.22597807E-01                         -32.92
  -0.18750            0.46547732E+01      0.29454             0.11323533E-01                         -38.92
  -0.15625            0.98048134E+01      0.24545             0.23851088E-01                         -32.45
  -0.12500            0.89295568E+01     -2.94524             0.21722676E-01                         -33.26
  -0.09375            0.84773788E+01      0.14728             0.20622676E-01                         -33.71
  -0.06250            0.13352559E+03      0.09818             0.32482386E+00                          -9.77
  -0.03125            0.31952835E+03      0.04910             0.77730745E+00                          -2.19
   0.00000            0.41107074E+03      0.00000             0.10000000E+01                           0.00
   0.03125            0.31952829E+03     -0.04909             0.77730733E+00                          -2.19
   0.06250            0.13352597E+03     -0.09817             0.32482481E+00                          -9.77
   0.09375            0.84782543E+01     -0.14725             0.20624805E-01                         -33.71
   0.12500            0.89295702E+01      2.94524             0.21722710E-01                         -33.26
   0.15625            0.98055725E+01     -0.24543             0.23853734E-01                         -32.45
   0.18750            0.46552730E+01     -0.29451             0.11324749E-01                         -38.92
   0.21875            0.92888660E+01      2.79798             0.22596758E-01                         -32.92
   0.25000            0.37874792E+01      2.74890             0.92136916E-02                         -40.71
   0.28125            0.81010160E+01     -0.44178             0.19707110E-01                         -34.11
   0.31250            0.42701693E+01     -0.49086             0.10387918E-01                         -39.67
   0.34375            0.62371702E+01      2.60163             0.15172985E-01                         -36.38
   0.37500            0.49267697E+01      2.55255             0.11985212E-01                         -38.43
   0.40625            0.29767649E+01     -0.63813             0.72414908E-02                         -42.80
   0.43750            0.26566935E+01     -0.68720             0.64628618E-02                         -43.79
   0.46875            0.30624733E+01      2.40525             0.74499911E-02                         -42.56
   0.50000            0.27877998E+01      2.35619             0.67818007E-02                         -43.37
   0.53125            0.16848651E+01     -0.83448             0.40987232E-02                         -47.75
   0.56250            0.16989101E+01     -0.88357             0.41328901E-02                         -47.67
   0.59375            0.10709805E+01      2.20894             0.26053437E-02                         -51.68
   0.62500            0.87996542E-01     -0.98177             0.21406666E-03                         -73.39
   0.65625            0.30750728E+01     -1.03083             0.74806414E-02                         -42.52
   0.68750            0.20590010E+01     -1.07992             0.50088726E-02                         -46.01
   0.71875            0.89105153E+00      2.01260             0.21676356E-02                         -53.28
   0.75000            0.79469484E+00      1.96350             0.19332314E-02                         -54.27
   0.78125            0.37916186E+00     -1.22717             0.92237617E-03                         -60.70
```

Figure A.5a. Numerical Pattern Cut

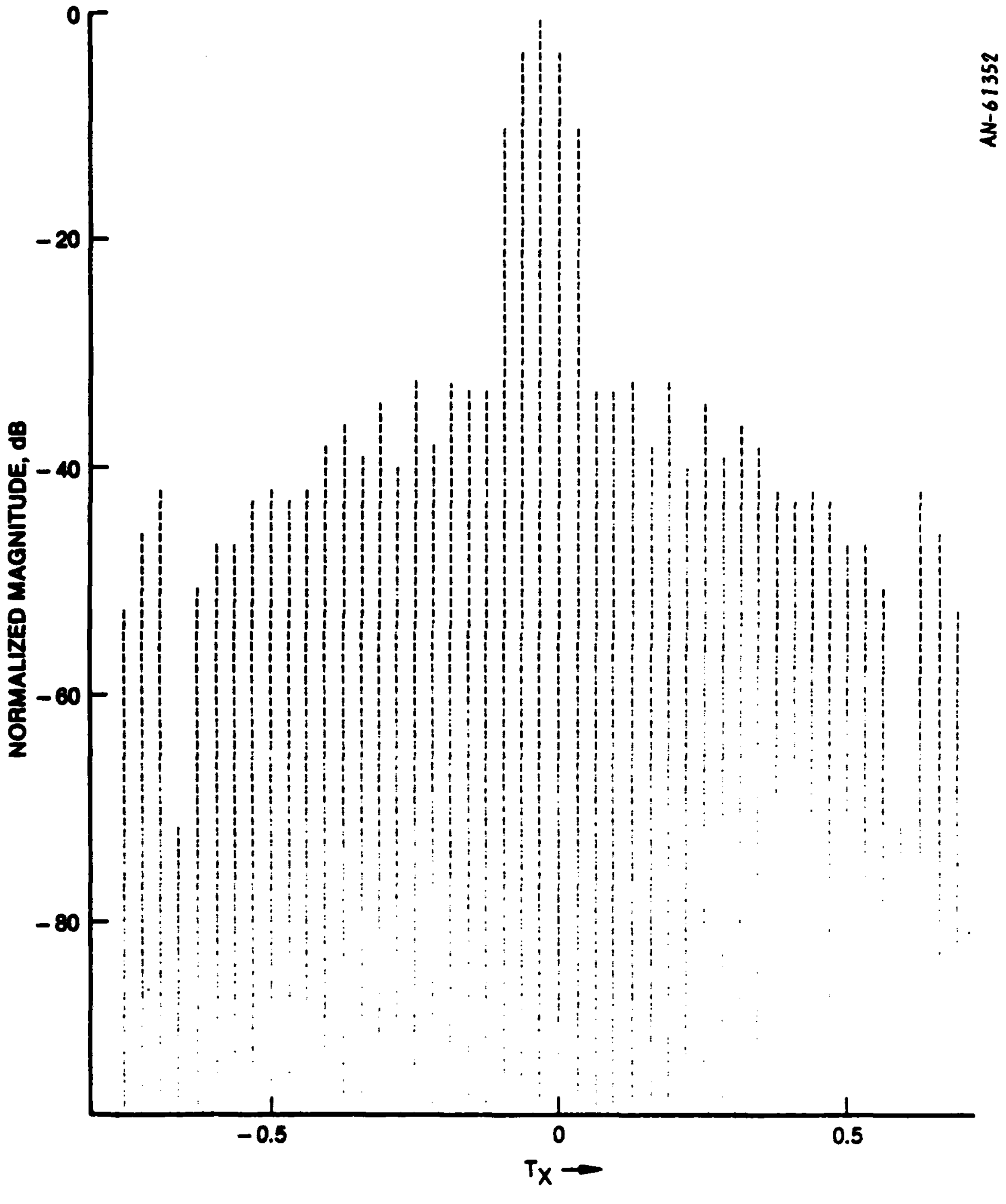

Figure A.5b. Histogram Pattern Cut

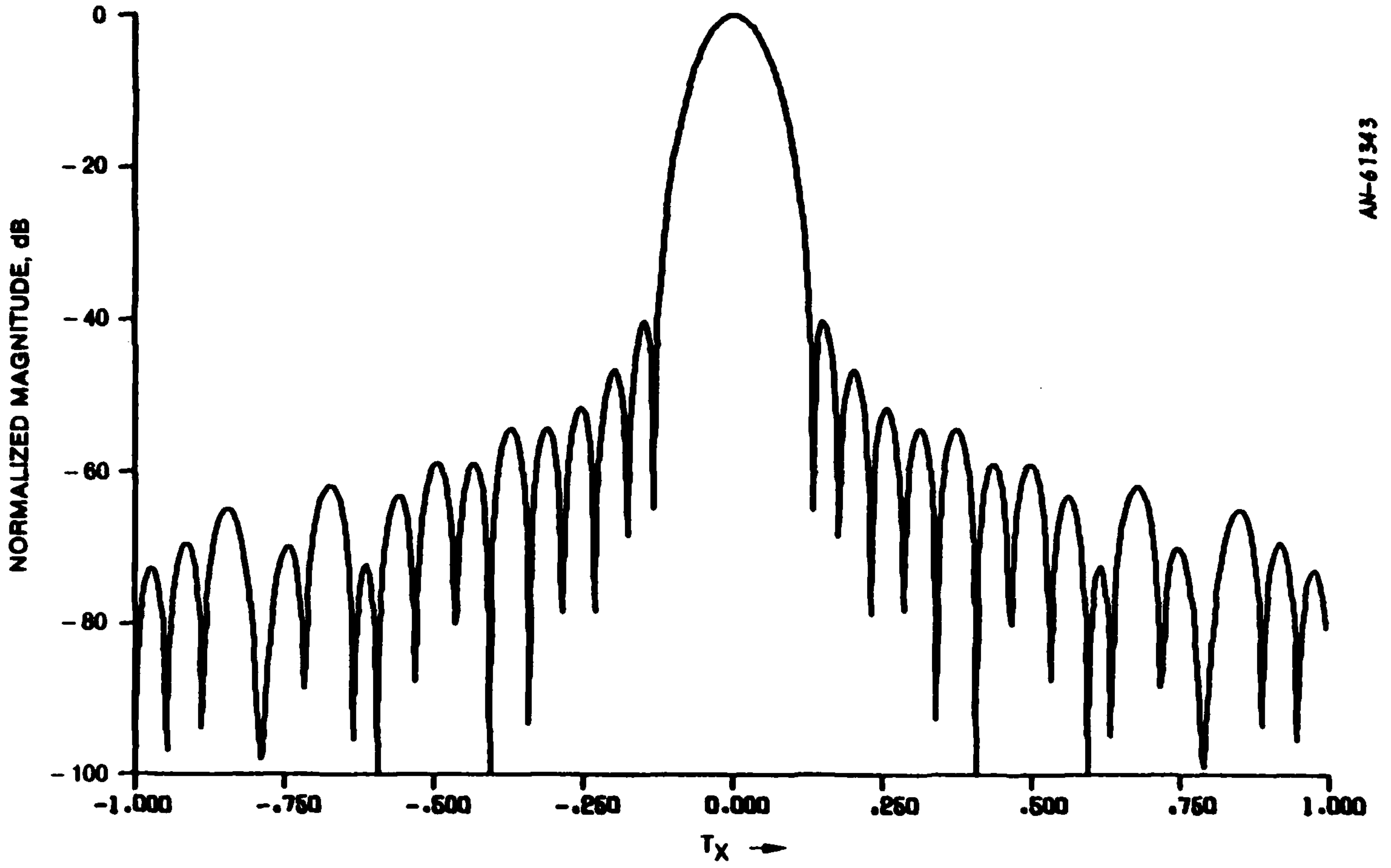

Figure A.6. Linear Pattern Plot, Bickmore-Spellmire (p = 0)

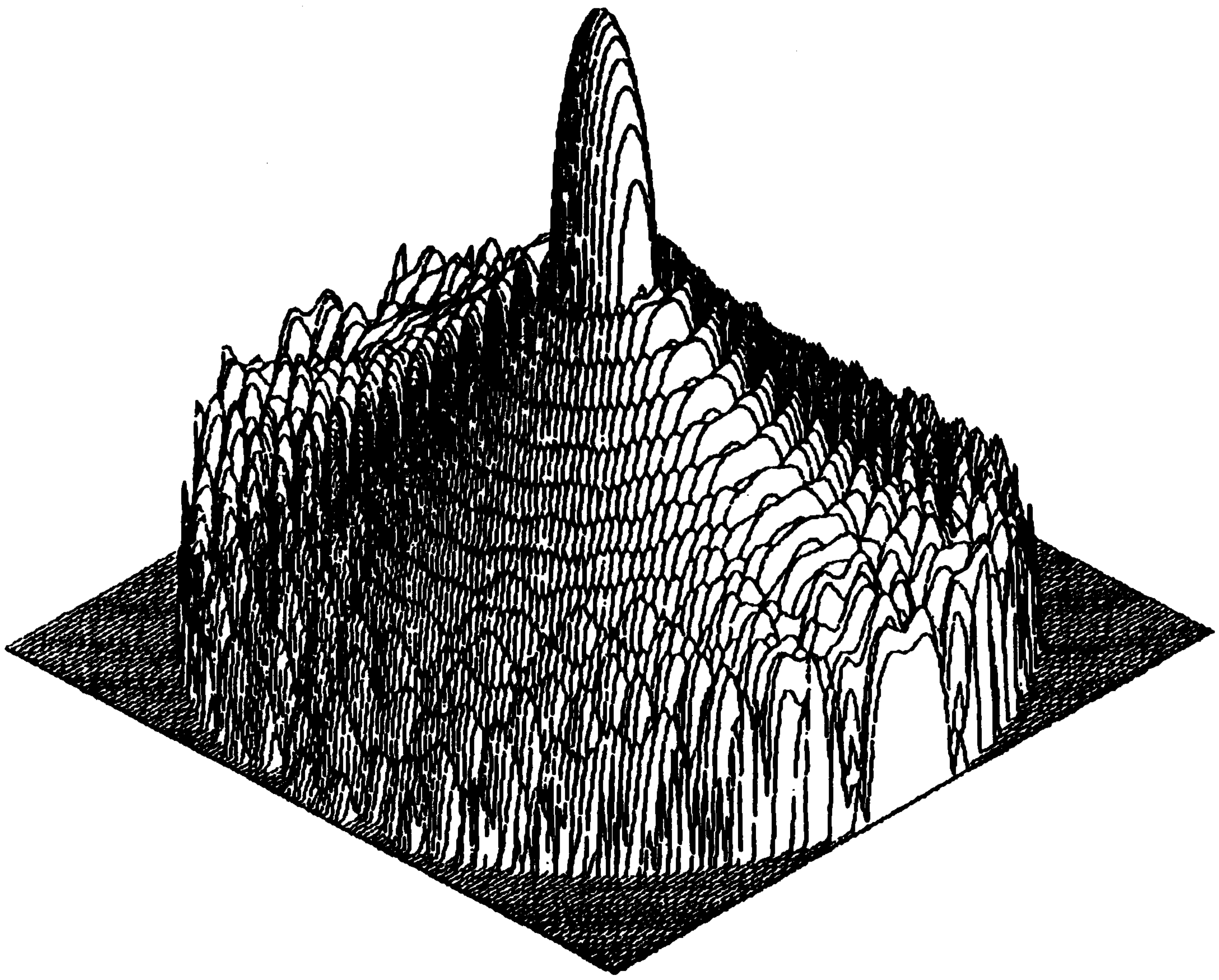

Figure A.7a. Three-Dimensional Antenna Pattern, E_x Field for Taylor ($p = 1$) Weighted Array

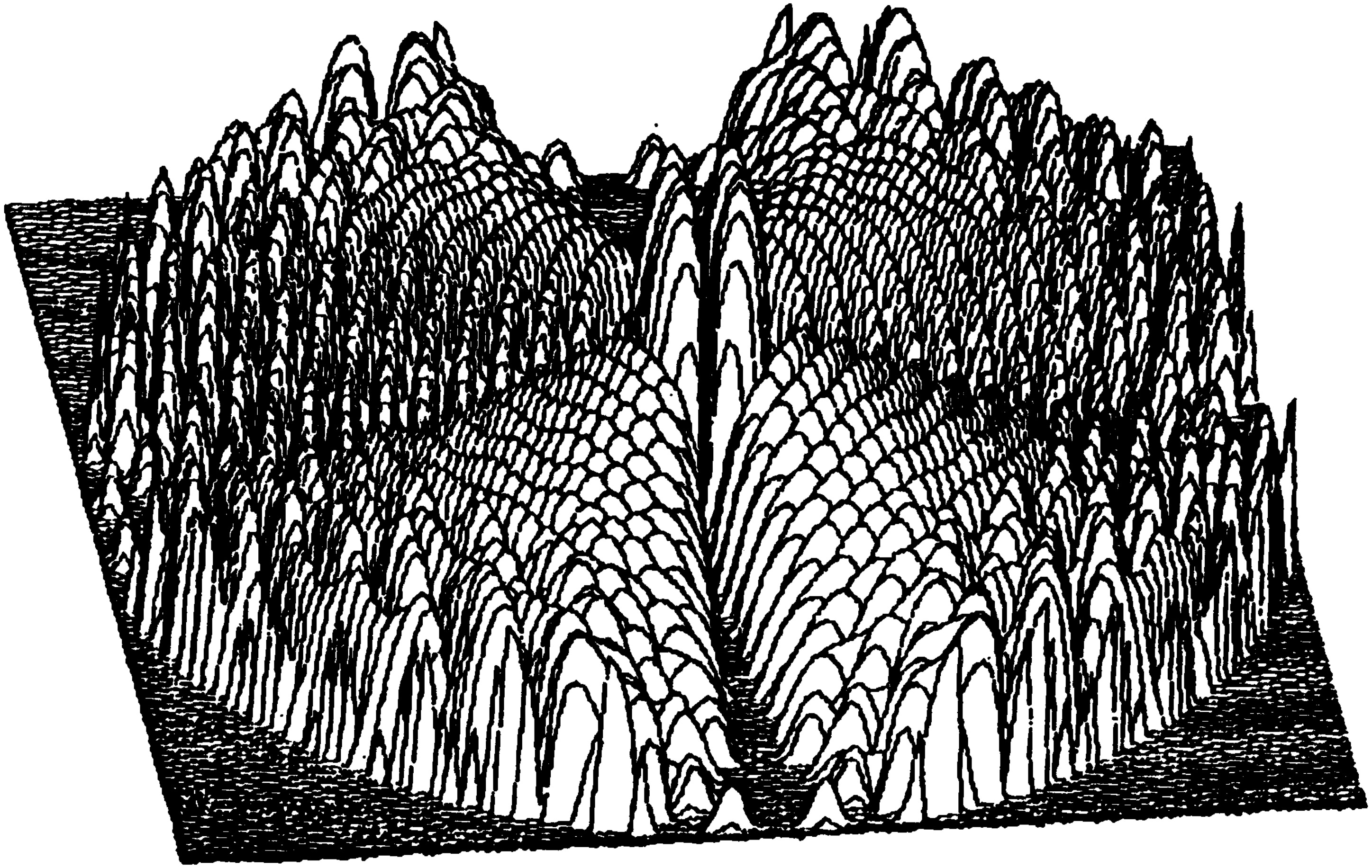

Figure A.7b. Three-Dimensional Antenna Pattern, E_y Field for Taylor (p = 1) Weighted Array

Another major addition to the SARF simulation provides polarization data through utilization of individual element patterns. The present algorithm assumes all element patterns are identical, hence it can be used in conjunction with the inverse FFT pattern calculation. The elements are represented by a set of from one to fifty source segments, each with given location, orientation, and magnitude. These segment patterns are then combined to determine the overall element pattern.

The remainder of this section discusses the two above major capabilities of the SARF simulation, and describes some analyses performed using these new tools.

A.2.4.1 Brute-Force Technique

The inverse FFT is an excellent means of computing far-field antenna patterns for arrays attached to a rectangular lattice. However, this method has some deficiencies. For example, arrays which are not on a rectangular lattice can only be approximated by choosing the closest grid point. This introduces errors in the calculated pattern, particularly for the wide angle sidelobes. Also, the FFT cannot be used if the array is non-planar or if the individual element patterns are not all identical (i.e., the element patterns are a function of their location in the array).

To provide for all these and other contingencies, a "brute-force" implementation of the far-field patterns was incorporated into the SARF simulation. This routine implements the following equation (using double precision variables):

$$E(\overline{R}) = \sum_{n,m} I_{nm}\overline{F}_{nm}(T_x, T_y)\ \exp\{jk\overline{\rho}_{nm} \cdot \overline{T}\}$$

where I_{nm} = the current excitation
$\overline{F}_{nm}$ = the element pattern field

$k = 2\pi/\text{wavelength}$

$\bar{\rho}_{nm}$ = the element location vector

The intermediate steps in this computation are performed in single precision (7 decimal digits of precision), but the summation, complex multiplications, and exponentiation are performed in double precision (16 significant decimal digits).

Since the primary purpose (in addition to validation) of the brute-force calculation is to determine the far-field pattern near null points, only a handful of pattern points will be actually calculated. This is important, since the time required to perform the brute-force calculation is considerably greater than for the FFT, as discussed in Sec. A.1.

The brute-force calculation provides an exact calculation of the antenna pattern. It also serves as a built-in test validation technique, since the input file data used to establish element locations and current excitations for the FFT approximation techniques (Eqs. A.12 and A.18) is also the same file used for the exact brute-force calculation.

A.2.4.2 Element Patterns and Polarization

Polarization is an important antenna characterization, and the addition of a vector pattern calculation is one of the major new capabilities of the SARF simulation. As part of the same software, another important capability, the analysis of complex element patterns, is also added. The elements can be bent or straight dipoles, turnstiles, or any other device that can be modeled by a set of current segments. Feedline radiation is also easily included.

This section first considers the vector pattern of a single current segment, and then modeling an array element with a number of segments. Since the complexity of the element model will directly impact computing time, it is important to determine exactly how much detail is necessary to obtain high fidelity antenna patterns. Therefore, a number of test cases are described to provide insight into this requirement.

A.2.4.2.1 Element Model

Polarization can be determined using FFT processing if the individual element patterns are not a function of the array coordinates (i.e., x,y,z). This is accomplished by multiplying the antenna pattern (output of FFT) matrix by the appropriate element pattern, as is shown by the equation below:

$$\bar{E}(\bar{R}) = \bar{F}_o(T_x,T_y) \sum_{n,m} I_{nm} \exp\{jk(n\ d_x\ T_x + m\ d_y\ T_y)\}$$

where d_x, d_y are the spacing between FFT grid points. Therefore, if all elements are identical, polarization effects can be determined by the utilization of the FFT and the appropriate multiplication by the element pattern. (The general case is discussed in Sec. A.1, but is not presently implemented in the software.)

To illustrate this technique, consider a current segment centered at the origin and consisting of a complex current whose magnitude is $|\bar{a}|$ (see Fig. A.8). Current segments will always be assumed to be $<<\lambda$, and will be modeled using the pattern of an infinitesimal current. Larger elements are simply constructed using an appropriate number of segments as discussed below. This model is essentially identical to the model used by ARC, and is compatible with utilizing ARC output data (see Appendix C).

Assuming the far-field (see Sec. A.1) and neglecting multiplicative constants, the vector electric field due to this current is given by:

$$\bar{F} = (e^{-jkr}/r)[\bar{a} - (\bar{a}\cdot\hat{i}_r)\hat{i}_r]$$

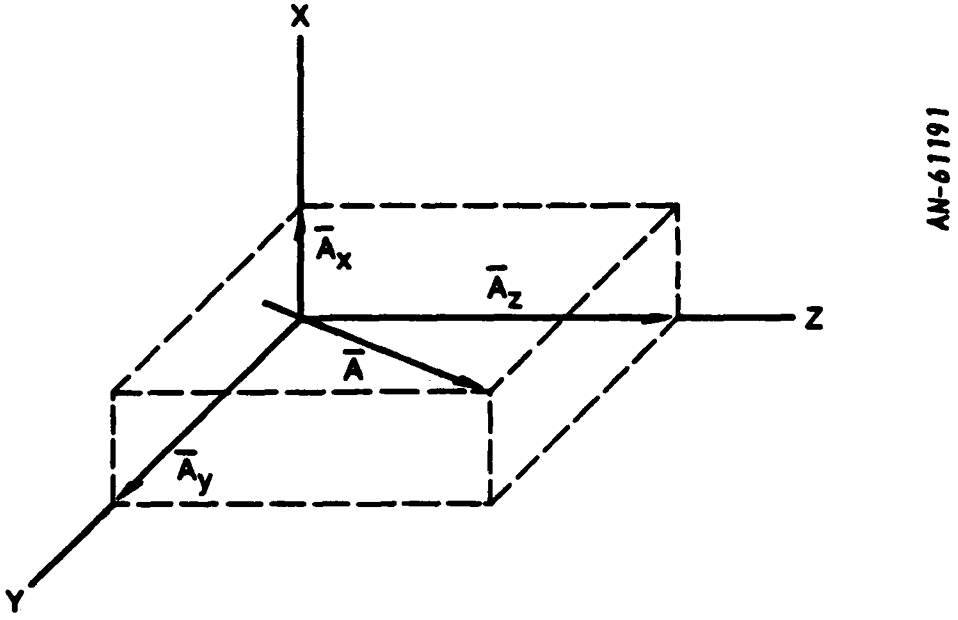

Figure A.8. Element Current at Origin

---

where

$$\bar{a} = a_x\hat{i}_x + a_y\hat{i}_y + a_z\hat{i}_z$$

$$\hat{i}_r = T_x\hat{i}_x + T_y\hat{i}_y + T_z\hat{i}_z$$

If e^{-jkr}/r is suppressed, the components of the element pattern are:

$$F_x = a_x(1 - T_x^2) - a_y(T_xT_y) - a_z(T_xT_z)$$

$$F_y = -a_x(T_xT_y) + a_y(1 - T_y^2) - a_z(T_yT_z)$$

where $\bar{F} = F_x\hat{i}_x + F_y\hat{i}_y$

If multiple current segments are required to model an element, the total element pattern is given by a summation of individual contributors

$$\bar{F}_{TOT} = \sum_{s=1}^{S} \frac{\exp(-jk\rho_s)}{\rho_s} [F_{xs}\hat{i}_x + F_{ys}\hat{i}_y]$$

where F_{xs}, F_{ys} = the x- and y-component of the element pattern due to the s<u>th</u> current segment

$\rho_s = r - \bar{r}_s . \hat{i}_r$

r_s = the location of the center of the current segment

This implementation not only provides polarization effects, but also allows a determination of complex element patterns. This technique will handle the case of perfect or imperfect groundplane as well as feedlines. It also allows for element deformations.

A.2.4.2.2 Element Model Validation and Error Tests

Once the above technique for modeling element patterns was implemented into the SARF simulation, an analysis was performed to determine the errors involved in modeling actual antenna elements with a sum of current segments.

Three measures of error were used in the following analysis. They are defined below.

The <u>normalized magnitude error</u> shows the deviation of the magnitude (in dB) between a reference and a measured pattern. In mathematical terms it is defined by:

$$20\left\{\log_{10}\left|\frac{F_{ref}}{F_{max}}\right| - \log_{10}\left|\frac{F_{meas}}{F_{max}}\right|\right\}$$

The phase error is a measurement of the difference in phases of the two fields in question and is defined by

$$\angle F_{ref} - \angle F_{meas}$$

where $\angle F$ implies the angle in polar coordinates of the complex number F

The last measure used is named the vector error and is defined by

$$20 \log_{10} \left\{ \frac{\left| \overline{F}_{ref} - \overline{F}_{meas} \right|}{\left| \overline{F}_{ref} \right|} \right\}$$

This error tends to show the "additive noise" level which is corrupting the true pattern, and includes both amplitude and phase error effects.

Error Introduced by Discrete Segments

If an ideal dipole (a continuous current distribution) is modeled by multiple discrete current segments, some error results. To determine the extent of this error an evaluation was performed which compared the exact equation for a 1/2-wavelength dipole radiator to that obtained from an approximation of 1, 2, 4, and 8 current segments.

For each case the segment current magnitudes were set equal to the value of a cosine function at the center point of the segment. The cosine function was maximum at the origin and zero at ±1/4 wavelength.

The results of these tests are shown in Figs. A.9a and A.9b. Note that the curves represent a cut through the T_x, T_y-plane at $T_y = 0$. This cut contains the largest magnitude error which occurs near the edge of the plane.

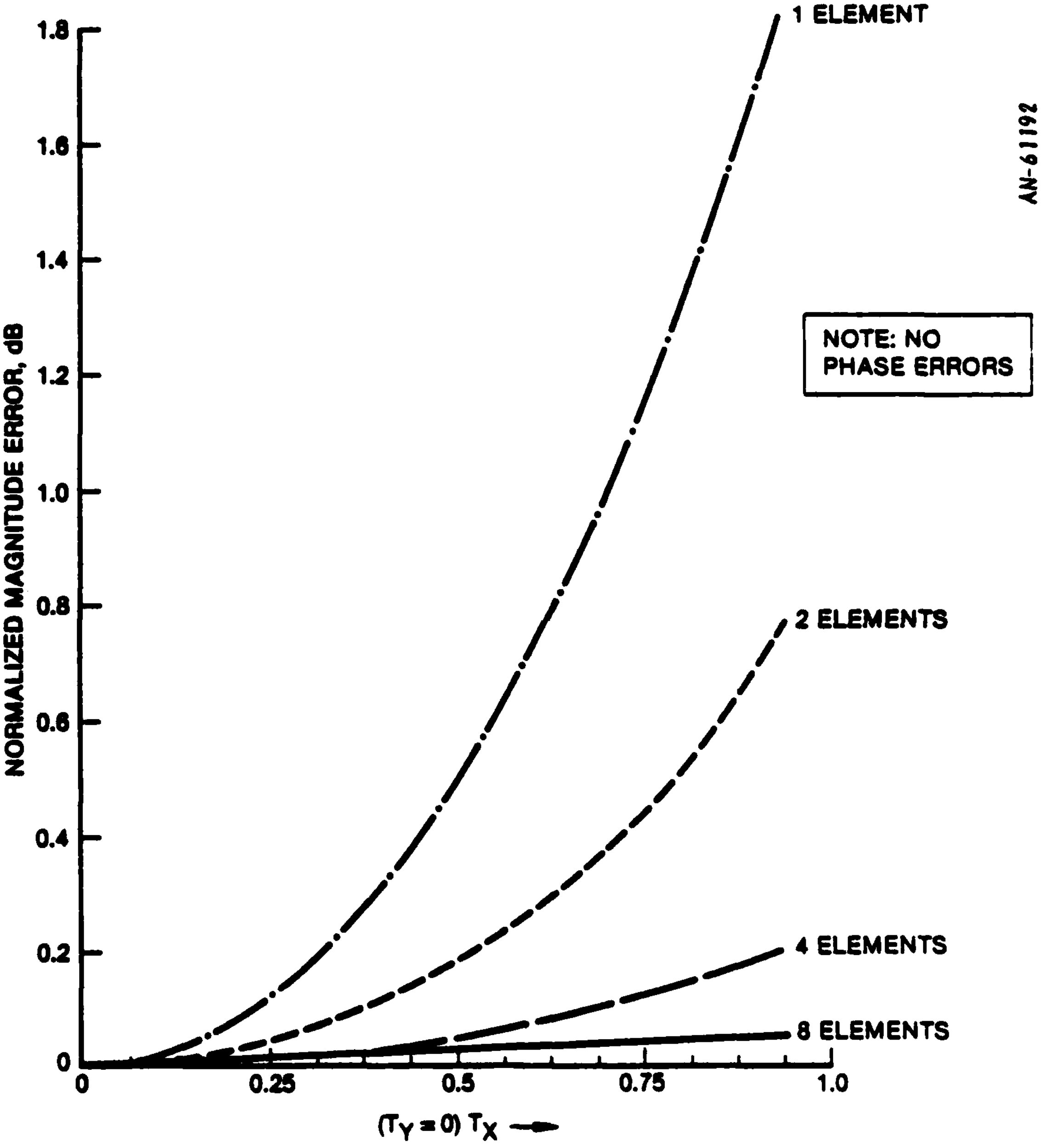

Figure A.9a. 1, 2, 4, 8 Element Currents Used to Simulate Dipole Radiator

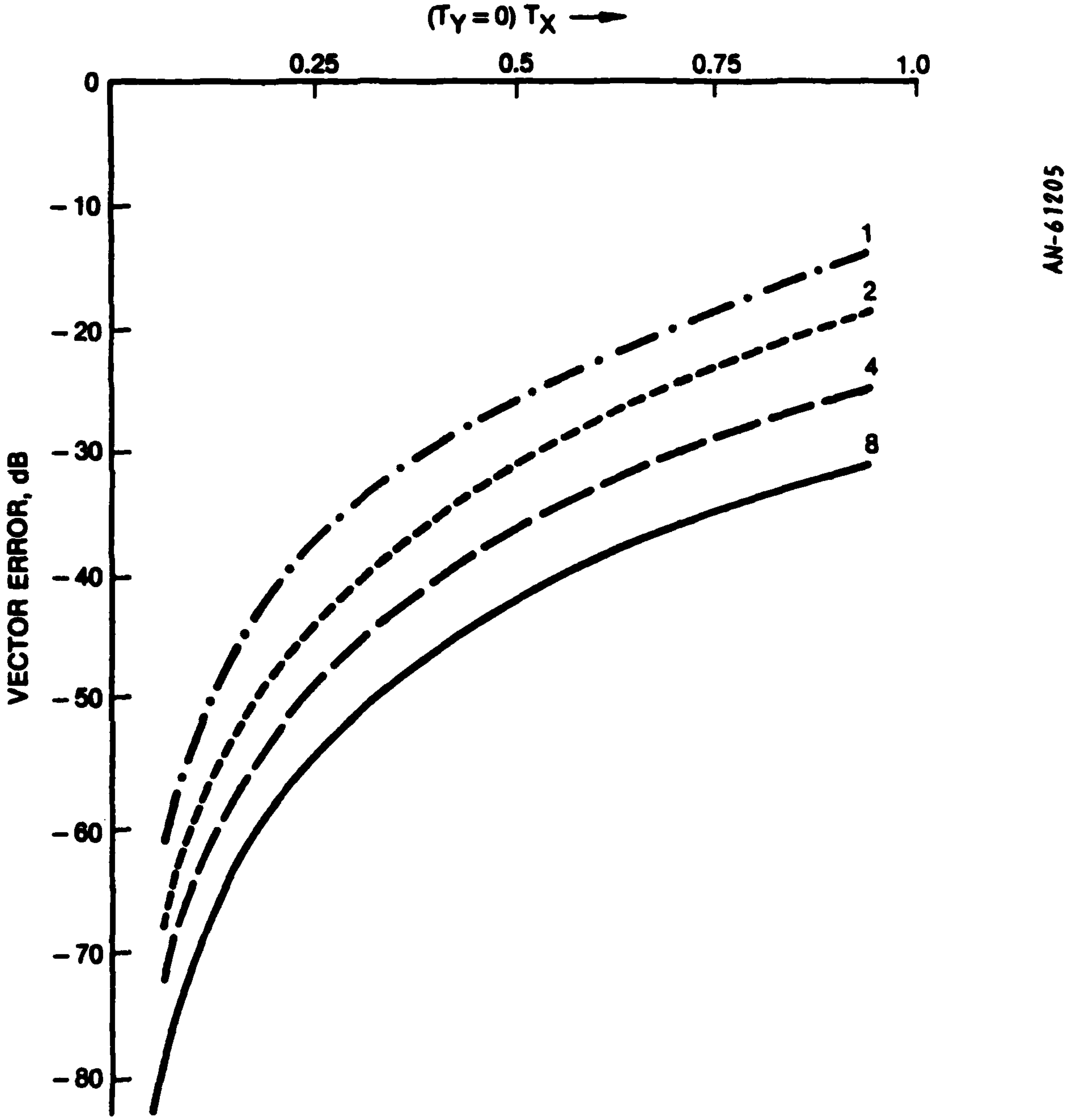

Figure A.9b. 1, 2, 4, 8 Element Currents Used to Simulate Dipole Radiator

Figure A.9a shows that near the edge of the T_x, T_y-plane a single segment has nearly 2 dB error in its magnitude; however, an 8-segment model has less than 0.05 dB maximum error. Note that the phase error is zero in all cases.

To view this from another perspective, Fig. A.9b shows that the deviation (near the aperture edge) for a single segment model is about 14 dB down from the actual measurement, whereas an 8-segment model has a maximum vector deviation which is over 30 dB below the actual value.

It is important to realize that these maximum deviations occur only near the edge of the T_x, T_y-plane . Hence, if only the close-in sidelobes are important in a particular evaluation, a single segment model is sufficient. If detailed information is needed for wide-angle sidelobes, more segments are necessary, but four or eight should be sufficient for 1/2-wavelength dipole size elements.

These results demonstrate that the segment model represents an actual continuous current distribution with little deviation. We now turn to the question of pattern deviations caused by perturbations in the actual current distribution. The number of segments in the model is selected to ensure that the modeling deviation is small compared to the deviation caused by the actual current perturbation. The three previously defined error measures will be adopted to represent the deviations in the remainder of this section.

Effect of Current Skew

Mutual coupling effects can distort the current on a dipole, causing an asymmetry or skew in the distribution. This effect is a function of scan angle, and it is important to determine how much detail is needed in the present model to obtain accurate antenna pattern results.

What effect does skewing the real part of the element currents have on the element pattern? This was the next question answered in the evaluation. The reference used for this case was the 8-segment model of a dipole radiator described above. Skewed element currents were obtained by sampling the two functions:

$$f_1(x) = K_1(x + 1/2) \cos \pi x$$

and

$$f_2(x) = K_2(x + 1/2)^2 \cos \pi x$$

at the same locations as the 8-segment dipole model (K_1 and K_2 are normalization constants).

The above two functions represent a considerable skew (relative to the analysis performed by Atlantic Research Corporation)[1] in the current as can be seen in Fig. A.10, which depicts the two skewed functions relative to a pure cosine function (8-function dipole model).

The deviation between the reference and the skewed case is shown in Figs. A.11 and A.12. Figure A.11 indicates a linear phase shift deviation is present in both skewed functions. Comparing the vector deviation with the magnitude deviation clearly shows that the phase deviation dominates the vector deviation.

As expected, the slope of the phase deviation shown for both skewed cases is in good agreement with the expected linear phase shift associated with a single element displaced to the mean value of the

---

[1] H.K. Schuman, et al., op. cit.

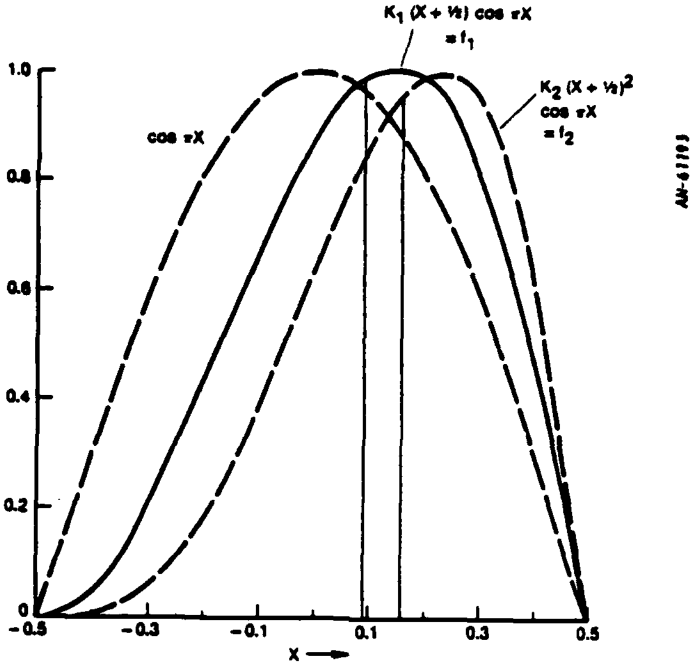

Figure A.10. Skewed 8-Segment Real Currents

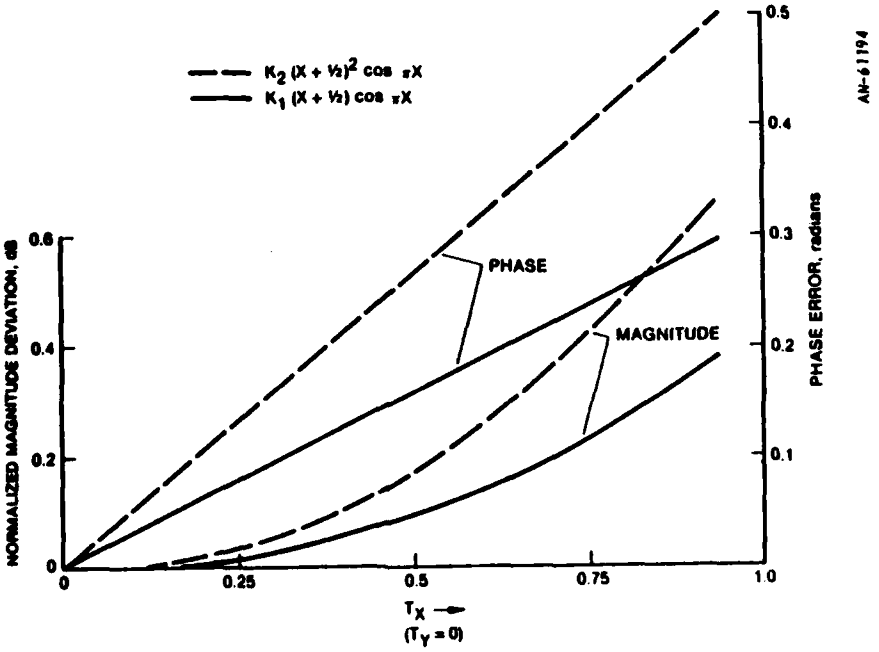

Figure A.11. Comparison of Skewed Element Pattern to 8-Segment Cosine

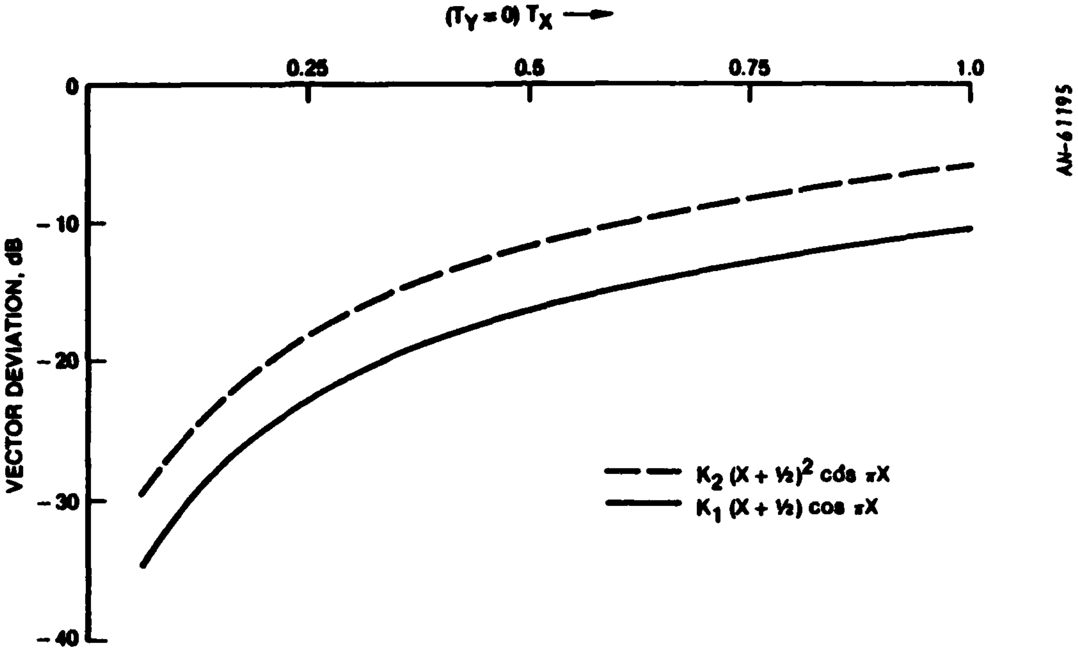

Figure A.12. Comparison of Skewed Element Pattern to 8-Segment Cosine

skewed function.[1] Put another way, current skew can be modeled by a slight spatial displacement of the current segments.

Imaginary Current Component, Including Skew

An imaginary component was added to the model for the next part of the evaluation. The imaginary component was represented by a sinusoid of twice the frequency of the real component which accurately models the results of Atlantic Research's analysis.[2]

---

[1] The mean of $f_1(f_2)$ is 0.095 (0.159). The slope of the phase shift due to $f_1(f_2)$ would be produced by a single element placed at 0.098 (0.164).

[2] H.K. Schuman, et al., op. cit.

Two cases were evaluated, each containing two different imaginary current components:

Case 1: Peaks of imaginary component equal

- (a) Ratio of real to imaginary peak = 2
- (b) Ratio of real to imaginary peak = 4

Case 2: Unequal (skewed) imaginary peaks

- (a) Real peak = 1.0, Imaginary peaks = 0.25 and 0.375
- (b) Real peak = 1.0, Imaginary peaks = 0.25 and 0.50

A sample of Case 2(b) is shown in Fig. A.13.

Figure A.14a indicates that the addition of the imaginary component causes little deviation in magnitude, but produces an approximately constant phase deviation which is equal to the ratio of the areas of the imaginary part to the real part. The slight variation in phase deviation from a constant is most probably due to the small magnitude deviation.

Case 2 (as shown in Fig. A.14b) provides similar results, however, the magnitude is greater, which causes the phase deviation to vary more from the constant value.

The vector deviation for both of these cases is totally dominated by the phase deviation and can be estimated by assuming no magnitude deviation, as shown below.

Assume the reference is given by:

$$\overline{E}_{ref} = |\bar{a}| \exp(j\alpha)\hat{i}_x$$

and

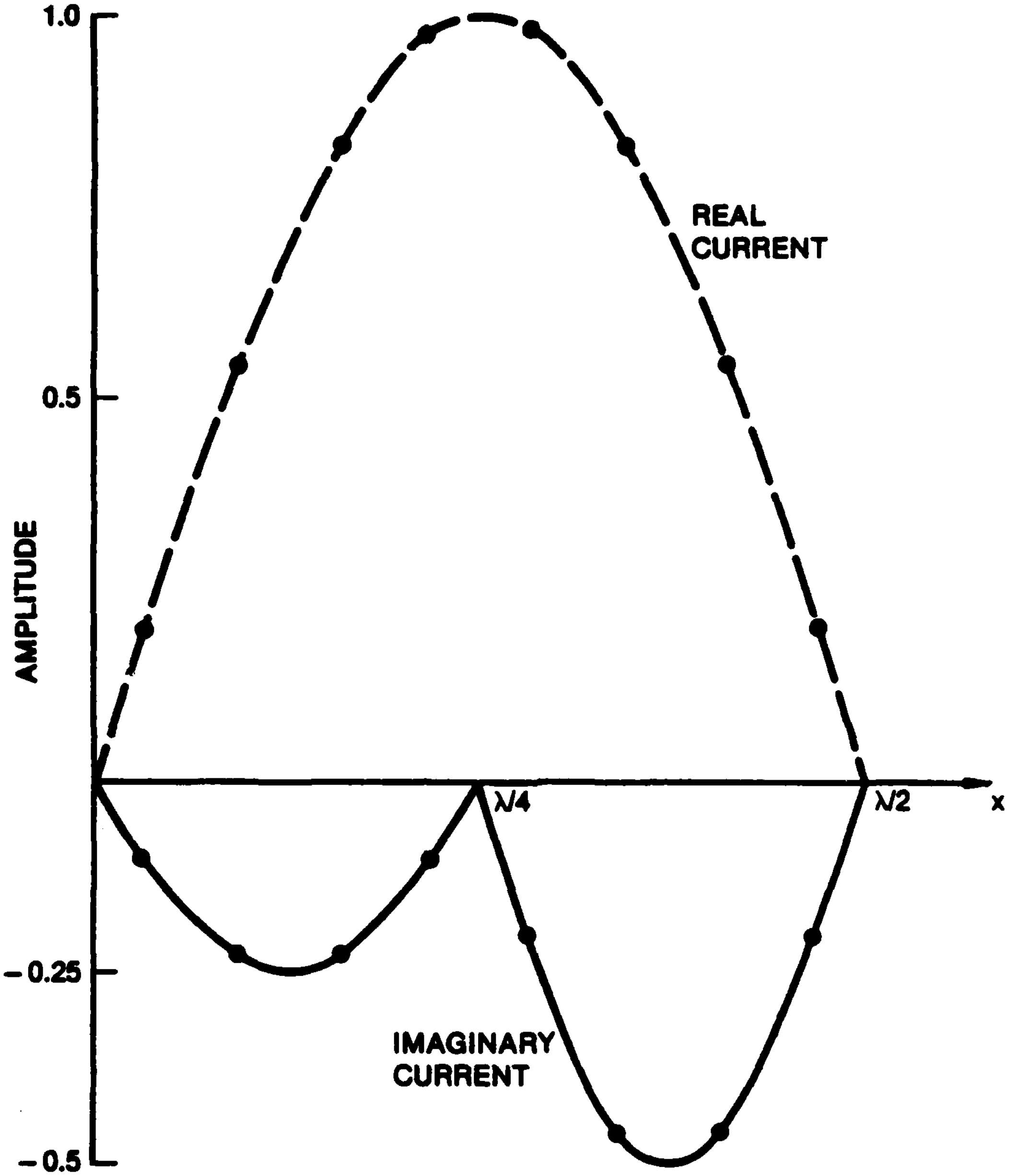

AN-61196

Figure A.13. Real and Imaginary Components for Skewed Imaginary Current

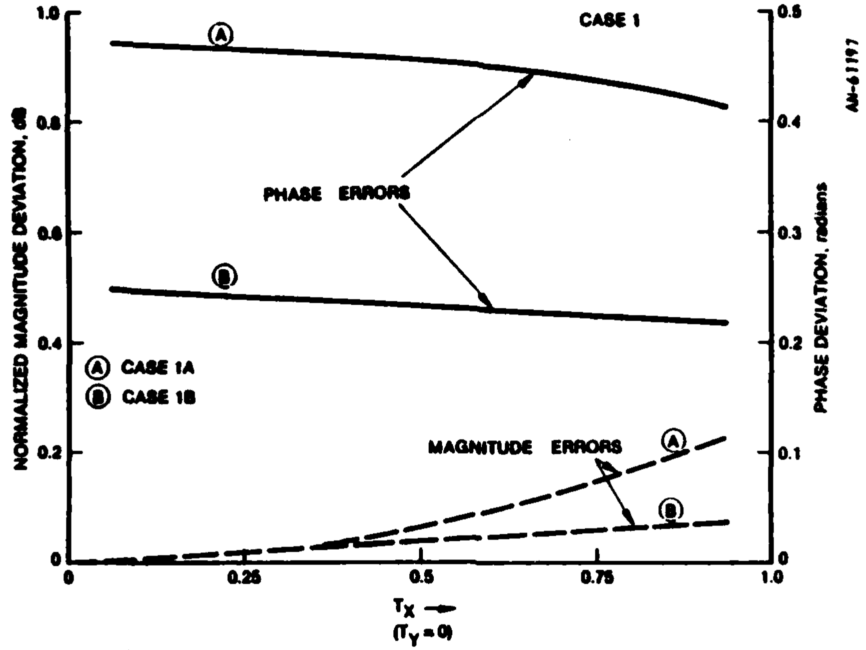

Figure A.14a. Real and Imaginary Current Compared to 8-Segment Real Reference

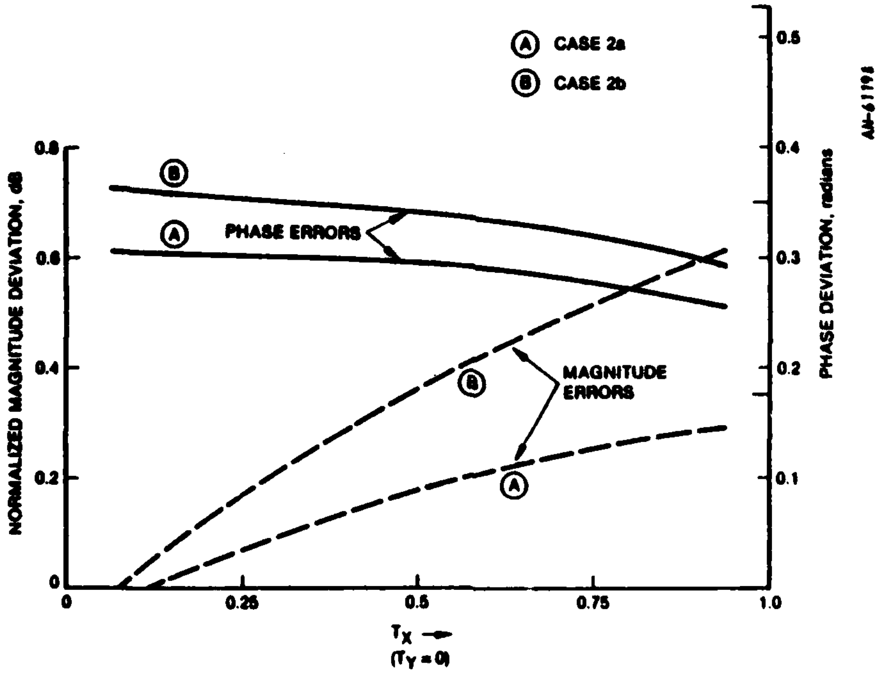

Figure A.14b. Skewed Imaginary Current Compared to 8-Segment Real Currents

$$\overline{E}_{meas} = |\bar{b}| \exp(j\beta)\hat{i}_x$$

then the vector deviation is given by

$$VE = \frac{|\overline{E}_{ref} - \overline{E}_{meas}|}{|\overline{E}_{ref}|} = \frac{|a \cos \alpha - b \cos \beta + j(a \sin \alpha - b \sin \beta)|^{1/2}}{|a|}$$

$$= \frac{|a^2 + b^2 = 2ab \cos(\alpha - \beta)|^{1/2}}{|a|}$$

if $a \approx b$

then

$$VE \approx \frac{|2a^2 - 2a^2 \cos(\alpha - \beta)|^{1/2}}{|a|}$$

$$= \sqrt{2[1 - \cos(\alpha - \beta)]} \qquad \text{(A.21)}$$

Figure A.15 plots the vector deviation for Case 1(a) and (b) and Case 2(b). The data from the figure agrees quite well with Eq. A.21.

The major consequence of the above results on the effects of the current distributions is that the overall effects on the antenna pattern can be modeled by (1) a small spatial displacement (to the current distribution mean) for the case of a skew in the real part, and/or (2) a constant phase shift (derived from the ratio of the areas of the imaginary and real parts) for the effect of the imaginary current. Therefore, instead of needing to model a complex current in detail, with many current segments (which can change as a function of scan angle) a simple

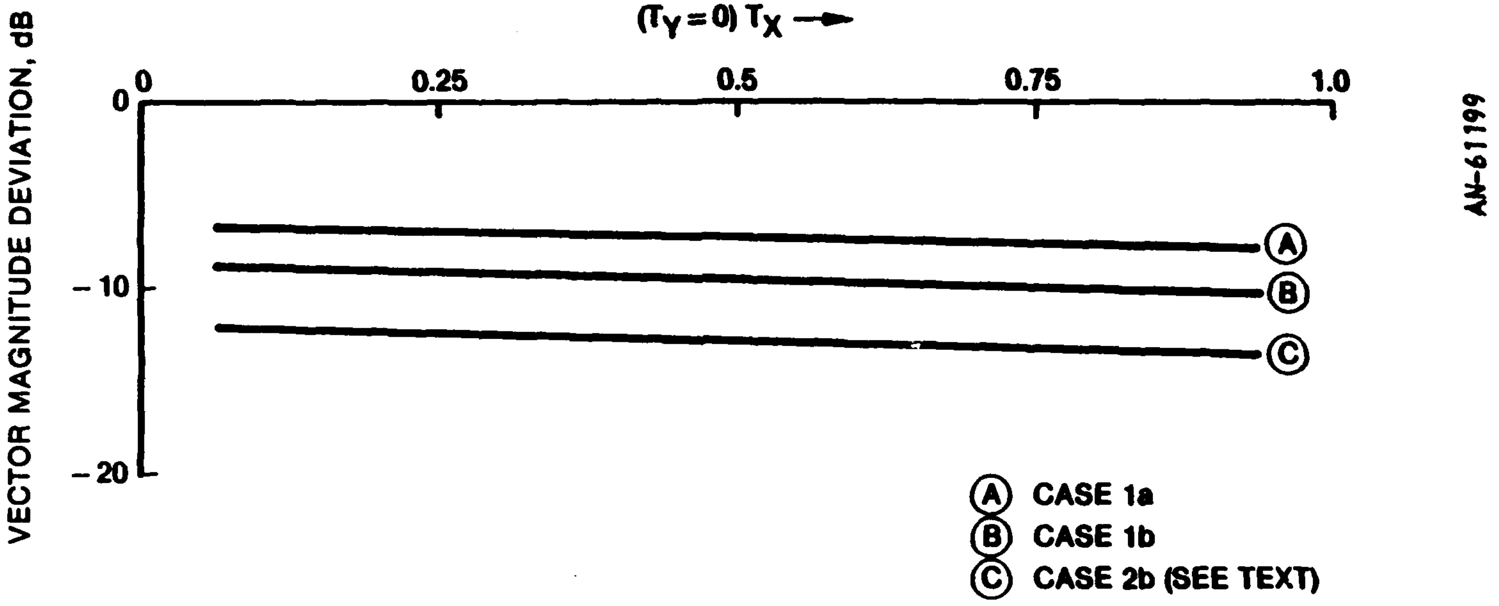

Figure A.15. Comparison of Effect Due to Imaginary Currents

4- or 8-segment model can be used along with a displacement and/or phase shift.

Ground Plane Mirror and Z-Directed Current

Another potential need for detail in the element current model is feedline radiation due to an imbalanced current. This would typically appear as a Z-directed current source. Therefore, the next area for evaluation was concerned with the effect of a current in the Z-direction when a ground plane is present. The reference for this case is eight real element segments plus eight real, mirrored element segments. The mirrored currents are positioned 1/2 wavelength (in the Z-direction) from the actual current elements to simulate a perfect ground plane.

Using the above 16-current elements oriented in the X-direction for a reference, a comparison was made with a similar set of element currents, except that a Z-directed imbalance current plus its mirror image were added.

The magnitude and phase deviation are shown in Fig. A.16, while the vector deviation is shown in Fig. A.17 for both a 2% imbalance as well as a 10% imbalance. These imbalance values were arbitrarily chosen as a reference for future data evaluation. It appears that a 10% imbalance is insignificant for near-in sidelobes; however, 10% imbalance causes significant deviations near the edge of the T_x,T_y-plane . The conclusion is that feedline radiation of this type will be insignificant unless the imbalance is on the order of 10% and $|T|$ is large (i.e., >0.75).

Cross Bar Tilt

The last part of the element pattern evaluation concerned the effect of tilting the element currents which represent the cross-bar of the dipole. This tilt was also mirrored in simulated ground plane (perfect reflection). The reference for comparison was the 16-segment mirrored element currents described previously.

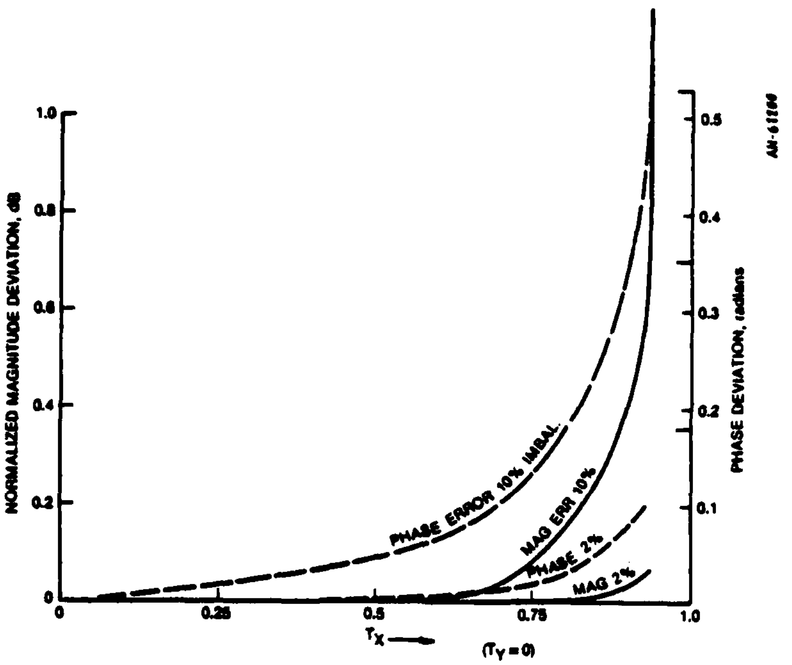

Figure A.16. Deviation Due to Imbalance Causing Current in Z-Direction

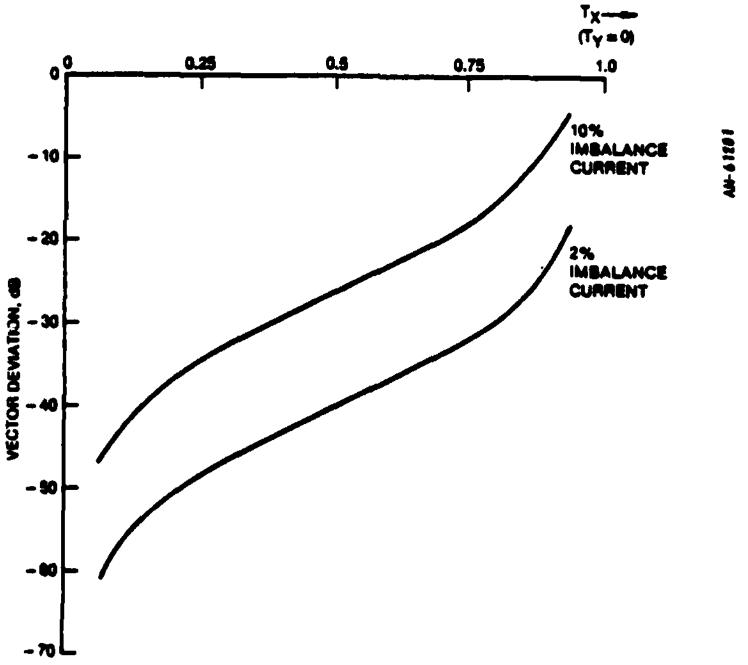

Figure A.17. Deviation Due to Imbalance Causing Current in Z-Direction All Currents Mirrored in Ground Plane

Figures A.18 and A.19 show the results of a 2° and 10° tilt. The results are similar to the 2% and 10% imbalance case. This seems reasonable, since the component for a tilted antenna is proportional to the sine of the angle of tilt, and for small angles the sine of the angle is approximately equal to the angle itself. Again the conclusion is that the effect can be neglected unless the tilt and |T| are large (i.e., >0.75).

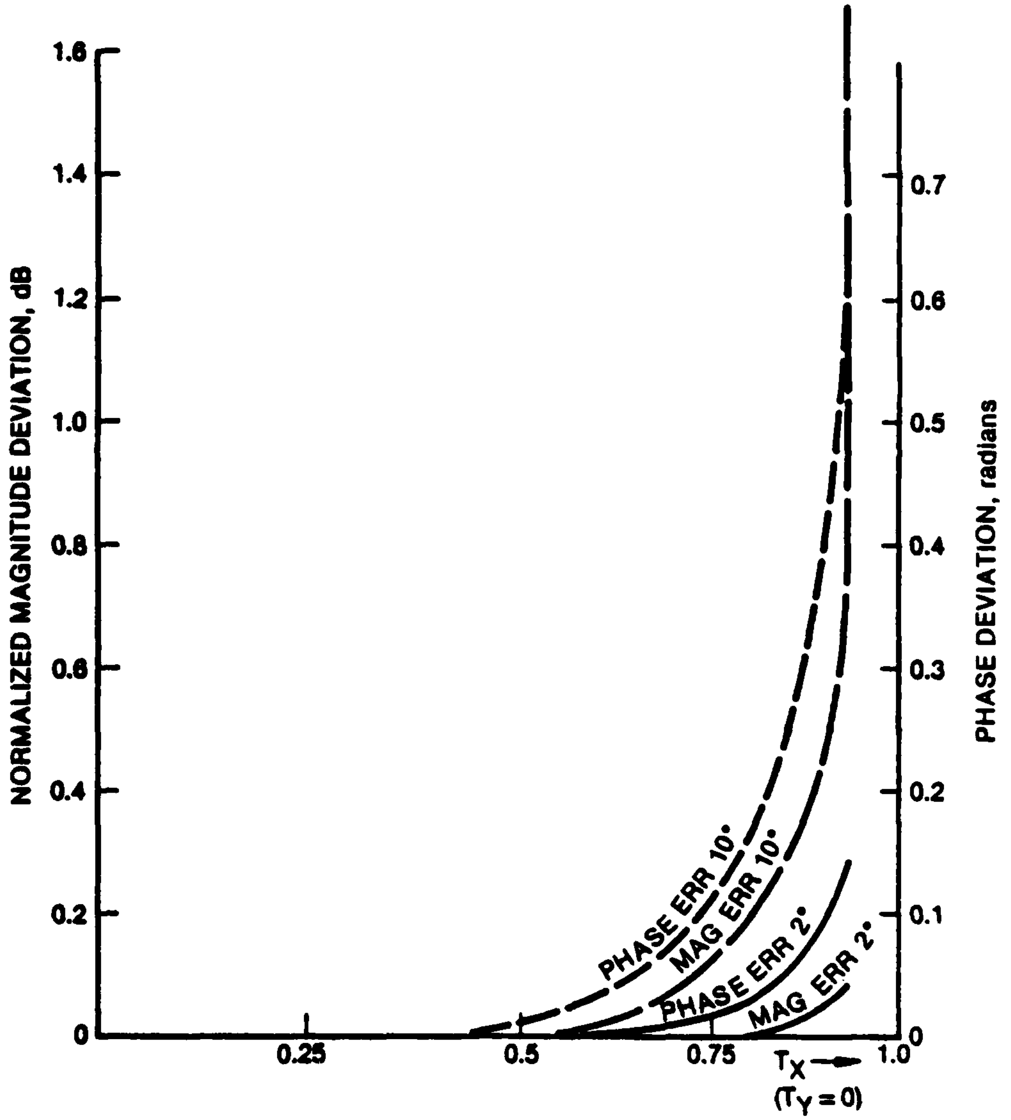

Figure A.18. Deviation Due to 2° and 10° Crossbar Tilt

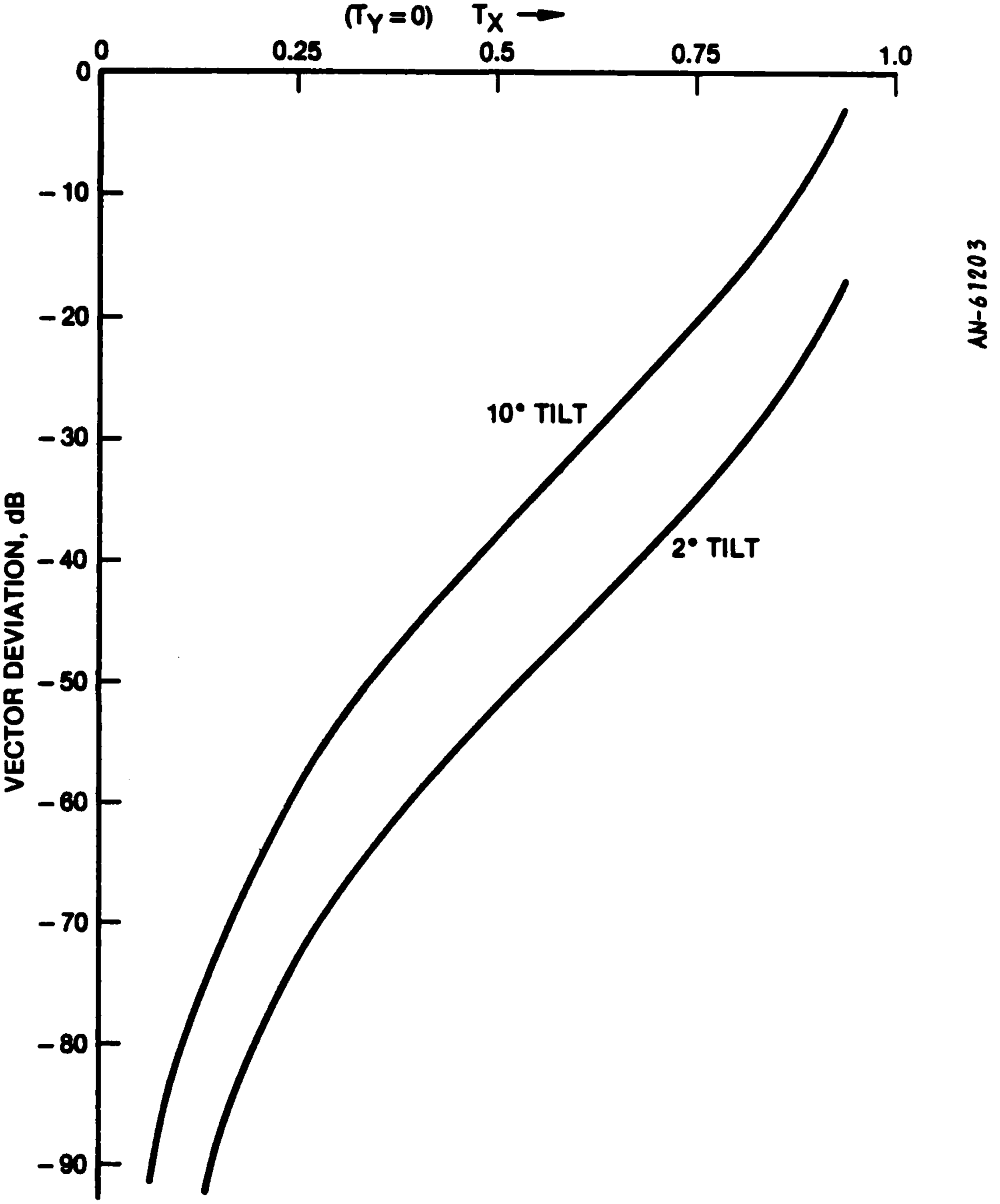

Figure A.19. Deviation Due to 2° and 10° Crossbar Tilt

A.2.4.3 Structural Deviations

Large scale structural deviations can be caused by differential structural heating or acceleration. These deformations can be described by first specifying the nominal location of a set of points $\{\overline{P}_k\}$, and a set of deformations $\{D\overline{P}_k\}$. By definition, then, the set of point locations with deformations is $\{\overline{P}_k + D\overline{P}_k\}$.

Typically a structural sample of 10 to 10^4 points provides sufficient detail for these deformations. To model the RF performance we need to know the deformation of each array element, which typically involves a set of 10^2 to 10^6 locations $\{\bar{x}_i\}$. The problem solved here is the interpolation of these deformations from the specified set of structural points $\{\overline{P}_k\}$ to the element locations $\{\bar{x}_i\}$.

A set of subroutines has been written to solve this interpolation problem. The program has been successfully tested on several sets of GRC-generated element locations using sample structural data supplied by Draper Labs in the format specified by Hancock (Appendix B).

An extrapolation of computer run times indicates that this program can process element locations numbering on the order of one-half million in about 2-3 min of CPU time. This is significantly more efficient than was initially expected.

The Problem

We are given a tape. The first file contains the coordinates of a set of structural sample points $\{\overline{P}_k\}$ in the X,Y-plane . (Elimination of the planar assumption is discussed below.) An example of such a set is given in Fig. A.20a.

This set may be cut into subsets, called "gores." A gore can be any subset of adjacent points in $\{\overline{P}_k\}$. One such example is illustrated in Fig. A.20b.

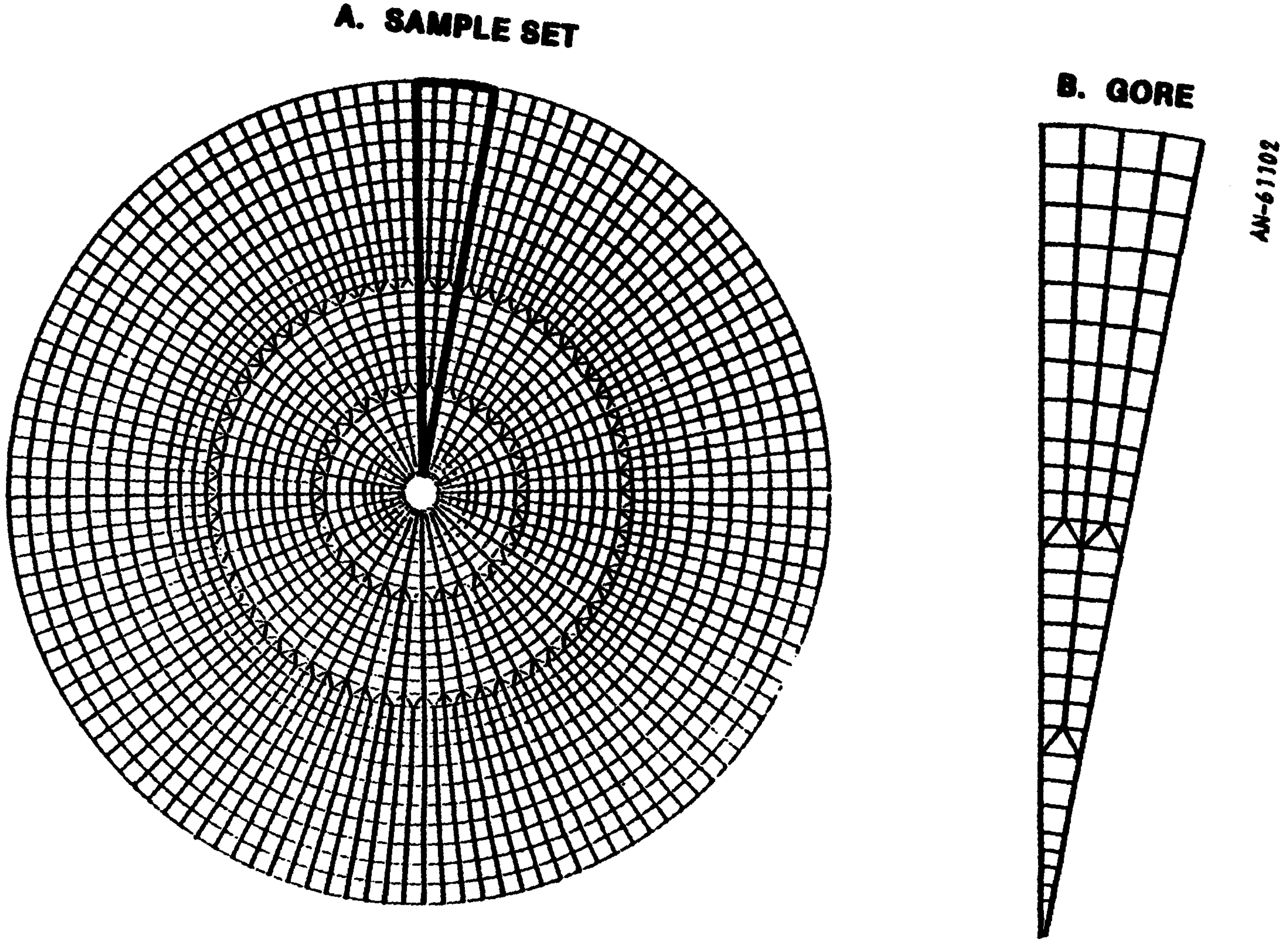

Figure A.20. Structural Sample Data

The next tape file contains a set of deformations $\{D\overline{P}_k\}$. Each vector $\overline{DP}_k$ corresponds to the $[\Delta x, \Delta y, \Delta z]$-structural deviation from the nominal point $\overline{P}_k$.

Finally, we are supplied with a set of nominal array element locations $\{\bar{x}_i\}$. The desired output will be a set of deformations $\{\overline{D}x_i\}$ which model the transformation characterized by the deformed structural data. We shall do this via a linear interpolation from the base sets $\overline{\{P_k\}}$ and $\{\overline{DP}_k\}$.

The Solution

The basic solution is very simple:

Step 1. Given $\bar{x}_i$, we find the three closest, non-colinear sample points $\overline{P}_{i_1}, \overline{P}_{i_2}, \overline{P}_{i_3}$.

Step 2. We solve for $\lambda_1, \lambda_2, \lambda_3$, satisfying

$$\bar{x}_i = \lambda_1\overline{P}_{i_1} + \lambda_2\overline{P}_{i_2} + \lambda_3\overline{P}_{i_3} \quad , \quad \lambda_1 + \lambda_2 + \lambda_3 = 1$$

Step 3. We have been given a mapping L , such that:

$$L\left(\overline{P}_{i_1}\right) = D\overline{P}_{i_1}$$

$$L\left(\overline{P}_{i_2}\right) = D\overline{P}_{i_2}$$

$$L\left(\overline{P}_{i_3}\right) = D\overline{P}_{i_3}$$

We then define

$$
\begin{aligned}
\overline{Dx}_i &= L(\bar{x}_i) \\
&= L\left(\lambda_1 \overline{P}_{i_1} + \lambda_2 \overline{P}_{i_2} + \lambda_3 \overline{P}_{i_3}\right) \\
&= \lambda_1 L\left(\overline{P}_{i_1}\right) + \lambda_2 L\left(\overline{P}_{i_2}\right) + \lambda_3 L\left(\overline{P}_{i_3}\right) \\
&= \lambda_1 D\overline{P}_{i_1} + \lambda_2 D\overline{P}_{i_2} + \lambda_3 D\overline{P}_{i_3}
\end{aligned}
$$

Special Considerations

Since the number of element locations is potentially quite large (>500,000), prime consideration is given to computational speed. Figure A.21 lists the basic algorithmic approach; notice that the actual interpolation time (Steps 2 and 3) is very short when compared with the time spent searching for the three closest points (Step 1).[1]

Given these conditions, we can easily see how best to use them to our advantage. Namely, we have many points $\{\ldots, \bar{x}_n, \bar{x}_{n+1}\ldots\}$, so it would make sense to ask: "Is $\bar{x}_{n+1}$ near $\bar{x}_n$?" If it is, then we may abandon the search on the $(n + 1)$st iteration and simply use

$$\left\{\overline{P}_{n_1}, \overline{P}_{n_2}, \overline{P}_{n_3}\right\}$$

from the nth iteration.

We accomplish this by performing Step 2 first. We then examine

---

[1] It is worth noting that, as the program is presently implemented, each $\bar{x}_n$ comes tagged with a gore identifier. The search is, therefore, restricted to one gore--not the entire sample set.

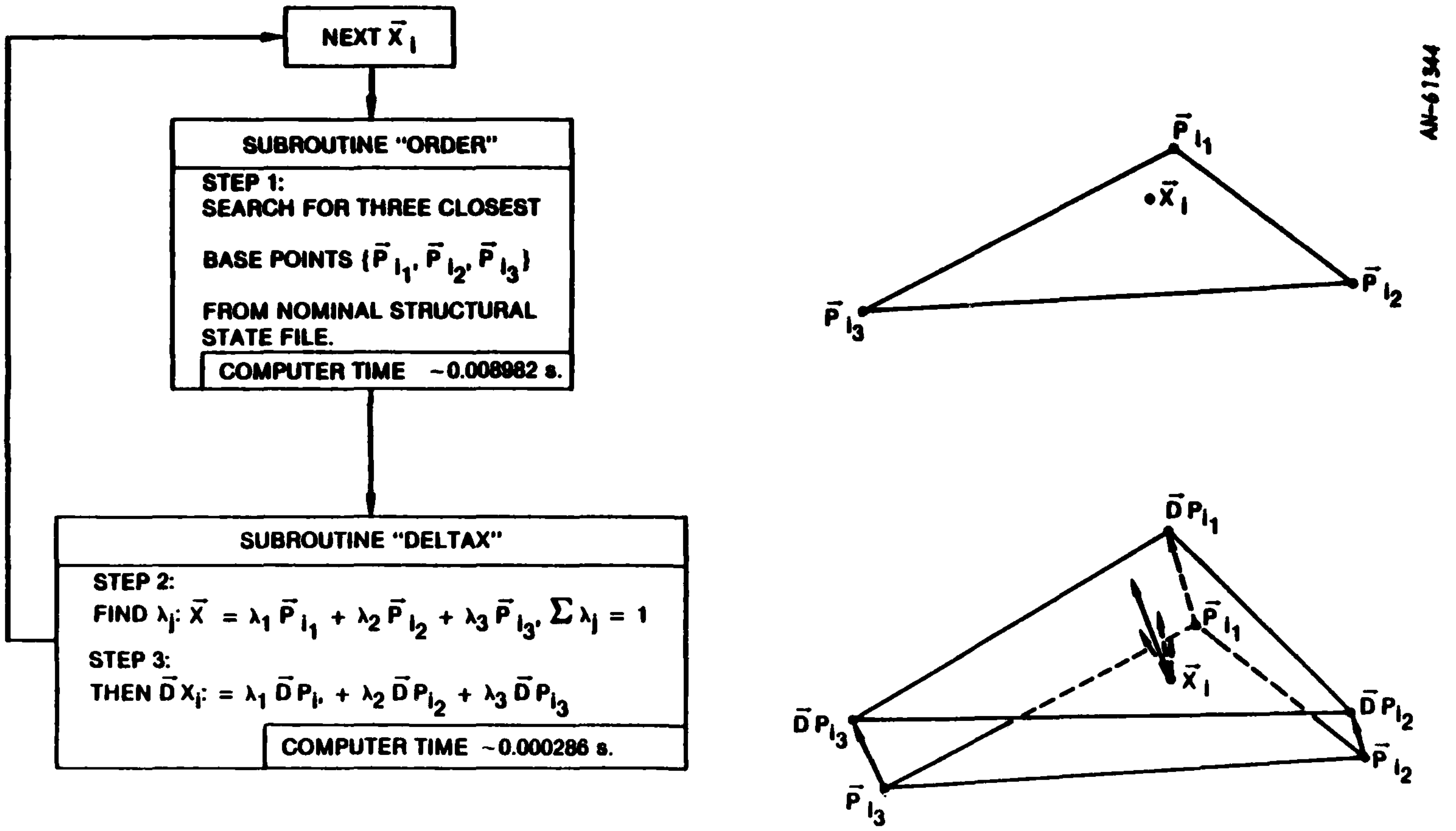

Figure A.21. Basic Algorithm

$$\left\{\lambda_j \quad \text{such that} \quad \bar{x}_{n+1} = \lambda_1 \overline{P}_{n_1} + \lambda_2 \overline{P}_{n_2} + \lambda_3 \overline{P}_{n_3} \quad , \quad \Sigma\lambda_j = 1\right\}$$

If convexity also holds (i.e., if $\lambda_j \geq 0$ for $j = 1,2,3$), then we know that $\bar{x}_{n+1}$ lies "inside" the triangle described by $\overline{P}_{n_1}$, $\overline{P}_{n_2}$, $\overline{P}_{n_3}$.

The computer code (Fig. A.22) documents the manner in which this modified algorithm proceeds.

Obviously, this scheme will work most efficiently only if the element locations are processed in an order which is "sensibly arranged." Figure A.23 shows the potential difference in run time.

For a "terribly arranged" sequence a search is performed for every element location. This is an extreme case which would be approached by

---

```
                PROGRAM GRMNTRP2

          INVOKE (READ DRAPER)
          INVOKE (READ GRC ELEMENT LOCATIONS)
          ETIME = CPUTIM()  !measures time to interp all points
    C
          DO (N=1,NUMGOR)
          .   DO (M=1,NUMELT)
          .   .   INVOKE (GIMME AN X)
          .   .   IF (M.EQ.1)
          .   .   .   INVOKE (DO IT ALL)
          .   .   ELSE !(M>1)
          .   .   .   CALL DELTAX2(P1,DP1,P2,DP2,P3,DP3,X,DX,INSIDE)
          .   .   .   IF (.NOT.INSIDE)
          .   .   .   .   INVOKE (DO IT ALL)
          .   .   .   END IF
          .   .   END IF
          .   .   INVOKE (STORE AN X)
          .   END DO
          END DO
    C
          ETIME = CPUTIM() - ETIME
          PRINT*, 'ETIME =', ETIME
          INVOKE (STORE NEW ELEMENT LOCATIONS)
```

Figure A.22. Modified Algorithm

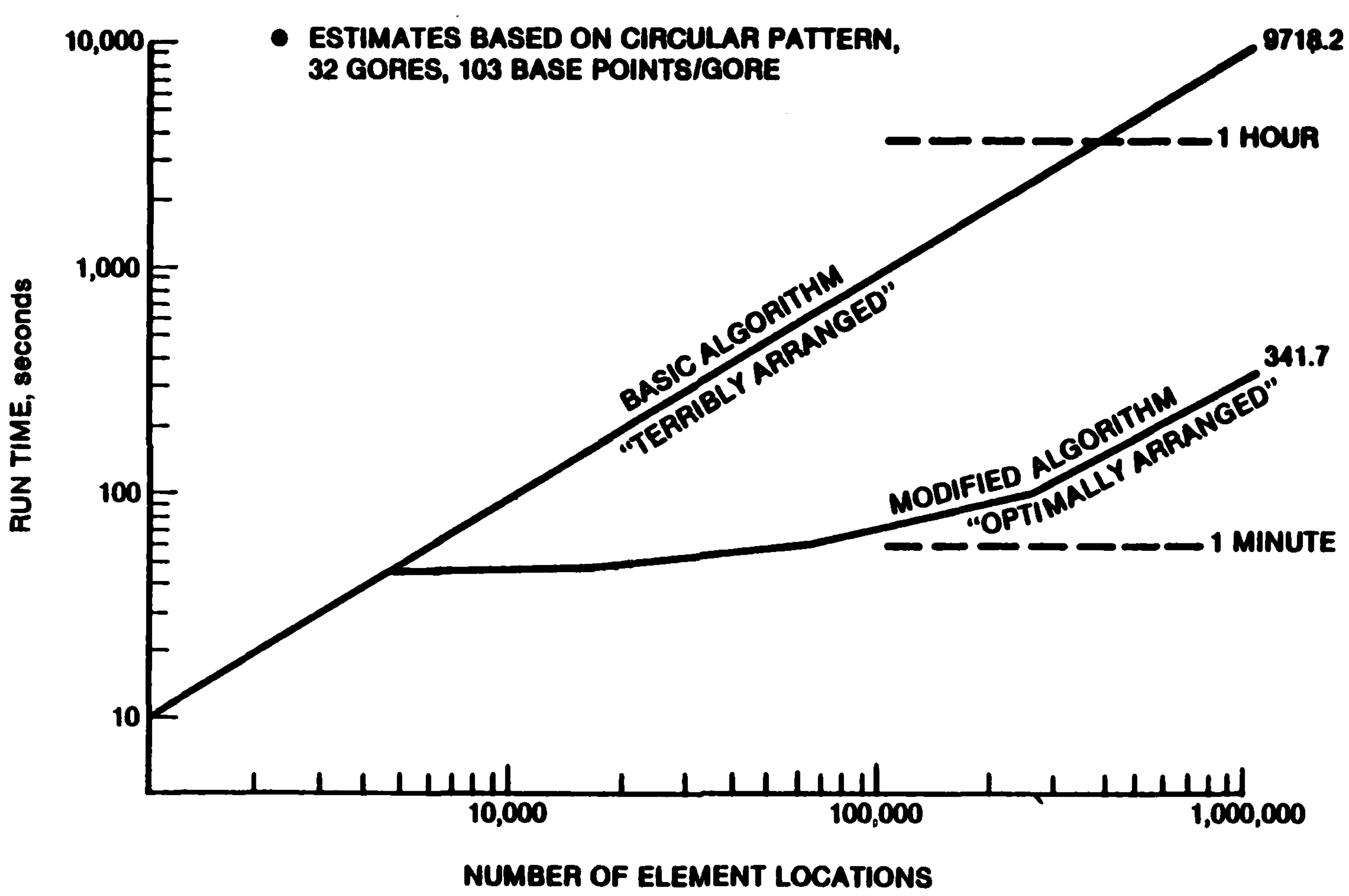

Figure A.23. Structural Deviation, CPU Time Versus Number of Element Locations a totally random sequence of element locations. Any "optimally arranged" sequence is the other extreme where all element points belonging inside a given set of 3 structural sample points are grouped consecutively. Realistic data sets will fall roughly in the middle of these two extremes.

Some additional effort will be devoted to generalizing the problem to sets of points lying on non-planar (e.g., parabolic) surfaces. The solution is similar to the one given here; we merely remove the affinity constraint on λ_j and substitute linear independence for non-colinearity when moving out into R^3.

A.2.5 Computer Running Time

Space-based radars typically contain arrays consisting of 10^5 to 10^6 elements. The processing and pattern calculation of such large arrays can require excessive computer (central processing unit or CPU) time. Several CPU timing tests were performed to determine the estimated times required to perform these lengthy computations. Timing tests were performed on array generation as well as pattern calculation via the inverse FFT algorithm.

The initial aperture distribution timing tests indicated that an extremely long run was needed to generate the circular Taylor-weighted array using the PAAS algorithms. (Some of these times are recorded in Table A.2.) Further investigation indicated the prime cause of this lengthy generation was due to the PAAS Bessel function routine. This routine was replaced by a GRC subroutine for generating Bessel functions, and the time required to generate the Taylor-weighted aperture was reduced by a factor of four.

The generalized Taylor ($p = 1$) weighting is generated by using a look-up table (as explained in Sec. A.2.3). Timing tests indicated that this technique was almost a factor of two faster than that used for the

TABLE A.2

APERTURE ARRAY GENERATION AND WEIGHTING

(CPU Time in Seconds)

Array Size (N × N)	32 × 32	64 × 64	128 × 128	256 × 256
PAAS Algorithm Taylor (p = 0)	15.2	58.0	Not performed	Not performed
GRC Algorithm Taylor (P = 0)	3.27	12.1	45.9	186.0
SARF Simulation Taylor (P = 0,1)	2.7	6.8	24.4	93.2
SARF Simulation Bickmore-Spellmire	1.9	6.8	26.1	102.4
Unweighted (Uniform)	1.7	5.7	21.2	83.7

Taylor (p = 0) case. Therefore, to provide consistency in the two Taylor distributions (p = 0 and p = 1) both are implemented as look-up table-interpolation algorithms.

Table A.2 shows the results of CPU timing tests for generating an unweighted (uniform), Taylor (p = 0, 1) and the Bickmore-Spellmire (p = 1) distribution as they are currently implemented in SARF simulation. Also included are the test results for the Taylor (p = 0) case using the PAAS algorithm. As expected, these tests show that the CPU time is directly proportional to K^2 ; where K is the number of grid points on a single side of the aperture array.

Timing tests were also performed for both expanded and unexpanded FFT arrays. An expanded FFT array is one in which part of the array (prior to transforming) is filled with zeroes so that the FFT output will have better pattern resolution. Two parameters are used to describe the array size: N represents the number of points on one side of the expanded array and K is the number of points in the unexpanded array. Therefore, the number of additional zeroes added to the expanded array is $N^2 - K^2$.

Table A.3 presents CPU time data obtained by performing the FFT for the case of

$$N = K$$

where N = the number of grid points on one side of the expanded input to the FFT

K = the number of grid points on one side of the unexpanded array

This table clearly shows that the CPU time is proportional to N^2 , not the expected $[N \log_2 N]^2$ as dictated by FFT processing. The most probable reason for this result is that reading and writing data to a file dominates processing time.

TABLE A.3

FFT CENTRAL PROCESSING TIME

FFT Array Size (N × N)	FFT Time (CPU seconds)	FFT Time/N^2
256 × 256	72.5	0.00111
128 × 128	18.1	0.00112
64 × 64	4.6	0.00112
32 × 32	1.3	0.00127

Figure A.24 shows the overall results of timing tests for various values of N and K. These results can be approximated quite well by the equation:

$$t = aK^{1/2}N^{3/2}$$

for $N/K = 1, 2, 4$

where t = CPU time in seconds
a = constant whose value is 0.0011

Both the above equations and Fig. A.24 show that K has little effect on the total CPU time and first-order estimate of the time needed is proportional to N^2, regardless of the value of K.

A.2.6 Validation

While validation may be the most tedious part of a simulation development, it is probably the most important part. The validation (to date) of the SARF simulation has been divided into three categories:

1. Validation of antenna patterns, computed using the PAAS inverse FFT algorithm
2. Validation of the brute-force calculation
3. Validation of element pattern and polarization computation

The completion of these three tasks not only guarantees that the software has been installed properly, but also provides a measure of the accuracy of the simulation.

PAAS FFT Validation

To verify proper installation and to determine the accuracy of PAAS, two types of validation tests were performed. The first type con-

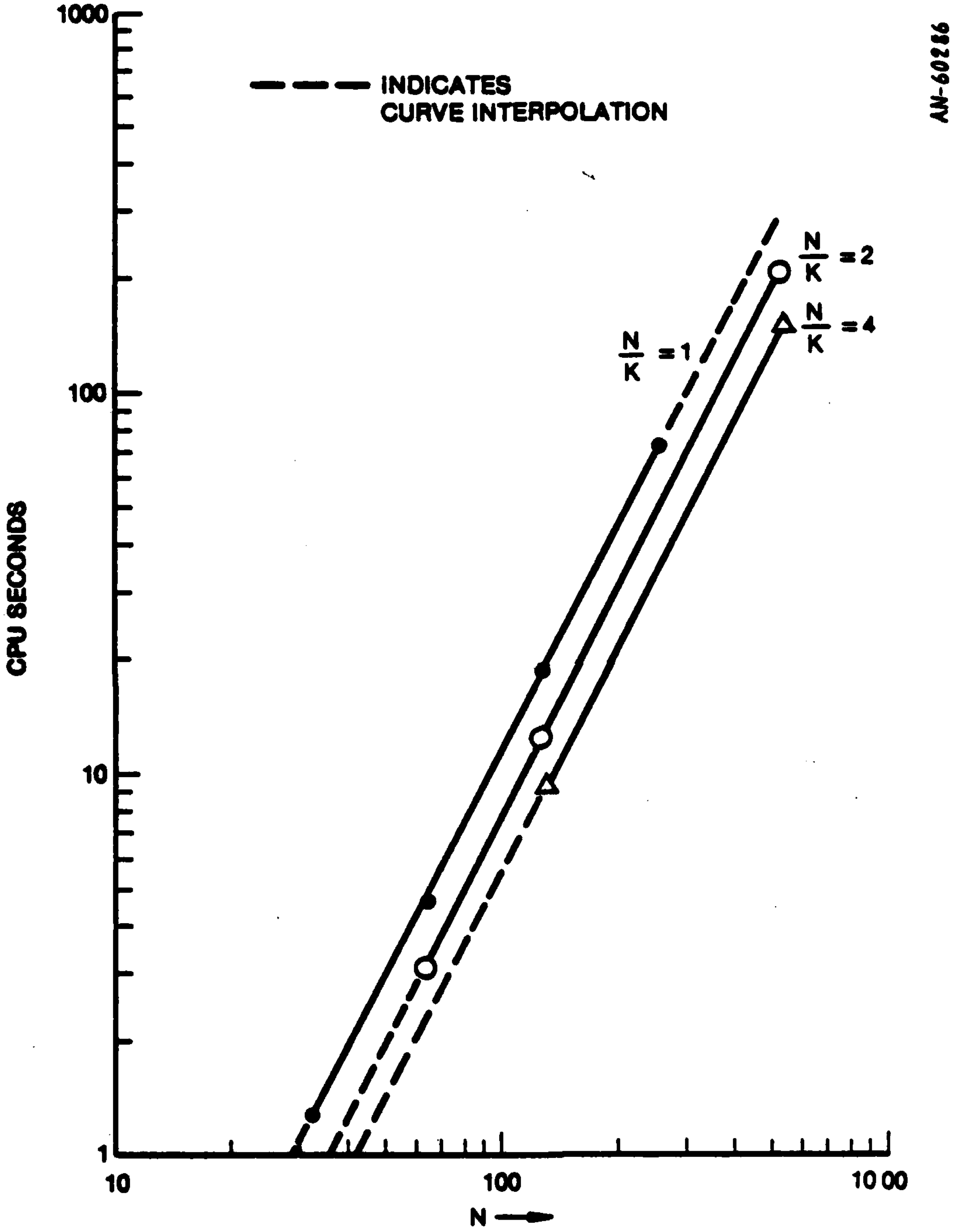

Figure A.24. FFT CPU Seconds Versus N for N/K = 1,2,4 sisted of comparing the PAAS[1] output with closed-form analytical antenna patterns. Two cases were tested: a uniform rectangular aperture and a binomial weighted rectangular aperture. The second type of validation test dealt with a comparison of the patterns generated by a circular array to that of a circular continuous (reflector) aperture.

The far-field antenna pattern for a uniformly illuminated linear array of N elements is given exactly by:

$$E(\theta) = \frac{\sin\left[N\pi\left(\frac{d}{\lambda}\right)\sin\theta\right]}{N\sin\left[\pi\left(\frac{d}{\lambda}\right)\sin\theta\right]}$$

where $E(\theta)$ = electric field vector

d = element spacing

λ = wavelength of the radiating aperture

θ = angle between the pattern and a line perpendicular to the array

This equation can be generalized for a planar array by using separable weighting functions, i.e., the planar array can be realized as the product of two linear arrays, which in turn provides separable far-field patterns.

To verify PAAS, a comparison was made for a uniform illumination with array sizes of 32 × 32, 64 × 64 and 128 × 128 elements. The results of these comparisons indicate that the maximum absolute error obtained (between PAAS output and the analytical expression) is 3×10^{-6}, while the typical error was 2×10^{-7} (see Table A.4).

---

[1] Since the FFT input array consists of an even number of points, the PAAS output contains a linear phase error. This error is equal to a shift of one-half grid spacing and is corrected in the SARF simulation. The validation of the PAAS FFT allowed for this phase error.

TABLE A.4

ABSOLUTE ERROR--FOR UNIFORM AND BINOMIAL ARRAYS (FFT PROCESSING)

Input Array Size (32 × 32)

Point Location on Pattern	Absolute Error* Uniform	Absolute Error* Binomial
-3 dB	2×10^{-6}	2×10^{-6}
-10 dB	2×10^{-6}	2×10^{-6}
-20 dB	2×10^{-6}	2×10^{-7}
-50 dB	Not applicable	3×10^{-7}
-100 dB	Not applicable	2×10^{-9}
First Sidelobe Peak	3×10^{-6}	Not applicable
Second Sidelobe Peak	3×10^{-6}	Not applicable

---

*Pattern peak value = 1.0.

Since the VAX-11 is a 32-bit machine with 23 bits of floating point precision, the truncation error is $2^{-23} = 1.19 \times 10^{-7}$. Therefore, the results of this test clearly show that the typical accuracy approaches the machine precision.

Another closed form analytical pattern, used for comparison, is represented by an array whose current excitations I_n are equal to the binomial coefficients, i.e.,

$$I_n = \frac{N!}{(N - n)!n!}$$

which yields an electric field of:

$$E(\theta) = \left[1 + e^{j2\pi(d/\lambda) \sin \theta}\right]^N$$

This pattern provides a means of testing the results at levels down to -120 dB and lower. A routine was designed and implemented to generate a binomial array. Tests were performed on 32 × 32 and 64 × 64 arrays. The results indicated typical errors of 2×10^{-6}, and truncation errors dominated at levels which were 120 dB below the peak value, as is shown in Table A.4. Nevertheless, this agrees with the expected results dictated by the machine precision of the VAX.

In addition to the above validation of exact (closed form analytical) solutions, two approximate comparisons were made. By approximate we mean that the pattern obtained for the discrete array (using the FFT algorithm) was compared to the analytical pattern for a continuous distribution. Obviously, some error is expected in these comparisons, since neither of the patterns is "band-limited," and the sampling theorem tells us that some aliasing will be involved.

The two distributions used for these tests were the circular Taylor ($p = 0$) and the circular Bickmore-Spellmire ($p = 1$). The results of these tests are summarized in Table A.5. As expected, the Taylor distribution shows a larger deviation than does the Bickmore-Spellmire. Since the Taylor sidelobes decay at a much slower rate than the Bickmore-Spellmire (see Figs. A.25a and A.25b), the former will be affected by more aliasing.

The results of these tests indicate considerably larger deviations than the tests of the previously discussed exact cases. This should not be a surprise, since we are comparing the continuous Fourier transforms of continuous functions to the discrete Fourier transforms of a discrete (sampled) functions. The important aspect of these tests is good agreement in the shape of the two patterns.

TABLE A.5

ABSOLUTE DEVIATION--FOR TAYLOR (p = 0) 40 dB AND BICKMORE-SPELLMIRE (p = 1) 40 dB

(FFT Processing)

Input Array Size = (128 × 128)

Point Location on Pattern	Absolute Deviation* Taylor	Absolute Deviation* Bickmore-Spellmire
-3 dB (mainlobe)	3.3×10^{-4}	8×10^{-6}
-10 dB (mainlobe)	4.8×10^{-4}	8×10^{-6}
-20 dB (mainlobe)	2.5×10^{-4}	1×10^{-6}
-50 dB (mainlobe)	9×10^{-5}	2×10^{-6}
First Sidelobe Peak	2×10^{-4}	1×10^{-6}
Second Sidelobe Peak	3×10^{-5}	1×10^{-6}

---

*Pattern peak value = 1.0.

Brute-Force Validation

Validation of the "brute-force computation" algorithm directly paralleled the PAAS FFT validation. Again, the validation was performed in two parts. The first part utilized the analytical patterns from the uniform and binomial weighted rectangular arrays (as described in the FFT validation).

Since the "brute-force" calculation is performed with double precision variables (16 decimal digits of precision), its output accuracy should exceed that of the FFT (7 decimal digits of precision). The "brute force" accuracy will be considerably less than 16 decimal places since the aperture weighting is performed using single-precision variables.

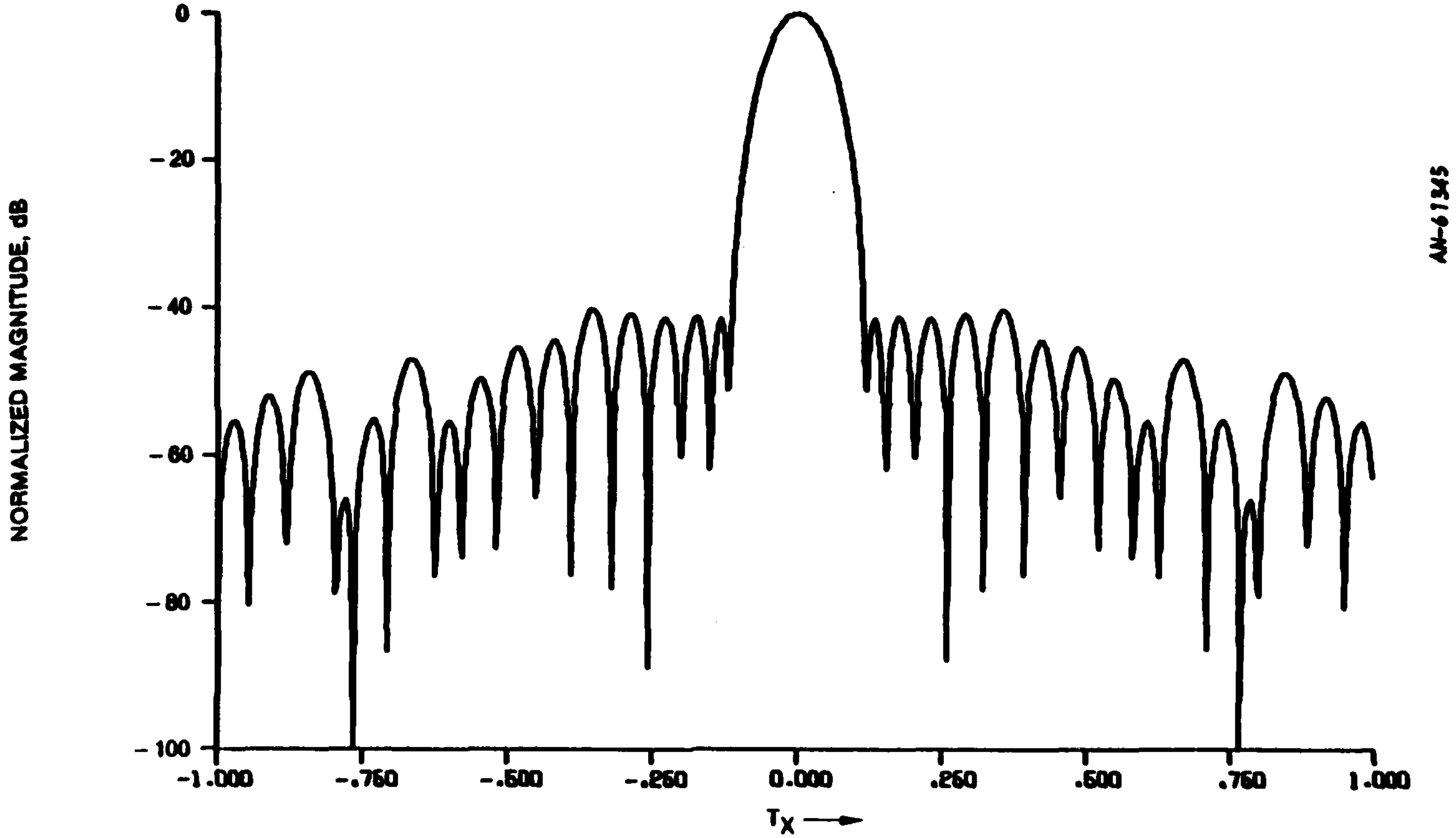

Figure A.25a. Pattern for Taylor (p = 0) Weighted Array

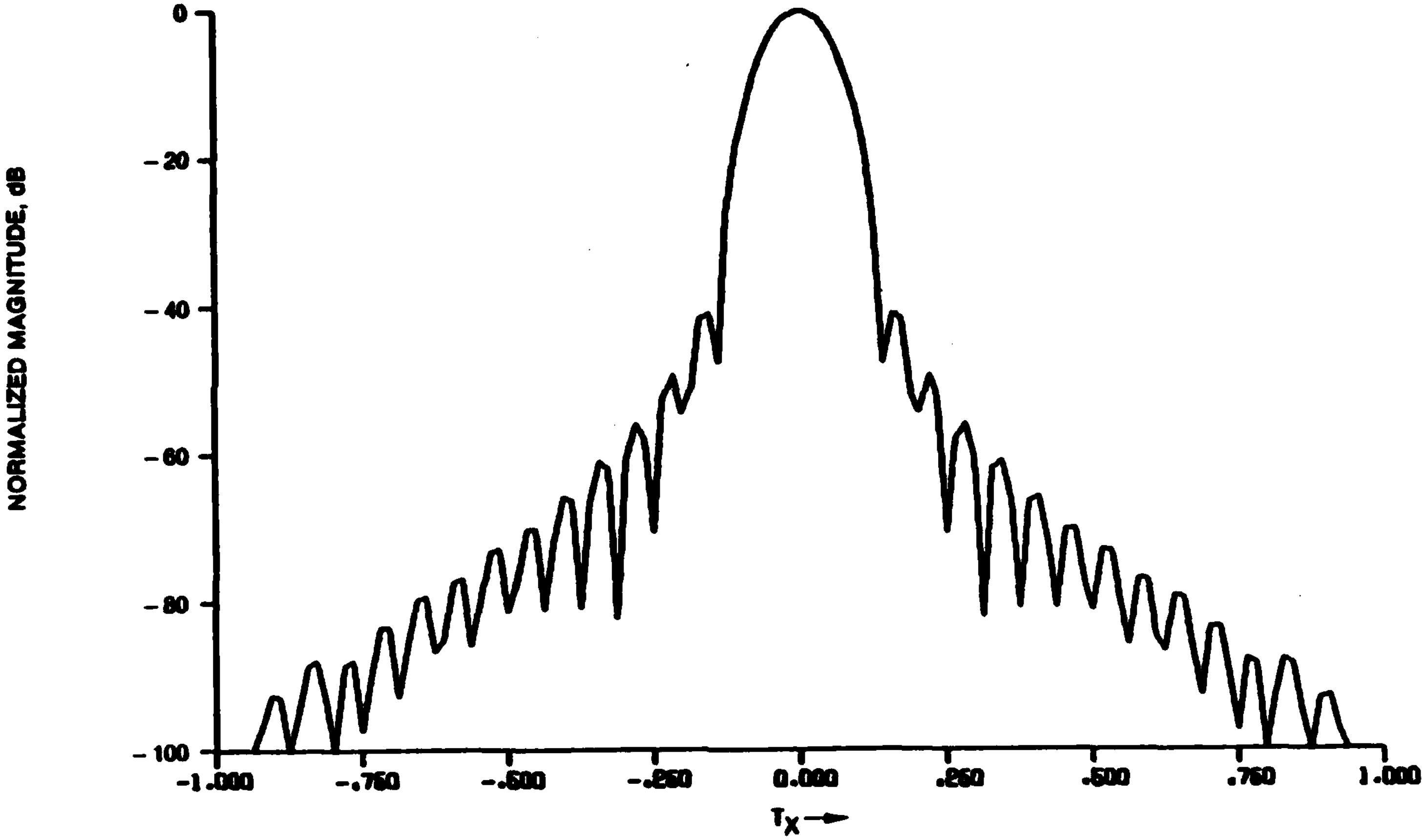

Figure A.25b. Pattern for Bickmore-Spellmire (p = 1) Weighted Array

The results of the comparison of the "brute-force" calculations to analytical counterparts are summarized in Table A.6. The accuracy is better for both patterns. Note that the error for the pattern of the binomial weighted array increases monotonically with decreasing pattern amplitude. This is shown graphically in Fig. A.26, which plots vector error versus T_x and pattern amplitude.

The second part of this validation consisted of a comparison of the FFT output with the "brute-force" output for a circular Taylor ($p = 0$) pattern. This pattern was chosen since it provided the largest deviation during the FFT validation (due to aliasing as discussed above). Table A.7 summarizes the results of this comparison and shows that the two methods are in close agreement.

The validation tests described in this section show that the "brute-force" computation provides sufficient accuracy to calculate any portion of antenna pattern that is 140 dB (or less) below the peak

TABLE A.6

ABSOLUTE ERROR (BRUTE-FORCE CALCULATION) FOR UNIFORM AND BINOMIAL WEIGHTED ARRAYS

Point Location on Pattern	Absolute* Error Uniform	Absolute* Error Binomial
-3 dB (mainlobe)	$<1 \times 10^{-8}$	$<1 \times 10^{-8}$
-10 dB (mainlobe)	$<1 \times 10^{-8}$	$<1 \times 10^{-8}$
-20 dB (mainlobe)	1×10^{-8}	1×10^{-8}
-50 dB (mainlobe)	Not applicable	6×10^{-9}
-100 dB (mainlobe)	Not applicable	1.5×10^{-10}
First Sidelobe Peak	1×10^{-8}	Not applicable
Second Sidelobe Peak	1×10^{-8}	Not applicable

---

*Peak = 1.0.

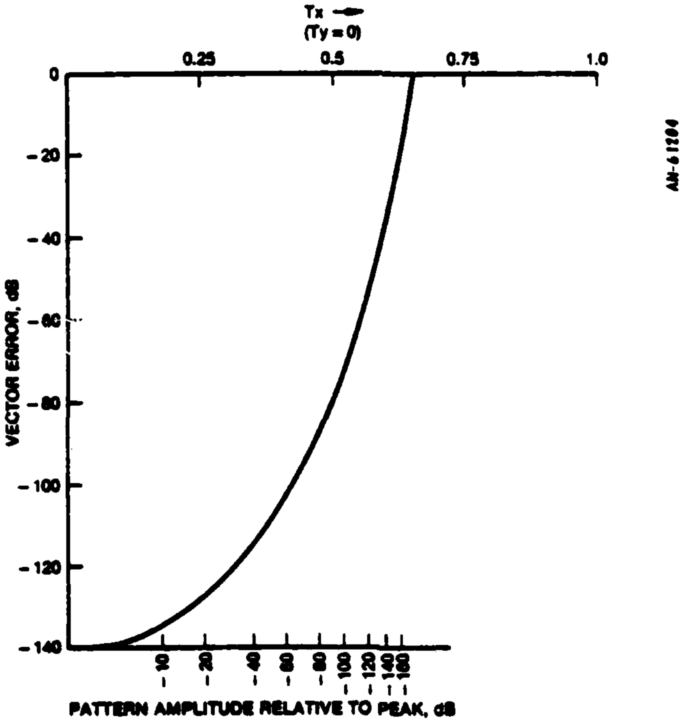

Figure A.26. Vector Error for Binomial Weighted "Brute-Force" Calculation

TABLE A.7

ABSOLUTE ERROR (BRUTE-FORCE CALCULATION FOR TAYLOR COMPARED TO FFT WEIGHTED ARRAY)

Point Location on Pattern	Absolute* Error
-3 dB	1×10^{-7}
-10 dB	1×10^{-6}
-20 dB	2×10^{-6}
-50 dB	5×10^{-6}
First Sidelobe Peak	5×10^{-6}
Second Sidelobe Peak	3×10^{-5}

---

*Peak = 1.0.

value. This allows accurate computation near antenna nulls with sufficient accuracy for almost any evaluation.

Element Pattern Evaluation

Validation of the element pattern computation was accomplished by comparing a 1/2-wave dipole to a series of infinitesimal current elements. This validation is described in detail in Sec. A.2.4.2.

MISSION
of
Rome Air Development Center

[illegible] executes research, development, test and [illegible] programs in support of Command, Control [illegible] intelligence (C^3I) activities. Technical [illegible] within areas of technical competence [illegible] Offices (POs) and other ESD [illegible] technical mission areas are [illegible] electromagnetic guidance and control, sur- [illegible] aerospace objects, intelligence data [illegible] information system technology, [illegible] solid state sciences, microwave [illegible] reliability, maintainability and [illegible]

END

FILMED

11-83

DTIC